Universiteit Antwerpen
Faculteit Wetenschappen
Departement Fysica

Quantitative atomic resolution electron microscopy using advanced statistical techniques

Kwantitatieve atomaire resolutie elektronenmicroscopie met geavanceerde statistische technieken

Proefschrift voorgelegd tot het behalen van de graad van
Doctor in de Wetenschappen
aan de Universiteit Antwerpen, te verdedigen door

Annick De Backer

Promotor:
Prof. dr. Sandra Van Aert

2015

Doctoral Committee

Chairman
Prof. dr. Jan Sijbers, University of Antwerp - Belgium

Promotor
Prof. dr. Sandra Van Aert, University of Antwerp - Belgium

Members
Prof. dr. Christoph T. Koch, University of Ulm - Germany
Prof. dr. Peter Goos, University of Leuven, University of Antwerp - Belgium
Prof. dr. Sara Bals, University of Antwerp - Belgium
Prof. dr. Jacques Tempère, University of Antwerp - Belgium
Prof. dr. Sabine Van Doorslaer, University of Antwerp - Belgium

This research was financially supported by the FWO, the Research Foundation Flanders.

Contact Information
Annick De Backer
University of Antwerp - Department of Physics
EMAT - Electron Microscopy for Materials Science
Groenenborgerlaan 171
B-2020 Antwerp
Belgium
annick.debacker@uantwerpen.be

Contents

Summary

The physical properties of nanostructures are controlled by their exact chemical and structural composition. In order to fully understand the structure-property relationship of materials, it is important to reliably quantify structure parameters, such as the positions of the atoms, the type of the atoms, and the number of atoms. Atomic resolution (scanning) transmission electron microscopy ((S)TEM) is established as a method to determine the internal structure of materials at a local scale. Recently, the introduction of aberration-corrected electron microscopy has improved the interpretability of the images. Nevertheless, it is impossible to directly extract numbers from the images by means of visual interpretation only. In this study, atomic scale aberration-corrected (S)TEM is therefore pushed toward precise measurements of unknown structure parameters using advanced statistical techniques in a model-based framework. The first part of this thesis mainly focuses on the methodology for a quantitative approach in atomic resolution (S)TEM. In the second part, the possibility to count the number of atoms in a projected atomic column has been investigated.

The starting point of a quantitative analysis is the availability of a physics-based model which depends on the unknown structure parameters and which describes the expectations of the images. In this way, quantitative structure determination can be reduced to a statistical parameter estimation problem. The pixel values in the recorded images are then the observations from which the structure parameters can be estimated by fitting the model to the experimental images using a criterion of goodness of fit, which quantifies the similarity between the experimental images and the model. Ultimately, the precision with which the parameters can be estimated is limited by noise. Statistical parameter estimation theory provides a theoretical lower bound on the variance of the parameters, i.e. the attainable precision, and thus represents an intrinsic limit on the precision. The concept of attainable precision can be used to determine how structure parameters of interest should be estimated from the available set of observations and whether the highest possible precision can be attained using a particular approach to estimate the structure parameters.
It has been investigated how to measure atomic column positions as accurate and precise as possible using a focal series of images, which is often recorded for the reconstruction of the wave function at the exit plane of the object. This exit wave is closely related to the object structure. Using simulations, it turns out that the reconstructed complex exit wave contains the same amount of information concerning the atomic column positions as the full series of focal images. In addition, it has been shown that the same amount of information can be retrieved from the phase of the reconstructed complex exit wave for thin samples, which act as weak phase objects.
The accuracy and precision of the estimated structure parameters of interest of annular dark

field (ADF) STEM images have also been investigated. Here, the atomic column positions and the scattering cross-sections have been evaluated. The latter parameter describes the total intensity of scattered electrons by an atomic column and has been shown to be successful for the quantitative interpretation of the image intensities of ADF STEM images in terms of atom type and number of atoms. Using detailed multislice simulations, it has been shown that even for low incident electron doses, the theoretical lower bound on the variance of the estimates has been attained by estimation of the structure parameters using the least squares estimator.
Direct implementation of the least squares estimator in which all parameters are estimated at the same time is only feasible for images containing a limited number of projected atomic columns. Therefore, an efficient algorithm has been proposed in order to analyse large fields of view. Several experimental data sets have been used to apply the novel algorithm in order to estimate unknown structure parameters. These applications illustrate the various possibilities for quantitative analyses at the atomic scale with high precision offered by the improved algorithm.

In the second part of this thesis, a statistics-based method in order to count the number of atoms of single-element crystalline nanostructures from ADF STEM images has been discussed in detail together with a thorough study on the possibilities and inherent limitations. In order to count the number of atoms, it is assumed that the total scattered intensity, i.e. the scattering cross-section, scales with the number of atoms per atomic column. The distribution describing the probability that scattering cross-sections are generated by atomic columns containing a specific number of atoms should be inferred on the basis of the experimental scattering cross-sections. The number of atoms per atomic column is quantified using this estimated probability distribution. The number of atomic columns available in the observed STEM image, the number of components in the estimated probability distribution, the width of the components of the probability distribution, and the typical shape of a criterion to assess the number of components in the probability distribution directly affect the accuracy and precision with which the number of atoms in a particular atomic column can be estimated. It has theoretically been shown that single atom sensitivity is feasible taking the latter aspects into consideration.
This method has been used to quantify the number of atoms for different nanostructures from experimental ADF STEM images. In this manner, it has also experimentally been shown that single atom sensitivity can be attained. From the experimental analyses, it could be concluded that the statistics-based method should be complemented with another method in order to confirm the validity of the atom-counting results. In this thesis, a simulation-based approach has mainly been used for this purpose. The experimental scattering cross-sections are then compared with simulated scattering cross-sections obtained using detailed STEM simulations.
Although quantitative ADF STEM has become a powerful technique to characterise nanoparticles at an atomic scale, the determination of the atomic structure may still be extremely challenging because of the limited size and beam sensitivity of such particles. Therefore, keeping the incoming electron dose to a minimum is important. However, this may reduce the reliability of quantitative ADF STEM which has experimentally been demonstrated for nanoparticle atom-counting in this thesis. The limits for atom-counting could be diagnosed using the combined approach of a thorough statistical method and detailed image simulations.
Finally, the principles of detection theory have been used to quantify the probability of error for atom-counting from STEM images. Binary and multiple hypothesis testing have been investigated in order to determine the limits to the precision with which the number of atoms

in a projected atomic column can be estimated. The probability of error has been calculated when using STEM images on a pixel by pixel basis, scattering cross-sections, or peak intensities as a criterion to count atoms. Based on this analysis, it has been concluded that scattering cross-sections perform almost equally well as images and perform better than peak intensities. Furthermore, it has been shown that the optimal STEM detector design can be derived for atom-counting using the expression for the probability of error. It has been found that for very thin objects low angle annular dark field STEM is optimal and that for thicker objects the optimal inner angle increases.

1 Introduction

Materials science: Discovery and design of new materials

In the last decades, materials science has evolved from macro- to micro- to nanoscience. In this field of science, there is an ever-increasing interest in the development of nanostructured materials with novel properties requiring new synthesis techniques. With respect to this research, the paradigm of the traditional materials science tetrahedron is highly relevant [Yang 2012]. The materials paradigm is shown in Fig. 1.1 and illustrates the relationship between material's synthesis, structure, properties, and performance. Materials characterisation resulting in the availability of precise structural information is a crucial point in understanding the interrelationships in this paradigm. In combination with recent developments in nanotechnology, where one is nowadays able to make nanostructures with a well-chosen and controlled structure, an evolution from describing toward understanding and designing materials may be realised [Olson 1997, Olson 2000]. In addition, designing a final application requires a synergistic combination from the research results of various individual subfields to solve technological challenges [Yang 2012].

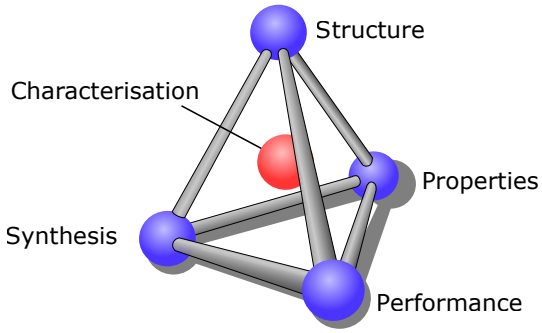

Figure 1.1: *Paradigm of materials science represented in the form of a tetrahedron (Adapted figure from [Wikipedia 2015]).*

Examples of such novel nanostructured materials having the attention from researchers are carbon nanotubes, fullerenes, metal nanoparticles, magnetic materials, ceramics, semi-conductor compounds, and catalytic nanoparticles [Klabunde 2002, Liz-Marzàn 2003]. The properties of these materials at the nano- or atomic scale change often significantly as compared to the properties of their bulk counterparts [Nebel 2003, Talapatra 2005, Huang 2010]. Moreover, for many nanomaterials their properties are significantly modified for extremely small changes in the local structure. Since the properties of materials are directly related to the atomic structure, the combination of theoretical and experimental studies is indispensable in order to understand the relation between structure and properties being one of the links in the materials paradigm. On the one hand, theoretical studies allow one to calculate properties of materials with a known atomic structure [Botti 2007]. On the other hand, experimental characterisation methods should be able to determine the structure at the atomic scale of new synthesised materials. The combination of both approaches provides a unique link between theory and experiment if precise structural information is available for the nanomaterial of interest.
Through the years, different characterisation techniques have been developed in order to provide precise structural information. X-ray and neutron diffraction can reveal the lattice structure at high resolution [Zanchet 2001]. However, since X-rays only interact weakly with matter, they provide an average result from diffraction, instead of local structure information. This technique is therefore only suitable for periodic systems whereas nanomaterials are usually aperiodic. Scanning probe techniques, like scanning tunnelling microscopy and atomic force microscopy, can be used to investigate materials at a local scale with atomic resolution [Wiesendanger 1994]. However, these techniques restrict investigations to surface information. Atomic resolution (scanning) transmission electron microscopy ((S)TEM) can be used to determine both the local and the internal structure of materials at the atomic scale, because of the strong interaction of electrons with small volumes of matter [Henderson 1995].
In a world evolving from macro- to micro- to nanoscience, these electron microscopy images need to be interpreted quantitatively instead of visually in terms of local atomic structure and chemical composition. This requires the electron microscope to evolve from a predominantly structure-oriented tool into a physical measurement instrument. Over the past decade, the focus in (S)TEM research has therefore moved gradually from obtaining a better resolution to improving the precision with which structural and chemical information can be extracted from (S)TEM data [Van Aert 2002b, Van Dyck 2003].

Research objective

The main objective of this thesis is to push aberration corrected (scanning) transmission electron microscopy toward precise measurements of unknown structure parameters using advanced statistical techniques. Although the resolution of the state-of-the-art instruments has greatly improved by optimising the lens design, equally fundamental changes in the image processing and acquisition methods are required in order to have the instrument performing at the limits of its capabilities. Ultimately, the precision with which atomic positions have to be measured should be of the order of 1 pm [Muller 1999, Springborg 2000, Kisielowski 2001a]. In addition, the chemical composition of nanostructures has to be discerned for atom types having a difference in atomic number equal to 1. In order to extract precise structural information from atomic resolution electron microscopy images, advanced statistical techniques will extensively be used in

this thesis. In the first part of the thesis, the focus will be mainly on the methodology for a quantitative approach. In the second part, the possibility to count the number of atoms in a projected atomic column will be investigated. The achievement of such high precision measurements is of great fundamental value since ab-initio calculations require precise structural and chemical information as an input in order to compute the properties of nanostructures.

In the next paragraphs of the introduction of this thesis, recent evolutions in the field of electron microscopy will be illustrated. First, state-of-the-art electron microscopy will be discussed. Next, an evolution from qualitative toward quantitative electron microscopy will be elucidated. Subsequently, the evolution from two-dimensional (2D) toward three-dimensional (3D) imaging will be explained. After that, the current possibilities on counting the number of atoms will be explained in more detail as this is an important part of this thesis. Finally, it will be described what can be expected in this thesis.

Atomic resolution (scanning) transmission electron microscopy

Atomic resolution transmission electron microscopy can be categorised into two groups. The first group is referred to as TEM. More details on TEM can be found in [Van Dyck 2002, De Graef 2003, Williams 2009]. The TEM is schematically illustrated in Fig. 1.2(a). Here the object is illuminated by a parallel incident electron beam. The interaction between the electrons of the plane wave and the object determines a complex electron wave function at the exit plane of the object, i.e. the so-called exit wave. If the object is oriented along a main zone axis and the distance between neighbouring columns is not too small, a one-to-one correspondence exists between the exit wave and the projected object structure [Van Dyck 1999, Geuens 2002]. The exit wave is magnified by a set of apertures and magnetic lenses. The wave propagates to the image plane where it forms the so-called image wave. Since the lenses are not perfect, the exit wave is distorted by lens aberrations such as spherical aberration, defocus, and chromatic aberration while propagating to the image plane. Therefore, the image wave is more difficult to interpret in terms of structure information. Finally the image wave is nowadays usually recorded with a charge coupled device (CCD) detecting the electron counts reaching this camera. During this process only the intensity is recorded. As a result, the phase of the image wave is lost. TEM is a coherent imaging mode. This means that contrast reversals can occur due to the lens aberrations and multiple elastic scattering.
The second group is referred to as scanning transmission electron microscopy (STEM) for which the details can be found in [Nellist 2000, Pennycook 2011]. In this mode, the electron beam is focused to a fine probe that is scanned across the specimen in a 2D raster as illustrated in Fig. 1.2(b). For each probe position, a so-called convergent beam electron diffraction pattern is formed in the back focal plane, where an annular detector is located. Only that part reaching the detector is integrated and displayed as a function of the probe position. Different detector geometries are nowadays available [Shibata 2010, Hovden 2012, Yang 2015]. Depending on the collection range of the detector, the atomic number Z-dependence of the contrast and the pixel signal-to-noise ratio will be different. For example, an annular dark field (ADF) STEM image is obtained if the inner detector angle β_1 in Fig. 1.2 is larger than the convergence angle α. If the inner collection angle β_1 is much larger than the probe convergence angle α, the imaging mode is referred to as high-angle annular dark field (HAADF) STEM. In this case, only the electrons

scattered over high angles are detected, which are mainly inelastically scattered. ADF STEM is an incoherent imaging mode. These images are directly interpretable in terms of structure since the image contrast depends on the atomic number of the atoms or the number of atoms in an atomic column, i.e. Z-contrast imaging. Another configuration is an axial detector with a small outer detector angle β_2 resulting in a bright field (BF) STEM image, which is mainly formed by elastically scattered electrons.

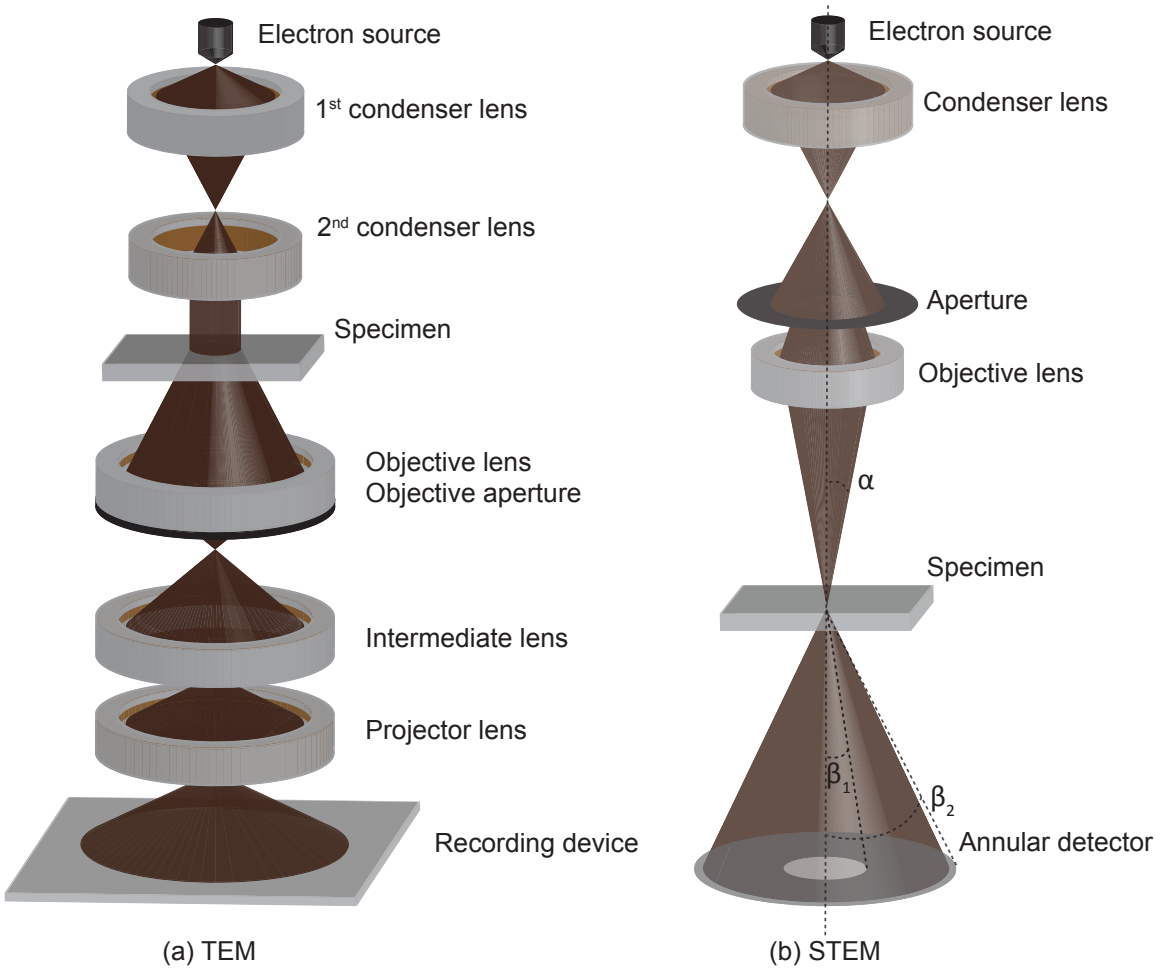

Figure 1.2: *General schematic of a TEM and STEM instrument. (a) A plane wave is illuminating the object after which an image is formed using a set of electromagnetic lenses. (b) An electron beam with convergence angle α is scattered by the specimen and collected by an annular detector with inner and outer angle β_1 and β_2, respectively.*

Ever since the construction of the first electron microscope, a lot of effort has been made to improve the image resolution. After the introduction of aberration corrected electron optics, a point resolution of the order of 100 pm in TEM and 50 pm in STEM can be obtained with the newest generation instruments at moderate accelerating voltages [Haider 1998b, Haider 1998a, Jia 2004, Erni 2009, Sawada 2009]. The point resolution represents the smallest detail directly interpretable from the experimental images. Therefore, these instrumental improvements significantly simplified the visual interpretation.

In TEM, the point resolution can be further improved by the use of higher voltages. Recently, a point resolution of 43 pm has been reported for an aberration corrected 1.2 MV cold field-emission transmission electron microscope [Akashi 2015]. However, such high voltages result in radiation damage, which is problematic for the analysis of light-element structures and catalytic nanoparticles. In TEM also another resolution measure can be considered, the so-called information limit. The information limit represents the smallest detail that is transferred from the object to the image, or in other words the smallest detail that can be resolved by the instrument. The information limit is inversely proportional to the highest spatial frequency transferred from the object to the image. By using image processing techniques the interpretable resolution can be pushed down from the point resolution to the information limit. For example, methods that reconstruct the exit wave from a focal series of images achieve this goal [Lichte 1986, Van Dyck 1993, Kirkland 1995, Op de Beeck 1996, Hsieh 2004, Haigh 2009]. Ideally, the exit wave is free from imaging artefacts which means that the visual interpretation is considerably enhanced as compared to the originally recorded images, especially in the case of thin objects. In this way, imaging with a resolution of 50 pm is possible [Kisielowski 2001b, Kisielowski 2008, Haider 2010, Alem 2011].
Based on classical resolution criteria, it is often concluded that the directly interpretable resolution from a single image is higher in incoherent ADF STEM as compared to TEM, given that the same imaging system is used in both cases. Lord Rayleigh proved in 1896 that incoherent imaging has a factor of two higher resolution than coherent imaging [Rayleigh 1896]. In accordance with his proof, the achievement of sub-Å resolution was achieved earlier in STEM than in TEM at intermediate accelerating voltages [Batson 2002, Nellist 2004]. In addition, the directly interpretable contrast in STEM is often desirable. However, since resolution is not unambiguously defined, a more objective criterion should be used instead to evaluate different imaging systems. If images are interpreted quantitatively, a measure for the statistical precision is appropriate [Van Aert 2006].

From qualitative toward quantitative imaging in electron microscopy

Nowadays there is an evolution from qualitative imaging toward quantitative imaging in electron microscopy. Therefore, statistical analysis methods are introduced in order to extract quantitative measurements from atomic resolution TEM images [Van Aert 2005, den Dekker 2005]. Using statistical parameter estimation theory, unknown structure parameters can be measured with high accuracy and precision from experimental images. This methodology is nowadays becoming recognised as the optimal method for quantitative electron microscopy. In this theory, the (S)TEM image is considered as a data plane from which the unknown structure parameters need to be estimated. The starting point is the availability of a parametric model describing the expectations of the experimental measurements. For atomic resolution (S)TEM images, the projected atomic columns can be assumed to be Gaussian functions peaked at the atomic column positions. The unknown parameters are estimated by fitting this model to the experimental images using a criterion of goodness of fit, quantifying the similarity between the experimental images and the model. The model parameters are estimated using an iterative optimisation scheme using the least squares estimator. In [Bals 2006, Houben 2006, Jia 2008, Urban 2008, De Backer 2011, Klingstedt 2012, Van Aert 2012], quantitative analyses have successfully been applied for 2D atomic column position measurements with a precision

in the picometre range from TEM images or reconstructed exit waves. More recently, ADF STEM has also become a popular technique for quantifying image intensities [Huijben 2006, Van Aert 2009a, Kimoto 2010, Kim 2012, Yankovich 2014].
The examples so far, mainly achieved a precise characterisation of the atomic column positions in 2D. Ultimately, locating the individual atoms with a precision of 1 picometre in 3D should be aimed for. In [Van Aert 2011], the level of quantification in STEM was therefore raised one step further by combining the as-described model-based fitting with another set of advanced statistical methods. In this analysis, the authors aimed for a precise quantification of the number of atoms in the third dimension from 2D projection images. This was the first achievement of three-dimensional reconstruction of a nanoparticle at the atomic scale. The 3D reconstruction of a Ag particle embedded in an Al matrix resulting from atom counts obtained from HAADF STEM images of the same particle viewed along two different zone axes is illustrated in Fig. 1.3.

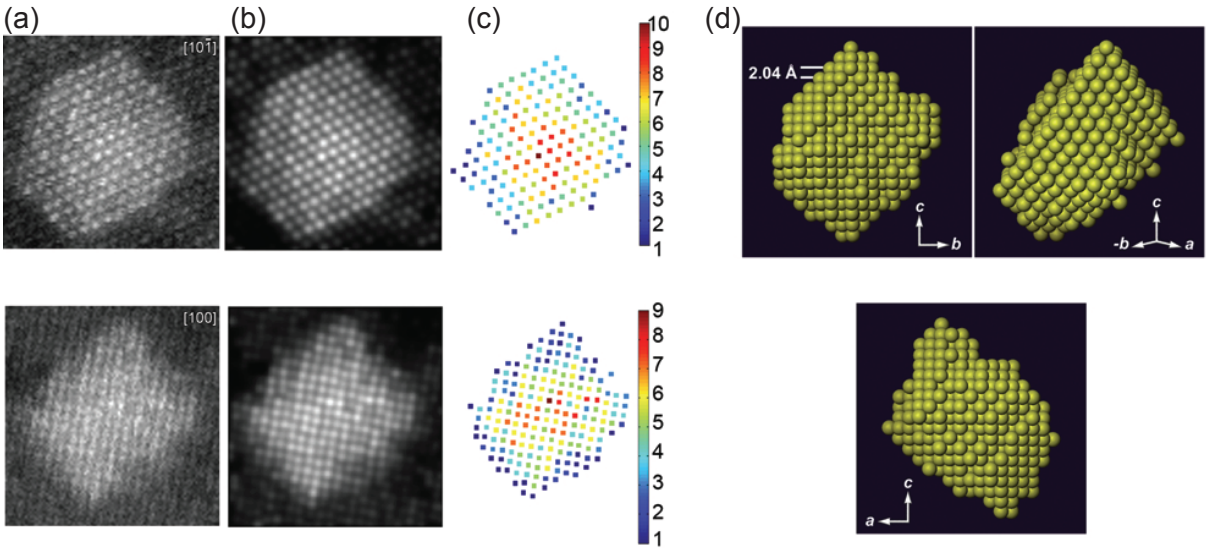

Figure 1.3: *Three-dimensional atomic imaging of crystalline nanoparticles. (a) Experimental HAADF STEM images of nanosized Ag clusters embedded in an Al matrix in* [10$\bar{1}$] *zone-axis orientation and* [100] *zone-axis orientation. (b) Refined models of the images in (a). (c) Number of Ag atoms per column. (d) The computed 3D reconstruction of the Ag nanocluster viewed along three different directions. Figures reproduced from [Van Aert 2011] with permission of S. Van Aert.*

The aim in quantitative electron microscopy is to estimate the structure parameters as precise as possible. Ultimately, this precision is only limited by the presence of noise. Due to noise, the pixel values in the experimental images will fluctuate randomly from experiment to experiment. These pixel values or observations can therefore be modelled as random variables, characterised by a joint probability density function (PDF) (in the case of continuous observations) or a joint probability function (PF) (in the case of discrete observations, such as Poisson counting results). The parametric imaging model introduced above describes the expectations of these observations. Use of the concept of Fisher information allows one to derive an expression for the highest attainable precision with which the structure parameters of the object under study can be estimated in an unbiased way [van den Bos 2001]. This ex-

pression defines a lower bound on the parameter variance. This bound, which is known as the Cramér-Rao lower bound (CRLB), can be derived from the P(D)F. The CRLB on the variance of the parameters can be attained when applying the maximum likelihood estimator. The CRLB is generally a function of the object parameters, the microscope parameters, and the electron dose. It provides quantitative insight into what precision might be achieved from the available image(s). It also provides insight into the sensitivity of the precision to the parameter values. An important application for which the CRLB can be used is statistical experiment design. Experiment design is the selection of free variables in an experiment to improve the precision of the estimated parameters. By calculating the CRLB as a function of the microscope settings, these experimental settings can be optimised so as to attain the highest precision [Bettens 1999, den Dekker 1999a, den Dekker 2001, Van Aert 2001, Van Aert 2002a, Van Aert 2002b, Van Aert 2002c, Van Aert 2004a, Van Aert 2004b, Van den Broek 2011]. The approach for experiment design also provides the possibility to decide if new instrumental developments result in significantly higher attainable precisions.
So far, studies on the precision of atomic scale measurements from (S)TEM considered the estimation of the position of atoms or atomic columns in projection [Van Dyck 1997, Bettens 1999, den Dekker 1999a, den Dekker 2001, Van Aert 2002a, Van Dyck 2003, den Dekker 2005, Van Aert 2005]. In this thesis, the problem of identifying the number of atoms will be considered. The number of atoms is a positive integer and therefore the number of atoms is a so-called restricted or discrete parameter. As a consequence, the P(D)F of the observations is not continuously differentiable with respect to the number of atoms which is a condition for the CRLB. Hence, the CRLB is not defined. Therefore, an alternative solution using the principles of detection theory will be proposed for determining the optimal experiment design [Kay 2009, den Dekker 2013, Gonnissen 2014, De Backer 2015a]. In this framework, the atom-counting problem can be formulated as a statistical hypothesis test, where each hypothesis corresponds to the assumption of a specific number of atoms in an atomic column. Statistical detection theory provides the tools to decide between these hypotheses and to compute the experimental settings minimising the probability to assign an incorrect hypothesis.

From 2D toward 3D imaging in electron microscopy

Besides an evolution from qualitative to quantitative imaging, there is also an evolution from two-dimensional imaging toward three-dimensional imaging, since 2D projection images may result in an incomplete characterisation of the material's structure. Atomic resolution (scanning) transmission electron microscopy (S)TEM images provide a 2D projection image of a 3D object. Two-dimensional projection images are sufficient for the investigation of periodic structures. However, as already mentioned before, a lot of interesting nanostructures are asymmetric in 3D. Different techniques to retrieve the 3D atomic structure have been suggested in the field of electron microscopy. The most known technique is electron tomography [Frank 1992, Midgley 2009]. A series of 2D projection images at different tilt angles, i.e. at incremental degrees of rotation around the specimen, in a (S)TEM is then used to obtain a 3D reconstruction. There are several limitations for a successful 3D reconstruction using electron tomography. First, the specimen needs to be stable under illumination of the electron beam during the acquisition of the tilt series. Second, the so-called projection requirement should be fulfilled [Hawkes 1992]. This means that the intensity in a projection image must be a mono-

tonic function of a physical quantity of the object, like e.g. the thickness. Third, due to the design of the electron microscope, the range of tilt angles is often limited. This is the so-called missing wedge and causes artefacts in the 3D reconstruction [Midgley 2003]. Finally, dedicated alignment and reconstruction algorithms are required for the computation of a 3D reconstruction of the imaged object. Most of the 3D reconstructions using electron tomography have been obtained at the nanoscale [Bals 2007, Ke 2010, Biermans 2010]. Only recently, the limits of electron tomography have been pushed beyond 3D characterisation at the nanoscale in order to resolve atomic positions in a 3D reconstruction. In order to avoid beam damage a limited number of high-resolution images is favourable. As illustrated in Fig. 1.3, Van Aert et al. could locate the atomic positions for the first time in three dimension from two atomic resolution projection images using discrete tomography [Van Aert 2011]. Shortly after, a reconstruction technique based on compressive sensing has been developed for a 3D reconstruction at the atomic scale [Goris 2012b]. This technique has successfully been applied at the atomic scale using ADF STEM for e.g. a determination of the surface facets in Au nanorods [Goris 2012a] and 3D elemental mapping in a bimetallic nanocrystal [Goris 2013].
A second possible technique for 3D structure characterisation is depth-sectioning by ADF STEM [van Benthem 2005, van Benthem 2006]. With a focal series of images in an aberration corrected STEM, it is possible to slice through the object. In this way, it is possible to detect the depth of heavy single impurity or dopant atoms. This technique is very promising for measuring 3D surface morphology, thickness, top/surface atomic structures, point defects in bulk materials, and even depth-sensitive spectroscopy such as energy dispersive X-ray spectroscopy at atomic dimensions [Ishikawa 2015]. Despite of revolutionary advances in aberration correctors, the depth-resolution is nowadays still insufficient to reach atomic depth-resolution limiting the practical applicability. A closely related technique is scanning confocal electron microscopy which requires adaptations to the electron optics [Nellist 2006]. This confocal mode can be obtained in a combined TEM/STEM instrument with two aberration correctors and by inserting an additional aperture in the image plane. A better depth resolution is then obtained, since out-of-focus trays are rejected. Different confocal modes are now available, but atomic depth-resolution is not reported so far [Hashimoto 2009, Hashimoto 2010, Wang 2010b, Wang 2011].
A third possible method for a 3D reconstruction at the atomic scale is provided by an advanced analysis of the exit wave in TEM. The exit wave is closely related to the object structure and can be reconstructed using a series of TEM images acquired at different focal values. The complex values at the atomic column positions of the reconstructed exit wave can be used to measure the thickness and to determine the surface profile using a so-called Argand plot [Wang 2010a, Wang 2012a]. In this plot, the real and imaginary values for each pixel value of the exit wave at the atomic column position are plotted as coordinates in a complex plane. The pixel values of columns with different number of atoms ideally form a circle sampled in discrete steps. Different heights of the atomic columns are observed along another circular curve. Combining the information of both curves enables one to determine the number of atoms and the surface profile. In other words, this method aims to invert the dynamical scattering between the electron beam and the atoms. The dynamical scattering can also be inverted by recasting the scattering process as an artificial neural network in order to retrieve the 3D object potential as proposed by Van den Broek and Koch [Van den Broek 2012, Van den Broek 2013]. An alternative method for the interpretation of the exit wave in terms of the 3D position of the individual atoms has been developed by Van Dyck et al. [Van Dyck 2012]. In this so-called 'Big Bang'

tomography, the reconstructed exit wave is considered as a superposition of spherical waves that have been scattered by the individual atoms of the object, assuming that the atoms are point-like objects. The phase of these spherical waves is proportional to the distance of propagation. A linear fit allows then to position each individual atom along the third dimension.
Another recently reported method suggests that it is possible to determine the 3D shape of a crystal at atomic resolution from a single TEM image [Jia 2014]. In this approach, the peak intensity in the TEM image is interpreted in terms of atom type, composition, number of atoms, and relative position along the third dimension. This is a promising method for the determination of the 3D structure of very thin, light element, radiation-sensitive crystals. So far, it has not yet been shown that this technique is widely applicable to heavier crystals or crystals having a thickness of more than 10 atoms.
The last technique discussed here, which aims to retrieve information on the third dimension at that atomic scale, relies on quantifying the number of atoms in nanoparticles from a single ADF STEM image. ADF STEM has become a popular technique for this purpose since the observed intensity in atomic resolution ADF STEM images is highly sensitive to the atom type and number of atoms. The first results on this approach have been presented by Li et al. [Li 2008]. However, the method presented there is only applicable for regularly shaped models in combination with a priori knowledge and detailed image simulations. Other early approaches rely on calibration standards only applicable to a particular sample under study [Young 2008, Song 2010]. Erni et al. attempted for the first time to count the number of atoms atomic column-by-atomic column by measuring the absolute differences in intensity of neighbouring atomic columns [Erni 2003]. More generally acknowledged methods for counting the number of atoms in each projected atomic column are presented by LeBeau et al. and Van Aert et al. [LeBeau 2010, Van Aert 2011]. The latter has already been quoted as an example of a quantitative analysis and has been illustrated in Fig. 1.3. The two atom-counting methods will be discussed in more detail in the next paragraph. The output of the atom-counting methods can be used as an input for a 3D reconstruction. By combining counting results obtained from images under different viewing directions the 3D space can be reconstructed at an atomic level using so-called discrete tomography. In [Van Aert 2011] counting results of two different projections have been used for discrete tomography to obtain a 3D reconstruction of a Ag nanoparticle embedded in an Al matrix. The same approach has been used to reconstruct the core of a PbSe-CdSe nanoparticle [Bals 2011]. Atom-counting results have also been combined with ab-initio calculations to study the dynamical behaviour of ultrasmall Ge clusters [Bals 2012] and have been helpful to understand the wire structure and bonding at the atomic scale of quantum gold nanowires [Kundu 2014]. More recently, atom counts are used to create atomistic models along with prior knowledge on the crystal [Jones 2014]. An energy minimisation is then used to relax the nanoparticle's 3D structure.

Nanoparticle atom-counting

Electron microscopists have wide interests in counting the number of atoms in a projected atomic column from a single ADF STEM image in order to retrieve information on the third dimension at the atomic scale. As discussed before, in general, two different approaches for atom-counting can be distinguished: a simulation-based method and a statistics-based method. The method of LeBeau et al. relies on a simulation-based approach [LeBeau 2010]. The im-

age intensities are then interpreted by a direct comparison of experimental image intensities and simulated intensities resulting from detailed numerical programs. This requires the intensity variations to be placed on an absolute scale by normalising the measured image intensities to the incident electron beam [LeBeau 2008a, Rosenauer 2009]. This comparison provides atomic column-by-atomic column measurements of the composition or number of atoms [Rosenauer 2009, LeBeau 2010, Martinez 2014b]. In this way, LeBeau et al. obtained atom counts for a thin wedge-shaped gold film viewed along the [110]-directions as illustrated in Fig. 1.4.

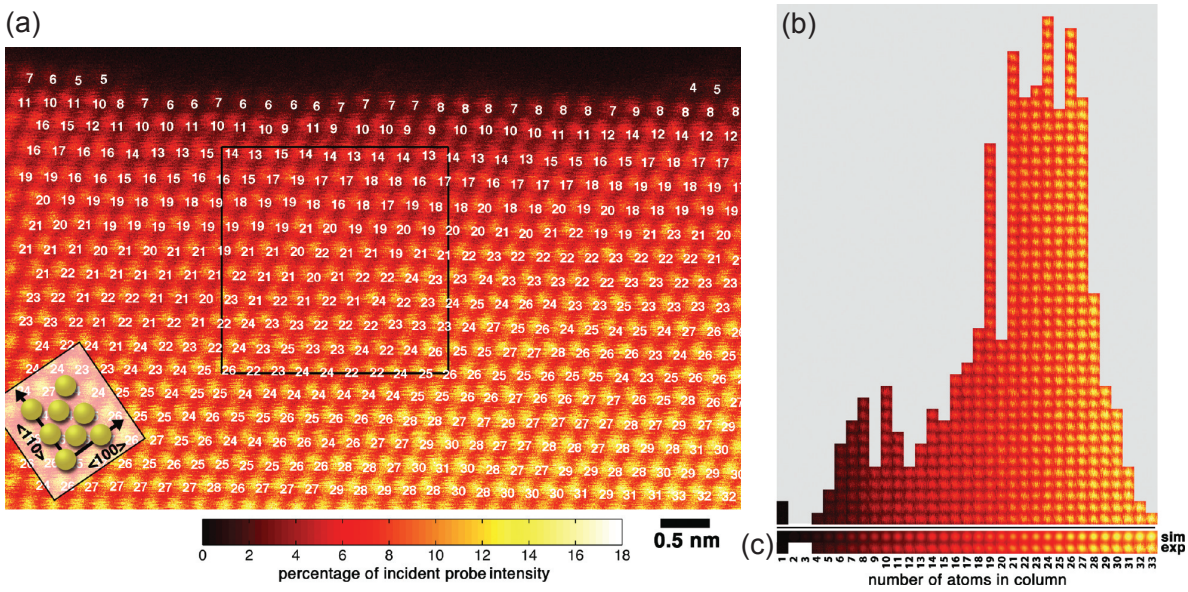

Figure 1.4: *Standardless atom-counting in STEM. (a) HAADF STEM image of a wedge-shaped gold file viewed along* [110]. *The intensity maxima correspond to gold atom columns and the white labels near the lower right of each atom column indicate the number of atoms contained in that column. The image intensities are shown on an absolute scale relative to the incident beam intensity (see scalebar). (b) Histogram of all the columns in (a) binned by the number of atoms they contain. (c) Atom column images extracted from simulation (top) and experiments (bottom) after averaging all the experimental columns in each bin shown in (b). Figures reproduced from [LeBeau 2010] with permission of J.M. LeBeau.*

The approach of Van Aert et al. for atom-counting, illustrated in Fig. 1.3 is a statistics-based approach [Van Aert 2011]. In combination with advanced statistical methods, the number of atoms in a single element atomic column can be counted with single atom sensitivity [Van Aert 2011, Van Aert 2013, De Backer 2013, De Backer 2015b]. Nanoparticle atom-counting is then achieved by quantitatively interpreting the total intensity of electrons of each atomic column scattered toward the ADF detector, i.e. the so-called scattering cross-section [Retsky 1974, Isaacson 1979, Singhal 1997, Van Aert 2009b, E 2013]. In Fig. 1.5, this approach is illustrated for the Ag particle embedded in the Al matrix of [Van Aert 2011]. The scattering cross-sections estimated from the projected STEM image can be presented in the form of a histogram as in Fig. 1.5(b). Ideally, this histogram would consist of isolated components, where each component is generated by a set of columns having the same number of atoms

projected on top of each other, that is in the direction perpendicular to the recorded image. In practice, however, the components are smeared out owing to a combination of experimental detection noise and residual instabilities. Therefore, these results cannot directly be interpreted in terms of number of atoms. By evaluation of the so-called Integrated Classification Likelihood criterion (Fig. 1.5(c)) in combination with Gaussian mixture model estimation, the number of statistically significant components and their respective locations can be determined. From the estimated locations of the components, the number of atoms in each atomic column can be quantified. The atom-counting results are shown in Fig. 1.3.

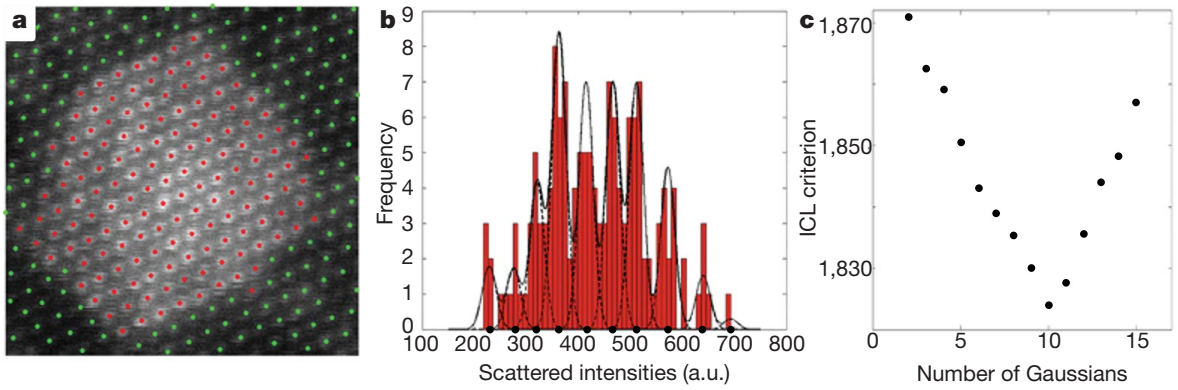

Figure 1.5: *Analysis of scattering cross-sections. (a) Columns containing Ag are indicated by red markers placed at the estimated positions. (b) Histogram of the scattering cross-sections of the Ag columns. The black solid curve shows the estimated mixture model; the individual components are shown as dashed curves. (c) The Integrated Classification Likelihood criterion evaluated as a function of the number of Gaussians in a mixture model. Figures reproduced from [Van Aert 2011] with permission of S. Van Aert.*

This PhD thesis

To begin with, it has been investigated how to measure atomic column positions as accurate and precise as possible using a focal series of images. In theory, it is expected that the precision would considerably improve using a maximum likelihood estimator based on the full series of focal images. As such, the theoretical lower bound on the variances of the unknown atomic column positions can be attained. However, this approach is numerically demanding. Therefore, maximum likelihood estimation has been compared with the results obtained by fitting a model to the reconstructed complex exit wave or to the phase of the reconstructed complex exit wave rather than to the full series of images.

Since ADF STEM has become a popular technique for quantitative structure characterisation, the accuracy and the precision with which measurements for the atomic column positions and scattering cross-sections from ADF STEM images can be estimated, have been investigated as well. The observations for ADF STEM are counting events, which are modelled as Poisson distributed variables. The expectation model of the observations is a sum of Gaussian peaks. Under these assumptions, the CRLB on the variance for the positions and scattering cross-sections can be computed. In practice, the expectation model is fitted using the well-known least squares es-

timator, which is identical to the maximum likelihood estimator for independent and identically normally distributed pixel values. However, this assumption about the statistical distribution of the pixel values is not always valid, especially not at low electron doses, needed to avoid radiation damage in beam sensitive matter. By means of image simulations, it has been investigated whether the variance on the least squares estimates of scattering cross-sections and atomic column positions attains the CRLB. This study reveals if quantitative ADF STEM analysis would benefit when applying the maximum likelihood estimator which has optimal statistical properties.
The up to now used implementation of the least squares estimator limits the area of a (S)TEM image that quantitatively can be analysed. Therefore, an efficient algorithm that solves some practical problems has been introduced. The new algorithm has been applied to several experimental studies to show that the proposed approach works in practice.
In the second part of the thesis, the possibility to count the number of atoms of mono-type crystalline nanostructures from atomic resolution ADF STEM images has been investigated. The methodology for atom-counting followed in this work has been proposed in [Van Aert 2011]. In that paper, the statistics-based atom-counting method has been proven to result in reliable counts for the number of atoms in a metal nanocluster embedded into a stabilising matrix with the same crystal nanostructure. Although, the results presented there are very promising, a thorough study on the possibilities and inherent limitations of the method is indispensable. This study has been carried out in detail in this thesis. Only because of such a study, it can be discovered whether the statistics-based atom-counting method gives reliable counting results for nanoparticles of arbitrary shape and size. Once the possibilities and limitations are known, the atom-counting method has been applied to several challenging nanostructures. Experimental atom-counting results have been validated by using detailed image simulations and electron tomography.
Since the aim in a quantitative atom-counting analysis is to extract as precise as possible the number of atoms in a projected atomic column from the experimental images, it will be shown how even higher precisions for the estimates of the number of atoms can be obtained by statistical experiment design. Designing the optimal experiment for nanoparticle atom-counting can greatly enhance the reliability of the atom-counting results, which is of great importance when studying beam sensitive materials. Often visual interpretability is used as a criterion to optimise the experiment. However, the dose efficiency is not taken into account in such an analysis. The dose efficiency is defined as the ratio of the number of detected electrons to the number of incident electrons. This ratio is affected by e.g. the detector geometry. For the often used HAADF STEM detector in STEM imaging, the inner detector angle β_1 is much larger than the probe convergence angle α. This results in high resolution and contrast at the expense of dose efficiency. In this thesis, the aim is to optimise the design in terms of precision with which the number of atoms can be counted. Therefore, the principles of detection theory have been used to optimise the experiment design, which corresponds in this thesis to deriving the optimal STEM detector for atom-counting. This technique of hypothesis testing can also be used to determine the minimally required electron dose in order to attain a pre-specified precision.

The outline of this thesis is as follows. In chapter 2, the basic principles of statistical parameter estimation theory will first be reviewed. These principles will then also be applied (1) in order to investigate how to obtain high precision measurements of atomic column positions using a

focal series of TEM images and (2) in order to evaluate the precision and accuracy that can be obtained for the position and scattering cross-section measurements from ADF STEM images. In chapter 3, an efficient algorithm for the estimation of the atomic column positions and intensities from (S)TEM images will be introduced. The proposed algorithm is applied to three different nanostructures for which the analysis of a large field of view is required. In chapter 4, the statistics-based atom-counting method will be discussed in detail together with a thorough study on the possibilities and limitations. In chapter 5, the statistics-based atom-counting method will be applied to various challenging nanoparticles. Furthermore, the obtained counting results will be validated using image simulations or electron tomography. In chapter 6, the optimal detector design will be derived for atom-counting. Finally, in chapter 7, conclusions will be drawn and future perspectives are considered.

2

Statistical parameter estimation theory: principles and simulation studies

2.1 Introduction

In this chapter, the basic principles of statistical parameter estimation theory will be introduced [van den Bos 2001, den Dekker 2005, Van Aert 2005, van den Bos 2007]. These principles are widely applicable in different fields of science where unknown parameters need to be measured from an experiment. Often indirect techniques are used to measure physical parameters since the unknown parameters are hidden in the available set of observations. The measurement of an unknown parameter always occurs in the presence of fluctuations in the observations limiting the precision with which the unknown parameters can be determined. Statistical parameter estimation theory and statistical optimal experiment design aim for the highest possible precision in the determination of the unknown parameters.
For high-resolution (scanning) transmission electron microscopy (HR(S)TEM) images, the observations are characterised by a set of pixel values from which unknown structure parameters such as, the atomic positions, atomic displacements, atom types, and/or number of atoms, have to be estimated. The experimental HR(S)TEM images fluctuate randomly about their expectation values due to the presence of noise. Therefore, the observations are modelled as stochastic variables. By definition, a stochastic variable is characterised by a probability (density) function, whereas a set of stochastic variables is characterised by the joint probability (density) function. The joint probability (density) function defines the expectation values of the observations and the fluctuations of the observations about the expectation values. The expectation values are described by the expectation model, i.e. a parametric model containing the unknown structure parameters.

Using the joint probability (density) function, which depends on the unknown structure parameters, the Fisher information matrix can be defined for continuous parameters. This concept can be used to quantitatively express the amount of information about the unknown structure parameters available in the observations. The Fisher information allows us to derive the attainable precision, i.e. the lowest possible variance, with which a continuous parameter can be estimated unbiasedly from a set of observations assumed to obey a certain distribution. This is the so-called Cramér-Rao lower bound (CRLB) giving the lower bound on the variance of the parameters. It is important to notice that this lower bound is independent of the estimation method used. This lower bound therefore represents the intrinsic limit on the precision. The joint probability (density) function can also be used to define the maximum likelihood estimator that achieves the CRLB asymptotically, i.e. for an increasing number of observations. The CRLB can therefore be used to quantify the precision of structure parameters.
It will be shown that the concept of attainable precision can be a powerful tool in order to decide how the structure parameters of interest should be estimated from the available set of observations. Here, it has been investigated how to measure atomic column positions as accurate and precise as possible using a focal series of HRTEM images, which is often recorded for the reconstruction of the wave function at the exit plane of the object. This exit wave is closely related to the object structure, has a better signal-to-noise ratio, and is free from residual lens aberrations. Using simulations it can be investigated whether the reconstructed complex exit wave contains the same amount of information concerning the atomic column positions as compared to the full series of focal images, and which amount of information can be retrieved from the phase of the reconstructed complex exit wave.
Finally, in practice, the least squares estimator is often used in order to derive unknown structure parameters from the available set of observations. It can be shown that the maximum likelihood estimator is identical to this well-known uniformly weighted least squares estimator if the observations are independent and identically normally distributed about their expectations [van den Bos 2001]. However, it is assumed that HR(S)TEM images are statistically independent counting results which can be modelled as Poisson distributed random variables. The Poisson distribution tends to be a normal distribution for increasing expectations of the image pixel values. However, this assumption about the statistical distribution of the pixel values is not always valid, especially not at low electron doses, needed to avoid radiation damage in beam sensitive matter. Therefore, it is important to verify whether the lower bound on the variance of the structure parameters is attained when applying the least squares estimator to the Poisson distributed observations for different electron doses. The accuracy and precision of the estimated structure parameters of interest of ADF STEM images, i.e. the atomic column positions and scattering cross-sections, will be evaluated. This result will be extremely important, if it can be concluded that the structure parameters of the ADF STEM image are estimated unbiasedly with the highest possible precision.

The chapter is organised as follows. In section 2.2, the framework of statistical parameter estimation theory will be discussed in detail. This includes the parametric statistical model of the observations, the derivation of the Fisher information and Cramér-Rao lower bound, i.e. the attainable precision, and the derivation of the maximum likelihood estimator. Section 2.3 shows how the attainable precision is used to theoretically examine the performance of different approaches for the estimation of the atomic column positions from a focal series of HRTEM

images. In section 2.4, the concepts of statistical parameter estimation theory are used to show that unbiased estimates with the highest possible precision are obtained for the parameters of interest from an ADF STEM image. Section 2.5 consists of conclusions.

2.2 Theory

In this section the principles of statistical parameter estimation theory will be introduced. More details and references on this theory can be found in [van den Bos 2007]. This requires the introduction of a parametric statistical model describing the observations. In subsection 2.2.1, a parametric statistical model will be proposed to model HR(S)TEM images. In subsection 2.2.2, it will be shown how an expression for the attainable precision of the parameter estimates, i.e. the CRLB, can be derived. In subsection 2.2.3, the maximum likelihood estimator will be derived from the parametric statistical model describing the observations.

2.2.1 Parametric statistical model

Due to the inevitable presence of noise, sets of observations made under the same conditions will differ from experiment to experiment. Therefore, the observations are modelled as stochastic variables. A set of pixel observations can be represented by a row vector of length $K \times L$ with $k = 1, \ldots, K$ and $l = 1, \ldots, L$:

$$\mathbf{w} = (w_{11}, w_{12}, w_{21}, \ldots, w_{KL})^T \tag{2.1}$$

where w_{kl} corresponds to the pixel value in a HR(S)TEM image at position (k, l). Each set of observations is characterised by a joint probability (density) function:

$$p(\omega_{11}, \omega_{12}, \omega_{21}, \ldots, \omega_{KL}) = p(\boldsymbol{\omega}). \tag{2.2}$$

This joint probability (density) function describes the probability for a set of given observations which are modelled as stochastic variables $\boldsymbol{\omega}$. The expectation value and variance of a continuous stochastic variable are defined by the joint probability density function:

$$\mu = \mathbb{E}[\boldsymbol{\omega}] = \int_{-\infty}^{\infty} \boldsymbol{\omega} p(\boldsymbol{\omega}) d\boldsymbol{\omega} \tag{2.3}$$

$$\sigma^2 = \mathrm{var}(\boldsymbol{\omega}) = \mathbb{E}\left[(\boldsymbol{\omega} - \mu)^2\right] = \int_{-\infty}^{\infty} (\boldsymbol{\omega} - \mu)^2 \, p(\boldsymbol{\omega}) d\boldsymbol{\omega}. \tag{2.4}$$

For discrete variables, the integration needs to be replaced by a summation.
Statistical parameter estimation theory uses a model that describes the expectation values of the observations as a function of the sought physical parameters. The expectation value of the pixel (k, l) is then given by:

$$\mathbb{E}[\omega_{kl}] = f_{kl}(\boldsymbol{\theta}) \tag{2.5}$$

where $\boldsymbol{\theta} = (\theta_1, \theta_2, \ldots, \theta_R)^T$ equals a $R \times 1$ vector with the unknown parameters.

For HR(S)TEM images, the observation at the pixel (k, l) is denoted as w_{kl}. The pixel values correspond to the electron counting results detected at the pixels of a CCD camera. When assuming that the pixels in a HR(S)TEM image are statistically independent electron counting results, they can be modelled as Poisson distributed random variables [Papoulis 1965, Herrmann 1997]:

$$\frac{(\lambda_{kl})^{\omega_{kl}}}{\omega_{kl}!} \exp\left(-\lambda_{kl}\right). \tag{2.6}$$

The expected value and variance of a Poisson distributed random variable equal λ_{kl} which on his turn equals the expectation model:

$$\mathbb{E}\left[\omega_{kl}\right] = \mathrm{var}\left(\omega_{kl}\right) = \lambda_{kl} = f_{kl}(\boldsymbol{\theta}). \tag{2.7}$$

The joint probability function for a set of pixel observations which are modelled as Poisson distributed random variables equals the product of the probabilities given by Eq. (2.6), assuming that the observations of the pixels are statistically independent:

$$p(\boldsymbol{\omega}) = \prod_{k=1}^{K} \prod_{l=1}^{L} \frac{(\lambda_{kl})^{\omega_{kl}}}{\omega_{kl}!} \exp\left(-\lambda_{kl}\right). \tag{2.8}$$

The unknown parameters are included through the expectation values λ_{kl} described by a suitable parametric model as noted in Eq. (2.7). For HR(S)TEM images, the intensity is often assumed to be sharply peaked at the atomic column positions. Therefore, HR(S)TEM images are often modelled as a superposition of Gaussian peaks. The expectation of the image at the pixel (k, l) at the position (x_k, y_l) can then be described as:

$$f_{kl}(\boldsymbol{\theta}) = \zeta + \sum_{i=1}^{I} \sum_{m_i}^{M_i} \eta_{m_i} \exp\left(-\frac{\left(x_k - \beta_{x_{m_i}}\right)^2 + \left(y_l - \beta_{y_{m_i}}\right)^2}{2\rho_i^2}\right) \tag{2.9}$$

with ζ a constant background, ρ_i the column type dependent width of the Gaussian peak, η_{m_i} the column intensity of the m_ith Gaussian peak, $\beta_{x_{m_i}}$ and $\beta_{y_{m_i}}$ the x- and y-coordinate of the m_ith atomic column respectively. The index i refers to a particular column type and the index m_i refers to the mth column of column type i. The indices in the summation of Eq. (2.9) can be simplified in the case of a mono-type crystalline nanostructure since in that case only one column type is present. The unknown parameters of the imaging model of Eq. (2.9) are given by the parameter vector:

$$\boldsymbol{\theta} = \left(\beta_{x_{1_1}}, \ldots, \beta_{x_{M_I}}, \beta_{y_{1_1}}, \ldots, \beta_{y_{M_I}}, \rho_1, \ldots, \rho_I, \eta_{1_1}, \ldots, \eta_{M_I}, \zeta\right)^T. \tag{2.10}$$

The proposed theoretical parametric model should model the image intensities accurately, in order to extract reliable quantitative measurements from HR(S)TEM images. This model, which consists of a superposition of Gaussian peaks as described by Eq. (2.9), is preferred above other more complicated models. Complicated models describe the image intensities in detail using a more physics-based approach, i.e. modelling the electron-object interaction and the transfer of the electrons through the microscope. However, the number of unknown parameters will

be higher for such models, since e.g. unknown microscope parameters should then be included in the parametric model. A higher number of unknown parameters is disadvantageous for the estimation of the unknown parameters. For a large number of unknown parameters, the optimisation might end up in a local minimum, if appropriate starting values for the unknown parameters are not available. Therefore, the lower number of parameters of the simpler model given by Eq. (2.9) is preferred. In addition, structure parameters of interest, such as atomic column positions and scattering cross-sections, can be described with the simpler model. Furthermore, the validity of the proposed model can be tested using statistical model assessment methods, such as the likelihood ratio test [den Dekker 2005]. The validity of the model given by Eq. (2.9) has been tested using different statistical model assessment methods in [Van Aert 2005].

2.2.2 Fisher information and Cramér-Rao lower bound

In this subsection, the parametrised probability function of the observations, which is derived in section 2.2.1, will be used to define the Fisher information matrix and to derive the Cramér-Rao lower bound on the variance, i.e. the attainable precision with which the unknown parameters can be estimated unbiasedly from the observations. Also an expression for the CRLB of a function of the parameters will be given. For example, this can be the distance between two atomic column positions which depends on the position coordinates of the atomic columns. More details about Fisher information and the CRLB can be found in [van den Bos 1982, Frieden 1998, van den Bos 2001].

Fisher information

The joint probability (density) function depends on the unknown parameters. This dependence can be expressed as: $p(\boldsymbol{\omega};\boldsymbol{\theta})$ and can be used to define a $R\times R$ covariance matrix. This covariance matrix is the so-called Fisher information matrix and is given by:

$$F_{\boldsymbol{\theta}} = -\mathbb{E}\left[\frac{\partial^2 \ln p(\boldsymbol{\omega};\boldsymbol{\theta})}{\partial \boldsymbol{\theta}^2}\right] \tag{2.11}$$

where $p(\boldsymbol{\omega};\boldsymbol{\theta})$ equals the joint probability (density) function of the stochastic variables $\boldsymbol{\omega}$. The expression between square brackets represents the Hessian matrix of $\ln p(\boldsymbol{\omega};\boldsymbol{\theta})$. The Fisher information is a measure for the physical fluctuation of the observations.
For the observed pixel values in an electron microscopy image, where $p(\boldsymbol{\omega};\boldsymbol{\theta})$ is given by Eq. (2.8), it follows from Eqs. (2.7), (2.8), and (2.11) that the (r, s)th element of $F_{\boldsymbol{\theta}}$ equals:

$$F_{rs} = \sum_{k=1}^{K}\sum_{l=1}^{L}\frac{1}{\lambda_{kl}}\frac{\partial\lambda_{kl}}{\partial\theta_r}\frac{\partial\lambda_{kl}}{\partial\theta_s}. \tag{2.12}$$

Cramér-Rao lower bound

Using the concept of Fisher information, a lower bound on the variance, i.e. the highest possible precision, can be defined for unbiased estimators. This lower bound is the so-called Cramér-Rao lower bound (CRLB). The Cramér-Rao inequality, with $\hat{\boldsymbol{\theta}}$ an unbiased estimator of $\boldsymbol{\theta}$, equals:

$$\mathrm{cov}\left(\hat{\boldsymbol{\theta}},\hat{\boldsymbol{\theta}}\right) \geq F_{\boldsymbol{\theta}}^{-1} \tag{2.13}$$

where:

$$\mathrm{cov}\left(\hat{\boldsymbol{\theta}},\hat{\boldsymbol{\theta}}\right)=\mathbb{E}\left[\left(\hat{\boldsymbol{\theta}}-\boldsymbol{\theta}\right)\left(\hat{\boldsymbol{\theta}}-\boldsymbol{\theta}\right)^{T}\right]. \tag{2.14}$$

This inequality expresses that the difference of the matrix $\mathrm{cov}\left(\hat{\boldsymbol{\theta}},\hat{\boldsymbol{\theta}}\right)$ and $F_{\boldsymbol{\theta}}^{-1}$ is positive semi-definite. Since the diagonal elements of $\mathrm{cov}\left(\hat{\boldsymbol{\theta}},\hat{\boldsymbol{\theta}}\right)$ represent the variances of $\hat{\theta}_1,\hat{\theta}_2,\ldots,\hat{\theta}_R$ and since the diagonal elements of a positive semi-definite matrix are non-negative, these variances are larger than or equal to the corresponding diagonal elements of $F_{\boldsymbol{\theta}}^{-1}$:

$$\mathrm{var}\left(\hat{\theta}_r\right)\geq\left[F_{\boldsymbol{\theta}}^{-1}\right]_{rr}. \tag{2.15}$$

The matrix $F_{\boldsymbol{\theta}}^{-1}$ is called the Cramér-Rao lower bound on the variance of $\hat{\boldsymbol{\theta}}$. The CRLB is independent of the estimation method, but depends on the statistical properties of the observations and the hypothetical true values of the parameters.
The general expression for the CRLB for vector functions of the vector parameters is of importance when one is interested in a new parameter which is a function of the proper parameters. Let $\boldsymbol{\gamma}(\boldsymbol{\theta})=(\gamma_1(\boldsymbol{\theta}),\gamma_2(\boldsymbol{\theta}),\ldots,\gamma_G(\boldsymbol{\theta}))^T$ a $G\times 1$ vector which depends on the $R\times 1$ parameter vector $\boldsymbol{\theta}=(\theta_1,\theta_2,\ldots,\theta_R)^T$. If $\hat{\boldsymbol{\gamma}}$ is an unbiased estimator, then it can be shown that:

$$\mathrm{cov}\left(\hat{\boldsymbol{\gamma}}\right)\geq\frac{\partial\boldsymbol{\gamma}(\boldsymbol{\theta})}{\partial\boldsymbol{\theta}^T}F_{\boldsymbol{\theta}}^{-1}\frac{\partial\boldsymbol{\gamma}(\boldsymbol{\theta})^T}{\partial\boldsymbol{\theta}} \tag{2.16}$$

where $\frac{\partial\boldsymbol{\gamma}(\boldsymbol{\theta})}{\partial\boldsymbol{\theta}}$ is the $G\times R$ Jacobian matrix of which the elements are given by:

$$\begin{pmatrix}\frac{\partial\gamma_1(\boldsymbol{\theta})}{\partial\theta_1} & \cdots & \frac{\partial\gamma_1(\boldsymbol{\theta})}{\partial\theta_R}\\ \vdots & \cdots & \vdots\\ \frac{\partial\gamma_G(\boldsymbol{\theta})}{\partial\theta_1} & \cdots & \frac{\partial\gamma_G(\boldsymbol{\theta})}{\partial\theta_R}\end{pmatrix}.$$

The matrix $\mathrm{cov}\left(\hat{\boldsymbol{\gamma}}\right)$ is the $G\times G$ covariance matrix of the estimator $\hat{\boldsymbol{\gamma}}$. It should be noticed that the CRLB can only be computed when the joint probability (density) function of the observations is known. However, the true parameters of the joint probability (density) function are often not known. Nevertheless, the highest possible precision can be quantified when substituting the real values by the estimated values [Van Aert 2005].

2.2.3 Maximum likelihood estimator

In the previous subsection, the concept of Fisher information and CRLB has been introduced. The Fisher information matrix contains information about the fluctuations of the observations. Furthermore, different estimators will show different precisions. When using the most precise estimator, the CRLB may be attained. In this subsection, it is discussed how the maximum likelihood estimator of the parameters of the statistical expectation model may be derived from the parametrised joint probability (density) function. The maximum likelihood estimator (MLE) is an estimator that achieves the CRLB asymptotically, i.e. for an increasing number of observations.

Definition

The MLE is derived following the steps below:

1. The joint probability (density) function depends on the unknown parameters $\boldsymbol{\theta} = (\theta_1, \theta_2, \ldots, \theta_R)^T$ through the statistical expectation model:

$$p(\boldsymbol{\omega}; \boldsymbol{\theta}).$$

2. The stochastic variables $\boldsymbol{\omega} = (\omega_{11}, \omega_{12}, \omega_{21}, \ldots, \omega_{KL})^T$ are replaced by the observations $\mathbf{w} = (w_{11}, w_{12}, w_{21}, \ldots, w_{KL})^T$:

$$p(\mathbf{w}; \boldsymbol{\theta}).$$

3. The true parameters $\boldsymbol{\theta} = (\theta_1, \theta_2, \ldots, \theta_R)^T$ are replaced by the independent variables $\mathbf{t} = (t_1, t_2, \ldots, t_R)^T$:

$$L(\mathbf{t}) \coloneqq p(\mathbf{w}; \mathbf{t})$$

   where $L(\mathbf{t})$ is the likelihood function.

4. The MLE $\hat{\boldsymbol{\theta}}_{ML}$ of the parameters $\boldsymbol{\theta}$ are defined by the values of $\mathbf{t}$ that maximise the likelihood function:

$$\hat{\boldsymbol{\theta}}_{ML} = \arg\max_{\mathbf{t}} L(\mathbf{t}) = \arg\max_{\mathbf{t}} \ln L(\mathbf{t})$$

   where $\ln L(\mathbf{t})$ is the log-likelihood function.

The joint probability (density) function evaluated at the maximum likelihood estimates $p(\boldsymbol{\omega}; \hat{\boldsymbol{\theta}}_{ML})$ generates the observations with a larger probability than the joint probability (density) function evaluated with any other set of parameters $p(\boldsymbol{\omega}; \mathbf{t})$ [Myung 2003].

Properties

The MLE has some important properties:

- *Invariance property*: if $\hat{\boldsymbol{\theta}}_{ML} = \left(\hat{\theta}_1, \hat{\theta}_2, \ldots, \hat{\theta}_R\right)^T$ is the MLE for the parameters $\boldsymbol{\theta} = (\theta_1, \theta_2, \ldots, \theta_R)^T$ and $\boldsymbol{\gamma}(\boldsymbol{\theta})$ is a function of the parameters $\boldsymbol{\theta}$, than $\hat{\boldsymbol{\gamma}}\left(\hat{\boldsymbol{\theta}}_{ML}\right)$ is the MLE of $\boldsymbol{\gamma}(\boldsymbol{\theta})$.

For an increasing number of observations, the most important properties are the following ones:

- *Consistency*: The MLE is consistent meaning that the MLE converges toward the true value of the parameters.

- *Asymptotic efficiency*: The MLE is asymptotically most precise. The MLE attains asymptotically the CRLB:

$$\operatorname{cov}\left(\hat{\boldsymbol{\theta}}_{ML}\right) \to CRLB.$$

- *Asymptotic normality*: The probability density function of the MLE asymptotically tends to be a normal distribution having the true parameters $\boldsymbol{\theta}$ as expectation values and the CRLB matrix as covariance matrix:

$$\hat{\boldsymbol{\theta}}_{ML} \sim \mathcal{N}(\boldsymbol{\theta}; CRLB).$$

Maximum likelihood estimator for independent normally distributed observations

The observations of an HR(S)TEM image are assumed to be statistically independent Poisson distributed. For an increasing expectation value λ_{kl} of the Poisson distribution, the Poisson distribution tends to be a normal distribution with expectation value and variance equal to λ_{kl} of the Poisson distribution. This approximation is justified if the magnitude of the observations is large compared to the square root of this magnitude [Koster 1987]. Moreover, if the contrast in the images is low, the deviations of the observations from their expectations may be supposed to be identically distributed, i.e. $\sigma_{kl} \approx \text{cte} = \sigma$ [Miedema 1994].
The MLE estimator can be calculated for statistically independent identical normally distributed observations having expectation value $\mathbb{E}[\omega_{kl}] = f_{kl}(\boldsymbol{\theta})$ and $\text{var}(\omega_{kl}) = \sigma^2$ following the steps described in the beginning of this section. The joint probability density function as a function of the parameters $\boldsymbol{\theta}$ is then given by:

$$p(\boldsymbol{\omega}) = \prod_{k=1}^{K} \prod_{l=1}^{L} \frac{1}{\sqrt{2\pi}\sigma} \exp\left(-\frac{(\omega_{kl} - f_{kl}(\boldsymbol{\theta}))^2}{2\sigma^2}\right). \tag{2.17}$$

The log-likelihood function is given by:

$$\ln L(\mathbf{t}) = -\frac{N}{2}\ln(2\pi) - N\ln(\sigma) - \frac{1}{2}\sum_{k=1}^{K}\sum_{l=1}^{L}\left(\frac{w_{kl} - f_{kl}(\mathbf{t})}{\sigma}\right)^2; \tag{2.18}$$

The MLE equals then:

$$\hat{\boldsymbol{\theta}}_{ML} = \arg\max_{\mathbf{t}} \ln L(\mathbf{t}) = \arg\min_{\mathbf{t}} \sum_{k=1}^{K}\sum_{l=1}^{L} (w_{kl} - f_{kl}(\mathbf{t}))^2 . \tag{2.19}$$

This means that for independent identically normally distributed observations the MLE estimator equals the uniformly weighted least squares estimator (LSE) . The uniformly weighted least squares estimates $\hat{\boldsymbol{\theta}}_{LS}$ of the unknown parameters $\boldsymbol{\theta}$ are given by the values $\mathbf{t}$ that minimise the uniformly weighted least squares criterion. The LSE will be used throughout this thesis. In chapter 3, an efficient algorithm for the least squares estimation of the parameters of the statistical expectation model for HR(S)TEM images will be discussed in detail.

In this section, it has been discussed how the parameters of a statistical expectation model can be determined using the maximum likelihood estimator. Furthermore, the lower bound on the variance of the parameters to be estimated was theoretically described. In the next sections, the precision and accuracy with which the unknown parameters are estimated from HR(S)TEM will be evaluated and the variance of the estimated parameters will be compared with the theoretical lower bound. First, it will be shown in section 2.3 how the tools described in this section can help to decide how to estimate the atomic column positions as precise as possible from a focal series of images. Second, the accuracy and precision of the parameters of interest estimated from ADF STEM images will be investigated in section 2.4.

2.3 Exit wave reconstruction: precise measurements of atomic column positions

In this section, the tools of statistical parameter estimation theory will be applied for precise measurements of the atomic column positions from a reconstructed exit wave[1]. The reconstructed exit wave is a complex wave. Often only the reconstructed phase is employed in a quantitative analysis, although it can be expected to obtain a better precision when using the full complex exit wave or the originally required focal series images. The precision of the atomic column position estimates obtained from the reconstructed phase and from the complex exit wave will therefore be compared with the attainable precision, i.e. the Cramér-Rao lower bound, calculated based on the full data set of the focal series. First a brief introduction is given on exit wave reconstruction. Next, the estimation of the atomic column positions for exit wave reconstruction and the attainable precision for the atomic column position estimates is described, before the results of a simulation study are discussed.

2.3.1 Brief introduction on exit wave reconstruction

The phase information in TEM is lost due tho the image recording process, which is a limiting factor since the phase contains significant information on the positions of the atomic columns. Therefore, the imaging process has to be inverted numerically in order to calculate the wave function at the exit plane of the object. A commonly applied technique is to use a series of images recorded at different focal values [Van Dyck 1990, Coene 1992, Coene 1996, Op de Beeck 1996, Thust 1996, Allen 2001, Allen 2004a, Meyer 2002, Kirkland 2004, Hsieh 2004]. In this way both the amplitude and phase information of the exit wave are recovered. In addition, a better signal-to-noise ratio is achieved and residual lens aberrations are eliminated [Thust 1996, Meyer 2002, Kirkland 2004, Houben 2006, Erni 2010]. The reconstructed exit wave is closely related to the object structure. In combination with quantitative methods, atomic column positions can be measured with a precision of a few picometres [Urban 2008, Jia 2008, Jia 2009a, Xu 2005, Bals 2006, Van Aert 2009a].

The ultimate goal is to determine structure parameters with the highest possible precision and accuracy. In the case of a focal series, this means that the parameters need to be determined using the maximum likelihood estimator applied to the originally recorded focal images, which is numerically demanding. In current studies, only the phase information of the reconstructed exit wave is used to determine the atomic column positions using a parametric model consisting of a superposition of Gaussian peaks [Jia 2009b, Houben 2006, Bals 2006, Van Aert 2009a, Klingstedt 2012]. In principle, more precise results might be expected if the reconstructed amplitude is also taken into account using a physics-based parametric model using the channelling theory [Van Dyck 1996, Van Dyck 1999, Geuens 2002, Geuens 2005, Van Aert 2007]. Here, a real space model-based approach for exit wave reconstruction based on the channelling theory is introduced in order to investigate the precision that can ultimately be obtained for the

[1]The results of this study are published in *A. De Backer*, S. Van Aert, and D. Van Dyck, High precision measurements of atom column positions using model-based exit wave reconstruction, Ultramicroscopy 111 (2011) 1475-1482.

atomic column positions. By means of image simulations of an ideal Au [100] sample, which are subject to counting noise, different parameter estimation methods have been compared. It has been investigated what precision could be obtained by using the phase information of the reconstructed exit wave only or by using the full complex exit wave for different specimen thicknesses. This precision has been compared with the attainable precision that could in principle be obtained by applying the maximum likelihood estimator to the full series of focal images. Although these simulations represent an idealistic case, they serve a a reference for model-based exit wave reconstruction and statistical parameter estimation theory of atomic column positions. These simulation should answer the question whether the use of only the phase information in a quantitative analysis is justified and if the analysis would benefit if the amplitude would be used in addition.

2.3.2 Model-based exit wave reconstruction

In order to investigate the ultimate precision with which the atomic column positions can be measured, a model-based exit wave reconstruction technique is considered here. The image intensities of the focal series are backpropagated to the zero-focus to reconstruct the wave at the exit face of the specimen. Next, the set of backpropagated images is averaged. This real space approach for exit wave reconstruction is very intuitive and understandable. In most reconstruction methods the only aim is to reconstruct the complex exit wave as such. However, since it is ultimately the purpose to derive also the crystal structure from the exit wave, we want to go one step further and include also the channelling theory for the electron interaction already in the exit wave. Therefore, this model-based approach for exit wave reconstruction is conceptually different from the existing focal series reconstruction methods [Van Dyck 1990, Coene 1992, Coene 1996, Op de Beeck 1996, Thust 1996, Allen 2001, Allen 2004a, Meyer 2002, Kirkland 2004, Hsieh 2004].
The channelling theory describes the quantum mechanical interaction of the electrons with the object and provides a closed analytical expression for the exit wave which is parametric in the structure parameters [Van Dyck 1996, Van Dyck 1999, Geuens 2002, Geuens 2005]. The complex exit wave of an object consisting of atomic columns described in the channelling theory consists of a vacuum wave and an interaction wave:

$$\begin{aligned}\psi_{\mathrm{ex}}(\mathbf{r},z) &= 1+\psi_{\mathrm{int}}(\mathbf{r},z)\\ &= 1+\sum_{i=1}^{I}\sum_{m_i=1}^{M_i} c_{m_i}\phi_{1\mathrm{s},m_i}(\mathbf{r}-\boldsymbol{\beta}_{m_i})\left[\exp\left(-i\pi\frac{E_{1\mathrm{s},m_i}}{E_0}\frac{1}{\lambda}z\right)-1\right]\end{aligned} \tag{2.20}$$

where $\mathbf{r}=(x,y)^T$ is a two-dimensional vector in the exit plane of the object, perpendicular to the incident beam direction; E_0 denotes the incident electron energy, λ the electron wavelength, and z the object thickness; $\phi_{1\mathrm{s},m_i}(\mathbf{r}-\boldsymbol{\beta}_{m_i})$ is the eigenfunction of the lowest energy bound state with energy $E_{1\mathrm{s},m_i}$. The corresponding excitation coefficients c_{m_i} may be found from [Van Dyck 1996]. The 1s-state of an atom column m_i at position $\boldsymbol{\beta}_{m_i}=\left(\beta_{x_{m_i}},\beta_{y_{m_i}}\right)^T$ can be approximated by [Geuens 2002]:

$$\phi_{1\mathrm{s},m_i}(\mathbf{r}-\boldsymbol{\beta}_{m_i}) = \frac{1}{a_{m_i}\sqrt{2\pi}}\exp\left(-\frac{\left(x-\beta_{x_{m_i}}\right)^2+\left(y-\beta_{y_{m_i}}\right)^2}{4a_{m_i}^2}\right) \tag{2.21}$$

where a_{m_i} is the column dependent width. The interpretation of Eq. (2.20) is as follows. Each atomic column acts as a channel in which the wave function oscillates periodically with depth [Van Dyck 1996, Van Aert 2007]. This periodicity is related to the average mass density of an atomic column and is given by

$$D_{1\mathrm{s}} = \left| \frac{2E_0\lambda}{E_{1\mathrm{s},m_i}} \right|. \tag{2.22}$$

This distance is called the extinction distance. The wave function in the image plane is given by the exit wave convoluted with a point spread function accounting for the effect of defocus ϵ and spherical aberration C_s [Van Dyck 2002]:

$$\psi_{\mathrm{im}}(\mathbf{r}, z; C_s, \epsilon) = 1 + \psi_{\mathrm{int}}(\mathbf{r}, z) * p_{C_s}(\mathbf{r}; C_s) * p_{\epsilon}(\mathbf{r}; \epsilon). \tag{2.23}$$

The intensity in the image plane is described by [Van Dyck 2002]

$$I(\mathbf{r}, z; C_s, \epsilon) = |\psi_{\mathrm{im}}(\mathbf{r}, z; C_s, \epsilon)|^2. \tag{2.24}$$

The intensity is the modulus squared of the image wave; other aberration effects are neglected in the simulations as it is assumed that they can be numerically corrected in the reconstruction [Coene 1996, Meyer 2002, Allen 2004a, Kirkland 2004, Allen 2004b].
In order to reconstruct the exit wave, the image intensities of the focal series are backpropagated. This backpropagation is performed by a convolution with the inverse point spread function of the defocus $p_{\epsilon}^{-1}(\mathbf{r}; \epsilon) = p_{\epsilon}^{*}(\mathbf{r}; \epsilon)$, which equals the point spread function of the defocus with the opposite focal value $p_{\epsilon}(\mathbf{r}; -\epsilon)$, In this way, a compensation is obtained for the effect of the defocus. The same procedure can be applied for spherical aberration resulting in the following expression:

$$\Psi_{\mathrm{rec}}(\mathbf{r}, z) = \langle I(\mathbf{r}, z) \rangle = \frac{1}{M} \sum_{m=1}^{M} I(\mathbf{r}, z; C_s, \epsilon) * p_{\epsilon}(\mathbf{r}, -\epsilon_m) * p_{C_s}(\mathbf{r}; -C_s) \tag{2.25}$$

The focal value ϵ_m corresponds to the focal value of an image of the focal series. Other aberrations, like incoherence effects present in the experimental can be corrected by including them in the backpropagation by the appropriate inverse point spread function [de Jong 1993, Allen 2004a]. It can be shown that the reconstructed exit wave using Eq. (2.25) will show good agreement with the true input exit wave [De Backer 2011]. This agreement enables us to use the parametric model from the channelling theory given by Eq. (2.20) in a statistical parameter estimation procedure applied to the reconstructed exit wave.
In the next subsection, the least squares estimation procedure when using the phase of the exit wave only or when using the full complex exit wave will be discussed.

2.3.3 Estimation of atomic column positions

Least squares estimator using the phase of the reconstructed exit wave

It is generally known that the phase of the exit wave is peaked at the atomic column positions. Accordingly, an empirical model is often used in which the phase is modelled as a superposition of Gaussian functions which are peaked at the atomic column positions [Houben 2006,

Bals 2006, Van Aert 2009a, Jia 2009b]. Therefore, the expectation at the pixel (k, l) at the position (x_k, y_l) of the phase of the exit wave can be described by the model of Eq. (2.9):

$$f_{kl}^{\mathrm{p}}(\boldsymbol{\theta}) = \zeta + \sum_{i=1}^{I} \sum_{m_i}^{M_i} \eta_{m_i} \exp\left(-\frac{\left(x_k - \beta_{x_{m_i}}\right)^2 + \left(y_l - \beta_{y_{m_i}}\right)^2}{2\rho_i^2} \right) \tag{2.26}$$

where the superscript p refers to the model for the phase. The parameters of this model

$$\boldsymbol{\theta} = \left(\beta_{x_{1_1}}, \ldots, \beta_{x_{M_I}}, \beta_{y_{1_1}}, \ldots, \beta_{y_{M_I}}, \rho_1, \ldots, \rho_I, \eta_{1_1}, \ldots, \eta_{M_I}, \zeta\right)^T \tag{2.27}$$

are estimated in the least squares sense. The uniformly weighted least squares estimated $\hat{\boldsymbol{\theta}}$ are given by the values of $\mathbf{t}$ that minimise the uniformly weighted least squares criterion:

$$\hat{\boldsymbol{\theta}} = \arg\min_{\mathbf{t}} \sum_{k=1}^{K} \sum_{l=1}^{L} \left(w_{kl} - f_{kl}^{\mathrm{p}}(\mathbf{t}) \right)^2 \tag{2.28}$$

with w_{kl} the value of the reconstructed phase at the pixel (k, l).

Least squares estimator using the phase and amplitude of the reconstructed exit wave

In order to attain a higher precision, especially for thicker specimens, all the information available in the reconstructed exit wave, i.e. phase and amplitude information, can be used to estimate the unknown parameters. The implementation for the complex exit wave is fully equivalent to the procedure for the phase, although more extended, and is based on the channelling theory. The complex exit wave is given by Eq. (2.20). This physics-based parametric model for this complex exit wave can be rewritten and separated in a real $\mathcal{R}$ and imaginary $\mathcal{I}$ part:

$$\begin{aligned} f_{kl}^{\mathrm{c}}(\boldsymbol{\theta}) =& \mathcal{R}(\boldsymbol{\theta}) + i\mathcal{I}(\boldsymbol{\theta}) \\ =& \left[\zeta_{\mathcal{R}} + \sum_{i=1}^{I} \sum_{m_i=1}^{M_i} \eta_{m_i}^{\mathcal{R}} \exp\left(-\frac{\left(x_k - \beta_{x_{m_i}}\right)^2 + \left(y_l - \beta_{y_{m_i}}\right)^2}{2\rho_i^2} \right) \right] \\ &+ i \left[\zeta_{\mathcal{I}} + \sum_{i=1}^{I} \sum_{m_i}^{M_i} \eta_{m_i}^{\mathcal{I}} \exp\left(-\frac{\left(x_k - \beta_{x_{m_i}}\right)^2 + \left(y_l - \beta_{y_{m_i}}\right)^2}{2\rho_i^2} \right) \right] \end{aligned} \tag{2.29}$$

where the superscript c refers to the model for the complex wave. The effect of the thickness of the object is incorporated in the parameters $\eta_{m_i}^{\mathcal{R}}$ and $\eta_{m_i}^{\mathcal{I}}$. The vector containing the unknown parameters for the complex model is:

$$\boldsymbol{\theta} = \left(\beta_{x_{1_1}}, \ldots, \beta_{x_{M_I}}, \beta_{y_{1_1}}, \ldots, \beta_{y_{M_I}}, \rho_1, \ldots, \rho_I, \eta_{1_1}^{\mathcal{R}}, \ldots, \eta_{M_I}^{\mathcal{R}}, \eta_{1_1}^{\mathcal{I}}, \ldots, \eta_{M_I}^{\mathcal{I}}, \zeta_{\mathcal{R}}, \zeta_{\mathcal{I}}\right)^T. \tag{2.30}$$

Minimisation of the uniformly weighted least squares criterion yields the estimated parameters:

$$\boldsymbol{\theta} = \arg\min_{\mathbf{t}} \sum_{k=1}^{K} \sum_{l=1}^{L} \left[\left(w_{kl}^{\mathcal{R}} - \mathcal{R}(\mathbf{t}) \right)^2 + \left(w_{kl}^{\mathcal{I}} - \mathcal{I}(\mathbf{t}) \right)^2 \right] \tag{2.31}$$

where $w_{kl}^{\mathcal{R}}$ and w_{kl}^{I} represent the real and imaginary parts of the reconstructed complex exit wave, respectively.

2.3.4 Attainable precision

It is expected that the lower bound on the variance of the unknown parameters can be attained by applying the maximum likelihood estimator to the originally recorded focal images, which is unpractical and computationally demanding. In order to derive this Cramér-Rao lower bound on the variance of the unknown parameters, the model describing the expectations of the original observations of the focal series is needed. The expectation model for the image intensity of an image of the recorded focal series used for this purpose equals:

$$f_{kl}^{\mathrm{i},m}(\boldsymbol{\theta}) = N\frac{I(\mathbf{r}, z; C_s, \epsilon_m)}{I_{\mathrm{norm}}}\Delta x\Delta y \tag{2.32}$$

where the superscript i refers to the model for the image intensity and m to the mth image of the focal series. This result defines the number of electrons expected to be found at a pixel (k, l) taking into account the electron dose. In this equation, N denotes the total number of incident electrons and Δx and Δy represent the sampling distances in the x- and y-directions and $I(\mathbf{r}, z; C_s, \epsilon_m)$ denotes the intensity in the image plane given by Eq. (2.24). The normalisation factor I_{norm} in Eq. (2.32) is given by:

$$I_{\mathrm{norm}} = \int I(\mathbf{r}, z; C_s, \epsilon_m)d\mathbf{r} \tag{2.33}$$

where the integral extends over the whole field of view. For HRTEM images in a focal series, the observations w_{kl}^m are assumed to be statistically independent having a Poisson distribution with the following joint probability density function equivalent to Eq. (2.8) [den Dekker 2005, Van Aert 2005]:

$$p(\boldsymbol{\omega}) = \prod_{m=1}^{M}\prod_{k=1}^{K}\prod_{l=1}^{L}\frac{\left(\lambda_{kl}^m\right)^{\omega_{kl}^m}}{\omega_{kl}^m!}\exp\left(-\lambda_{kl}^m\right) \tag{2.34}$$

where λ_{kl}^m is the expectation of a pixel value, i.e. $\mathbb{E}\left[\omega_{kl}\right] = \lambda_{kl}^m = f_{kl}^{\mathrm{i},m}(\boldsymbol{\theta})$. The Fisher information matrix for this set of Poisson distributed observations then becomes (equivalent to Eq. (2.12))

$$F_{rs} = \sum_{m=1}^{M}\sum_{k=1}^{K}\sum_{l=1}^{L}\frac{1}{\lambda_{kl}^m}\frac{\partial\lambda_{kl}^m}{\partial\theta_r}\frac{\partial\lambda_{kl}^m}{\partial\theta_s}. \tag{2.35}$$

The CRLB on the variance is given by the inverse of the Fisher information matrix. The derivatives in Eq. (2.35) are calculated with respect to the parameters $\boldsymbol{\theta}$ in the expectation model given by Eq. (2.32), i.e. the positions, the width, and the height of the atomic columns and a constant background. The diagonal elements of the inverse Fisher information matrix define lower bounds on the parameters $\boldsymbol{\theta}$. The thus obtained numbers will be compared with the variance of the structure parameters estimated from the phase of the reconstructed exit wave and estimated from the reconstructed complex exit wave. The exit wave is reconstructed using the method described in subsection 2.3.2. This comparison is first carried out for an isolated atomic column and next for an assembly of atom columns. Furthermore, the comparison is done for different specimen thicknesses. For thin specimens for which the weak phase object approximation

(WPOA) is valid, most objected information will be contained in the phase of the reconstructed exit wave. The weak phase object approximation is valid if [Van Dyck 1996, Geuens 2005]:

$$\left|E_{1\mathrm{s},n}\right| < \frac{E_0\lambda}{\pi z} \tag{2.36}$$

This can be rewritten in terms of the extinction distance $D_{1\mathrm{s}}$ of Eq. (2.22), i.e. the WPOA is valid if the specimen thickness is smaller than $0.16D_{1\mathrm{s}}$.

2.3.5 Simulations of Au [100]

Focal series for different thicknesses are simulated of an isolated Au [100] atomic column and of a 7×7 lattice of projected Au [100] atomic columns, modelled using the channelling theory. The microscope parameters for the simulation of the focal series are shown in Table 2.1; the value of C_s is arbitrarily chosen non-zero. For Au [100], the extinction distance $D_{1\mathrm{s}}$ equals 5.7 nm, i.e. about 14 atoms. This means that the WPOA is valid for a specimen thickness less than two atoms. However, it should be noted that some deviations can be expected from Eq. (2.22) for very heavy atoms.
The complex exit wave is reconstructed for 100 different Poisson distributed noise realisations of a focal series calculated from the expectation model given by Eq. (2.32). The unknown parameters of the parametric models for the phase of the reconstructed exit wave and the reconstructed complex exit wave, described by Eqs. (2.26) and (2.29), respectively, are estimated in the least squares sense. The sample mean and sample variance are computed from the 100 estimates and compared with the true values and the Cramér-Rao lower bound on the variance of the position parameters, respectively.

Parameter	Symbol	Value
Atomic number	Z	79
Column dependent width	a_{m_i} (Å^2)	0.13
1s state energy	$E_{1\mathrm{s},m_i}$ (eV)	−210.8
Interatomic distance	d (Å)	4.08
Extinction distance	$D_{1\mathrm{s}}$ (nm)	5.7
Extinction distance	$D_{1\mathrm{s}}$ (atoms)	14
Accelerating voltage	$V_0(kV)$	300
Mean focal value	ϵ(nm)	−75
Focal step	γ(nm)	2.5
Spherical aberration constant	C_s(mm)	0.5
Number of focal images	M	21
Pixel size	$\Delta x = \Delta y$ (Å)	0.1
Number of pixels x- and y-direction	$K = L$	1024
Electron dose	N_d (e^-Å^{-2})	7854

Table 2.1: *Object and microscope parameters for the simulation of the focal series.*

Isolated atomic column

In this analysis unbiased estimates have been obtained for the x- and y-coordinates. The results of the analysis of the attainability of the CRLB for an isolated column as a function of the object thickness are presented in Fig. 2.1. The figure shows the ratio of the estimated variance to the calculated CRLB for the x- and y-position coordinates. The CRLB on the variance of the position parameters also depends on the object thickness as is shown in the inset of Fig. 2.1. The attainable precision for the position parameters is highest when the thickness equals half the extinction distance, $0.5D_{1s}$. Here, the electrons are most strongly localised at the atomic column positions implying that the exit wave is peaked maximally at the atomic positions. From Fig. 2.1, it can be concluded that the lower bound on the variance is attained for all thicknesses when the column position coordinates are estimated from the complex reconstructed exit wave using the parametric model given by the channelling theory (Eq. (2.29)). This result is also valid for thicknesses larger than $0.5D_{1s}$ and will show a periodic behaviour since the exit wave varies periodically with depth. By estimating the position coordinates from the phase of the reconstructed exit wave using the model of Gaussian peaks of Eq. (2.26), the CRLB is attained only when the WPOA is valid, i.e. if the thickness is smaller than $0.16D_{1s}$. It is clear that for larger object thicknesses, for which the WPOA is no longer valid, estimating the position coordinates from the complex reconstructed exit wave is necessary in order to attain the highest possible precision.

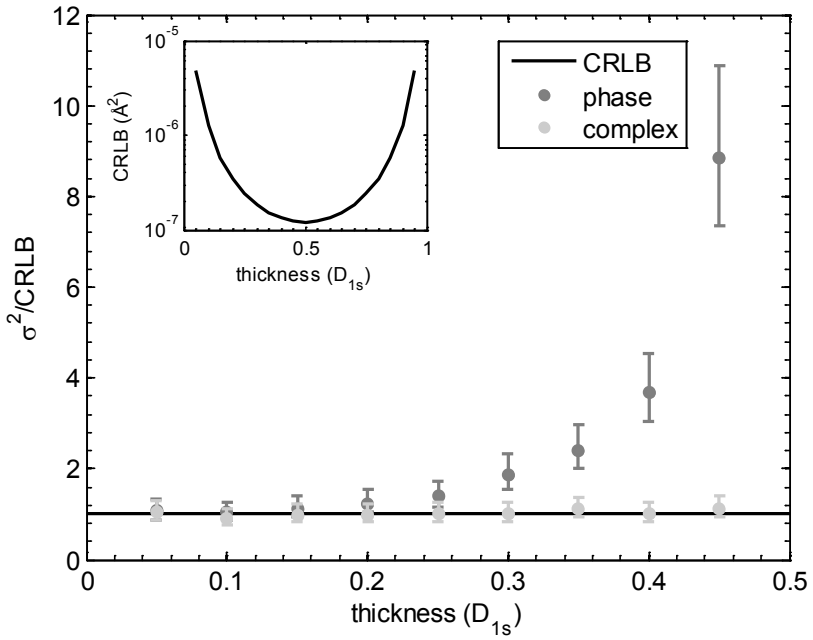

Figure 2.1: *Attainability of the CRLB as a function of the object thickness for an isolated Au* [100] *atomic column. The error bars show the* 95% *confidence intervals for the estimated variances. The inset shows the CRLB as a function of the object thickness.*

Assembly of atomic columns

To evaluate the effect of neighbouring atomic columns, a 7×7 lattice of projected Au [100] atomic columns is modelled. For an assembly of atomic columns two different thicknesses are considered: $z_1 = 0.1D_{1s}$ corresponding to a specimen thickness of only one atom and $z_2 = 0.4D_{1s}$ corresponding to a specimen thickness of five atoms. The WPOA is valid for z_1 but not for z_2. The positions of the central 5×5 atomic columns are considered in the analysis in order to avoid boundary effects at the outermost atomic columns of the simulations. Like for isolated atomic columns, the estimates for the position coordinates are unbiased. The results for the attainability of the CRLB for both thicknesses z_1 and z_2 are presented in Fig. 2.2. The ratio of the estimated variance of the x- and y-coordinates to the CRLB are plotted for the 25 atomic columns. As expected for the thin object the variances on the position parameters correspond to the theoretical lower bound on the variance for both estimating the position coordinates from the phase information only or from the full complex exit wave. For the thicker object, where the WPOA is no longer valid, the CRLB can only be attained by estimating the position coordinates from the complex model for the exit wave to the reconstructed exit wave. If the position parameters are determined based on the full complex exit wave, the precision is approximately three to four times better in terms of the variance than determining the atomic column positions from the phase of the reconstruction. This result is in agreement with the results of the isolated atomic column.

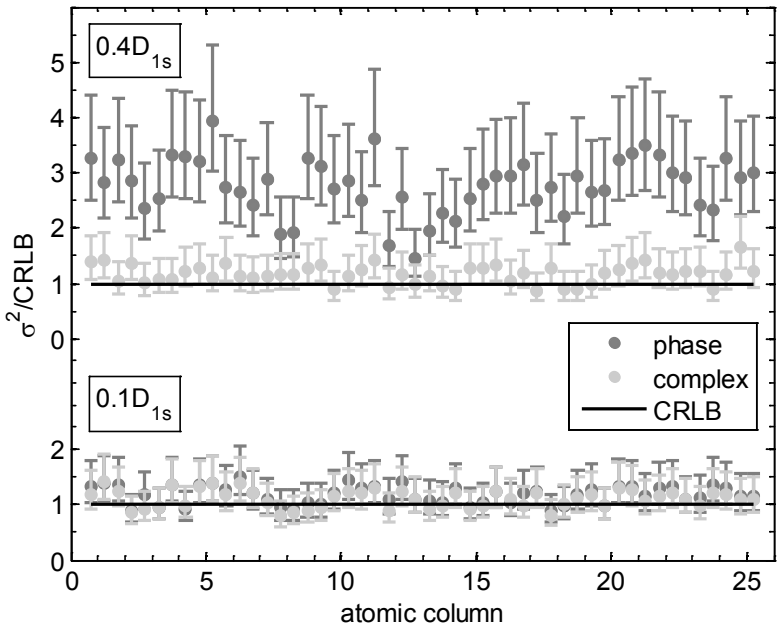

Figure 2.2: *Attainability of the CRLB for* 25 *position estimates of Au* [100] *atomic columns. The bottom of the graph shows the result for thickness* $z_1 = 0.1D_{1s}$ *and the top of the graph shows the result for thickness* $z_2 = 0.4D_{1s}$*, Each atomic column position corresponds to two estimated ratios in the graph, the x-coordinate and y-coordinate, resulting in* 50 *data points on the horizontal axis. The error bars show the* 95% *confidence intervals for the estimated variances.*

Discussion

In order to evaluate the precision that can be attained for the estimation of the atomic column positions from a focal series of images, the reconstructed complex exit wave, or the reconstructed phase of the complex exit wave, the simplified channelling theory has been used in order to describe the dynamical scattering of the electrons through the object. Obviously, this approximation is of limited validity. However, the analysis presented here focuses on the question whether the use of only the phase information in a quantitative analysis for atomic column measurements is justified or if the analysis would benefit if the amplitude would be used in addition. The simplified model-based channelling theory is very useful for this purpose and the results will be independent of the approximations made.
Furthermore, it should be noted, even when using a more accurate simulation approach, that in practice the lower bound and estimated variances will be typically larger, since their actual values critically depend on the image contrast. A reduction of contrast will indeed result in a loss of precision [Van Aert 2009a]. So far, the contrast mechanism in HRTEM images is not yet fully understood. The contrast in experimental images is typically a factor of three lower than in simulated images. This is the well-known contrast problem, often referred to as the Stobbs-factor [Hÿtch 1994, Boothroyd 1998, Thust 2009]. Phonon scattering and different experimental conditions, like the stability of the specimen and the microscope, atomic thermal vibrations, lattice configuration, residual microscope aberrations, time dependent incoherence may contribute to a loss of image contrast. So far, it is impossible to take all these factors properly into account in the theory.

Summary

In this section, the variance of the atomic column positions has been compared with the theoretical lower bound on the variance. Although it was expected that the CRLB could only be attained when deriving the maximum likelihood estimates from the full series of focal images, it has been demonstrated that the reconstructed complex exit wave contains the same amount of information on the positions parameters. Estimating the position parameters from the complex exit wave using the parametric model from the channelling theory results in the highest possible precision. This precision cannot be obtained when using the phase information only except for thin specimens where the weak phase approximation is valid, that is, thinner than $0.16D_{1s}$ with D_{1s} the extinction distance. For thicker specimens, an improvement of a factor of about four in terms of the variance with which the atomic column position can be estimated is observed, when using the full complex exit wave in the estimation procedure. From this study we can conclude that it is therefore recommendable to use the full complex exit wave to determine quantitative information about the atomic column positions.

In the next section, the concepts of statistical parameter estimation theory will be used to evaluate the accuracy and precision of the measurements of the atomic column positions and the scattering cross-sections from ADF STEM images.

2.4 ADF STEM: accurate and precise measurements of the scattering cross-sections and atomic column positions

Since ADF STEM images show Z-contrast and are sensitive to the number of atoms in the atomic columns, ADF STEM has become a popular technique for chemical composition determination and atom-counting because it provides directly interpretable images. Statistical model-based estimation procedures are required in this field, because it is impossible to e.g. directly count the number of atoms by means of visual interpretation only. Statistical parameter estimation theory enables one to extract quantitative information, such as chemical composition [Van Aert 2009b, Martinez 2014b] or the number of atoms [Van Aert 2011, Van Aert 2013]. In the next chapters of this thesis, a statistics-based method for atom-counting will be discussed in detail and will be applied to different nanostructures. Here, the aim is to count the number of atoms with single atom sensitivity. The parameters of the imaging model are therefore interpreted in terms of total intensities of scattered electrons by the atomic columns. These so-called scattering cross-sections are further explored in order to count the number of atoms that are present in an atomic column. The goal is then to estimate these scattering cross-sections and atomic column positions unbiasedly with the highest possible precision. Therefore, it is important to assess the accuracy and precision of the estimated parameters. Furthermore, it should be noticed that it is assumed that ADF STEM images are statistically independent counting results which can be modelled as Poisson distributed random variables. For the estimation of the unknown parameters of the expectation model, the least squares estimator is employed, which equals the maximum likelihood estimator in the case of independent normal distributed random variables as derived in subsection 2.2.3. The Poisson distribution tends to be a normal distribution for increasing expectation values for the pixel values. However, this assumption about the statistical distribution of the pixel values is not always valid, especially not at low electron doses, needed to avoid radiation damage in beam sensitive matter. In order to evaluate the accuracy and precision of the estimated parameters, use will be made of detailed ADF STEM multislice simulations. The true values of the parameters will be compared with the sample means in order to verify the accuracy. This will be done for the scattering cross-section and atomic column positions obtained from different noise realisations of a ADF STEM multislice simulation. The variance of the estimates computed using the Cramér-Rao lower bound will be compared with the sample variance.

First the model-based parameter estimation will be reformulated for ADF STEM images in subsection 2.4.1. Here, also the parameter of interest for the interpretation of the ADF STEM image intensities, i.e. the scattering cross-section, will be introduced. Next, the attainable precision for the position parameters and scattering cross-sections will be defined in subsection 2.4.2. Then, the ADF STEM simulations will be discussed briefly in subsection 2.4.3 before the results of the simulation study for the assessment of the accuracy and precision of the parameters of interest will be shown in subsection 2.4.4.

2.4.1 Model-based parameter estimation in ADF STEM

As a first step in the quantitative analysis of ADF STEM images, such as the statistics-based atom-counting analysis for mono-type crystalline nanostructures which will be presented in chapter 4, the ADF STEM images will be considered as a data plane from which the structure parameters have to be determined with the highest possible precision and accuracy. Therefore, the expectation model of Eq. (2.9) will be used:

$$f_{kl}(\boldsymbol{\theta}) = \zeta + \sum_{n=1}^{N} \eta_m \exp\left(-\frac{(x_k - \beta_{x_n})^2 + \left(y_l - \beta_{y_n}\right)^2}{2\rho^2}\right). \tag{2.37}$$

The unknown parameters are thus given by the parameter vector:

$$\boldsymbol{\theta} = \left(\beta_{x_1}, \ldots, \beta_{x_N}, \beta_{y_1}, \ldots, \beta_{y_N}, \rho, \eta_1, \ldots, \eta_N, \zeta\right)^T. \tag{2.38}$$

The parametric model of Eq. (2.37) is fitted to the experimental data using the least squares criterion quantifying the similarity between the experimental images and the model:

$$\hat{\boldsymbol{\theta}} = \arg\min_{\mathbf{t}} \sum_{k=1}^{K} \sum_{l=1}^{L} \left(w_{kl} - f_{kl}(\mathbf{t})\right)^2. \tag{2.39}$$

The volume under a peak above a background reflects the total intensity of electrons scattered toward the ADF detector for every atomic column. These are the so-called scattering cross-sections which can be used to quantify chemical composition or number of atoms in a projected atomic column from an ADF STEM image. These scattering cross-sections can be calculated as follows [Van Aert 2009b]:

$$\hat{V}_n = 2\pi\hat{\eta}_n\hat{\rho}^2. \tag{2.40}$$

The precision and accuracy of the estimated atomic column positions $\hat{\beta}_{x_n}$ and scattering cross-sections $\hat{V}_n$ will be evaluated in the next paragraphs.

2.4.2 Attainable precision

It is expected that the lower bound on the variance of the unknown parameters, i.e. the atomic column positions and the scattering cross-sections, can be attained when applying the maximum likelihood estimator and if unbiased estimates are obtained. Here, the least squares estimator of Eq. (2.39) is used, although the observations are modelled as independent Poisson distributed variables. The Poisson distribution tends to be a normal distribution, for an increasing expectation value λ_{kl} as discussed in section 2.2.3. This means, that when the detected electron dose is high, the uniformly weighted least squares estimator gives maximum likelihood estimates for the unknown parameters. Therefore, the attainability of the lower bound on the variance of atomic column position and scattering cross-section will be investigated for different incident electron doses.

The Fisher information matrix for ADF STEM images, which are a set of Poisson distributed observations equals (Eq. (2.12)):

$$F_{rs} = \sum_{k=1}^{L} \sum_{l=1}^{L} \frac{1}{\lambda_{kl}} \frac{\partial \lambda_{kl}}{\partial \theta_r} \frac{\partial \lambda_{kl}}{\partial \theta_s} \tag{2.41}$$

The diagonal elements of the inverse Fisher information matrix define lower bounds on the parameters $\boldsymbol{\theta}$. Following Eq. (2.16), the expression for the CRLB on the variance of the scattering cross-sections, which is a function of the parameters $\boldsymbol{\theta}$ is given by:

$$\sigma^2_{V_n} = \frac{\partial V_n}{\partial \boldsymbol{\theta}} F^{-1}_{\boldsymbol{\theta}} \left(\frac{\partial V_n}{\partial \boldsymbol{\theta}} \right)^T \tag{2.42}$$

where V_n is the scattering cross-section for the nth atomic column in the ADF STEM image given by Eq. (2.40). The elements of the Fisher information matrix are given by Eq. (2.41). The vector $\frac{\partial V_n}{\partial \boldsymbol{\theta}}$ is a $(3N + 2)$-vector consisting of zeros except for the $(2N + 1)$th and $(2N + 1 + n)$th elements. These elements are equal to:

$$\left[\frac{\partial V_n}{\partial \boldsymbol{\theta}} \right]_{1,2N+1} = \frac{\partial V_n}{\partial \rho} = 4\pi \eta_n \rho$$
$$\left[\frac{\partial V_n}{\partial \boldsymbol{\theta}} \right]_{1,2N+1+n} = \frac{\partial V_n}{\partial \eta_n} = 2\pi \rho^2.$$

Explicit numbers for the CRLB on the variance of the atomic column positions and the scattering cross-sections can be computed by substituting the values of the true parameters into Eqs. (2.41) and (2.42). However, since the observations are Poisson distributed noise realisations of detailed ADF STEM simulations using the STEMsim software [Rosenauer 2008], only the true parameters of the atomic column positions are available. Therefore, the elements F_{rs} and $\sigma^2_{V_n}$ may only be estimated. This will be done by substituting estimated values for the parameters ρ and η_n for the true parameters. These estimates for the true parameters of ρ and η_n are obtained by fitting the model given by Eq. (2.37) to the detailed STEMsim model for the ADF STEM image, i.e. in absence of noise, which will be described in the next subsection. The estimated Fisher information matrix and estimated lower bounds on the variances will be denoted as $\hat{F}_{\boldsymbol{\theta}}$ and $\hat{\sigma}^2$, respectively.

2.4.3 HAADF STEM simulation study

The analysis presented here will make use of multislice simulations under the absorptive potential approximation [Ishizuka 2002] because of their suitability to describe electron-sample interaction for thin samples. The ADF STEM images are calculated using the STEMsim software [Rosenauer 2008]. The absorptive potential approximation is computationally less demanding while it still describes the image intensities properly up to 50 nm thickness of the sample [Rosenauer 2009]. We simulated a Pt structure in [100] and [110] zone axis up to 75 atoms thickness, i.e. $\approx$ 30 nm and $\approx$ 21 nm, respectively. The simulated images were convolved with a Gaussian function to account for spatial incoherence. The simulation settings are summarised

in Table 2.2. The Debye-Waller factor in the table describes the atomic vibrations. This Debye-Waller factor is temperature dependent and has been parametrised for several elemental crystals and compounds with zinc-blende structure by [Gao 1999].
Using the model described by Eq. (2.37), the scattering cross-sections and atomic column positions are estimated from the simulated images. As presented in [Martinez 2014b], fitting a constant background to a simulation is not needed, since this background considers signals that do not originate from the sample under study, such as the sample support or grid. Consequently, a background with value 0 was considered for this analysis.
The analysis of simulated images for two different zone axes is intended to consider different atomic column spacings, having a different effect on the cross-talk of the electron beam through the sample.

Parameter	Symbol	Value
Acceleration voltage	V_0 (kV)	300
Defocus	ϵ (nm)	−8.8741
Spherical aberration	C_s (mm)	0.04
Spherical aberration of 5th order	C_5 (mm)	10
Objective aperture angle	α (mrad)	21.1
Spatial incoherence of source	FWHM (Å)	0.7
Number of unit cells per supercell	$N_a \times N_b$	9×9
HAADF inner collection angle	β_1 (mrad)	60
HAADF outer collection angle	β_2 (mrad)	190
Maximum specimen thickness [100]	$z_{[100]}$ (nm)	29.4
Maximum specimen thickness [110]	$z_{[110]}$ (nm)	20.8
Debye-Waller factor	B (Å^2)	0.384
Pixel size [100]	$\Delta x = \Delta y$ (Å)	0.1569
Pixel size [110]	$\Delta x = \Delta y$ (Å)	0.1121

Table 2.2: *Settings used for absorptive potential multislice simulations of Pt in* [100] *and* [110] *zone axes*

2.4.4 Results

Detailed ADF STEM simulations are available for an increasing thickness from 1 to 75 atoms for Pt in the [100] and [110] orientation as described in the previous subsection. In order to evaluate the attainability of the CRLB, different values for the incident electron dose N_d (e$^-$/Å^2) are considered:

$$\lambda_{kl} = N_p f_{kl} = N_d \Delta x \Delta y f_{kl} \tag{2.43}$$

where λ_{kl} equals the expectation model including the electron dose, f_{kl} equals the detailed ADF STEM simulation, N_p equals the incident electron dose per pixel, $\Delta x = \Delta y$ equals the pixel size, and N_d the incident electron dose per area. Atomic resolution imaging is still possible with doses on the order of $N_d = 10^2\ e^-$Å^{-2} for LAADF STEM according to [Buban 2010]. Therefore electron doses of $N_d = 5 \cdot 10^2\ e^-$Å^{-2}, and $N_d = 5 \cdot 10^5\ e^-$Å^{-2} are used in the simulation study

based on HAADF STEM images. For each thickness, 100 noise realisations are simulated for the two different doses. Next, the noise realisations are normalised with respect to the incident electron dose, i.e. divided by the incident electron dose placing the noise realisations on the same intensity scale as the detailed image simulations f_{kl} from STEMsim. The detailed STEM simulations and corresponding noise realisations are illustrated in Fig. 2.3.
From the noise realisations, the parameters of the parametric model given by Eq. (2.37) are estimated. The parameters that are evaluated here are the normalised scattering cross-section and the x-coordinate of the central atomic column in the simulated ADF STEM image. Only the x-coordinate is evaluated since the x- and y-coordinate show exactly the same behaviour for this symmetric simulation. In order to evaluate the accuracy of the estimates, the sample means have been compared with the reference values. For the atomic column positions, the reference

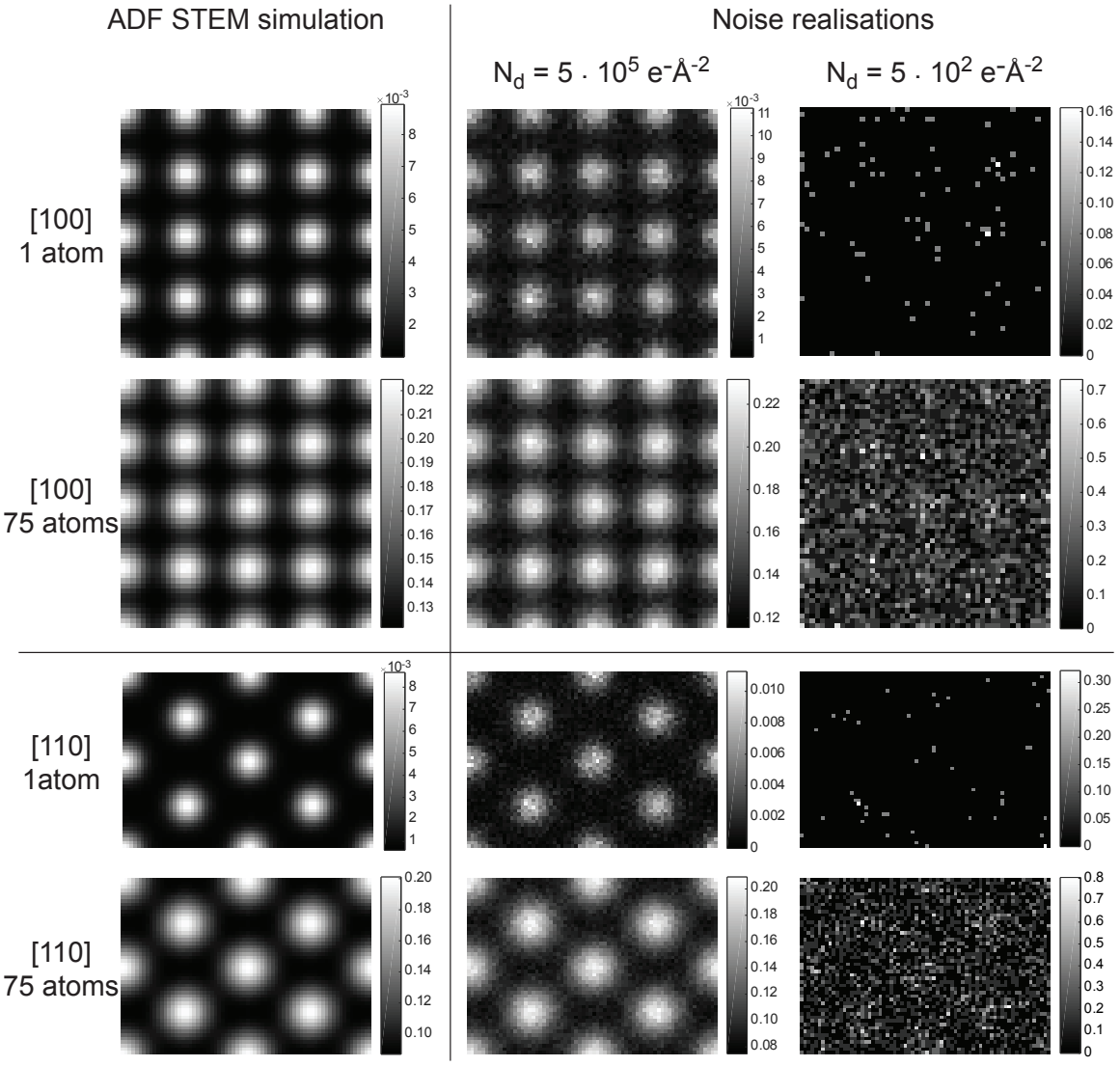

Figure 2.3: *Detailed ADF STEM simulations for [100] and [110] orientation for 1 atoms and 75 atoms thickness. The corresponding normalised noise realisations for an incoming electron dose of* $N_d = 5 \cdot 10^2\ e^{-}\text{Å}^{-2}$ *and* $N_d = 5 \cdot 10^5\ e^{-}\text{Å}^{-2}$ *are also shown.*

value equals the true value of the atomic column position from the input structure of the STEM simulation described in the previous paragraph. For the scattering cross-sections, the estimated values from the detailed ADF STEM simulation f_{kl} (in absence of Poisson distributed noise) is taken as a reference. The $(1-\alpha)\times 100\%$ confidence intervals of the sample mean of the x-coordinate $\bar{\beta}_x$ and the scattering cross-section $\bar{V}$ of the central atom are given by:

$$\left[\bar{\beta}_x - t_{1-\frac{\alpha}{2},N-1}\frac{s_{\beta_x}}{\sqrt{N}}, \bar{\beta}_x + t_{1-\frac{\alpha}{2},N-1}\frac{s_{\beta_x}}{\sqrt{N}}\right] \tag{2.44}$$

$$\left[\bar{V} - t_{1-\frac{\alpha}{2},N-1}\frac{s_V}{\sqrt{N}}, \bar{V} + t_{1-\frac{\alpha}{2},N-1}\frac{s_V}{\sqrt{N}}\right] \tag{2.45}$$

with s_{β_x} and s_V the standard deviation and $t_{1-\frac{\alpha}{2},N-1}$ equals the $1-\frac{\alpha}{2}$-quantile of the Student's t distribution with $N-1$ degrees of freedom, where N equals the sample size.
In order to evaluate the precision of the estimates, the sample variances are compared with the estimated lower bounds on the variances. The $(1-\alpha)\times 100\%$ confidence intervals on the sample variance of the x-coordinate $s^2_{\beta_x}$ and on the sample variance of the scattering cross-section s^2_V are given by:

$$\left[\frac{(N-1)s^2_{\beta_x}}{\chi^2_{\frac{\alpha}{2},N-1}}, \frac{(N-1)s^2_{\beta_x}}{\chi^2_{1-\frac{\alpha}{2},N-1}}\right] \tag{2.46}$$

$$\left[\frac{(N-1)s^2_{V}}{\chi^2_{\frac{\alpha}{2},N-1}}, \frac{(N-1)s^2_{V}}{\chi^2_{1-\frac{\alpha}{2},N-1}}\right] \tag{2.47}$$

with $s^2_{\beta_x}$ and s^2_V the sample variances for β_x and V, respectively, and $\chi^2_{1-\frac{\alpha}{2},N-1}$ and $\chi^2_{\frac{\alpha}{2},N-1}$ are the $1-\frac{\alpha}{2}$- and $\frac{\alpha}{2}$-quantiles of the χ^2 distribution with $N-1$ degrees of freedom, respectively.
The results of the study of the accuracy of the scattering cross-sections and position coordinates are shown in Figs. 2.4 and 2.5 for electron doses of $N_d = 5\cdot 10^5\ e^-\text{Å}^{-2}$ and $N_d = 5\cdot 10^2\ e^-\text{Å}^{-2}$, respectively. The sample means from the estimates resulting from the 100 noise realisations are plotted together with the true values of the scattering cross-sections and x-coordinate of the central atomic column. It is clear that unbiased estimates are obtained for both the scattering cross-sections as well as the x-coordinate of the central atomic column. For an incident electron dose of $N_d = 5\cdot 10^5\ e^-\text{Å}^{-2}$, the 95% confidence intervals of the scattering cross-sections are too small to be visible in Fig. 2.4. It is clear that the confidence intervals on the sample means become larger when reducing the incident electron dose to $N_d = 5\cdot 10^2\ e^-\text{Å}^{-2}$. The estimates for the scattering cross-sections and the x-coordinates of the central atomic column are still accurate for this lower incident electron dose.

The results for the precision of the estimated scattering cross-sections and position coordinates are shown in Figs. 2.6 and 2.7 for electron doses of $N_d = 5\cdot 10^5\ e^-\text{Å}^{-2}$ and $N_d = 5\cdot 10^2\ e^-\text{Å}^{-2}$, respectively. In these figures, the sample variances from the estimates of the 100 noise realisations are plotted together with the theoretical lower bound on the variance, the CRLB. Two main conclusions can be drawn from these Figs. 2.6 and 2.7. First, the CRLB allows us to evaluate the precision as a function of the number of atoms for the scattering cross-sections and position coordinates. The variance on the scattering cross-section increases with increasing

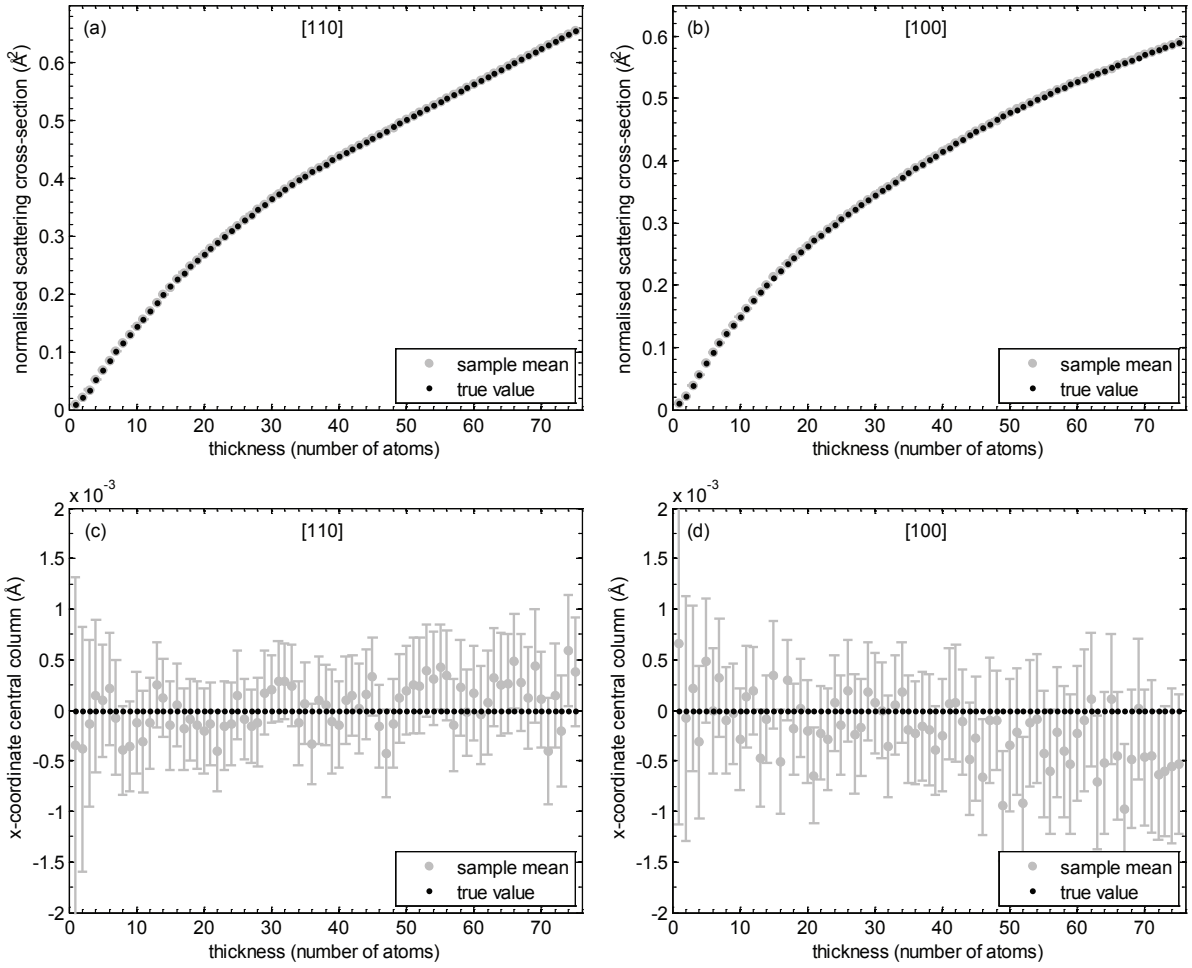

Figure 2.4: ***Accuracy*** *of the estimated scattering cross-sections and position coordinates for an incoming electron dose of* $\boldsymbol{N_d = 5 \cdot 10^5\ e^-Å^{-2}}$*. The true values and the sample mean together with the* 95% *confidence interval are shown for the (a) scattering cross-sections of Pt* [110]*, (b) scattering cross-sections of Pt* [100]*, (c) x-coordinate of the central atomic column of Pt* [110]*, and (d) x-coordinate of the central atomic column of Pt* [100]*.*

number of atoms in a projected atomic column. The variance of the position coordinate of the atomic columns decreases up to 20 atoms. Beyond this thickness, the probe will be delocalised and the variance on the position coordinates increases. Second, the attainability of the CRLB can be evaluated from these figures. For an incident electron dose of $N_d = 5 \cdot 10^5\ e^-Å^{-2}$ in Fig. 2.6, the CRLB is attained for the whole range of number of atoms. For the reduced electron dose of $N_d = 5 \cdot 10^2\ e^-Å^{-2}$ in Fig. 2.7, the CRLB on the variance of the scattering cross-sections and x-coordinate of the central atomic column is not attained for very small number of atoms. This result is not unexpected since the detected number of electrons is very low in this case. Indeed, with a pixel size of 0.1121 Å for Pt [110], the incident electron dose per pixel equals approximately 6 e^-/pixel; for Pt [100], with a pixel size of 0.1569 Å, the incident electron dose per pixel equals approximately 12 e^-/pixel. Since the maximal pixel intensity for single atom thickness expressed as a fraction of the incident electron beam equals approximately 0.01, the probability that an electron is detected will be very low. This is also clear from the noise real-

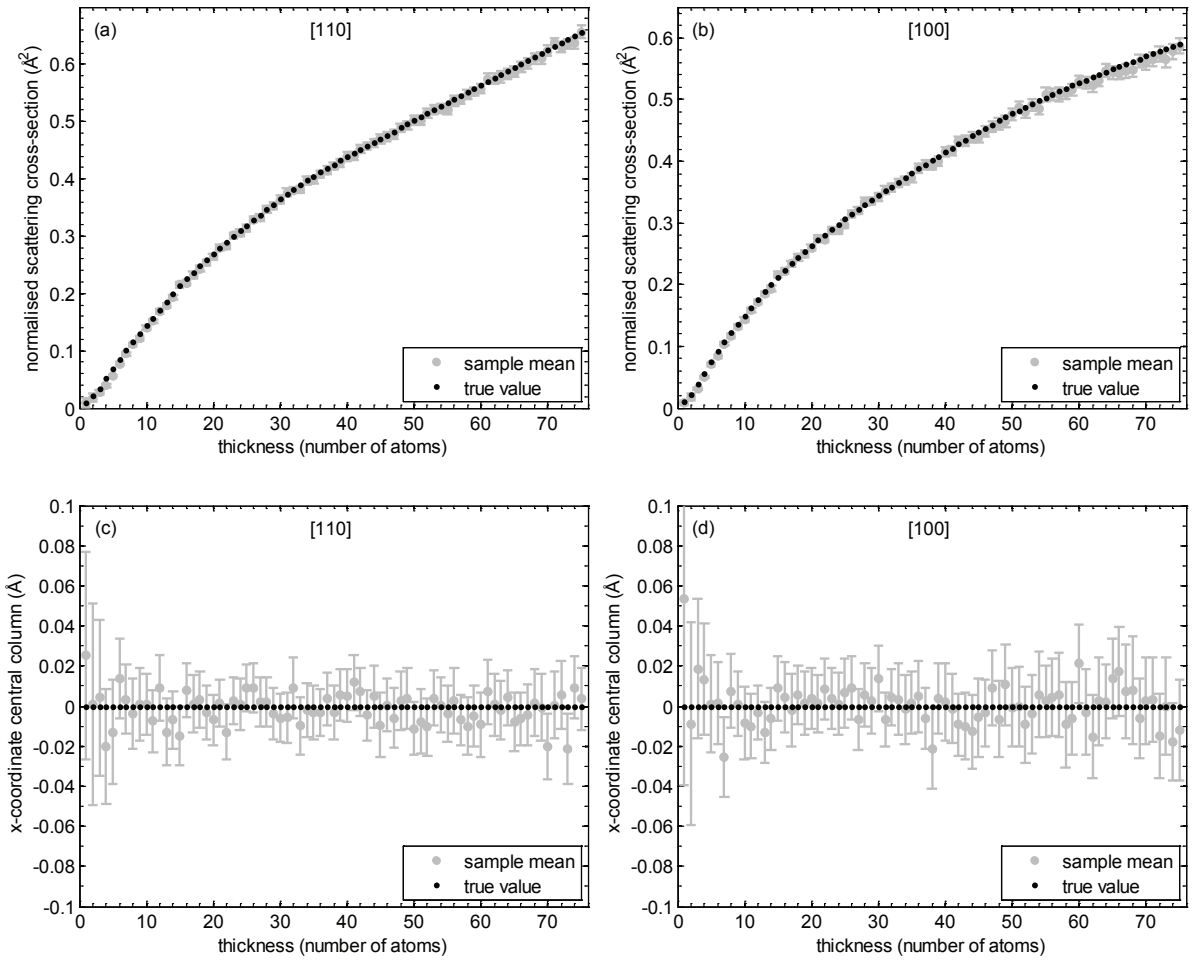

Figure 2.5: ***Accuracy*** *of the estimated scattering cross-sections and position coordinates for an incoming electron dose of* $\boldsymbol{N_d = 5 \cdot 10^2\ e^-\text{Å}^{-2}}$*. The true values and the sample mean together with the* 95% *confidence interval are shown for the (a) scattering cross-sections of Pt* [110]*, (b) scattering cross-sections of Pt* [100]*, (c) x-coordinate of the central atomic column of Pt* [110]*, and (d) x-coordinate of the central atomic column of Pt* [100]*.*

isations with $N_d = 5 \cdot 10^2\ e^-\text{Å}^{-2}$ in Fig. 2.3. In this case, the noise realisation does not show the shape of the atomic columns anymore. Because of the prior knowledge of the presence of atomic columns, an attempt to estimate the model parameters is made, although the model estimation starts to fail here. For practical applications requiring the same low incident electron dose, the detected dose should be increased, which can be done by increasing the pixel size and/or decreasing the inner detector angle. Nevertheless, this simulation study shows that the lower bound on the variance is attained for the estimation of the scattering cross-sections and position coordinates from ADF STEM images which are assumed to have independent Poisson distributed pixel values, using the least squares estimator. This result is of great importance, since this means that the estimated scattering cross-sections, which will be extensively used as an input for the atom-counting method, are obtained with the highest possible precision.

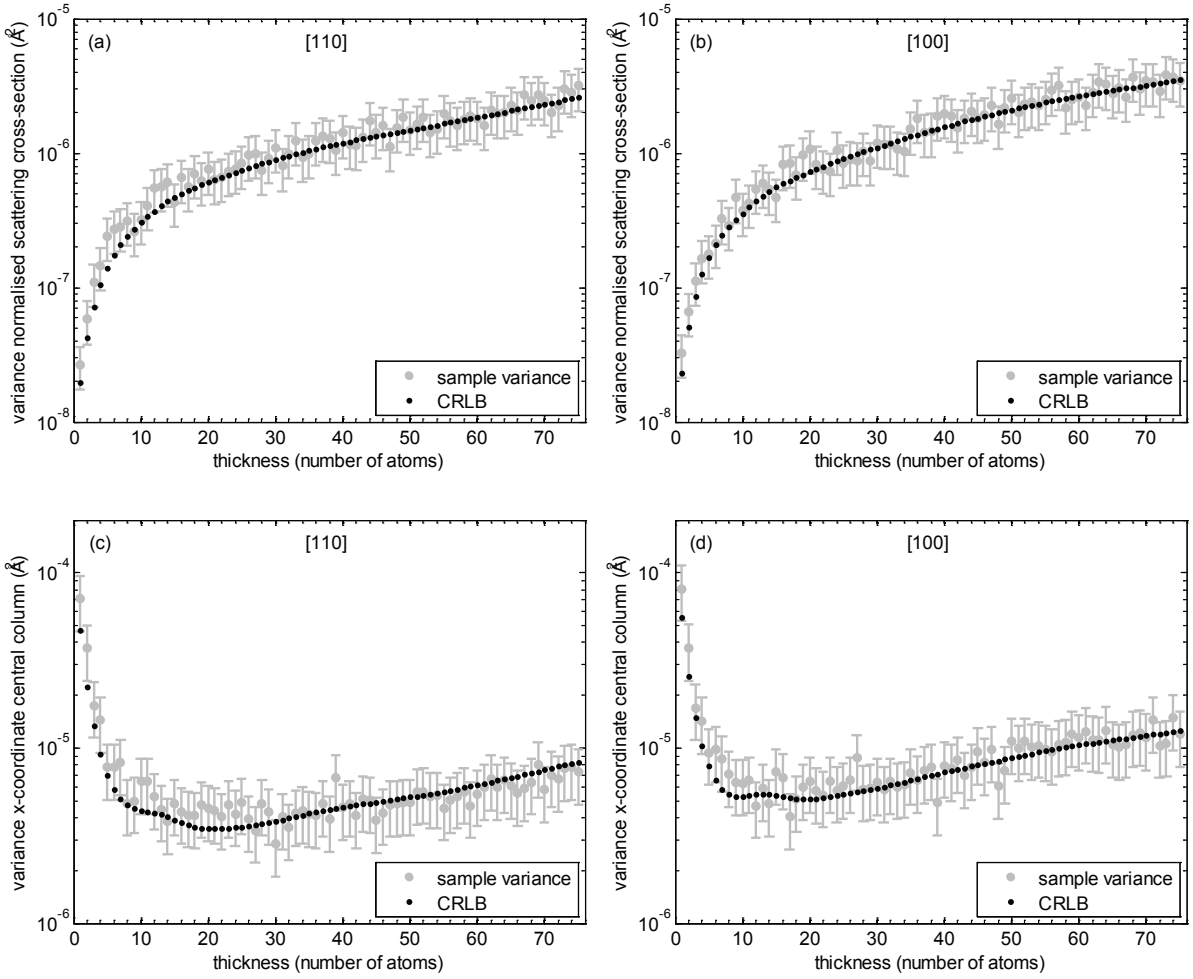

Figure 2.6: ***Precision*** *of the estimated scattering cross-sections and position coordinates for an incoming electron dose of* $N_d = 5 \cdot 10^5\ e^- Å^{-2}$*. The Cramér-Rao lower bound and the sample variances together with the* 95% *confidence interval are shown for the (a) scattering cross-sections of Pt* [110]*, (b) scattering cross-sections of Pt* [100]*, (c) x-coordinate of the central atomic column of Pt* [110]*, and (d) x-coordinate of the central atomic column of Pt* [100].

2.5 Conclusions

In this chapter, the principles of statistical parameter estimation theory have been introduced. Within this framework, electron microscopy observations can be described by a parametric statistical model defining the expectations of the observations and the fluctuations of the observations about these expectations. Furthermore, statistical parameter estimation theory provides a theoretical lower bound, i.e. the Cramér-Rao lower bound, on the variance of an unbiased estimator which can be reached asymptotically using the maximum likelihood estimator. In practice, the least squares estimator which equals the maximum likelihood estimator for independent normally distributed random values, is used to estimate the unknown parameter of the model.

The Cramér-Rao lower bound has been used to study the amount of information on the position

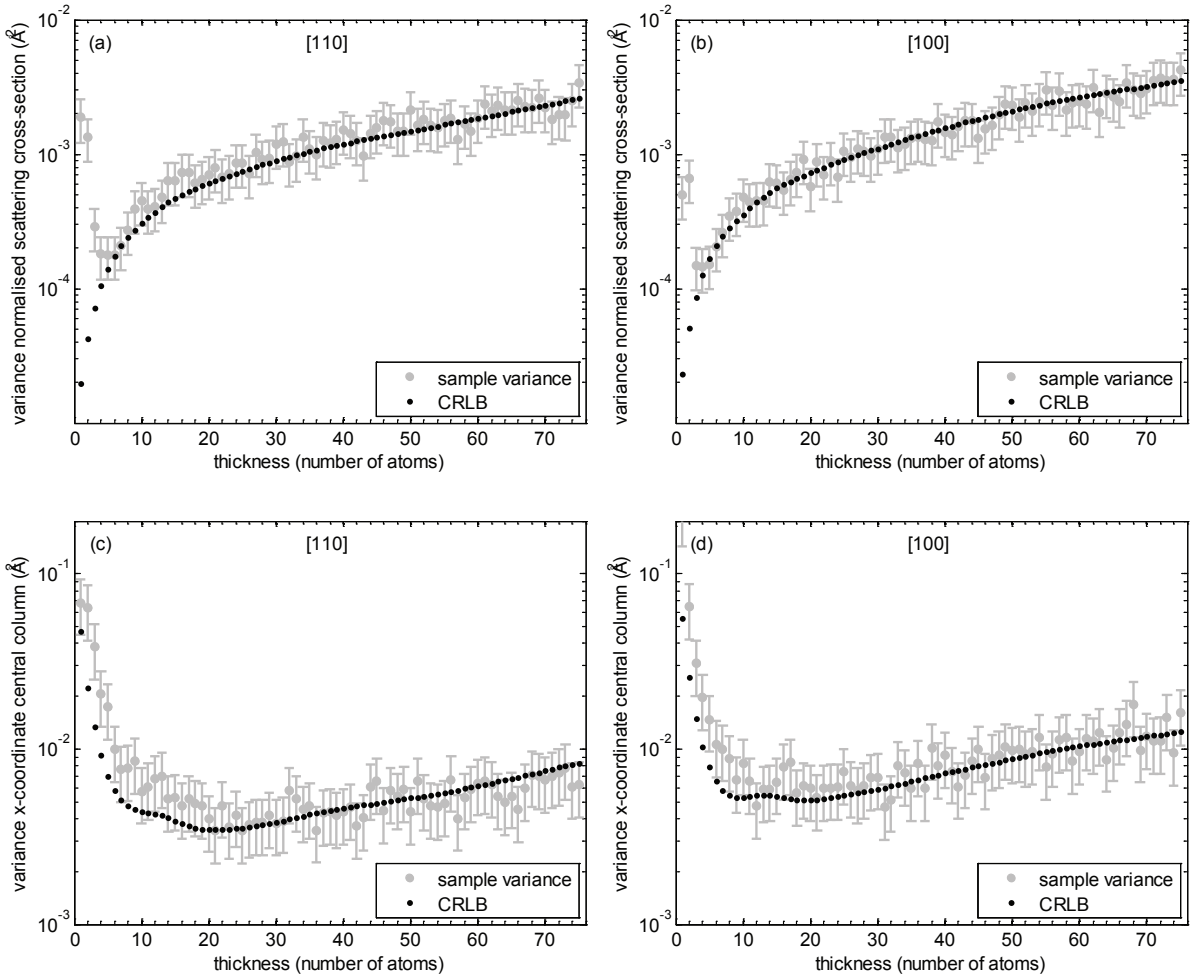

Figure 2.7: ***Precision*** *of the estimated scattering cross-sections and position coordinates for an incoming electron dose of* $N_d = 5 \cdot 10^2\ e^-Å^{-2}$*. The Cramér-Rao lower bound and the sample variances together with the* 95% *confidence interval are shown for the (a) scattering cross-sections of Pt* [110]*, (b) scattering cross-sections of Pt* [100]*, (c) x-coordinate of the central atomic column of Pt* [110]*, and (d) x-coordinate of the central atomic column of Pt* [100].

parameters contained in a reconstructed exit wave. It has been shown that the same precision can be obtained from the reconstructed complex exit wave and the full series of focal images. This precision cannot be obtained when using the phase information only, except for thin specimens where the weak phase object approximation is valid.

In order to explore the ultimate limits in ADF STEM, the precision and accuracy of the estimates for the atomic column position coordinates and scattering cross-sections have been evaluated using multislice simulations. Although, the pixel values of ADF STEM images are modelled as independent Poisson distributed variables, it turns out that even for low incident electron doses, the Cramér-Rao lower bound on the variance of the estimates has been obtained. This conclusion is extremely important, since these estimates will be extensively used as an input for a statistics-based atom-counting method discussed in chapter 4.

Concluding, based on statistical parameter estimation theory, electron microscopy images may

be analysed quantitatively and estimates for the structure parameters, such as the atomic column positions and scattering cross-sections can be obtained with the highest possible precision.
In chapter 3, the implementation of the least squares estimator will be reviewed. A direct implementation of the least squares estimator limits the area that can be analysed, since the estimation of all the parameters of the parametric model at the same time is computationally very intensive. Therefore an efficient implementation of the least squares estimator is required, which will enable us to quantify larger areas.

3 Efficient fitting algorithm

3.1 Introduction

Nowadays, more and more quantitative measurements for the analysis of nanomaterials are required. This includes locating atomic column positions with a precision in the picometre range, a precise determination of the chemical composition of materials, and counting the number of atoms with single atom sensitivity. Moreover, one is interested in a quantitative analysis of larger areas preserving the highest possible precision that can be attained using statistical parameter estimation theory. Therefore, in this chapter, the implementation of the least squares estimator (LSE), which is used for the estimation of the parameters of the model describing the observations in a (S)TEM image, will be reviewed.
As discussed in chapter 2, in subsection 2.2.3, the maximum likelihood estimator (MLE) equals the LSE for independent normally distributed variables. However, direct implementation of the LSE in which all parameters are estimated at the same time is computationally very intensive and feasible only from images containing a limited number of projected atomic columns in a HR(S)TEM image, i.e. a limited field of view. Therefore, a more efficient algorithm is proposed for obtaining the unknown structure parameters. The use of this algorithm enables us to analyse large fields of view.
The basic idea of the new algorithm is the segmentation of the image into smaller sections containing individual columns. In this way, only the parameters corresponding to a single atomic column are estimated at the same time, instead of all the parameters of the parametric model. Two different efficient model estimation methods will be proposed for two different variants of the parametric models discussed in chapter 2. For the first model estimation method, each atomic column will be modelled with a Gaussian peak having a different width; this method will be referred to as 'model estimation A'. In the second model estimation method, the same width will be estimated for atomic columns of the same atom type; this method will be referred to as 'model estimation B'. Different widths for each Gaussian in the parametric model corresponding to the intensity of an atomic column in the HR(S)TEM image, as in 'model estimation

A', are required if no prior knowledge is available on e.g. the atomic column types. However, if prior knowledge is available, the number of parameters of the expectation model that needs to be estimated in the model can be reduced, as in 'model estimation B'. This approach enhances the precision of the parameter estimates. In addition, the estimation of the parameters of such a model will be more robust in the case of the inevitable presence of different types of noise (e.g. scanning noise in HRSTEM images). The estimates for the parameters for 'model estimation A' do often not converge because of noise.
In section 3.2, this efficient algorithm for the estimation of atomic column positions and intensities from HR(S)TEM images will be introduced. After this, the efficient estimation algorithm will be applied to three different nanostructures for which the analysis of a large field of view is required. In the first example in section 3.3, estimated models will be obtained for ADF STEM images of a core-shell nanostructure recorded along different zone axes. The estimated models as such will be used as an input for a three-dimensional reconstruction in order to determine the position and atom type of each atom. In the next two examples in section 3.4, the estimated atomic column position coordinates will be used to make displacement maps of a large field of view. This will be done for five-fold-twinned decahedral Au nanoparticles in subsection 3.4.1 and for the positions of Al-columns within LaAlO in subsection 3.4.2.

3.2 Efficient model estimation algorithm

In this section, two different efficient model estimation methods will be proposed[2]. The parametric model that will be implemented is a superposition of Gaussian peaks describing the peaked intensity at the atomic column positions as described in chapter 2 in subsection 2.2.1. The idea of the new algorithms is a segmentation of the image into smaller sections containing individual atomic columns. Therefore, it is required that the image can be described as a superposition of the individual atomic columns. For example, incoherent imaging in ADF STEM meets this necessary condition.
In subsection 3.2.1, 'model estimation A' with a different width assumed for each Gaussian is introduced. Next, subsection 3.2.2 introduces 'model estimation B' where the same width is assumed for Gaussian peaks at the atomic columns of the same atom type.

3.2.1 Model estimation A

Different width for each estimated Gaussian peak of an atomic column

When a different width is assumed for each estimated Gaussian corresponding to the intensity of an atomic column, the parametric model of Eq. (2.9) can be rewritten as:

$$f_{kl}(\boldsymbol{\theta}) = \zeta + \sum_{n=1}^{N} \eta_n \exp\left(-\frac{(x_k - \beta_{x_n})^2 + \left(y_l - \beta_{y_n}\right)^2}{2\rho_n^2}\right). \tag{3.1}$$

[2]The efficient model estimation method is introduced in A. J. den Dekker, J. Gonnissen, *A. De Backer*, J. Sijbers, and S. Van Aert, Estimation of unknown structure parameters from high-resolution (S)TEM images: What are the limits?, Ultramicroscopy 134 (2013) 34-43.

with ζ a constant background, ρ_n and η_n the width and height of the nth Gaussian peak, β_{x_n} and β_{y_n} the x- and y-coordinate of the nth atomic column respectively, and N the total number of atomic columns. The unknown parameters of the expectation model are then given by:

$$\boldsymbol{\theta} = \left(\beta_{x_1}, \ldots, \beta_{x_N}, \beta_{y_1}, \ldots, \beta_{y_N}, \rho_1, \ldots, \rho_N, \eta_1, \ldots, \eta_N, \zeta\right)^T . \tag{3.2}$$

It is assumed that proper starting values are available for the parameters of the empirical model. Good starting values are necessary in order to avoid ending up in a local minimum during the model estimation procedure. Initial values for the widths ρ_n of the Gaussians are easy to provide and starting coordinates for the positions β_{x_n} and β_{y_n} of projected atomic columns can be given using e.g. a peak finding routine. For this purpose, the quality of the image has to be sufficient, i.e. the image resolution should be high enough. This means that a high-resolution image is required, where individual columns are atomically resolved. If the resolution is only just sufficient, prior knowledge on the structure, e.g. the presence of dumbbells, can still provide the starting values for atomic column positions.

The parameters β_{x_n}, β_{y_n}, and ρ_n are the non-linear parameters of the model and will be denoted as $\boldsymbol{\alpha}$. An initial guess for the linear parameters, i.e. the heights η_n and background ζ denoted as $\boldsymbol{\xi}$, is not needed, since the linear parameters in the model can be replaced by their linear least squares estimates given the values of the non-linear parameters of the model [Lawton 1971]. These linear least squares estimates are the best companion values for the linear parameters and the computation involves only a simple linear regression. In addition, this approach has a second benefit apart from the fact that no starting guesses are needed for the linear parameters. The number of parameters that needs to be estimated in an iterative procedure is reduced, since the best companion values for the linear parameters are used in each iteration increasing the convergence of the model estimation.

Schematically, the proposed algorithm for model estimation is outlined in Fig. 3.1. The basic idea of this algorithm is the segmentation of the image into smaller sections containing individual atomic columns. Next, the parameters of these columns are estimated atomic column-by-atomic column without ignoring overlap between neighbouring atomic columns. In the first step (B.), initial guesses are obtained for the non linear-parameters $\boldsymbol{\alpha}_1$ for the input image (A.). Next, the iterative part of the fitting procedure can be executed (shown in grey in Fig. 3.1). Based on the values of the non-linear parameters $\boldsymbol{\alpha}_j$, starting values for the linear parameters $\boldsymbol{\xi}_j$ are calculated by means of linear regression (C.), where j corresponds to the number of the iteration. Having starting values for the linear and non-linear parameters of the jth iteration available (D.), the actual estimation of the parameters can be done. Therefore, regions of interest containing single atomic columns are selected from the HR(S)TEM image (E.). The regions are defined based on the average distance between the atomic columns in the image. These distances can be calculated from the coordinates given by the peak finding routine. Next, the parameters of the neighbouring projected atomic columns are selected (F.) in order to take overlap between neighbouring Gaussian shapes into account. The values of the non-linear and linear parameters are given by the values that result from, respectively, step (B.) and (C.) in the first iteration and by the values that resulted from, respectively step (N.) and (C.) in further iterations. The contributions of the tails of these neighbouring Gaussian peaks are calculated in the region of interest of the single atomic column (G.). Then, these contributions are subtracted from the image of the single atomic column (H.). Ideally, the thus obtained image only contains scattered intensities resulting from this single projected atomic column and can be used

for a non-linear least squares estimation of the non-linear parameters of this single Gaussian (I.). Steps (E.) till (I.) are repeated for each projected atomic column in the HR(S)TEM image in order to obtain a complete set of estimated non-linear parameters $\hat{\boldsymbol{\alpha}}_j$ for the jth iteration. Next, the best companion values for the linear parameters for the jth iteration, $\hat{\boldsymbol{\xi}}_j$ are calculated (J.). Once the parameters are estimated, convergence is evaluated (L.). If convergence is not yet obtained (M.), the non-linear starting values for the $(j + 1)$th iteration are calculated (N.). The updates for the non-linear parameters are computed based on the starting and estimated values for the non-linear parameters of the jth iteration. The updates are modified by a scaling factor ν in order to avoid divergence on the parameters to be estimated. Having a new set of non-linear parameters available, the iterative part of the fitting algorithm can be executed again from step (C.). The iterative approach allows a better modelling of the overlap between neighbouring Gaussian peaks. If convergence is attained (O.), the model can be calculated based on the estimated parameters (P.).

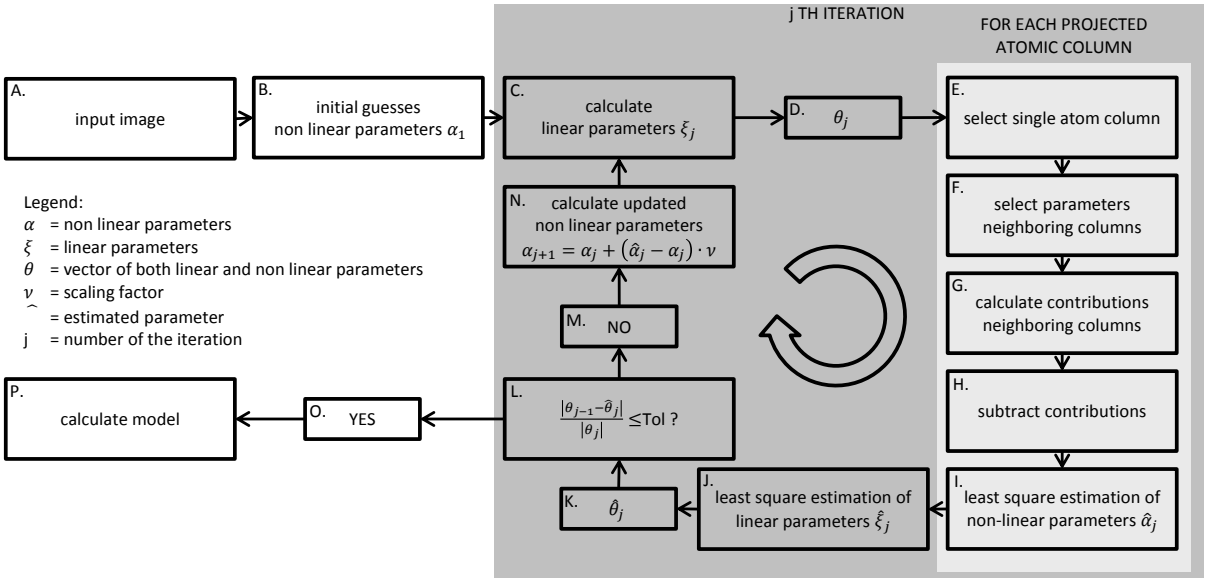

Figure 3.1: *Schematic for model estimation A: algorithm for the expectation model having a different width for each estimated Gaussian peak.*

3.2.2 Model estimation B

Same width for estimated Gaussian peaks of atomic columns of the same atom type

When the same width is estimated for Gaussian peaks of atomic columns of the same atom type, the expectation model and corresponding unknown structure parameters are given by Eqs. (2.9) and (2.10) which are for clarity's sake repeated here:

$$f_{kl}(\boldsymbol{\theta}) = \zeta + \sum_{i=1}^{I} \sum_{m_i}^{M_i} \eta_{m_i} \exp\left(-\frac{\left(x_k - \beta_{x_{m_i}}\right)^2 + \left(y_l - \beta_{y_{m_i}}\right)^2}{2\rho_i^2} \right) \tag{3.3}$$

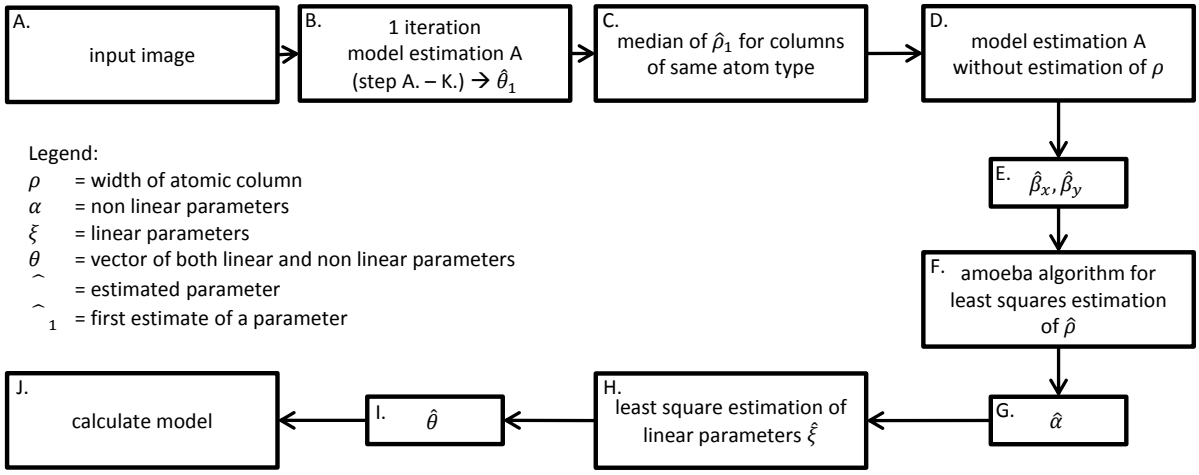

Figure 3.2: *Schematic for model estimation B: algorithm for the expectation model having the same width for Gaussian peaks of atomic columns of the same atom type.*

with unknown parameters:

$$\boldsymbol{\theta} = \left(\beta_{x_{1_1}}, \ldots, \beta_{x_{M_I}}, \beta_{y_{1_1}}, \ldots, \beta_{y_{M_I}}, \rho_1, \ldots, \rho_I, \eta_{1_1}, \ldots, \eta_{M_I}, \zeta\right)^T . \tag{3.4}$$

The basic idea of this routine is equivalent to the method for the model having different widths for each estimated Gaussian. The estimation method is subdivided into the estimation of the position parameters $\beta_{x_{m_i}}$ and $\beta_{y_{m_i}}$, and next the estimation of the width ρ_i for each atom type. This approach is valid since the correlation between the position parameters and the width of the Gaussian peaks equals almost zero. Throughout the estimation routine, the best companion values for the linear parameters $\boldsymbol{\xi}$ are used in each iteration increasing the convergence of the model estimation.

A schematic is shown in Fig. 3.2. As a first step, 1 iteration of the model estimation A (B.) is executed on the input image (A.). This corresponds to the evaluation of steps (A.) till (K.) of model estimation A described in Fig. 3.1. From this first estimate for the parameters of the expectation model, a rough estimate for the width can be obtained. This is done in step (C.) by calculating the median of the widths obtained in step (B.) for the columns of the same atom type. Next model estimation A is performed till convergence is reached (D.) without estimation of the parameter for the width of the Gaussian peaks, i.e. with a fixed value for the width ρ_i set in step (C.). In this way, estimates are obtained for the x- and y-coordinates $\beta_{x_{m_i}}$ and $\beta_{y_{m_i}}$ (E.). Next, estimates for the width ρ_i and the companion values for the linear parameters $\boldsymbol{\xi}$ need to be estimated for the fixed positions obtained from the first part of this method. The optimisation of the parameter ρ_i is done using the full image containing all atomic columns. In order to reduce the memory consumption, a derivative-free unconstrained non-linear optimisation method is used (F.) [Lagarias 1998]. If good starting values are available for the parameters ρ_i and a limited number of parameters needs to be estimated, than the so-called amoeba method converges toward good estimates for the parameters. Since the number of different atom types in a HR(S)TEM image is limited, this method gives efficiently accurate estimates. After the optimisation of the parameter ρ_i, estimates are available for all the non-linear parameters $\hat{\boldsymbol{\alpha}}$ in the parametric model (G.). Finally, the best companion values for the

linear parameters $\hat{\boldsymbol{\xi}}$ (H.) and the model based on the estimated parameters (I. and J.) can be calculated.
In this section, the implementation of the least squares estimator has been adapted enabling us to analyse large fields of view of HR(S)TEM images in a quantitative way. This algorithm, model estimation A or B, allows one to evaluate larger nanostructures in a quantitative way by means of a least squares estimation of the parameters of the statistical expectation models. In the next sections, this algorithm will be applied to different nanostructures in which a quantitative analysis of a large field of view is required. It will be shown that the analysis of larger fields of views opens up a variety of new possibilities for the characterisation of nanomaterials. In the first example, the estimated models as such will be used to reduce scanning errors in HAADF STEM images of a core-shell (Au@Ag) nanorod. The refined models serve as an input for atomic resolution electron tomography aiming to determine the position and atom type of each atom in a three-dimensional reconstruction. In the second set of examples, the positions of the atomic columns are interpreted for large fields of view in order to make displacement maps of the atomic column positions.

3.3 Three-dimensional elemental mapping in bimetallic nanocrystals

The first application of this efficient algorithm is the estimation of models for two-dimensional (2D) projection images of a bimetallic nanocrystal as an input for electron tomography[3]. A thorough understanding of the three-dimensional (3D) structure and composition of core-shell nanostructures is indispensable to obtain a deeper insight on their physical behaviour. Such 3D information can be reconstructed from 2D projection images using electron tomography. Different electron tomography techniques have already enabled the 3D characterisation of a variety of nanostructures at the atomic level [Van Aert 2011, Bals 2011, Scott 2012, Chen 2013]. However, these methods have all focused on the investigation of nanomaterials containing only one type of chemical element. Now, for the first time, the positions and atom type of each atom in a hetero-nanostructure will be determined using a combination of statistical parameter estimation techniques and compressive sensing based tomography [Donoho 2006, Goris 2012a]. As an example, the interface in core-shell Au@Ag nanorods will be investigated.
These bimetallic nanostructures are of great interest as they provide additional flexibility, stability, or even novel properties as compared to their mono-metallic counterparts [Henglein 2000, Hodak 2000, Tedsree 2011, Cortie 2011]. The deposition of Ag-coated Au (Au@Ag) nanorods, in particular, has been extensively studied because of the possibility to tune their overall geometry (and optical response) by changing the size and aspect ratio of the original Au nanorods [Liu 2004, Yang 2006, Xiang 2008, Park 2011, Ma 2010, Sanchez-Iglesias 2010, Cardinal 2010]. However, to understand and tailor the properties of these Au@Ag nanorods a thorough knowledge of the structure and the chemical composition at the atomic scale, in particular at the interfaces between the metallic components, is required.

[3]The results of this study are published in B. Goris, *A. De Backer*, S. Van Aert, S. Gómez-Graña, L. Liz-Marzán, G. Van Tendeloo, and S. Bals, 3D elemental mapping at the atomic scale in bimetallic nanocrystals, Nano Letters 13(9) (2013) 4236-4241.

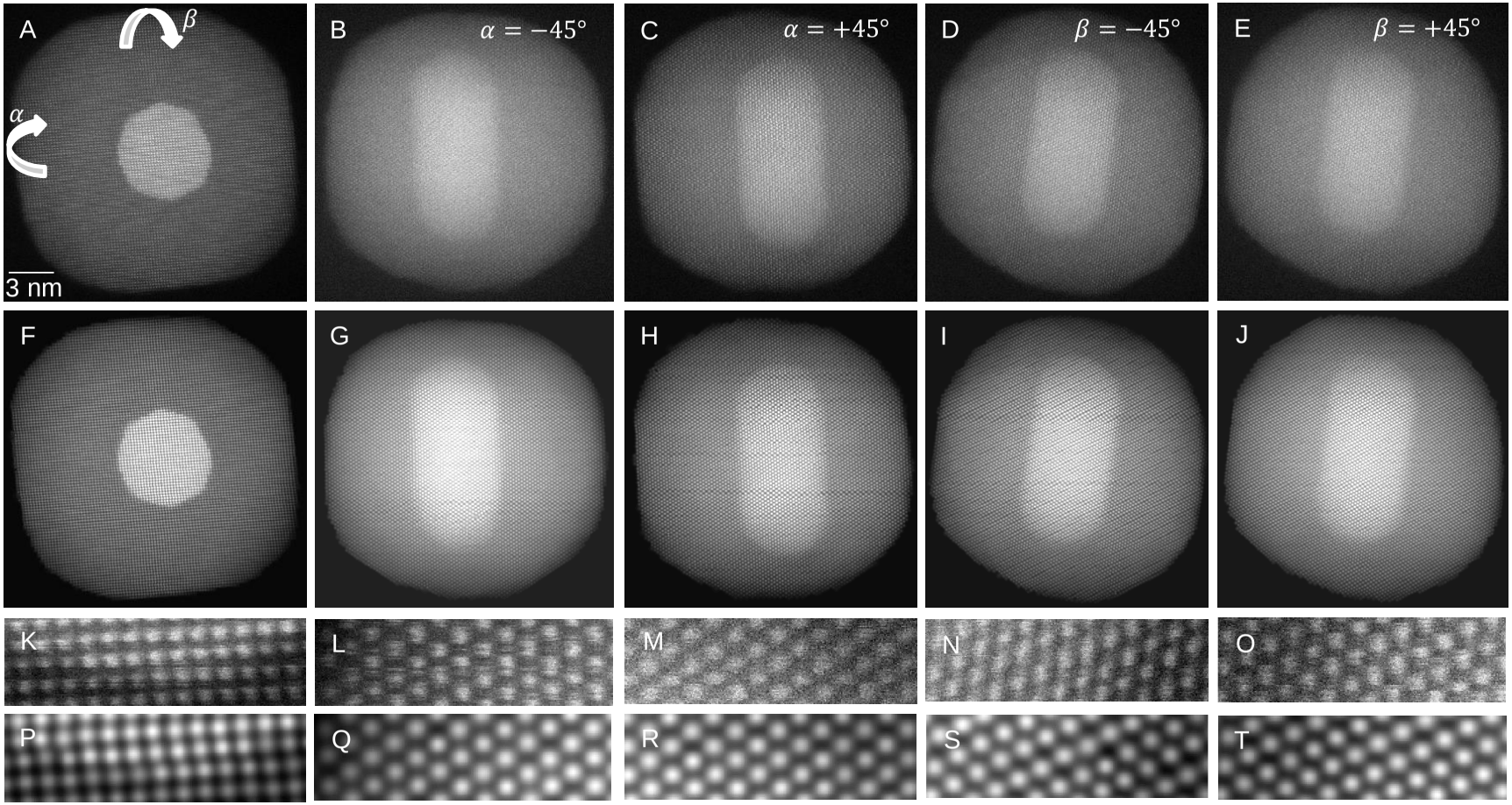

Figure 3.3: *A-E: Five high-resolution HAADF STEM projection images of a Au@Ag nanorod obtained by tilting the nanorod along the different tilt axes that are mutually orthogonal. F-J: Refined models for experimental images A-E. K-T: More detailed view on the observations and corresponding models for each of the experimental images. Noise and scanning artifacts are reduced in the refined models.*

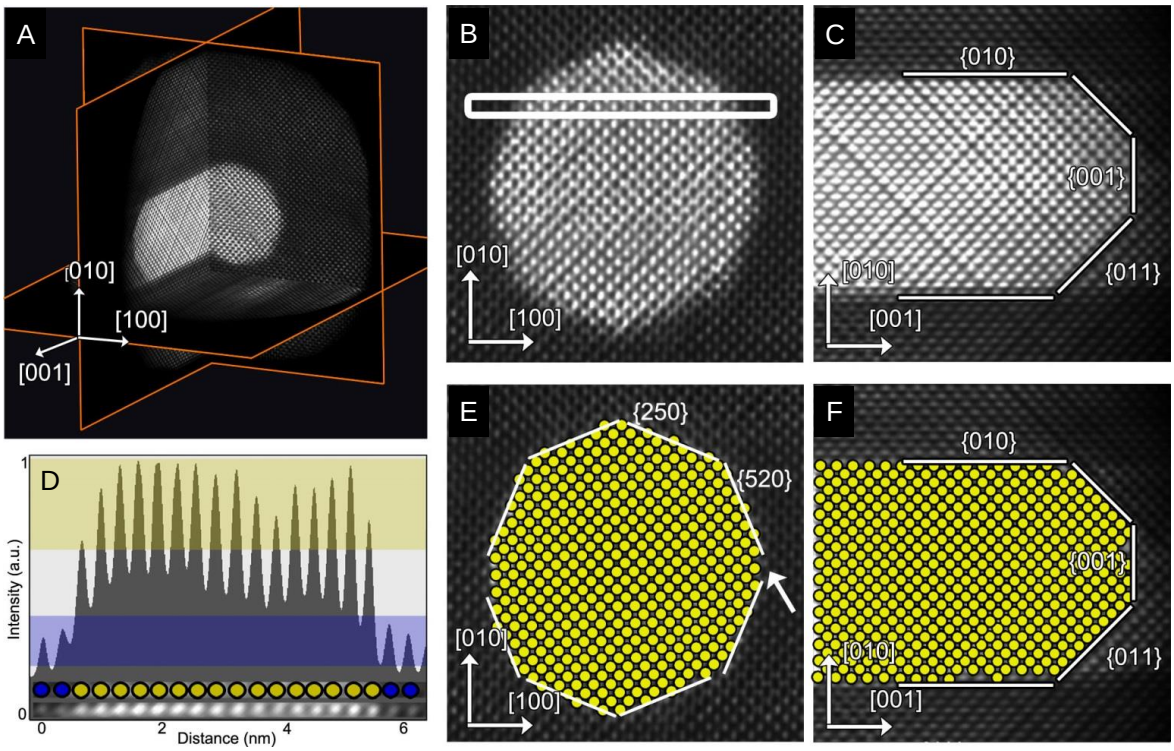

Figure 3.4: *Orthogonal slices through the 3D reconstruction. (A) Three orthogonal slices through the reconstruction show the core-shell structure of the nanorod. The atomic lattice can be resolved in all three slices. (B,C) Detailed view of slices through the reconstruction perpendicular and parallel to the major axis of the nanorod. (D) An intensity profile is acquired along the direction indicated by the white rectangle in (B). (E,F) Slices corresponding to B and C, in which each Au atom is indicated by a yellow disc. In this manner, the correct interfacial planes can be determined based on intensity profiles through the reconstruction.*

Five high-resolution HAADF STEM projection images of the same nanorod were acquired along different major zone axes as shown in Fig. 3.3 (A-E). The aim is to identify the position and atom type of individual atoms from a reliable, atomic resolution 3D reconstruction. Since the compressive sensing based electron tomography method can strongly be influenced by (scanning) noise, a reliable way to reduce these effects is by modelling the projection images. No prior knowledge was available on the atom type of each atomic column, although it was known that the nanoparticles under study are core-shell Au@Ag particles. However, it is impossible to visually discern for each atomic column between Au and Ag at the interface from the 2D HAADF STEM projection images. Therefore, model estimation method A has been used, where each atomic column in the 2D projection images was estimated with a different width. The quality of the images was sufficient in order to use this model estimation method. Fig. 3.3(F-J) show the corresponding estimated models of the originally recorded projection images shown in Fig. 3.3 (A-E). A more detailed view on the observations and corresponding models for each of the experimental images is provided in Fig. 3.3 (K-T). An excellent agreement between the refined models and the experimental projection images is observed, and indeed noise and scanning artifacts are reduced in the refined models. In this analysis, the model-based estimation acts as an ideal image filter.

The refined models (F-J) of Fig. 3.3 are used as an input for 3D reconstruction. The result of this reconstruction and a detailed analysis of the position and type of the atoms is shown in Fig. 3.4. This analysis was done from the orthogonal slices through the reconstruction. Since HAADF STEM images were obtained from the underlying data for the 3D reconstruction, the intensity of each reconstructed atom is related to its atomic weight. Therefore, individual Ag and Au atoms can be distinguished, also at the interface by comparing their relative intensities. An intensity profile was acquired along the direction indicated by the white rectangle in Fig. 3.4 (B). From this intensity profile, which is presented in Fig. 3.4 (D), it is clear that Au and Ag atoms can indeed be identified from their intensities using a threshold value. In this manner, each atom in the slices presented in Fig. 3.4 (B) and (C) was assigned to be Ag or Au. The result is shown in Fig. 3.4 (E) and (F) and enables us to carry out a correct indexing of the type of interfacial planes. We thus conclude that the interface between the Au core and the Ag shell is sharp without intermixing. This result could only be obtained by a combination of statistical parameter estimation and a 3D reconstruction based on compressive sensing.

3.4 Displacement mapping

The analysis of a large field of view, with very precise and accurate measurements of the positions of the projected atomic columns allows one to construct displacement maps in the case of strained structures. As a first example, a displacement map is obtained for a five-fold-twinned decahedral Au nanoparticle. Secondly, the displacement of Al atomic column positions within a $BiFeO_3$/$LaAlO_3$ heterostructure is discussed.

3.4.1 Five-fold-twinned decahedral Au nanoparticles

The first example is the mapping of the displacements within a five-fold-twinned decahedral Au nanoparticle. These complex decahedral particles exhibit highly localised surface plasmon resonances and are therefore of special interest because of their great potential for applications such as biosensing and cancer therapy [Zhao 2006, Willets 2007, Jain 2007]. The exact optical properties are size and shape dependent. Current synthesis techniques enable a high degree of size and shape control resulting in decahedral nanoparticles with the same optical properties [Sánchez-Iglesias 2006, Pastoriza-Santos 2007, Grzelczak 2008]. Since the internal structure determines their growth, surface structures and stability, the characterisation of the internal structure is required for further engineering their electronic and optical properties.
These types of Au particles are intrinsically strained as a result of their unique geometry as illustrated in Fig. 3.5(a). The decahedral particle consists of 5 tetrahedral subunits with an FCC crystal structure and {111} crystallographic faces. For perfect FCC tetrahedral subunits, the angle between adjacent {111} faces is 70.53° resulting in a solid-angle deficiency of 7.35°. As a result, these particles are strained or contain defects.
According to several studies, different strain models have been proposed for these five-fold-twinned decahedral Au nanoparticles [Johnson 2008]. Strain maps and displacement fields are often obtained by the geometrical phase technique. Within this method, a small aperture is centred around a strong reflection in the Fourier transform of a high-resolution image of the crystal lattice [Hÿtch 1998]. Using this method, the displacement field can be measured with

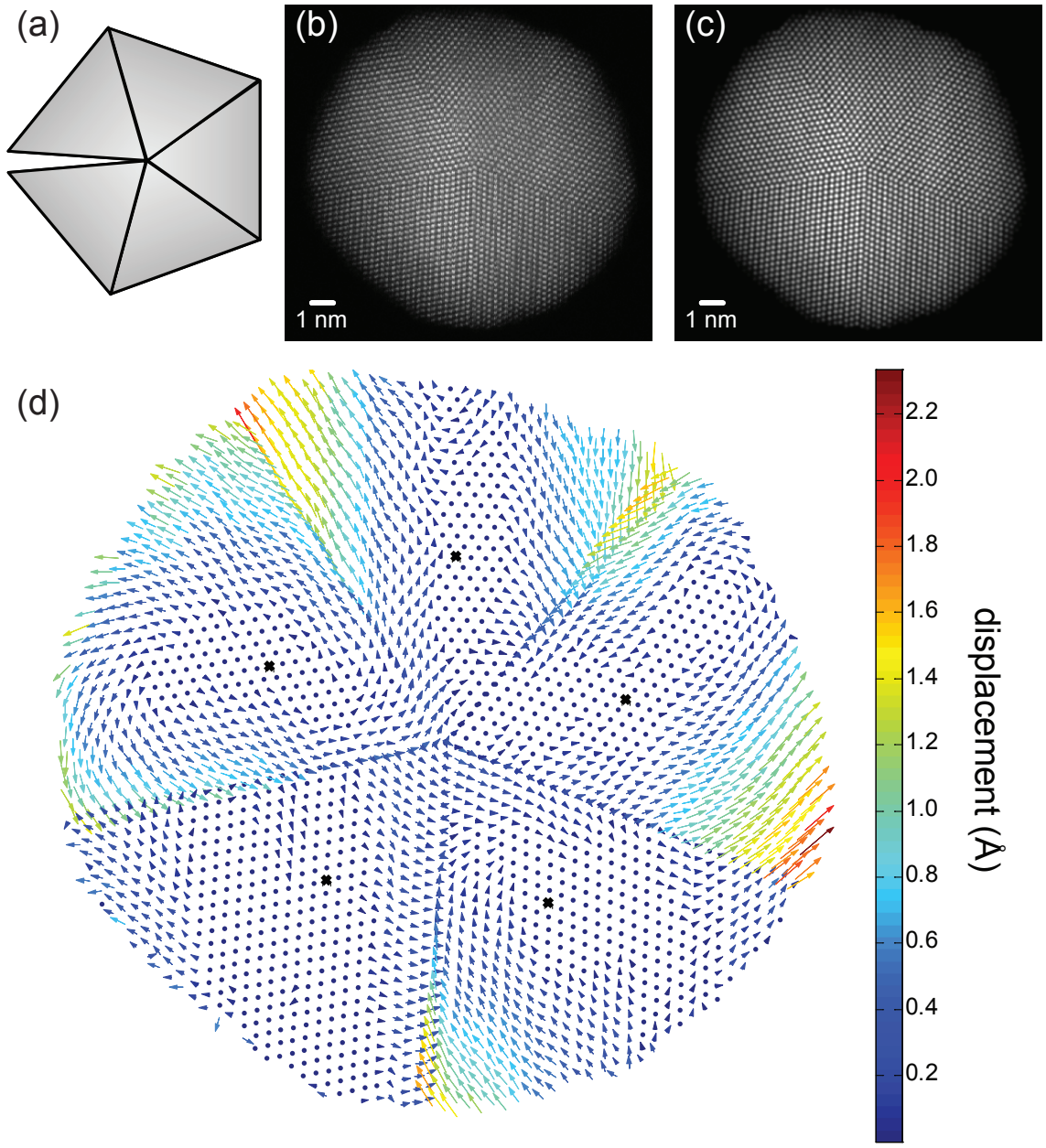

Figure 3.5: *Defect-free five-fold-twinned decahedral Au nanoparticle (a) For perfect FCC tetrahedral subunits a solid angle deficiency of 7.35° exists viewed along the pentagonal axis. (b) HAADF STEM image along the* [110] *zone axis. (c) Refined model. (d) Displacement map. The black crosses indicate from which atomic column in each tetrahedral subunit the reference lattice is extended.*

a precision of a few picometre [Hÿtch 2003]. However, the spatial resolution is limited to the nanometre range due to the aperture used in Fourier space. Using statistical parameter estimation theory, we can attain the same precision for the displacement measurements. In addition, the spatial resolution is not limited to the nanometre scale since atomic column positions can be measured with high precision as shown in chapter 2.
Therefore, statistical parameter estimation theory is used to create a displacement map for a

five-fold-twinned decahedral Au nanoparticle in order to study the internal structure. A high-resolution HAADF STEM projection image of such a nanoparticle free of defects shown in Fig. 3.5(b) was acquired along the [110] zone axis, i.e. along the pentagonal axis. Next, the parameters of the model were estimated using model estimation method B. Fig. 3.5(c) shows the estimated model which is in good agreement with the original image shown in Fig. 3.5(b). The estimated atomic column position coordinates were used to construct displacement maps for the atomic column positions. In order to measure the displacement for each atomic column, a reference lattice should be defined. For the five-fold-twinned decahedral nanoparticle, a reference lattice is defined for each tetrahedral subunit. It is assumed that the lattice is minimally distorted around the central projected atomic column. The lattice parameters of the reference lattice in *a*- and *b*-direction are then defined from the average interatomic distances in the two directions in the measured lattice around the central projected atomic column. Atomic columns up to two interatomic distances from the central column in a tetrahedral subunit are taken into account for the measurement of the reference lattice parameters. In this way, the lattice parameters of the reference lattice are defined with a precision better than 1 pm. The angle under which the reference lattice should be expanded has also been measured from the estimated atomic column positions. The reference lattice is expanded from the central projected atomic column in each tetrahedral subunit following a perfect FCC structure. By comparing the atomic column positions from the reference lattice with the measured atomic column positions, displacements can be measured. The displacement map of the five-fold-twinned decahedral nanoparticle is illustrated in Fig. 3.5(d). The black crosses indicate the atomic column position from which the reference lattice is expanded. For clarity, displacements of less than 0.25 Å are not plotted by arrows; in this case the reference lattice is plotted by dark blue dots. From this map, it can be seen that the displacements are not homogeneously distributed. It is expected that this information in combination with a 3D reconstruction at the atomic scale can give unique insights in the connection between structure and properties at the atomic scale of these nanoparticles.

3.4.2 $BiFeO_3/LaAlO_3$ heterostructure

The second application where a displacement map is created for a large field of view is for the Al atomic column positions within $BiFeO_3/LaAlO_3$, a functional oxide material. These types of materials have been studied for decades because of the abundance in interesting physical properties depending on the composites and more recently in interface engineering [MacLaren 2014]. Particularly, the contribution of perovskite compounds cannot be ignored.
Perovskite oxides comprise a large family of compounds with a general formula ABO_3, named after a mineral perovskite $CaTiO_3$. In a regular perovskite structure, small B cations (typically transition metal cations) are coordinated by octahedra of 6 oxygen atoms. The octahedra are connected into a corner-sharing three-dimensional framework. Cuboctahedral cavities of the framework are occupied by relatively large A cations (e.g. alkali, alkali-earth or rare-earth cations). Due to the inherent flexibility of the octahedral framework, the perovskite structure can accommodate a large number of various cations both in the A and B position. Depending on the composition, structure distortions and specific interatomic interactions, perovskites can demonstrate a plethora of physical properties, such as electronic and ionic conductivity, ferroelectricity, magnetism, catalytic activity and many others [Mitchell 2003, Abakumov 2013].

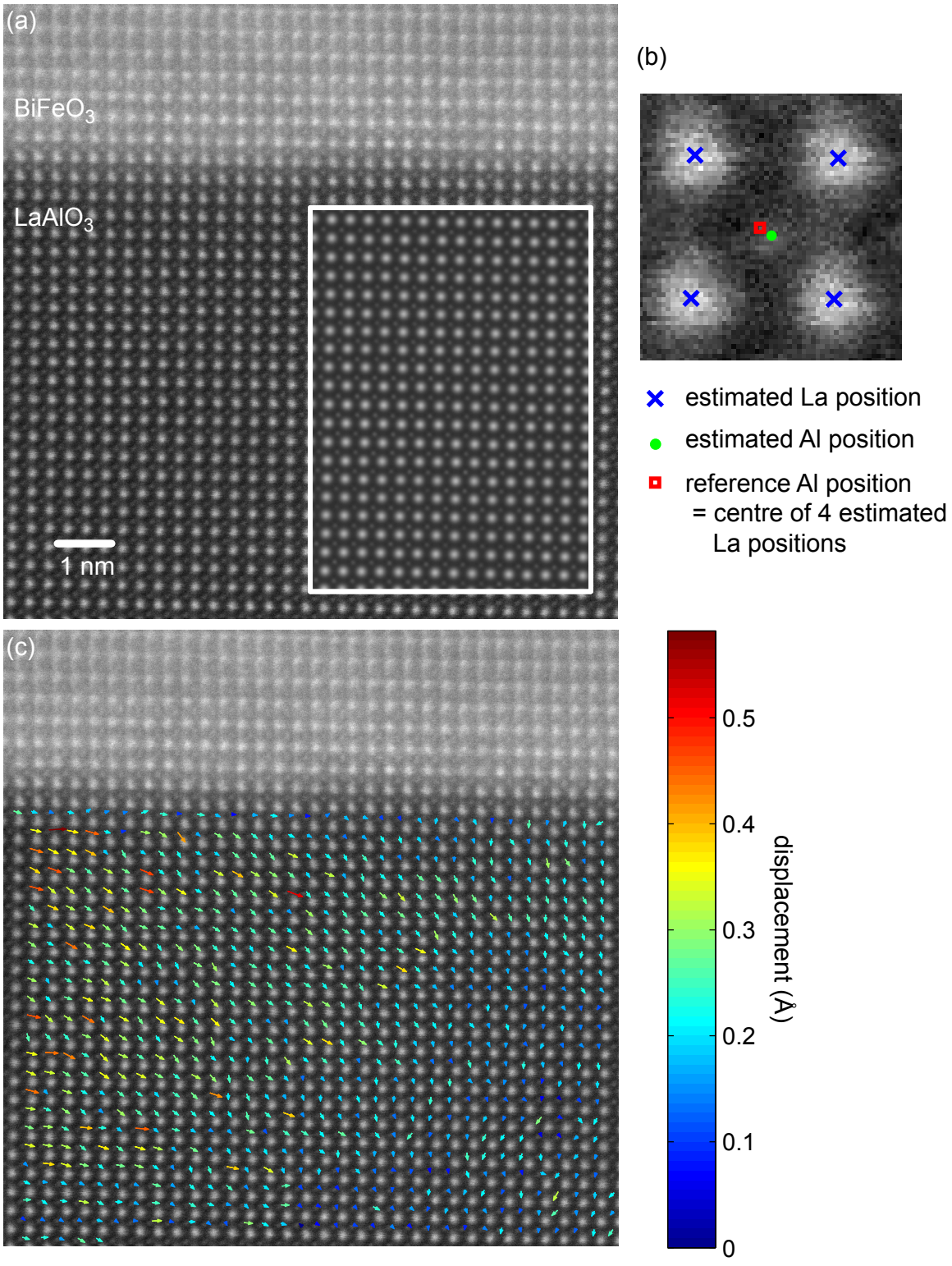

Figure 3.6: *(a) HAADF STEM image of $BiFeO_3$/$LaAlO_3$; the inset in the white rectangle shows a part of the estimated model for the LAO region. (b) Illustration of the measurement of the displacement of the estimated Al atomic column from its reference position. (c) Displacement map.*

Specifically, the ferroelectricity in perovskites is typically associated with the off-centre displacements of the B cations away from the centre of the octahedra. One of the well-known perovskite ferroelectrics is $PbZr_xTi_{1-x}O_3$, a so-called PZT ceramic [Hao 2014]. Above the Curie temperature (T_c), the ceramic has a cubic centrosymmetric structure with no electric dipole moment within its unit cell. Nevertheless, below T_c, the positively charged B-site cations of Ti/Zr shift away from the centre along certain crystallographic directions and lower the crystal symmetry by distorting the lattice to noncentrosymmetric. Since positively charged cations are deviated from the central anions octahedron, i.e. the oxygen octahedron, an electric dipole is therefore present.
It is therefore obvious that the study of the deviation of B cations from the central oxygen octahedron is one of the key elements in understanding the fundamentals of perovskite materials in order to further engineer these materials. Particularly in the recent ten years, the discovery of multiferroics, where ferroelectricity and ferromagnetism coexist and interplay with each other, stimulates numerous studies in developing a variety of materials both experimentally and theoretically. One active field is the heterostructure design through thin film fabrication [Zeches 2009, Heron 2014]. By epitaxially growing a thin film on a selected substrate, strain is introduced into the heterostructure due to the lattice mismatch. Consequently, local displacements of the atoms contribute enormously to novel behaviour at the heterostructure interface.

HAADF STEM is a powerful imaging technique in order to retrieve the information from the heterostructure interface where atomic columns of A/B cations could be imaged in a straightforward manner. Here a quantitative measurement of the displacements of the B-site cations with regard to the A-site cations is demonstrated on a BFO/LAO ($BiFeO_3/LaAlO_3$) hetero-interface which is shown in Fig. 3.6(a). Moreover, a mapping of a large field of view is performed in order to investigate whether domains are present where polarisation switches. In order to quantitatively measure the displacements, the atomic column positions are estimated using statistical parameter estimation theory. Therefore, the LAO region has been analysed. The inset in Fig. 3.6(a) shows the refined model for a part of the LAO region. In order to construct a displacement map, the Al atomic column positions are compared with a reference position. The centre of the 4 surrounding La atomic column positions defines the reference position as illustrated in Fig. 3.6(b). From the reference position and the estimated La atomic column position the displacement can be measured. The measured displacements are shown in Fig. 3.6(c) and range between 2 pm and 58 pm. From the displacement map, it can be observed that the polarisation changes within the analysed field of view. Since the thickness of $LaAlO_3$ is less than 10 nm, the displacements measured from the 2D projection image are representative. It is expected that displacement mapping like demonstrated here in combination with imaging of the oxygen atomic columns using ABF STEM imaging can enhance understanding the physical properties of functional oxide materials [Lubk 2013, Li 2013, Gao 2014, Kim 2014].

3.5 Conclusions

In this chapter, an efficient algorithm for the model estimation has been implemented in order to analyse large fields of view. In the previous approach, all parameters of the parametric model were estimated at the same time, which is a computationally very intensive task. The basic

idea of the new algorithm is the segmentation of the image into smaller sections containing individual atomic columns for the estimation of the non-linear parameters of the model. The availability of this new algorithm opens up new possibilities for quantitative analyses of large fields of view.
As a first application, model estimation has been combined with 3D reconstruction techniques allowing to reconstruct the 3D position and type of the atoms in a Au@Ag nanorod for the first time. Secondly, it has been illustrated how displacement mapping can be performed in a large field of view. This has been demonstrated for the atomic column positions in a five-fold-twinned decahedral Au nanoparticle and for the displacement of the Al column within $LaAlO_3$. From these examples, it is expected that the improved algorithm will offer good prospects for quantitative analyses of nanomaterials at the atomic scale with high precision.

4

Statistics-based atom-counting: Methodology, possibilities, and inherent limitations

4.1 Introduction

In the past, different approaches have been proposed to count the number of atoms of a nanostructure in ADF STEM. Erni et al. attempted to count the number of atoms by measuring the absolute differences in intensity of neighbouring atomic columns [Erni 2003]. LeBeau et al. proposed to solve the counting problem by comparing simulated atomic column intensities with normalised experimentally measured atomic column intensities as illustrated in the introduction in Fig. 1.4 [LeBeau 2010]. A few years ago, Van Aert et al. introduced a new statistical model-based approach to count the number of atoms from ADF STEM images of a structure viewed along a zone-axis [Van Aert 2011]. This method has also been illustrated in the introduction in Figs. 1.3 and 1.5 and may lead to promising results for the determination of the three-dimensional arrangement of atoms in crystalline nanoparticles [Van Aert 2011, Bals 2011, Bals 2012]. By repeating the counting method for different viewing directions, the 3D atomic structure can be reconstructed using discrete tomography [Batenburg 2007, Jinschek 2008]. Moreover, this statistics-based atom-counting method promises counting results with single atom sensitivity for each atomic column. In this chapter, this statistics-based method to count the number of atoms of mono-type crystalline nanostructures from high-resolution annular dark field (ADF) scanning transmission electron microscopy (STEM) images is discussed in detail together with a thorough study on the possibilities and inherent limitations imposed by unavoid-

able statistical uncertainties [4]

Although ADF STEM images are highly sensitive to the number of projected atoms, it is impossible to directly count the atoms by means of visual interpretation only. Hence, the starting point of the method will be the use of the statistical model-based estimation procedures described in chapter 2 to extract quantitative information from the ADF STEM images. In order to count the number of atoms, it is assumed that the total intensity of scattered electrons per atomic column in ADF STEM images, the so-called scattering cross-section, scales with the number of atoms in the column. The statistics-based approach proceeds in two steps.

In the first step of the counting procedure, the ADF STEM image will be considered as a data plane from which structure parameters have to be determined with the highest possible precision and accuracy [den Dekker 2005]. In section 2.4 of chapter 2 it is shown that statistical parameter estimation theory can be used to obtain accurate measurements with the highest possible precision. A parametric model is then fitted to the experimental data using a criterion of goodness of fit, quantifying the similarity between the experimental images and the model. Estimates for the scattering cross-sections per atomic column can be obtained from the estimates of the parameters of the parametric expectation model.

These estimates can be used as an input for the second step in the procedure to count the number of atoms per atomic column. Therefore, the estimated scattering cross-sections of all atomic columns can be visualised in a histogram. Ideally, this histogram would consist of isolated components, where each component is generated by a set of columns having the same number of atoms projected on top of each other, that is in the direction perpendicular to the recorded image. In practice, however, the components are smeared out which makes a visual determination of their locations impossible. This is due to a combination of different effects, such as experimental detection noise, instabilities of the material under the electron beam, different vertical onset of columns of the same height, vacancies, relaxation at the boundaries, contamination, intensity transfer between columns, and the influence of neighbouring columns of different heights. In order to solve this problem, estimated scattering cross-sections will be regarded as a statistical draw from an unknown probability distribution consisting of a superposition of Gaussian components. On the basis of the measured scattering cross-sections, the locations and the number of components of this distribution will be estimated. This will require a combination of an estimation procedure to determine the locations of the components and the use of order selection criteria to determine the number of statistically significant components. Once the distribution is known, the number of atoms in a particular projected atomic column can be identified at the atomic scale by assigning its scattering cross-section to the component of the estimated probability distribution with the largest probability to generate this scattering cross-section.

By means of simulations the possibilities and inherent limitations of the method to estimate the number of atoms will be studied. For this purpose, the performance of different order selection criteria will be compared and the interpretation of the order selection criterion which outperforms the other will be studied in more detail. Furthermore, the precision with which the number of atoms in a structure can be determined using this statistics-based method will be investigated.

This chapter will be organised as follows. In section 4.2, the methodology to estimate the num-

[4]The results of this chapter are published in *A. De Backer*, G.T. Martinez, A. Rosenauer, and S. Van Aert, Atom counting in HAADF STEM using a statistical model-based approach: methodology, possibilities, and inherent limitations, Ultramicroscopy 134 (2013) 23-33.

ber of atoms of a nanostructure using statistics-based methods is described in detail. This is followed by an example in section 4.3 illustrating the successive steps to count the number of atoms. In section 4.4, the possibilities and inherent limitations of the method are investigated. Finally, in section 4.5, conclusions are drawn.

4.2 Methodology

4.2.1 Model-based parameter estimation

The first step of the proposed method is to obtain precise and accurate measurements for the scattering cross-sections for each atomic column from the ADF STEM image. Therefore, use is made of statistical parameter estimation theory [den Dekker 2005, van den Bos 2007, Van Aert 2009a], which is discussed in detail in chapter 2. In subsection 2.4 of this chapter, it is shown that accurate estimates with the highest possible precision are obtained within this approach.
The ADF STEM image is considered as a data plane from which the unknown parameters have to be estimated in a statistical way and the expectation at the pixel (k, l) at the position (x_k, y_l) of the ADF STEM image for mono-type crystalline nanostructures can be described as:

$$f_{kl}(\boldsymbol{\theta}) = \zeta + \sum_{n=1}^{N} \eta_n \exp\left(-\frac{(x_k - \beta_{x_n})^2 + \left(y_l - \beta_{y_n}\right)^2}{2\rho^2}\right). \tag{4.1}$$

The unknown parameters of this model are estimated in the least squares sense. From the obtained estimated parameters, the estimated scattering cross-sections can be calculated [Van Aert 2009a]:

$$\hat{V}_n = 2\pi\hat{\eta}_n\hat{\rho}^2. \tag{4.2}$$

These numbers are the volumes under the Gaussian peaks above the background and correspond to the total intensity of electrons scattered toward the ADF detector. In the next subsection, it will be described how these estimates can be analysed to quantify the number of atoms in each projected atomic column.

4.2.2 Probability distribution of the estimated scattering cross-sections

The estimated scattering cross-sections calculated using statistical parameter estimation can be visualised in a histogram. Ideally, this histogram would consist of isolated components as shown in Fig. 4.1(a), where each component is generated by a set of atomic columns having the same number of atoms projected on top of each other. In practice, however, the components are smeared out such that it is impossible to visually determine their locations as shown in Fig. 4.1(b). Therefore, instead of visually interpreting histograms, the location and the number of components of the unknown distribution underlying the histogram are estimated on the basis of the measured scattering cross-sections. A combination of an algorithm to estimate the location

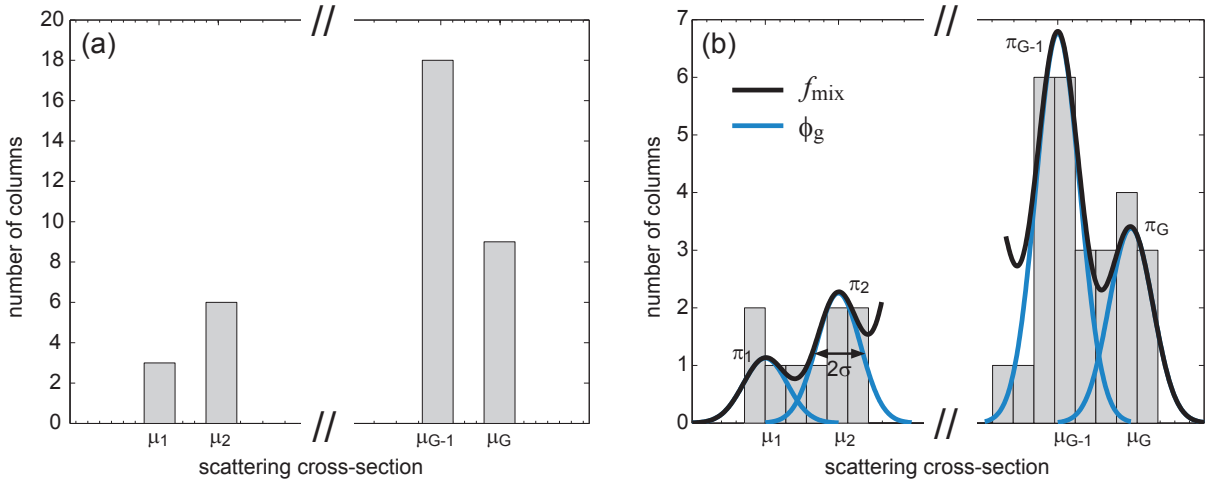

Figure 4.1: *Distribution of the scattering cross-sections. (a) Example of a histogram of the scattering cross-sections in the ideal case. (b) Example of a histogram in the presence of noise. The parameters μ_g, π_g, and σ and the individual components ϕ_g of the mixture model f_{mix} are indicated.*

of the components and the use of order selection criteria to evaluate the number of significant components is proposed [McLachlan 2000, Van Aert 2011, Van Aert 2013]. This procedure, of which the result only depends on the values of the estimated scattering cross-sections, leads to an accurate and precise estimate of the probability distribution as will be discussed in section 4.4. Another advantage is that the result is independent of the subjective choice of bins in the histogram.

The estimated scattering cross-sections are regarded as independent statistical draws from a so-called Gaussian mixture model. In a sense, the assumption of independent statistical draws implies that cross-talk between neighbouring atomic columns is not significantly contributing [Fertig 1981, Nellist 1999, Allen 2003]. The model is defined as a superposition of Gaussian components and describes the probability that a specific scattering cross-section value is observed. The probability density function of a mixture model with G components can parametrically be written as:

$$f_{\mathrm{mix}}\left(V_n;\mathbf{\Psi}_G\right)=\sum_{g=1}^{G}\pi_g\phi_g\left(V_n;\mu_g,\sigma\right). \tag{4.3}$$

This parametric probability density function is illustrated in Fig. 4.1(b). The symbol V_n represents the stochastic variable for the nth scattering cross-section and the symbol $\mathbf{\Psi}_G$ represents the vector containing all unknown parameters in the mixture model with G components:

$$\mathbf{\Psi}_G=\left(\pi_1,\ldots,\pi_{G-1},\mu_1,\ldots,\mu_G,\sigma\right)^T. \tag{4.4}$$

The parameters π_g, μ_g, and σ denote the mixing proportion of the gth component, the location of the gth component, and the width of the components, respectively. The mixing proportions π_g define the probability that a column contains g atoms with g ranging between 1 and a maximum number of components G, which is generally not known beforehand. The mixing proportions

π_g sum up to unity. Therefore, the Gth mixing proportion is omitted in the parameter vector $\mathbf{\Psi}_G$. Each component $\phi_g\left(V_n;\mu_g,\sigma\right)$ of the mixture model is generated by a set of columns having the same number of atoms. Generally, if there is an increase of one atom between subsequent components, component g corresponds to atomic columns with g atoms, and G is the number of atoms found in the thickest atomic column. Depending on the nanostructure under study, it is possible that the first component does not correspond to one atom, but corresponds to a higher number of atoms. In that case, an offset should be taken into account when assigning number of atoms to atomic columns of the different components.
The components $\phi_g\left(V_n;\mu_g,\sigma\right)$ are modelled as homoscedastic normal components, i.e. with common variance σ^2:

$$\phi_g\left(V_n;\mu_g,\sigma\right) = \frac{1}{\sqrt{2\pi}\sigma}\exp\left(-\frac{\left(V_n-\mu_g\right)^2}{2\sigma^2}\right). \tag{4.5}$$

The parameters $\mathbf{\Psi}_G$ of the Gaussian mixture model, Eq. (4.3), can be computed using the maximum likelihood estimator [Hasselblad 1969, Day 1969, Wolfe 1970, McLachlan 2000] for which the estimates are found by maximising the log likelihood function of the unknown parameter vector $\mathbf{\Psi}_G$ for a given set of observed scattering cross-sections $\hat{\boldsymbol{V}}$, which is defined as:

$$\log L\left(\mathbf{\Psi}_G\right) = \sum_{n=1}^{N}\log\left(\sum_{g=1}^{G}\pi_g\phi_g\left(\hat{V}_n;\mu_g,\sigma\right)\right). \tag{4.6}$$

The maximum likelihood estimates of $\mathbf{\Psi}_G$ are computed by solving the likelihood equation:

$$\frac{\partial \log L(\mathbf{\Psi}_G)}{\partial \mathbf{\Psi}_G} = 0. \tag{4.7}$$

This equation can only be solved iteratively. A very useful method is the so-called expectation maximisation (EM) algorithm [Dempster 1977]. Using this algorithm, a solution for the parameters $\mathbf{\Psi}_G$ can be obtained for a fixed number of G components. The algorithm proceeds in two steps: the E-step for expectation and the M-step for maximisation. In practice, the posterior probability that the nth scattering cross-section with observed value $\hat{V}_n$ belongs to the gth component of the mixture is calculated in the E-step, i.e.

$$\tau_g\left(\hat{V}_n;\mathbf{\Psi}_G^{(k)}\right) = \frac{\pi_g^{(k)}\phi_g\left(\hat{V}_n;\mu_g^{(k)},\sigma^{(k)}\right)}{\sum_{h=1}^{G}\pi_h^{(k)}\phi_h\left(\hat{V}_n;\mu_h^{(k)},\sigma^{(k)}\right)} \tag{4.8}$$

for $g = 1,\ldots,G$ and $n = 1,\ldots,N$. The iteration step is denoted by k.
The M-step calculates the updated estimate $\mathbf{\Psi}_G^{(k+1)}$. The updated estimates for the mixing proportions, $\pi_g^{(k+1)}$, can be calculated as follows:

$$\pi_g^{(k+1)} = \sum_{n=1}^{N}\tau_g\left(\hat{V}_n;\mathbf{\Psi}_G^{(k)}\right)/N \tag{4.9}$$

for $g = 1, \ldots, G$. Updates for the unknown parameters $\mu_g^{(k+1)}$ and $\sigma^{(k+1)}$ of the component densities are given by:

$$\mu_g^{(k+1)} = \frac{\sum_{n=1}^{N} \tau_g\left(\hat{V}_n; \mathbf{\Psi}_G^{(k)}\right) \hat{V}_n}{\sum_{n=1}^{N} \tau_g\left(\hat{V}_n; \mathbf{\Psi}_G^{(k)}\right)} \tag{4.10}$$

$$\sigma^{(k+1)} = \sqrt{\frac{\sum_{g=1}^{G} \sum_{n=1}^{N} \tau_g\left(\hat{V}_n; \mathbf{\Psi}_G^{(k)}\right)\left(\hat{V}_n - \mu_g^{(k+1)}\right)^2}{N}}. \tag{4.11}$$

By means of simulations which are discussed in subsection 4.4.3, it has been found that unbiased estimates for the parameters of the mixture model are obtained with following input values for the algorithm. Reliable starting values for the mixing proportions π_g are given by equal probabilities:

$$\pi_g^{(0)} = \frac{1}{G}. \tag{4.12}$$

The starting value for the variance σ of the components can be chosen as:

$$\sigma^{(0)} = \frac{\max\left(\hat{\mathbf{V}}\right) - \min\left(\hat{\mathbf{V}}\right)}{2G}. \tag{4.13}$$

For the starting values of the locations, different sets are used with the locations ranging between the minimum and maximum of the data set. The E- and M-step are iterated until convergence is attained and estimates are obtained for each set of starting parameters. The estimates $\hat{\mathbf{\Psi}}_G$ of the parameters in the mixture model are then given by the set of estimated parameters having the maximal log likelihood value. For the true number of components G, the obtained locations μ_g of the components correspond to the average scattering cross-sections for sets of atom columns having the same number of atoms.
However, so far, only the estimation of the probability distribution of the scattering cross-sections is considered presuming a specific number of components. Subsection 4.2.3 deals with determining the number of components G in a mixture model using order selection criteria.

4.2.3 Assessing the number of components in the mixture model using order selection criteria

In subsection 4.2.2, it is explained how we can obtain the probability density for a mixture model presuming a certain number of components in the mixture model. However, determining the order of the mixture model, i.e. the number of components in the distribution of the scattering cross-sections using so-called order selection criteria, is a difficult task. Different approaches are available to assess the number of components in a mixture model. A brief overview is given here. For other approaches and references, we refer to [McLachlan 2000].
The information criteria for model selection calculate a measure for the goodness of fit taking the complexity of the model into account. Therefore, they include a criterion specific penalty term which increases with the number of parameters in the Gaussian mixture model, i.e. with the number of components in the distribution. As such, a good tradeoff between the goodness

of fit and the complexity of the model arises. The general expression for information criteria is twice the negative penalised log likelihood criterion:

$$-2\log L(\hat{\mathbf{\Psi}}_G) + 2C \tag{4.14}$$

where the first term accounts for the lack of fit and the second term for the complexity of the model. The model that minimises the negative penalised log likelihood is selected as the probability density describing the observed scattering cross-sections. In practice, the values of the criterion will be plotted as a function of the number of components. In the ideal case, the values of the criterion will show a sharp minimum for the true number of components of the underlying probability density function.
Different criteria which all account for the complexity of the model in a different way have been proposed in the literature.
In Akaike's Information Criterion (AIC) [Akaike 1974], the penalty term simply equals the total number of parameters of the model:

$$\mathrm{AIC}(G) = -2\log L(\hat{\mathbf{\Psi}}_G) + 2d \tag{4.15}$$

with d the number of parameters in the mixture model where $d = 2G$ assuming Eq. (4.3). A very similar criterion is the Generalised Information Criterion (GIC) [Broersen 1993], where the contribution of the penalty term can be modified by the parameter r:

$$\mathrm{GIC}(G) = -2\log L(\hat{\mathbf{\Psi}}_G) + r \cdot d \tag{4.16}$$

Throughout this chapter, the parameter r of the GIC is chosen equal to 3 [Broersen 1996], penalising more heavily for the complexity of the model as compared to AIC.
Another criterion considered here is the Bayesian Information Criterion (BIC) [Schwarz 1978]:

$$\mathrm{BIC}(G) = -2\log(\hat{\mathbf{\Psi}}_G) + d\log(N) \tag{4.17}$$

Here, the penalty term depends on the sample size N. If the sample size $N > 8$, then BIC accounts more for the complexity of the model as compared to AIC.
In the Classification Likelihood information Criterion (CLC) [Biernacki 1997], the entropy $\mathrm{EN}(\hat{\tau})$ associated to the model with G components is used as the term that penalises the complexity of the model:

$$\mathrm{CLC}(G) = -2\log L(\hat{\mathbf{\Psi}}_G) + \mathrm{EN}(\hat{\tau}). \tag{4.18}$$

The entropy associated to the model with G components is given by:

$$\mathrm{EN}(\hat{\tau}) = -\sum_{g=1}^{G}\sum_{n=1}^{N} \tau_g\left(\hat{V}_n; \hat{\mathbf{\Psi}}_G\right) \log \tau_g\left(\hat{V}_n; \hat{\mathbf{\Psi}}_G\right) \tag{4.19}$$

where $\tau_g\left(\hat{V}_n; \hat{\mathbf{\Psi}}_G\right)$ is given by Eq. (4.8). The entropy of the model expresses how well the components of the mixture model are separated, i.e. how many overlap there is between neighbouring components. If the components are well separated, then $\mathrm{EN}(\hat{\tau})$ is close to zero. In other words, the separation of the components in the mixture model defines how drastically the log

likelihood is penalised.
The Approximate Weight of Evidence criterion (AWE) depends on this entropy term, the number of parameters and the sample size N [Banfield 1993]:

$$\mathrm{AWE}(G) = -2\log L(\hat{\mathbf{\Psi}}_G) + 2\mathrm{EN}(\hat{\tau}) + 2d(3/2 + \log N). \tag{4.20}$$

If the components are well separated, the performance of the AWE criterion resembles BIC.
Since BIC and CLC tend to underestimate and overestimate the number of components of the probability distribution respectively [Celeux 1996, Biernacki 1999], the Integrated Classification Likelihood criterion (ICL) is introduced to overcome these shortcomings [Biernacki 1998]:

$$\mathrm{ICL}(G) = -2\log L(\hat{\mathbf{\Psi}}_G) + 2\mathrm{EN}(\hat{\tau}) + d\log N \tag{4.21}$$

In section 4.4.1, the performance of these criteria is compared by means of simulations.

4.3 Counting atoms based on a simulated gold wedge

An example illustrating the procedure to count the number of atoms is worked out in this section. The STEMsim software [Rosenauer 2008] has been used to simulate a HAADF STEM image of a Au wedge. The parameters of the multislice simulation are listed in Table 4.1. The value for the Debye-Waller factor is taken from [Gao 1999]. The input structure for the STEM simulation is shown in Fig. 4.2(a). The noise in the simulated image, shown in Fig. 4.2(b), has been assumed to be Poisson distributed. First, estimates for the unknown parameters are obtained from the simulated image in the least squares sense using the expectation model given by Eq. (4.1). The thus obtained model for the HAADF STEM image evaluated at the estimated parameters is shown in Fig. 4.2(c). The volume under the peak above the background $\hat{\mathbf{V}}$, i.e.

Parameter	Symbol	Value
Acceleration voltage	V_0 (kV)	300
Defocus	ϵ (Å)	-83.01
Spherical aberration	C_s (mm)	0.035
Spherical aberration of 5th order	C_5 (mm)	0
Objective aperture angle	α (mrad)	21.7881
Spatial incoherence of source	FWHM_S (Å)	0.7
HAADF inner collection angle	β_1 (mrad)	50
HAADF outer collection angle	β_2 (mrad)	50
Slice thickness	z_{slice} (Å)	2.04
Debye-Waller factor	B (Å^2)	0.6373
Pixel size	$\Delta x = \Delta y$ (Å)	0.09955
Number of pixels x-direction	K	320
Number of pixels y-direction	L	170
Incident electron dose	N_d (e^-Å^{-2})	$6{\cdot}10^4$

Table 4.1: *Parameters for the multislice simulation of a HAADF STEM image of a Au wedge using the STEMsim software.*

the scattering cross-section, is calculated from the estimated parameters for each atomic column. These estimated scattering cross-sections $\hat{\mathbf{V}}$ are used to determine the number of atoms in each atomic column. The estimated scattering cross-sections $\hat{\mathbf{V}}$ are analysed through the combination of the expectation maximisation algorithm to determine the locations of the Gaussian mixture model and the ICL criterion to assess the number of significant components in the mixture model. Fig. 4.3(b) shows the ICL. The criterion shows a sharp minimum at 7, corresponding to the estimated number of components in the probability distribution. Fig. 4.3(a) shows the histogram of estimated scattering cross-sections together with the estimated mixture model. From Fig. 4.3(a) it is clear that the Gaussian components are approximately equidistantly separated meaning that the estimated scattering cross-sections increase linearly with the number of atoms in an atomic column. This knowledge can be used to determine the number of atoms in the atomic column assigned to the first component. The mean of the first components equals 2.2 e^{-}Å^2. The average increment between the successive scattering cross-sections equals 2.0 e^{-}Å^2. From this ratio between both values, it can be concluded that the number of atoms in the atomic columns assigned to the first component equals one. Finally, based on the analysis shown in Fig. 4.3(a) en 4.3(b), a figure can be constructed that shows the number of atoms per atomic column by assigning each scattering cross-section to the component of the estimated probability distribution with the largest probability for this scattering cross-section. This counting result equals the original input used for the STEMsim simulation shown in Fig. 4.2(a). The total number of atoms in the Au wedge equals 448.

4.4 Possibilities and limitations

In sections 4.2 and 4.3, it is described and shown how values for the scattering cross-sections per atomic column can be obtained from ADF STEM images and next how the distribution of these scattering cross-sections is analysed to determine the number of atoms per atomic column using statistical model-based methods. Experimental examples will be discussed in chapter 5. In this section, we will discuss the possibilities and inherent limitations of this statistics-based atom-counting method.

The ultimate goal is to determine the number of atoms in an atomic column with the highest possible accuracy and precision. However, on the one hand, modelling errors in the Gaussian mixture model for the probability distribution limit the accuracy resulting in systematic errors for the number of atoms. In subsections 4.4.1 and 4.4.2 it is studied under which conditions unbiased measurements can be obtained for the number of atom in an atomic column by using information criteria to assess the order of the mixture model. On the other hand, the precision on the estimated number of atoms is limited due to the unavoidable presence of noise in the estimated scattering cross-sections as discussed in subsection 2.4 of chapter 2. In sections 4.4.3 and 4.4.4, the variance on the parameters of the Gaussian mixture model and subsequently the precision with which the number of atoms can determined is analysed.

4.4.1 Performance of the order selection criteria

In subsection 4.2.3, different order selection criteria which are present in the literature are briefly discussed. In this subsection, the performance of these criteria is studied by simulating random

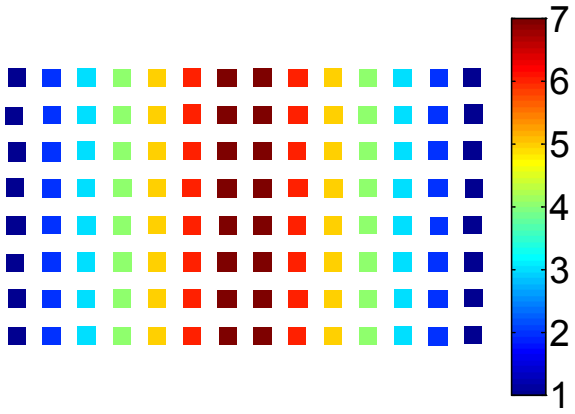

(a) input structure

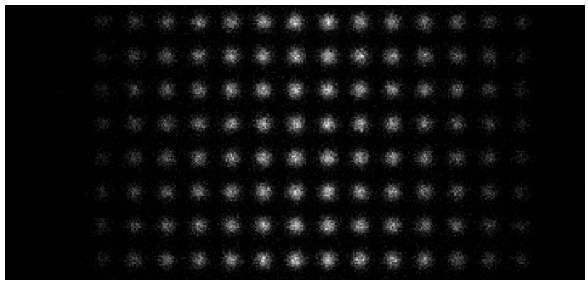

(b) simulation

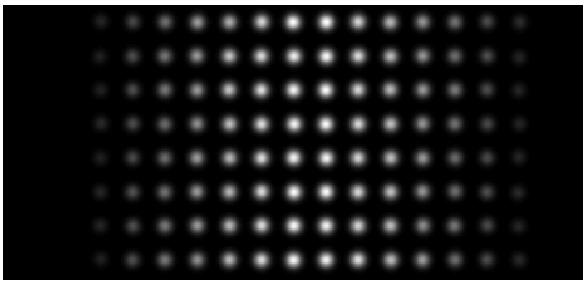

(c) model

Figure 4.2: *Input structure, simulated HAADF STEM image and corresponding model of a Au wedge.*

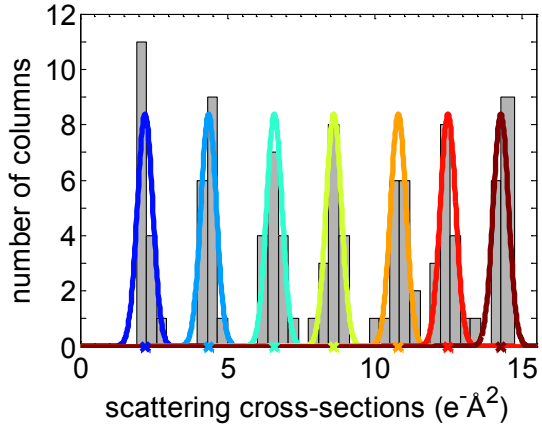

(a) histogram

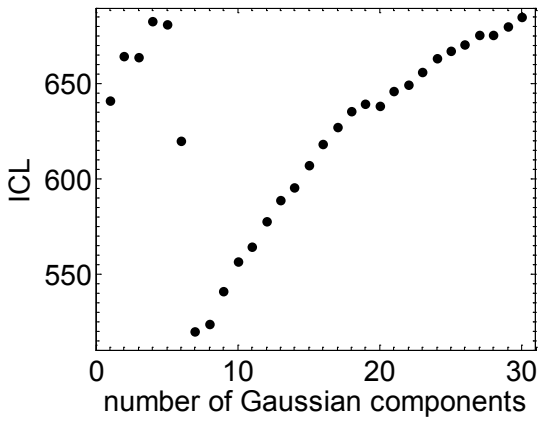

(b) ICL

Figure 4.3: *Analysis of the estimated scattering cross-sections: (a) histogram of the estimated scattering cross-sections* $\hat{\mathbf{V}}$ *with the curve indicating the estimated mixture model and the points indicating the estimated locations of the components, (b) ICL criterion evaluated as a function of the number of Gaussian components in the Gaussian mixture model.*

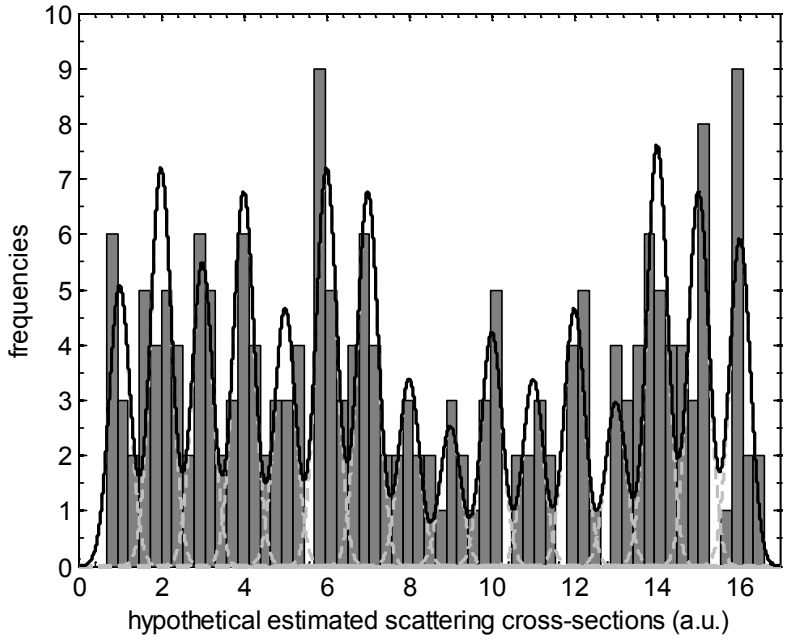

Figure 4.4: *Example of a histogram (random draw) together with the underlying simulated probability distribution with 16 components and relative width* $\sigma/\delta = 0.25$.

draws from probability distributions as a function of the relative width of the Gaussian components. This relative width expresses the ratio between the width σ of the Gaussian components and the increment δ between successive components. The locations of the different components are equidistantly chosen as it is assumed that the scattering cross-sections almost linearly increase with the number of atoms in a column for thin specimens. Statistical draws from a probability distribution with 16 components located at $\mu = 1, 2, \ldots, 16$ are simulated using the probability distribution of the Gaussian mixture model given by Eq. (4.3). The relative width σ/δ of these components is varied between $0.01 \leq \sigma/\delta \leq 0.30$ and describes how well the different components in the histogram are separated. The proportions π_g for the different components are multinomially distributed with equal probability of $1/16$. The number of observations N, i.e. the number of atomic columns, equals 200. For each value of the relative width σ/δ, 100 random draws from the Gaussian mixture model are simulated. An example of such a random draw of a probability distribution is shown in Fig. 4.4 for $\sigma/\delta = 0.25$. The information criteria, which are discussed in subsection 4.2.3, are evaluated for these simulated random draws from the distributions assuming that the number of components may vary between 5 and a maximum value of 30. The minimum of 5 is set based on the characteristic shape of the criterion discussed in more detail in subsection 4.4.2. In Table 4.2, the performance of different order selection criteria is shown in terms of the percentage of correctly determined number of components as a function of the relative width of the Gaussian components. The number of components is chosen based on the minimum of the criterion without visual inspection of the criterion. From the results in Table 4.2, it can be concluded that the ICL outperforms the other information criteria for assessing the number of components in a Gaussian mixture model for atom-counting applications. In combination with visual inspection of the criterion and a higher

σ/δ	CLC	AIC	GIC	AWE	BIC	ICL
0.01	77	81	91	100	100	100
0.05	45	45	80	100	97	98
0.10	14	21	60	100	93	98
0.15	19	27	77	92	99	100
0.20	27	38	74	0	68	99
0.25	8	45	44	0	0	78
0.30	1	30	1	0	0	8

Table 4.2: *Performance of different order selection criteria in terms of the percentage of correctly determined number of components as a function of the relative width σ/δ of the components. The average number of data points per component N/G equals* 12.5. *The largest value σ/δ for which a percentage above 50 is still observed, is highlighted for each criterion.*

number of scattering cross-sections N, it is expected that the percentage of correctly determined number of components will increase. Consequently also more reliable results will be possible for higher relative widths σ/δ, as will be shown in subsection 4.4.2.

4.4.2 Interpretation of the Integration Classification Likelihood criterion

The purpose of this subsection is to get more insight in the ICL criterion since it turns out that this criterion has optimal properties. When evaluating ICL as a function of the number of components of the Gaussian mixture model, it has been observed that the true number of components often corresponds to a local optimum. This knowledge may help interpreting ICL in a correct way and may improve the reliability of the selected number of components. Fig. 4.5 shows the shape of ICL for an underlying distribution consisting of 8 and 16 components as a function of an increasing number of observations corresponding to the number of atomic columns N. The random draws from the distributions are simulated under the same conditions as described in subsection 4.4.1. The relative width of the components equals $\sigma/\delta = 0.25$. Two main conclusions can be drawn from Fig. 4.5. First, it is observed that the shape of the criterion is comparable for the different cases. It appears that ICL is relatively small for a small number of components and shows an extra minimum at the correct number of components, especially when the number of components is larger. This behaviour hampers finding the correct number of components of the underlying distribution by using ICL without visual inspection and explains the sudden drop down in the performance of the ICL criterion in Table 4.2. Therefore, small values corresponding to a small number of components are neglected during visual inspection as it can be assumed that in the atom-counting analysis at least a certain number of components will be available in the distribution of the estimated scattering cross-sections. This number can be determined based on some prior knowledge about the size of the particle under study. It should be noticed that if the number of components of the underlying distribution is small, no local minima are found for a higher number of components in ICL.
Secondly, it has been observed from Fig. 4.5 that the minimum of interest in the ICL criterion corresponding to the correct number of components becomes more pronounced if the number of observations N increases. In addition, if the underlying distribution consists of many compo-

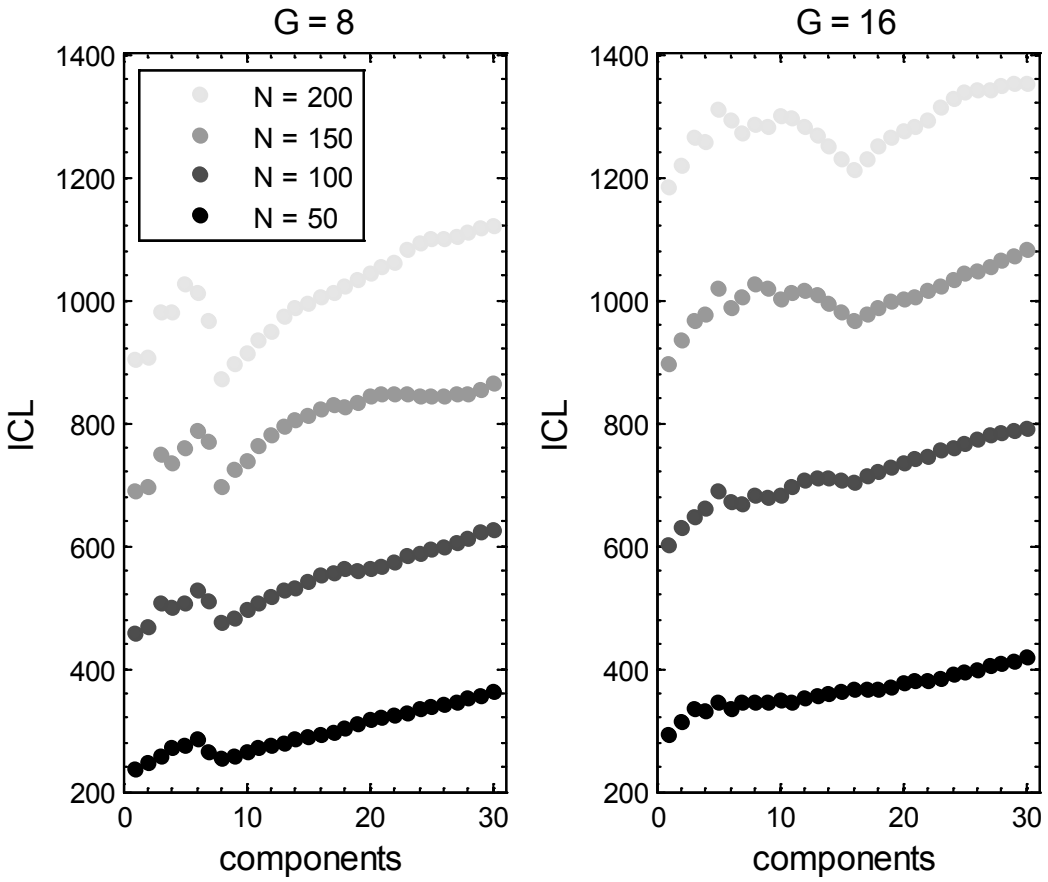

Figure 4.5: *ICL as a function of an increasing number of atomic columns N for* $G = 8$ *components at the left side and* $G = 16$ *components at the right side with* $\sigma/\delta = 0.25$.

nents, the number of observations N should be larger than for a distribution with a small number of components to determine the correct order of the mixture model. This conclusion follows from Fig. 4.5 where a minimum in ICL for $G = 16$ components for $N = 50$ and $N = 100$ is rather unclear whereas a more pronounced minimum for $G = 8$ components is already observed for $N = 50$. This means that the quality of the ICL increases for an increasing ratio of N/G. While the number of observations corresponds to the number of atomic columns in an experimental image when a single image is recorded, this number can be increased by analysing larger fields of view or multiple images, if experimental conditions are favourable.

Based on these conclusions, the number of observations, i.e. atomic columns, needed in order to obtain reliable results from the evaluation of ICL can be derived as a function of the number of components in the probability distribution. Therefore, simulations similar to those discussed in subsection 4.4.1 are used. The relative width of the components equals $\sigma/\delta = 0.25$. The percentage of correctly determined number of components is calculated for random draws from probability distributions consisting of a certain number of observations and components. This calculation is repeated increasing the number of observations till this percentage equals 95%. The results of this analysis are shown in Fig. 4.6. From this figure, it can be concluded that the necessary number of observations increases almost linearly with the number of components

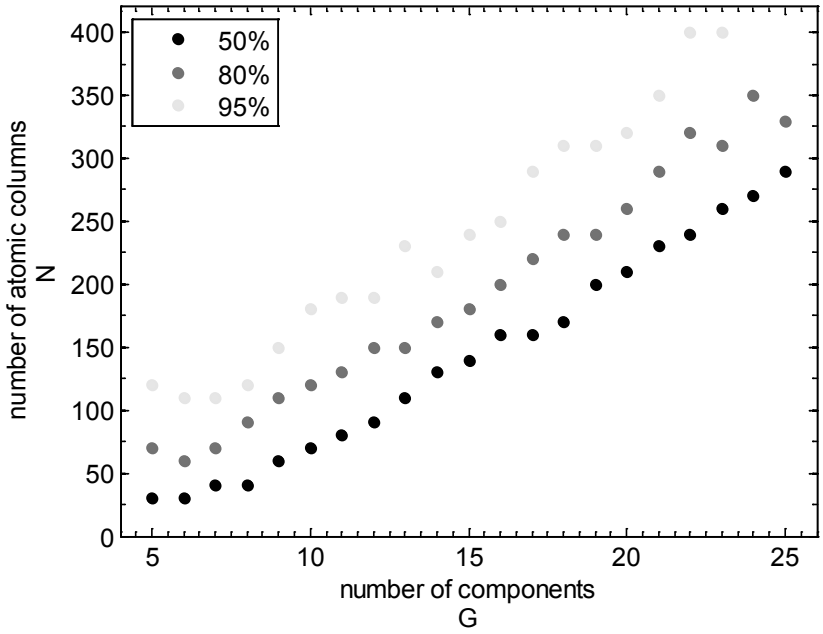

Figure 4.6: *The number of atomic columns needed to obtain reliable results from the ICL criterion for a given number of components with $\sigma/\delta = 0.25$. Different levels have been chosen to express the reliability in terms of the percentage of correctly assigned number of components. The black, dark grey and light grey dots correspond to 50%, 80% and 95% respectively.*

of the underlying Gaussian mixture model. It should be mentioned that the results in Fig. 4.6 are obtained without any visual inspection of ICL. This means that the necessary number of observations needed to obtain reliable results can slightly be reduced when accompanying this analysis with a visual inspection of the ICL criterion.

Since the necessary number of observations increases almost linearly with the number of components, the number of observations per component N/G can be considered as a measure to extend this analysis for higher relative widths. Then, the reliability of the ICL can be derived more generally as a function of the relative width σ/δ. The results of these simulations are shown in Fig. 4.7 for relative widths σ/δ between 0.2 and 0.4. For these simulations, probability distributions with 10 components were used under the same simulations conditions as those of section 4.4.1. The ICL is evaluated from 8 to 12 components. From the figure, it can be concluded that the number of observations per component N/G should be increased for higher relative widths σ/δ in order to retain the high reliability of the ICL. A reliability of 50% is still possible for high overlap between neighbouring components.

In general, it can be concluded that the use of the ICL criterion leads to unbiased measurements for the number of components in a mixture model provided that enough observations are available. Since the number of components determines the number of atoms that will be assigned to each atomic column, the analysis also reflects the accuracy of the method to count the number of atoms. In subsections 4.4.3, it will be mentioned that unbiased estimates for the parameters of the Gaussian mixture model are obtained which are also required for accurate atom-counting results. The precision of the atom-counting method will be discussed in subsections 4.4.3 and

4.4.4.

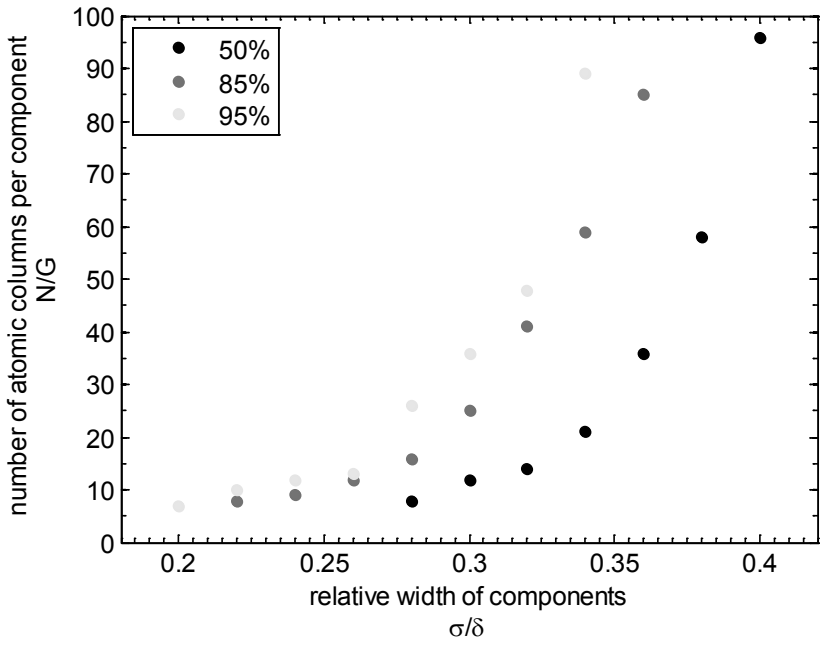

Figure 4.7: *The number of atomic columns per component needed to obtain reliable results from the ICL criterion for a certain relative width. Different levels have been chosen to express the reliability in terms of the percentage of correctly assigned number of components. The black, dark grey and light grey dots correspond to 50%, 80% and 95% respectively.*

4.4.3 Precision of the estimated parameters of the Gaussian mixture model

The precision of the number of atoms is mainly determined by the width σ of the Gaussian components in the mixture model, and the precision of the locations μ_g of the components in the Gaussian mixture model. The parameter μ_g can be estimated by maximising the likelihood function using the expectation maximisation algorithm discussed in subsection 4.2.2. As extensively discussed in chapter 2, statistical parameter estimation theory provides an expression for the highest precision, or in other words, the minimum variance, with which the parameters of the Gaussian mixture model can be determined, i.e. the so-called Cramér-Rao lower bound (CRLB) [den Dekker 2005, van den Bos 2007, Van Aert 2002c], which is the theoretical lower bound on the variance of any unbiased estimator for unknown model parameters. One of the properties of the maximum likelihood estimator is that it achieves the CRLB asymptotically, i.e. for an infinite number of observations. Consequently, if the CRLB is attained using the expectation maximisation algorithm, the CRLB provides a useful measure for the error bar on the estimated parameters of the Gaussian mixture model. In Appendix A on page 77, it is summarised how the CRLB is here computed for the estimated parameters of the Gaussian mixture model.
In this subsection, it is investigated by means of simulations if the lower bound on the variance

	CRLB	sample variance	95% confidence interval
π_1	0.0017	0.0022	[0.0017; 0.0030]
π_2	0.0018	0.0026	[0.0020; 0.0035]
π_3	0.0018	0.0019	[0.0014; 0.0025]
π_4	0.0018	0.0017	[0.0013; 0.0029]
π_5	0.0017	0.0017	[0.0013; 0.0024]
μ_1	0.0038	0.0041	[0.0032; 0.0056]
μ_2	0.0048	0.0048	[0.0037; 0.0065]
μ_3	0.0048	0.0055	[0.0042; 0.0074]
μ_4	0.0048	0.0045	[0.0035; 0.0061]
μ_5	0.0038	0.0031	[0.0024; 0.0041]
σ	0.00044	0.00043	[0.00033;0.00057]

Table 4.3: *Attainability of the CRLB on the estimated parameters of a Gaussian mixture model with* 5 *components. The sample variances are computed from parameter estimates obtained from* 100 *noise realisations of the Gaussian mixture model and compared with the CRLB on the variance of the model parameters.*

of the estimated parameters is attained. Therefore, 100 different noise realisations of a Gaussian mixture model with 5 components are simulated. The values for the true parameters in the simulation are set as follows: the proportions are the same for each component, i.e. $\pi_g = 0.2$, and the relative width equals $\sigma/\delta = 0.25$. The number of observations N equals 100. In this analysis unbiased estimates have been obtained for the parameters of the Gaussian mixture model, which is fundamental for obtaining an accurate estimate for the number of atoms. The results for the attainability of the Cramér-Rao lower bound on the variance of the estimated parameters of the mixture model are presented in Table 4.3. This table shows the computed value for the lower bound on the variance of a particular parameter in the second column. The third column shows the sample variance obtained from the parameter estimates from the 100 noise realisations using the expectation maximisation algorithm; in the last column the corresponding 95% confidence intervals on the sample variances are given. Since the 95% confidence interval of the sample variance encloses the CRLB, it can be concluded from Table 4.3 that the CRLB on the variance of the parameters of the Gaussian mixture model is attained using the expectation maximisation algorithm. This means that the Cramér-Rao lower bound can be used as a measure for the variance on the estimated parameters of the Gaussian mixture model. This variance will be used to determine the precision with which the number of atoms in a particular atomic column can be estimated and this will be subject of the following subsection.

4.4.4 Single atom sensitivity

The number of atoms in a particular atomic column is determined by assigning each estimated scattering cross-section to the component of the estimated probability distribution with the largest probability to generate this scattering cross-section. In this way, the precision of the number of atoms is mainly defined by the overlap between neighbouring components in the Gaussian mixture model. Single atom sensitivity is defined as an error bar of ±0 atoms: if there is no overlap between neighbouring components in the Gaussian mixture model single atom

sensitivity is attained as in this case an estimated scattering cross-section can unambiguously be assigned to a certain location μ_g. However, overlap between neighbouring components in the Gaussian mixture model is unavoidable and is given by a combination of the precision with which the location parameter μ_g in the Gaussian mixture model can be determined, the width σ and the proportions π_g of the components in the Gaussian mixture model. Nevertheless, the probability to assign the correct number of atoms, i.e. the fraction of the analysed atomic columns without error, can be computed.
The precision of the location parameter μ_g can be quantified using the Cramér-Rao lower bound on the variance of the estimated parameters of the Gaussian mixture model as discussed in subsection 4.4.3, and will be denoted as $CRLB_\mu$. The width σ of the components is non-zero due to a combination of experimental detection noise and instabilities. These two parts define an effective width σ_{eff} for the normal components:

$$\sigma_{\text{eff}} = \sqrt{CRLB_\mu + \sigma^2}. \tag{4.22}$$

The amount of overlap between neighbouring components is furthermore influenced by the proportions π_g and is also used to define the probability to assign the correct number of atoms to a specific component. This procedure on how to compute these probabilities is illustrated in Fig. 4.8. The component shown in colour (light and dark grey) will be used for this purpose and will be referred to as component ϕ_g. This distribution ϕ_g will be generated by a set of atomic columns having the same number of atoms in it. Atomic columns having scattering cross-sections belonging to interval I_g of the component ϕ_g indicated in Fig. 4.8, will be assigned to component ϕ_g. This central part I_g is bounded by the intersections of component ϕ_g with ϕ_{g-1} and ϕ_g with ϕ_{g+1}. The location of the intersection between component ϕ_g and ϕ_{g+1}, $S_{g(g+1)}$ can be expressed as a function of σ_{eff}, π_g, and μ_g:

$$S_{g(g+1)} = \frac{2\sigma_{\text{eff}}^2 \ln\left(\frac{\pi_g}{\pi_{g+1}}\right) - \mu_g^2 + \mu_{g+1}^2}{2\left(\mu_{g+1} - \mu_g\right)}. \tag{4.23}$$

Using these locations of the intersections which define the interval I_g, the posterior probability with which a scattering cross-section belonging to component ϕ_g resides in I_g can be computed as follows:

$$P(I_g|\phi_g) = \Phi\left(\frac{S_{g(g+1)} - \mu_g}{\sigma_{\text{eff}}}\right) - \Phi\left(\frac{S_{(g-1)g} - \mu_g}{\sigma_{\text{eff}}}\right) \tag{4.24}$$

where $\Phi\left(\frac{S-\mu_g}{\sigma_{\text{eff}}}\right)$ corresponds to the cumulative distribution function of the standard normal distribution evaluated at $\frac{S-\mu_g}{\sigma_{\text{eff}}}$. The posterior probability that a scattering cross-section belonging to the central dark grey part I_g stems from component ϕ_g is then given by Bayes' rule:

$$P(\phi_g|I_g) = P(I_g|\phi_g) \cdot \frac{P(\phi_g)}{P(I_g)} \tag{4.25}$$

where $P(\phi_g)$ equals the mixing proportion π_g of the gth component and $P(I_g)$ corresponds to the area below the Gaussian mixture model between $S_{(g-1)g}$ and $S_{g(g+1)}$, hatched in Fig. 4.8:

$$P(I_g) = \int_{S_{(g-1)g}}^{S_{g(g+1)}} f_{\text{mix}}(V; \mathbf{\Psi}_G) dV. \tag{4.26}$$

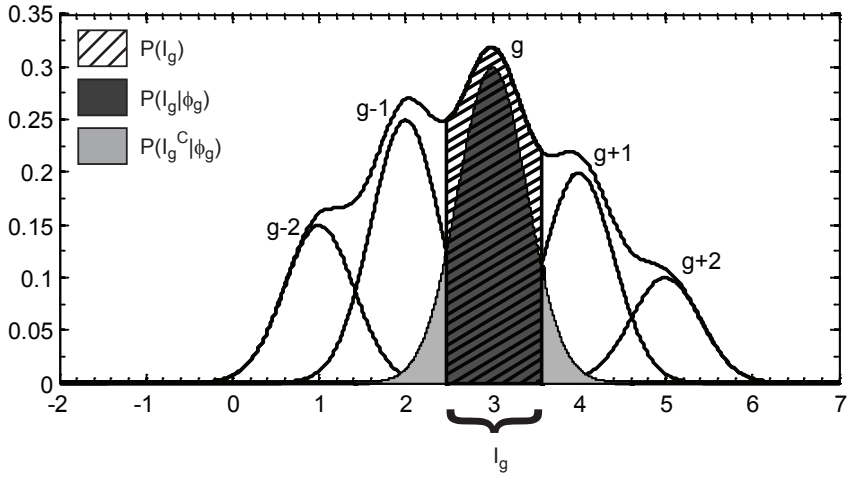

Figure 4.8: *Overlap between neighbouring components in the Gaussian mixture model to illustrate the concept of single atom sensitivity. Scattering cross-sections belonging to interval I_g will be assigned to component ϕ_g. The probability $P(I_g)$ that a scattering cross-section resides in I_g is indicated by the hatched area; the posterior probability $P(I_g|\phi_g)$ with which a scattering cross-section belonging to ϕ_g resides in I_g is indicated by the dark grey area; the posterior probability $P(I_g^C|\phi_g)$ with which a scattering cross-section belonging to ϕ_g resides not in I_g is indicated by the light grey area.*

Eq. (4.25) expresses the probability that a scattering cross-section of interval I_g originates from the correct component ϕ_g and thus identifies the percentage of atomic columns that has been determined with single atom sensitivity. For the whole structure of interest, the probability to count the number of atoms in an atomic column without error can then be obtained by averaging the probabilities of Eq. (4.25) for all the components in the Gaussian mixture model.
Similarly, the probability to miscount the number of atoms with ± 1 can be computed. This probability is related to the outermost light grey parts in Fig. 4.8. Atomic column scattering cross-sections whose scattering cross-sections belong to these parts will be assigned to component $g-1$ or $g+1$. In practice, the probability to miscount the number of atoms with ± 2 will generally equal zero, but can be computed in the same way taking the overlap of distribution g with the second neighbouring components into account.
If equal proportions are assumed for the components in the Gaussian mixture model, the intersection between neighbouring components is located in the middle between the locations μ_g of the considered components. The probability of counting the number of atoms correctly, i.e. with an error of ± 0 atoms, is then defined only by σ and $CRLB_\mu$. In order to illustrate how this probability relates to the latter parameters, tolerance levels for single atom sensitivity are drawn on a plot of $CRLB_\mu$ as a function of the relative width σ/δ in Fig. 4.9. For this figure, the Cramér-Rao lower bound on the variance of the location parameter μ_g has been calculated for different values of the parameters π_g, μ_g, and σ of the Gaussian mixture model based on the formulae in Appendix A. In addition, the number of components G and the number of observations N have been varied. Based on the computed values, it was observed that the value of $CRLB_\mu$ is determined by the relative width σ/δ of the components and the number of observations per component N/G. Therefore, $CRLB_\mu$ has been calculated for the central component of a probability distribution with equal proportions for different values of σ/δ and N/G. The values of $CRLB_\mu$ increase for a decreasing ratio of N/G and an increasing relative width σ/δ. Based on

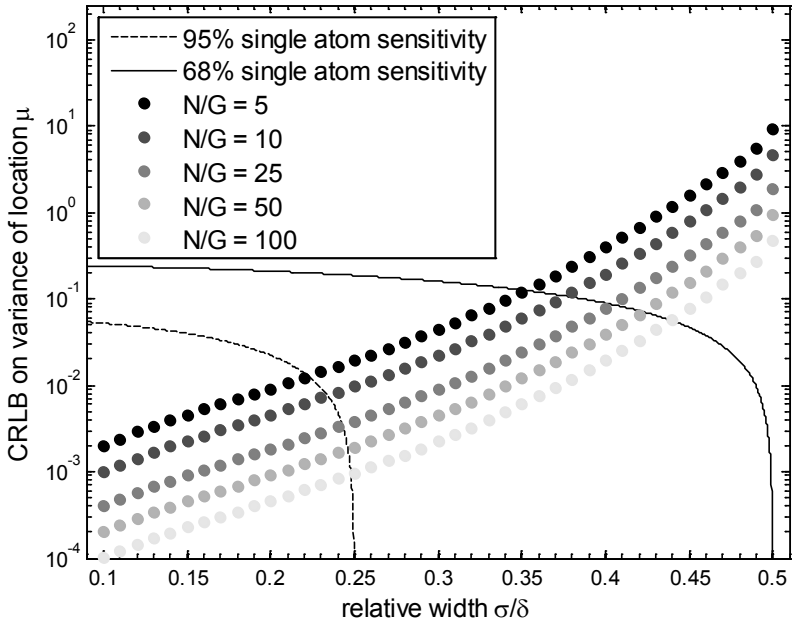

Figure 4.9: *Precision on the location μ for a given relative width σ/δ and number of observations per component N/G. The dashed line indicates the* 95% *tolerance level for single atom sensitivity; the full line indicates the* 68% *tolerance level for single atom sensitivity.*

Eq. (4.25), lines are drawn in Fig. 4.9 for the 68% and 95% tolerance levels. These lines show that the precision with which the number of atoms can be counted in a particular atomic column is limited by the relative width of the components. Indeed, if the relative width goes beyond a certain value, then neighbouring components will strongly overlap. Fig. 4.9 can be used to give an indication of the probability to count the correct number of atoms for a specific case.
The precision with which the number of atoms is determined in the example of the Au wedge described in section 4.3 can be derived using Eq. (4.25). For this example, it can be concluded that single atom sensitivity is attained for 99.9% of the analysed atomic columns. The fact that this probability is larger than 95% can also be derived from Fig. 4.9, since the number of observations per component N/G equals 16 and the average relative width σ/δ equals 0.15.

4.5 Conclusions

In this chapter, a statistics-based method to count the number of atoms in a nanostructure containing one atom type from ADF STEM images has been explained in detail together with a thorough study on the possibilities and inherent limitations imposed by unavoidable statistical uncertainties. It has been shown that the method largely proceeds in two steps. First a parametric model is fitted to the experimental ADF STEM images in order to extract quantitative values for the scattering cross-sections. These values can be used to determine the number of atoms per atomic column, if it is assumed that the scattering cross-section scales with the number of atoms. In the second step, the number of atoms per atomic column is determined by fitting a Gaussian finite mixture model to the probability distribution of the estimated scattering cross-

sections using the expectation maximisation algorithm. This probability distribution consists of components of set of atomic columns having the same number of atoms. The number of components in the probability distribution needs to be determined by the use of an order selection criterion.

By means of simulations, the possibilities and inherent limitations of this statistics-based atom-counting method have been investigated. The performance of different order selection criteria has been evaluated. It turns out that the Integrated Classification Likelihood (ICL) criterion outperforms other selection criteria when one is evaluating probability distributions for counting the number of atoms in a nanostructure. In addition, it has been shown that different aspects need to be taken into account for a correct interpretation of the ICL criterion. The number of observations N, the number of components G in the probability distribution, the width of the components σ, the average increment between the components δ, and the typical shape of the criterion directly affect the accuracy with which the number of atoms can be determined. Also the precision with which the number of atoms in a particular atomic column can be estimated has been studied. It has been shown that the variance of the expectation maximisation estimates for the parameters of the Gaussian mixture model attains the Cramér-Rao lower bound, i.e. the highest precision with which the parameters of the model can be determined. Moreover, it has been shown that single atom sensitivity is feasible.

In conclusion, the statistics-based method to count the number of atoms can be used without prior knowledge of the atomic structure and is independent of image simulations. This powerful method enables one to identify the percentage of atomic columns that has been determined with single atom sensitivity. In the next chapter, the practical use of this statistics-based atom-counting method will be tested on experimental images and applied to different nanostructures.

Appendix A

CRLB for the parameters of the Gaussian mixture model: Fisher information and attainable precision

The concept of Fisher information and attainable precision is discussed in detail in chapter 2. Here, these principles will be applied for the parameters of the Gaussian mixture model. For the Gaussian mixture model, the observations, i.e. the estimated scattering cross-sections, are assumed to be statistical independent having the following joint probability distribution:

$$p(\mathbf{V}, \mathbf{\Psi}_G) = \prod_{n=1}^{N} f_{\text{mix}}(V_n; \mathbf{\Psi}_G) \tag{A.1}$$

where $f_{\text{mix}}(V_n; \mathbf{\Psi}_G)$ is the probability density function of a mixture model given by Eq. (4.3) and $\mathbf{V}$. The dependence of the joint probability density function on the unknown parameters $\mathbf{\Psi}_G$ defines the Fisher information matrix and the Cramér-Rao lower bound. The Fisher information matrix is defined as:

$$F_{\mathbf{\Psi}} = -\mathbb{E}\left[\frac{\partial^2 \ln p(\mathbf{V}; \mathbf{\Psi}_G)}{\partial \mathbf{\Psi}_G \partial \mathbf{\Psi}_G^T}\right]. \tag{A.2}$$

In practice, the following integral is numerically integrated:

$$F_{\mathbf{\Psi}_G} = -N \int_{-\infty}^{\infty} \frac{\partial^2 \ln f_{\text{mix}}(V; \mathbf{\Psi}_G)}{\partial \mathbf{\Psi}_G^2} f_{\text{mix}}(V; \mathbf{\Psi}_G) dV. \tag{A.3}$$

The calculation of the Fisher information matrix of Eq. (A.3) requires the calculation of the second order derivatives of the logarithm of the joint probability distribution with respect to the parameters of the Gaussian mixture model. In order to simplify the notation for the derivatives, we will use the following notation:

$$\phi_g(V_n; \mu_g, \sigma) = \phi_g, \tag{A.4}$$
$$f_{\text{mix}}(V_n; \mathbf{\Psi}_G) = f_{\text{mix}}, \tag{A.5}$$
$$p(\mathbf{V}, \mathbf{\Psi}_G) = p. \tag{A.6}$$

The first order derivatives are given by the following expressions:

$$\frac{\partial \ln p}{\partial \pi_i} = \sum_{n=1}^{N} \frac{(\phi_i - \phi_G)}{f_{\text{mix}}},$$
$$\frac{\partial \ln p}{\partial \mu_i} = \sum_{n=1}^{N} \frac{\pi_i \phi_i}{f_{\text{mix}}} \frac{V_n - \mu_i}{\sigma^2},$$
$$\frac{\partial \ln p}{\partial \sigma} = \sum_{n=1}^{N} \frac{1}{f_{\text{mix}}} \sum_{g=1}^{G} \pi_g \phi_g \left(\frac{\left(V_n - \mu_g\right)^2}{\sigma^3} - \frac{1}{\sigma} \right).$$

The different second order derivatives are then given by:

$$\frac{\partial^2 \ln p}{\partial \pi_i^2} = -\sum_{n=1}^{N} \frac{(\phi_i - \phi_G)^2}{f_{\text{mix}}^2},$$

$$\frac{\partial^2 \ln p}{\partial \pi_i \partial \pi_k} = -\sum_{n=1}^{N} \frac{(\phi_i - \phi_G)(\phi_k - \phi_G)}{f_{\text{mix}}^2},$$

$$\frac{\partial^2 \ln p}{\partial \pi_i \partial \mu_i} = \sum_{n=1}^{N} \frac{\phi_i (V_n - \mu_i)}{f_{\text{mix}} \sigma^2} \left(1 - \frac{\pi_i (\phi_i - \phi_G)}{f_{\text{mix}}}\right),$$

$$\frac{\partial^2 \ln p}{\partial \pi_i \partial \mu_k} = -\sum_{n=1}^{N} \frac{\pi_k \phi_k}{f_{\text{mix}}^2} \frac{V_n - \mu_k}{\sigma^2} (\phi_i - \phi_G),$$

$$\frac{\partial^2 \ln p}{\partial \pi_i \partial \mu_G} = -\sum_{n=1}^{N} \frac{\phi_G (V_n - \mu_G)}{f_{\text{mix}} \sigma^2} \left(1 + \frac{\pi_G (\phi_i - \phi_G)}{f_{\text{mix}}}\right),$$

$$\frac{\partial^2 \ln p}{\partial \pi_i \partial \sigma} = \sum_{n=1}^{N} \frac{1}{f_{\text{mix}}} \left(\left(\frac{(V_n - \mu_i)^2}{\sigma^3} - \frac{1}{\sigma} \right) \phi_i - \left(\frac{(V_n - \mu_G)^2}{\sigma^3} - \frac{1}{\sigma} \right) \phi_G \right.$$
$$\left. - (\phi_i - \phi_G) \frac{\sum_{g=1}^{G} \pi_i \phi_i \left(\frac{(V_n - \mu_i)^2}{\sigma^3} - \frac{1}{\sigma} \right)}{f_{\text{mix}}} \right),$$

$$\frac{\partial^2 \ln p}{\partial \mu_i^2} = \sum_{n=1}^{N} \frac{\pi_i \phi_i}{f_{\text{mix}} \sigma^2} \left(\frac{(V_n - \mu_i)^2}{\sigma^2} - 1 - \frac{\pi_i \phi_i (V_n - \mu_i)^2}{f_{\text{mix}} \sigma^2} \right),$$

$$\frac{\partial^2 \ln p}{\partial \mu_i \partial \mu_k} = -\sum_{n=1}^{N} \frac{f_{\text{mix}}^2}{\pi_k \phi_k \pi_i \phi_i} \frac{(V_n - \mu_k)}{\sigma^2} \frac{(V_n - \mu_i)}{\sigma^2},$$

$$\frac{\partial^2 \ln p}{\partial \mu_i \partial \sigma} = \sum_{n=1}^{N} \frac{\phi_i (V_n - \mu_i) \pi_i}{f_{\text{mix}} \sigma^2} \left(\frac{(V_n - \mu_i)^2}{\sigma^3} - \frac{3}{\sigma} - \frac{\sum_{g=1}^{G} \pi_i \phi_i \left(\frac{(V_n - \mu_i)^2}{\sigma^3} - \frac{1}{\sigma} \right)}{f_{\text{mix}}} \right),$$

$$\frac{\partial^2 \ln p}{\partial \sigma^2} = \sum_{n=1}^{N} \frac{1}{f_{\text{mix}}} \left(\sum_{g=1}^{G} \frac{\pi_i \phi_i}{\sigma^2} \left(\left(\frac{(V_n - \mu_i)^2}{\sigma^2} - 1 \right)^2 + 1 - \frac{3(V_n - \mu_i)^2}{\sigma^2} \right) \right.$$
$$\left. - \frac{1}{f_{\text{mix}}} \left(\sum_{g=1}^{G} \pi_i \phi_i \left(\frac{(V_n - \mu_i)^2}{\sigma^3} - \frac{1}{\sigma} \right) \right)^2 \right).$$

These second order derivatives are used for the calculation of the Fisher information matrix of Eq. (A.3).

5

Practical applications: Nanoparticle atom-counting from experimental ADF STEM images

5.1 Introduction

In [Van Aert 2011], it has been proven that the statistics-based atom-counting method described in chapter 4 is successful for the determination of the number of atoms in a metal nanocluster embedded into a stabilising matrix with the same crystal structure. The atom-counting results were consistent for two different viewing directions. Furthermore, the first 3D reconstruction at the atomic scale could be realised by combining these counting results using discrete tomography as illustrated in the introduction of this thesis. In this chapter, the statistics-based method for atom-counting will be applied to more challenging structures: Ge clusters, larger Au nanorods, and Pt/Ir bimetallic catalysts.

As a first application in section 5.2, an attempt will be made to count the number of atoms in a Ge cluster. Since this Ge cluster is not embedded in a stabilising matrix, it is moving easily under illumination of the electron beam. This makes the atom-counting much more challenging as compared to atom-counting of a cluster embedded in a stabilising matrix with the same crystal structure as in [Van Aert 2011]. The atom-counting method described in chapter 4 will be recapitulated briefly for this application. Although this atom-counting method is a straightforward procedure, this exploratory example will show that the interpretation of the output given by this method is absolutely not straightforward. Therefore, a combination with other complementary methods will be required in order to obtain reliable atom counts with single atom sensitivity.

As a second application, atom-counting for a Au nanorod will be discussed in section 5.3. The counting results will be validated using a comparison with detailed ADF STEM image simulations. This requires the intensity variations to be placed on an absolute scale by normalising

the measured image intensities to the incident beam. Furthermore, atom-counting results from a Au nanorod will be compared with the number of atoms that can be counted from a slice through the 3D atomic scale reconstruction from electron tomography. Additionally, it will be illustrated how the atom-counting results can be used to create 3D atomistic models.
In a third, more elaborate analysis in section 5.4, the number of atoms will be counted for a Pt/Ir nanoparticle, i.e. a industrial bimetallic catalyst. The goal here is to elucidate the experimental constraints on the atom-counting reliability which become extremely important when looking at beam sensitive systems. The inherent limitations of the atom-counting method discussed in chapter 4 are clearly illustrated by the analysis of the experimental data. Finally, the conclusions of this chapter will be summarised in section 5.5.

5.2 Ge cluster: an exploratory example

In this section, atom-counting on a Ge cluster using the statistics-based method will be illustrated. For this purpose, the statistics-based atom-counting method will be briefly summarised. Next, it will be shown that the interpretation of the output of the atom-counting method not always leads to a unique trustworthy solution.

5.2.1 Experiment

HAADF STEM images of a nanometre sized Ge-cluster were taken at the Qu-Ant-EM, a double-corrected FEI Titan^3 working at 300 kV with a 21.4 mrad semi-convergence angle. It is assumed that defocus ϵ, spherical aberration C_s, and spherical aberration of the fifth order C_5 equal 0 for this experiment. A series of images was taken while the Ge-cluster was rotating under the electron beam. The images are taken under the same conditions and the pixel size Δx equals 0.25 Å. The structure along the [110] direction has a dumbbell structure, i.e. pairs of atoms with a distance of 140 pm. The images along the [110] direction are shown in Fig. 5.1 (A-E). Because of instabilities of the material under the electron beam and slight mistilt, overlap of neighbouring atomic columns in the Ge dumbbells cannot be avoided, and therefore the dumbbells are not resolved in the high-resolution HAADF STEM images.

5.2.2 Methodology

The statistics-based atom-counting method, explained in detail in chapter 4 has been employed to obtain atom counts for the 5 high-resolution HAADF STEM images shown in Fig. 5.1 (A-E). As a first step, the scattering cross-sections are quantified atomic column-by-atomic column by fitting the empirical imaging model to the experimental images. This parametric model consists of a sum of Gaussian peaks describing the atomic column intensities:

$$f_{kl}(\boldsymbol{\theta}) = \sum_{n=1}^{N} \eta_n \exp\left(-\frac{(x_k - \beta_{x_n})^2 + \left(y_l - \beta_{y_n}\right)^2}{2\rho^2}\right) \tag{5.1}$$

as described in detail in chapter 2 and subsection 4.2.1 of chapter 4. Strong correlation effects hinder precise measurements of the individual scattering cross-sections of each column in the

Ge dumbbell. Therefore, the scattering cross-sections along each column of Ge dumbbells has been estimated rather than the individual column scattering cross-sections. The refined models of the observations are shown in Fig. 5.1 (F-J) and are in excellent agreement with the recorded images in Fig. 5.1 (A-E) demonstrating the quality of the parametric model used. The estimated scattering cross-sections are expected to increase monotonically with the number of atoms. The estimated scattering cross-sections of the images of Fig. 5.1 (A-E) are visualised in a histogram as shown in Fig. 5.2 (F-J), respectively. Ideally, this histogram would consist of isolated components. However, due to a combination of instabilities of the microscope and sample, and noise effects, the components are smeared out. For this reason, visual interpretation of the experimental histogram may lead to deceptive results. Instead, the statistical approach introduced in (sub)sections 4.2.2, 4.2.3, and 4.3 of chapter 4 is used allowing one to determine the locations of all statistically meaningful components. For this approach, the estimated scattering cross-sections are regarded as a statistical draw from an unknown probability distribution consisting of a superposition of Gaussian components, i.e. the Gaussian mixture model given by:

$$f_{\text{mix}}\left(V_n;\boldsymbol{\Psi}_G\right)=\sum_{g=1}^{G}\pi_g\frac{1}{\sqrt{2\pi}\sigma}\exp\left(-\frac{\left(V_n-\mu_g\right)^2}{2\sigma^2}\right). \tag{5.2}$$

This model defines the probability that a specific scattering cross-section value V_n would be estimated for a particular atomic column n. The vector $\boldsymbol{\Psi}_G$ contains the unknown parameters π_g, μ_g, and σ being the mixing proportion of the gth component, the mean scattering cross-section of the gth component, and the width of the components, respectively. The parameters $\boldsymbol{\Psi_G}$ can be estimated from the experimental estimated scattering cross-sections using the maximum likelihood estimator for a given number of components G. In practice, the value of G is unknown and has to be inferred from the available scattering cross-sections as well. The number of significant components, i.e. the model order G can be retrieved by evaluating the so-called Integrated Classification Likelihood (ICL) criterion, which is shown in Fig. 5.2 (A-E) for the images of Fig. 5.1 (A-E). This order selection criterion balances the model fit against the model quality. Indeed the model fit will typically improve for increasing number of components and more details in the available set of scattering cross-sections will be described. However, for high-order models, these details are random and as consequence the model quality will degrade with the model order. The estimated model order is given by the number of components for which ICL reaches a minimum, which is arrowed in Fig. 5.2 (A-E). The ICL criterion indeed shows the typical shape described in subsection 4.4.2 of chapter 4. The minimum often corresponds to a local optimum rather than a global optimum. Fig. 5.2 (F-J) shows the corresponding estimated Gaussian mixture models for the number of components arrowed in the ICL criterion. Based on these estimated probability distributions, the number of atoms in a particular projected atomic column can be identified by assigning each scattering cross-section to the components of the mixture model with the largest probability to generate this scattering cross-section. As discussed in section 4.3 of chapter 4, the location of the first component with respect to the average increment δ between the successive components can be used to determine the number of atoms in the atomic columns assigned to this first component. This has been done for the construction of the scatter plots in Fig. 5.2 (K-O). Here, the locations of the components of the Gaussian mixture model are plotted as a function of the number of atoms corresponding to the component. Finally, atom-counts along each Ge atomic dumbbell of the nanoparticle are

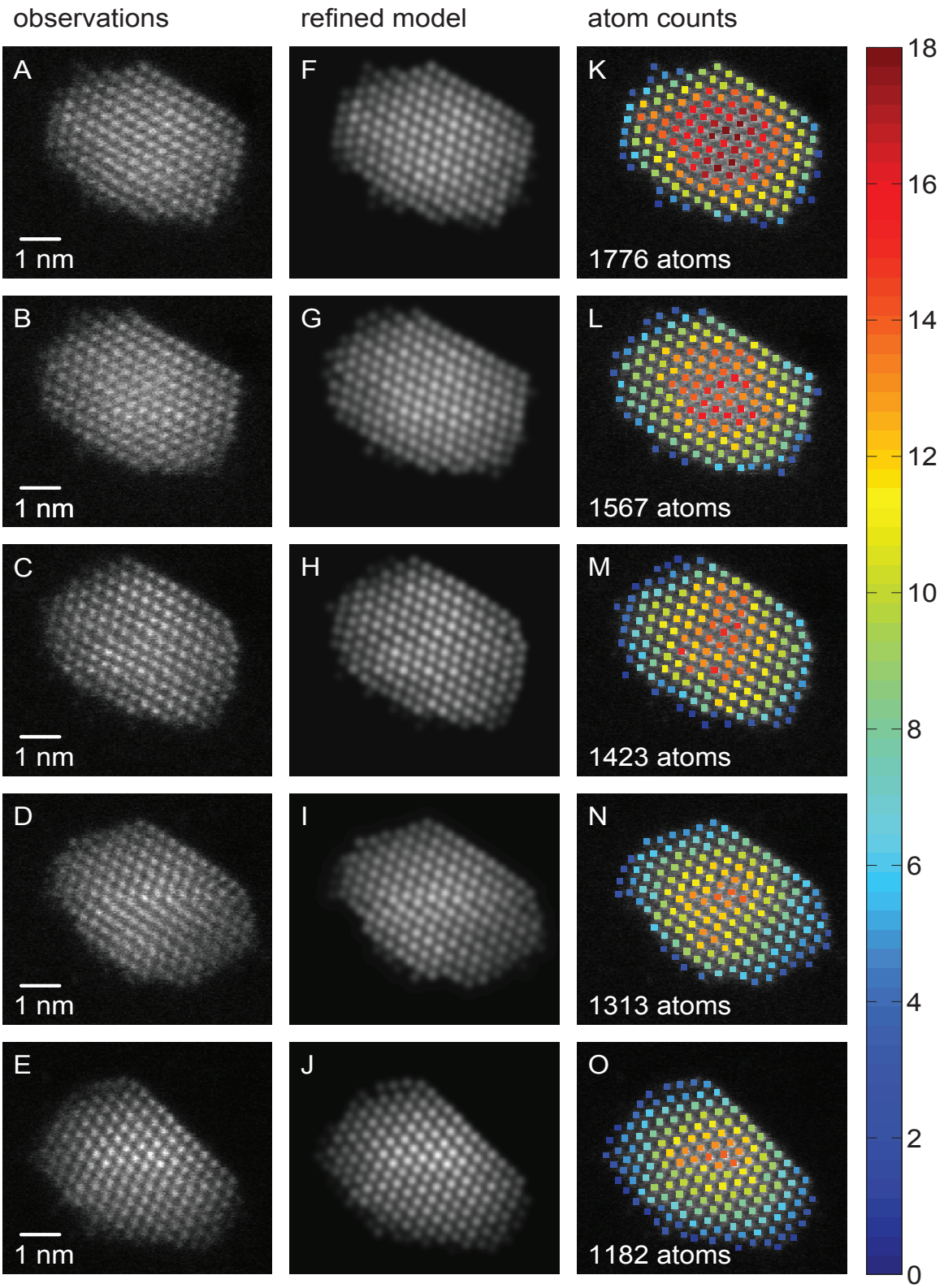

Figure 5.1: *Ge cluster. (A-E) Experimental HAADF STEM images of the cluster along the* [110] *direction. (F-J) Corresponding refined models for the experimental observations. (K-O) Atom-counting results based on the analysis presented in Fig. 5.2.*

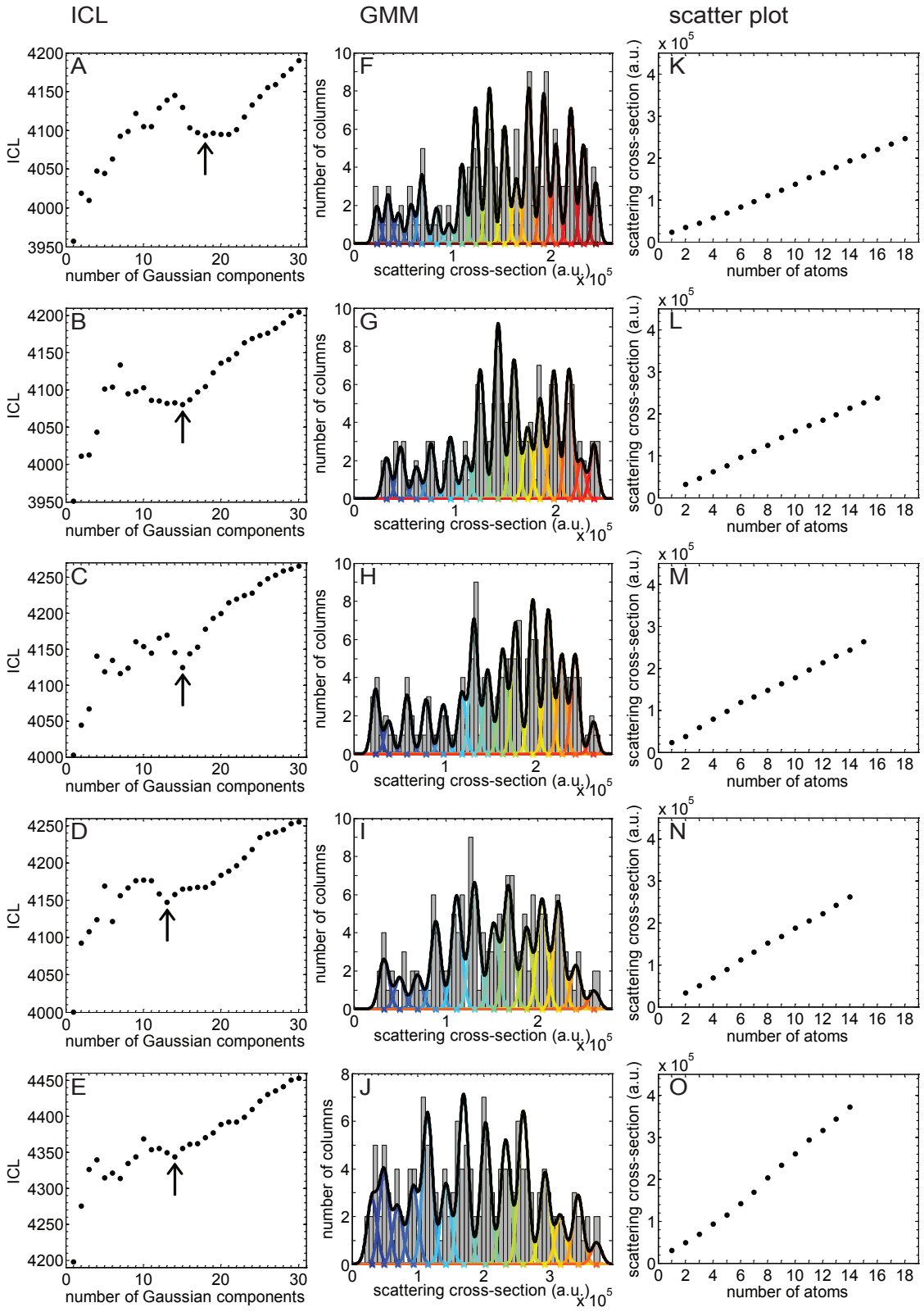

Figure 5.2: *Atom-counting analysis. (A-E) Integrated Classification Likelihood criterion evaluated as a function of the number of Gaussian components in the Gaussian mixture model (GMM). (F-J) Histograms of the scattering cross-sections of the Ge dumbbells together with the estimated mixture model (black curve) and its individual components (coloured curves). (K-O) Scatter plot of the estimated locations of the components in the Gaussian mixture model as a function of the number of atoms corresponding to this component.*

quantified in Fig. 5.1 (K-O) for the different observed images together with the estimated total number of atoms in the Ge cluster. These results will be discussed in the next subsection.

5.2.3 Results and discussion

In the previous subsection, the statistics-based atom-counting method described in detail in chapter 4 has been summarised briefly and has been applied to the experimental set of HAADF STEM images of a Ge cluster. The results are shown in detail in Figs. 5.1 and 5.2. In this subsection, these results will be discussed.
First, it is noted that the total number of atoms is reduced by more than 30 % from the first to the last frame as can be seen from Fig. 5.1 (K-O). This can be caused by beam damage sputtering atoms from the nanoparticle. Then the mean scattering cross-section value of the last component, i.e. the thickest atomic column, should decrease. Therefore, second, the scatter plots of Fig. 5.2 (K-O), in which the locations of the components are plotted versus the corresponding number of atoms are studied into more detail. For these scatter plots, it is expected that the slope of the curve is the same for each recorded frame, since a certain number of atoms corresponds to a specific value for the scattering cross-section which is determined from the Gaussian mixture model estimation. However, the slope in the scatter plots here changes through the different frames. Furthermore, if the total number of atoms is decreasing throughout the experiments, it is expected that the largest scattering cross-section value is observed for the first frame whereas the opposite is observed for these data.
From these observations, it is clear that for these experimental data the interpretation of the output of the atom-counting method is not straightforward and cannot provide a unique solution. In addition, the available data do not allow to diagnose whether the atom-counting method results in inaccurate atom-counts for this experiment or whether the experimental conditions have been changed during the recording of the HAADF STEM images. Therefore, a combination with other techniques will be required in order to obtain trustful atom-counting results with single atom sensitivity. The combination of the statistics-based atom-counting method with detailed STEM image simulations and electron tomography will be used for the analysis of Au nanorods and Pt/Ir particles, which will be the subject of the next sections.

5.3 Atom-counting in Au nanorods

In the previous section, it has been illustrated that although the application of the statistical methods is relatively straightforward, the interpretation of the output of these methods is certainly not straightforward. If no unique solution can be found from the output of the statistics-based atom-counting method, this statistics-based method should be complemented with another approach. In the literature, also a simulation-based approach for atom-counting is available as illustrated in Fig. 1.4 in the introduction of this thesis [LeBeau 2010]. This method is completely independent of the statistics-based method. In contrast to the statistics-based method, the simulation-based method does not provide the precision with which the number of atoms can be counted, but can validate the atom-counting results obtained with the statistics-based atom-counting method. In subsection 5.3.1, it will first be shown how atom-counting results can be obtained with single atom sensitivity for a Au nanorod through a combination

of the simulation- and statistics-based approach. Second, in subsection 5.3.2, an alternative for validation of the atom-counting results is illustrated by comparing the obtained atom counts with the result from atomic resolution tomography. After that, it will be illustrated in subsection 5.3.3, how 3D atomistic models can be created from reliable atom-counting results.

5.3.1 Validation using detailed image simulations

Experiment and simulation

In order to evolve toward accurate atom-counting results, the statistics-based atom-counting method described in chapter 4 is combined with detailed image simulations[5]. This is done for a Au nanorod, shown in Fig. 5.3(a) which has been imaged along the [100] zone axis at the Qu-Ant-EM, a double aberration-corrected Titan^3 operated at 300 kV with a 21.8 mrad convergence angle. The detailed experimental settings are listed in Table 5.1. The value for the Debye-Waller factor is taken from [Gao 1999]. When the experimental data are normalised with respect to the incoming electron beam [LeBeau 2008b, Rosenauer 2009], the scattering cross-sections resulting from the experiment can be compared with the scattering cross-sections determined from a set of simulations with increasing thickness.
Following the method described in [LeBeau 2008b, Rosenauer 2009, Mehrtens 2013a], the experimental image intensities I_{exp} are converted to a fraction of the incident probe using the following equation:

$$I_{\text{norm}} = \frac{I_{\text{exp}} - I_{\text{vac}}}{I_{\text{det}} - I_{\text{vac}}} \tag{5.3}$$

where I_{norm} is the normalised intensity, which can directly be compared with simulated images; I_{vac} is the mean number of counts in the vacuum due to the detector's amplifier offset and I_{det} is the mean number of counts generated by the probe hitting the detector area. In other words, this normalisation places STEM experiments on the same absolute intensity scale as used in theoretical simulations. As such, the accuracy of the counting procedure can be tested.
Nevertheless, this analysis allowing for a comparison between experimental and simulated scattering cross-sections, should be carried out very carefully. The accurate measurement of inner and outer ADF detector angle is of critical importance since the variation of the scattering cross-section value highly depends on it, as shown in [Martinez 2015]. Moreover, the importance of the detector response is often overlooked leading to a discrepancy between experiment and simulation. A full characterisation of the ADF detector should be carried out if the highest quality for a match between simulations and experiment is to be achieved [LeBeau 2008b, Rosenauer 2009]. This procedure requires to scan the STEM probe over the ADF detector to obtain a response map, which has been found to be both inhomogeneous and asymmetric [Findlay 2013, MacArthur 2014]. The detector response at small scattering angles varies significantly from that at higher angles, and therefore, this should be taken into account while performing image simulations. Here, this effect is incorporated by including a detector sensitivity profile in the image simulation, which azimuthally weights the contribution of the

[5]The results of this analysis are published in S. Van Aert, *A. De Backer*, G.T. Martinez, B. Goris, S. Bals, G. Van Tendeloo, and A. Rosenauer, Procedure to count atoms with trustworthy single-atom sensitivity, Physical Review B 87 (2013) 064107.

scattered electron with respect to its scattering angle [Grieb 2012, Mehrtens 2013b]. Including this detector sensitivity profile allows a significantly improved agreement between experiment and simulated images.
Detailed image simulations were carried out using the STEMsim program [Rosenauer 2008] under the frozen lattice approach taking into account the microscope settings and detector sensitivity. Table 5.1 summarises the settings used throughout the simulations. The frozen lattice approximation considers uncorrelated phonon distributions of atomic displacements due to the thermal vibrations of the crystal and therefore describes the so-called thermal diffuse scattering (TDS).

Parameter	Symbol	Value
Acceleration voltage	V_0 (kV)	300
Defocus	ϵ (nm)	−8.301
Spherical aberration	C_s (mm)	0.035
Objective aperture angle	α (mrad)	21.8
Spatial incoherence of source	FWHM (Å)	0.7
HAADF inner collection angle	β_1 (mrad)	62
HAADF outer collection angle	β_2 (mrad)	190
Number of unit cells per supercell	$N_a \times N_b$	11×11
Supercell size	$N_a \times N_b$ (Å^2)	44.88×44.88
Maximum specimen thickness	$z_{[100]}$ (nm)	40.8
Debye-Waller factor	B (Å^2)	0.637
Pixel size	$\Delta x = \Delta y$ (Å)	0.102
Pixel size to sample atomic potential	$\Delta x_V = \Delta y_V$ (Å)	0.0261
Number of phonon configurations		20

Table 5.1: *Experiment and frozen lattice simulations settings for Au in* [100] *zone axis*

Atom-counting results and single atom sensitivity

The experimental image of the Au nanorod is shown in Fig. 5.3(a). This image can be analysed along the same lines as the Ge clusters discussed in the previous section. The refined model of the experimental image is shown in Fig. 5.3(b). The ICL criterion, shown in Fig. 5.3(d), reveals the presence of 47 different column types each consisting of a specific number of atoms. The histogram of scattered intensities is shown in Fig. 5.3(e) together with the estimated probability distribution. The number of Au atoms for every column of the nanorod is shown in Fig. 5.3(c). As expected for this symmetric nanorod, the thickness that can be derived from this atom counting analysis along the perpendicular direction matches the diameter obtained from Fig. 5.3(a). Since the intensities in the HAADF STEM image have been normalised with respect to the incident beam as discussed in the previous paragraph, the accuracy of the counting procedure can be tested. This validation is required since more local minima are present in the ICL criterion as shown in Fig. 5.3(d). Fig. 5.3(f) shows the experimental mean scattering cross-sections - corresponding to the component locations in Fig. 5.3(e) - together with the scattering cross-sections estimated from the frozen phonon calculations using the STEMsim program under the same experimental conditions which are listed in

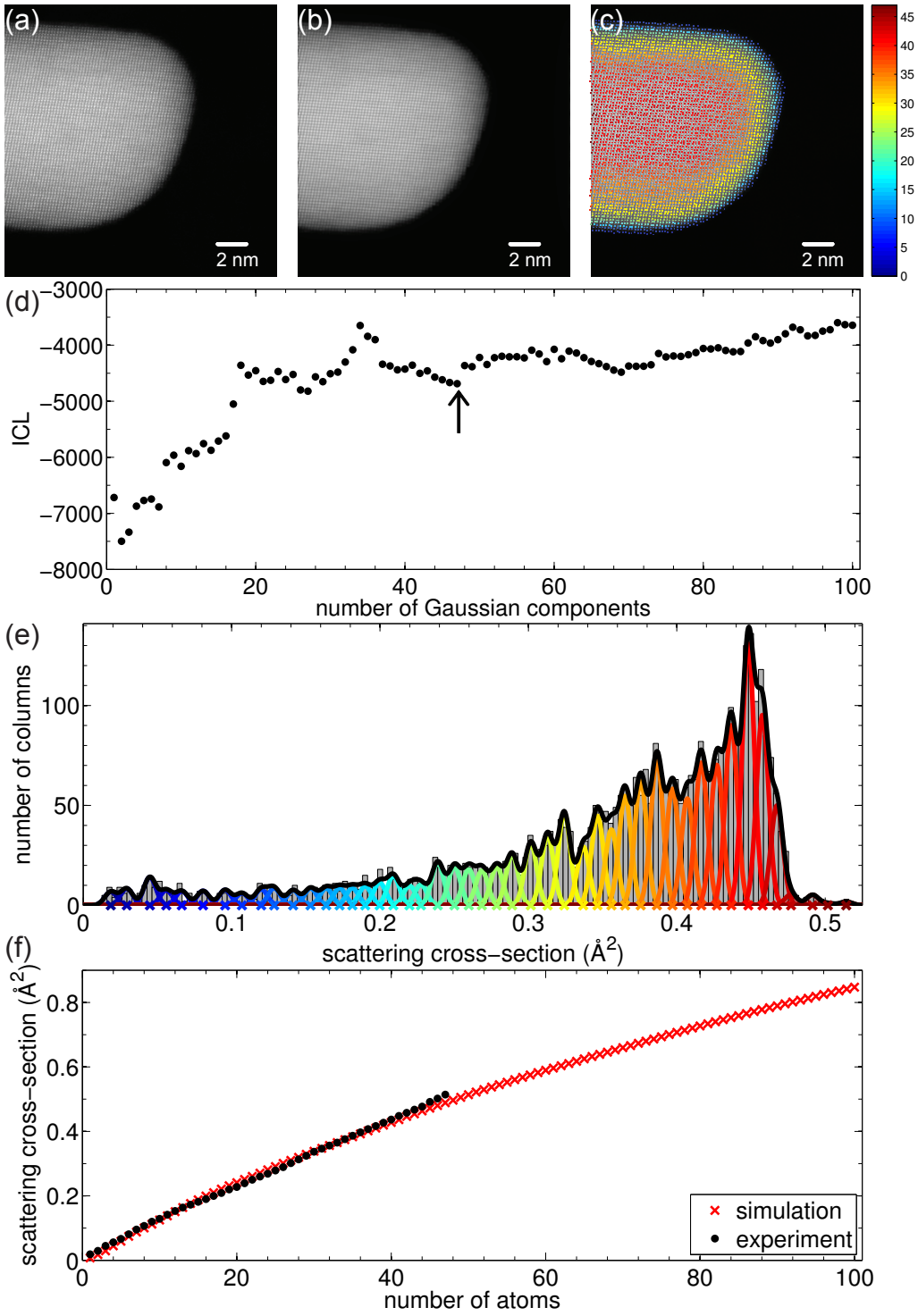

Figure 5.3: *(a) HAADF STEM image of a Au nanorod. (b) Refined model. (c) Number of Au atoms per column. (d) The Integrated Classification Likelihood criterion evaluated as a function of the number of Gaussian components in the mixture model. (e) Histogram of scattering cross-sections of the Au columns together with the estimated mixture model and its individual components. (f) Comparison of experimental and simulated scattering cross-sections.*

Table 5.1 [Rosenauer 2008]. The excellent match of the experimental and simulated scattering cross-sections within the expected 5%-10% error range validates the accuracy of the obtained atom counts [LeBeau 2008a, Rosenauer 2011]. Minor deviations can indeed not be avoided because of remaining uncertainties in the microscope settings, the effect of amorphous layers, and practical limitations to fully take the complex dependence of the Debye-Waller factor on both the particle's size and its different behaviour for surface atoms as compared to bulk-like atoms into account [Clark 1965, Buffat 1977, Mkhoyan 2008, Aveyard 2014]. However, from an alternative point of view, the experimental mean scattering cross-sections can be used as a reference to further improve the accuracy of imaging models taking all important physical effects into account. The steady increase of the simulated scattering cross-sections even above 47 atoms as shown in Fig. 5.3(f), proves the high sensitivity of the scattering cross-sections for the number of atoms. The precision, on the other hand, is limited by the unavoidable presence of noise in the experimental images resulting into fluctuations of the scattering cross-sections $\hat{V}$ around the mean values μ_g. The precision is then set by the overlap of the Gaussian components shown in Fig. 5.3(e). When the overlap increases, the probability that a wrong number of atoms is assigned to a particular column indeed increases. The procedure on how to calculate the percentage of atomic columns for which the number of atoms is counted with single atom sensitivity has been discussed in chapter 4 in subsection 4.4.4. First, the posterior probability $P(I_g|\phi_g)$ given by Eq. (4.24) that a scattering cross-section belonging to component ϕ_g resides in the central part of a component I_g (i.e. interval I_g as illustrated in Fig. 4.8 of chapter 4) is computed. On average, that is, by averaging fractions for the components 1 up top 47, this probability corresponds to 79.89%. Next, the posterior probability $P(\phi_g|I_g)$ given by Eq. (4.25) that a scattering cross-section belonging to the central part I_g stems from component ϕ_g is calculated for each component. On average, this percentage equals 80.55%. This means that for 80.55% of all atomic columns the number of atoms is measured without error. Similarly, the probability to miscount the number of atoms with ±1 can be computed. For this purpose, the posterior probability that the scattering cross-section belonging to the component ϕ_{g-1} or ϕ_{g+1} resides in the interval I_g equals $P(I_g|\phi_{g-1})+P(I_g|\phi_{g+1}) = 19.91\%$, and the probability to miscount the number of atoms with ±1 equals $P(\phi_{g-1}|I_g) + P(\phi_{g+1}|I_g) = 19.43\%$, which is the posterior probability that a scattering cross-sections belonging to I_g stems from component ϕ_{g-1} or ϕ_{g+1}. Consequently, the probability to have an error of ±2 atoms is almost zero. In contrast to the results obtained when using simulations alone, the amount of overlap with neighbouring components can be determined when using this statistics-based procedure, resulting in an estimation of the precision that can be achieved. However, since both approaches, a simulations-based and statistics-based atom-counting method, are independent of each other, the combination of the two methods allows for reliable atom-counting results with single atom sensitivity.

5.3.2 Comparison with atomic resolution electron tomography

In this section, an alternative validation for the atom-counting results using electron tomography is briefly illustrated.

Three projection ADF STEM images of a Au nanorod have been acquired along different major zone axes using the X-Ant-EM, a probe corrected Titan^3 operated at 200 kV with a 24 mrad convergence angle. The inner and outer detector collection angle ranged from $45 - 160$ mrad. The experimental images are shown in Fig. 5.4(a-c). These images were used as an input for

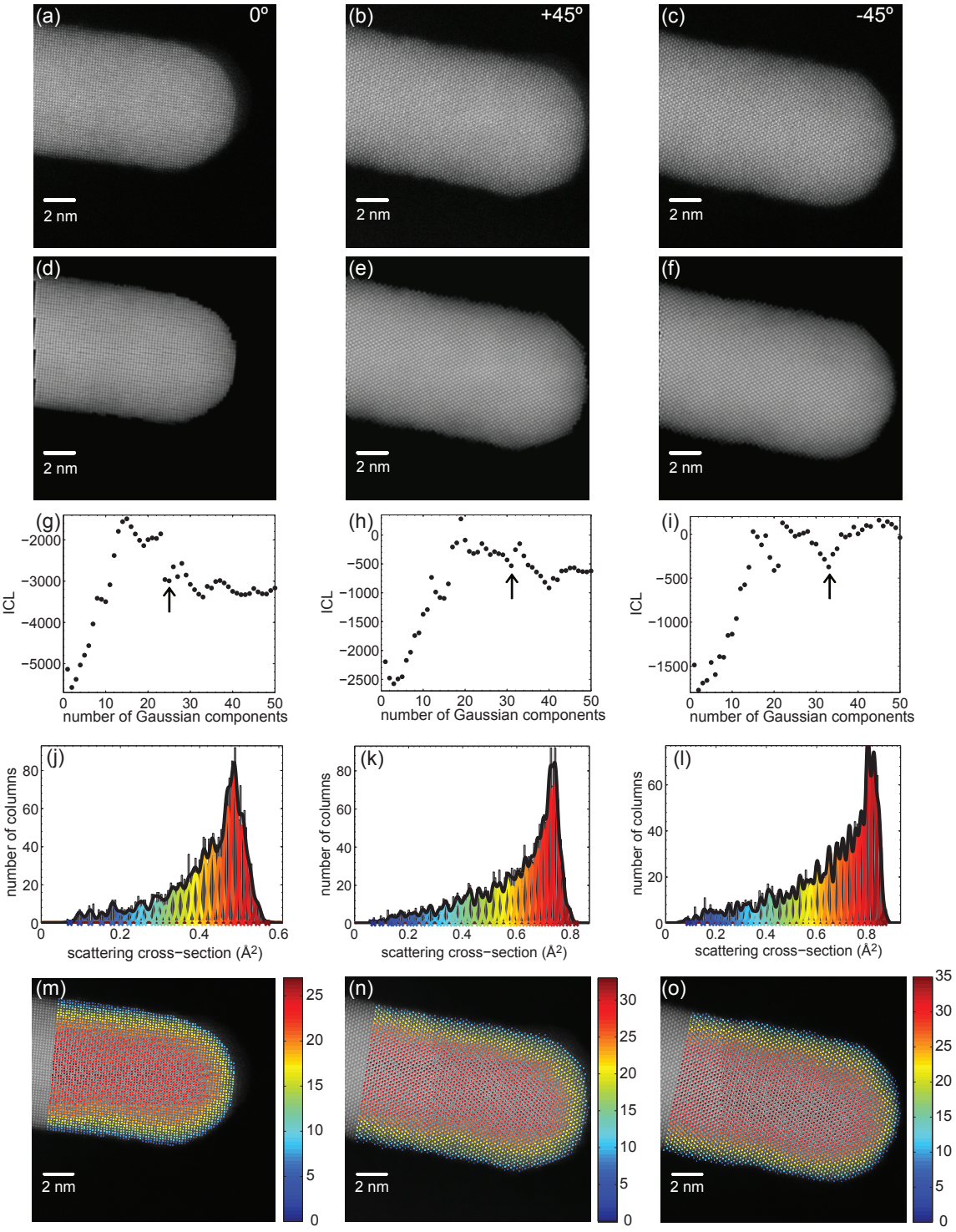

Figure 5.4: *(a-c) Experimental ADF STEM images of a Au nanorod along different major zone axes. (d-f) Corresponding refined models. (g-i) Integrated Classification Likelihood criteria evaluated as a function of the number of Gaussian components in the mixture model. (j-l) Histograms of the scattering cross-sections of the Au columns together with the estimated mixture model (black curve) and its individual components (coloured curves). (m-o) Number of Au atoms per column.*

a 3D reconstruction using a compressive sensing based tomography method as explained in [Goris 2012a]. For a 3D reconstruction at the atomic scale, the sparsity of the object can be exploited in the reconstruction algorithm, as only a limited number of voxels contain an atom and most voxels correspond to vacuum. For each of the projection images also the number of atoms in the projected atomic columns have been counted using the statistics-based atom-counting method described in chapter 4. This analysis is illustrated in Fig. 5.4. Since different viewing directions of the nanorod are available, the choice of the local minimum in the ICL criterion was guided by the prior knowledge of a symmetric nanorod.

In the previous subsection, the atom-counting results have been validated through a comparison with detailed image simulations. Here, the thus obtained atom counts are compared with the number of atoms that can be derived from an orthogonal slice from the atomic resolution reconstruction from electron tomography. This comparison is illustrated in Fig. 5.5. Slight deviations can be expected, since the 3D reconstruction using tomography represents an average structure

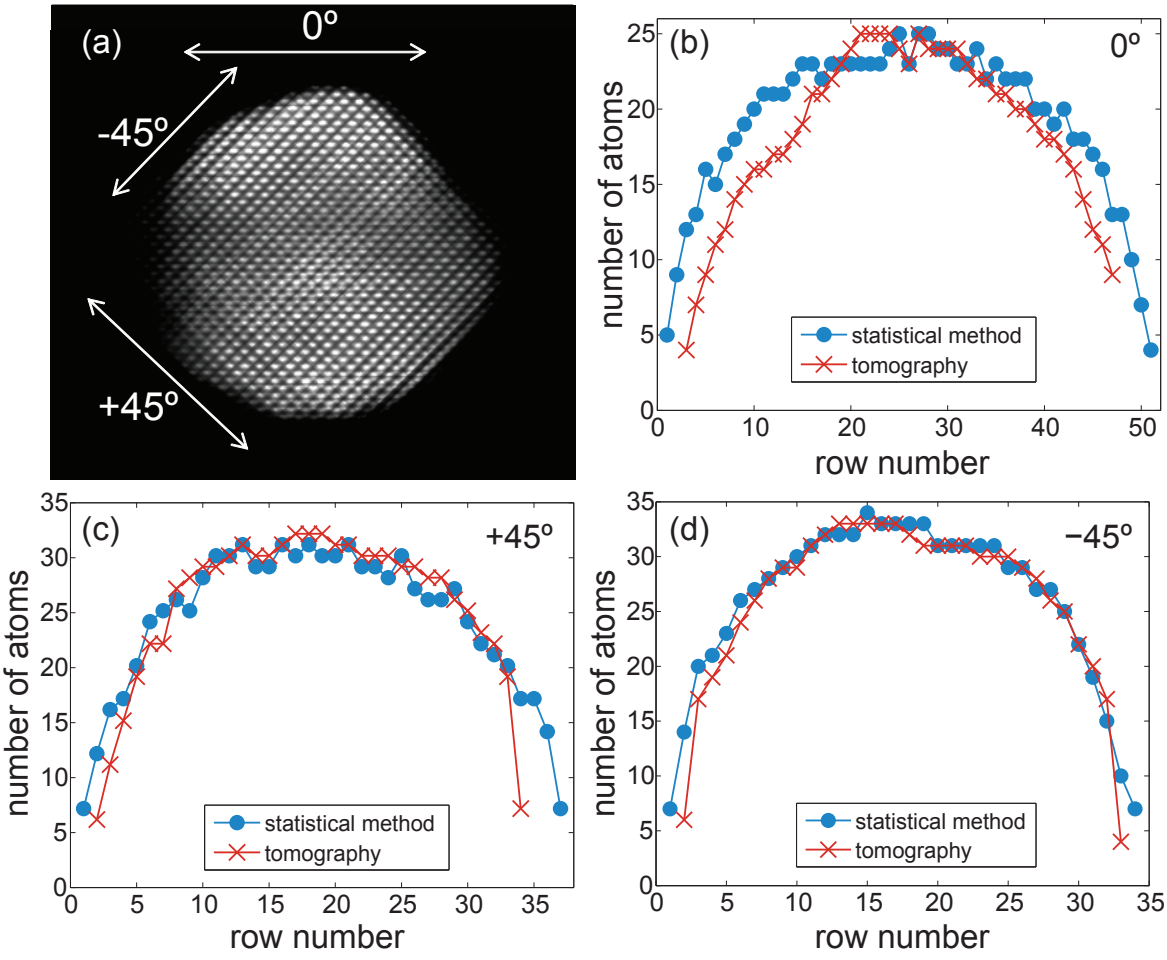

Figure 5.5: *Comparison between atom-counts and atomic resolution electron tomography. (a) Orthogonal slice from the 3D reconstruction of the 40th atomic plane from the tip. (b-d) Comparison of the counts along the different orientations.*

based on the three high-resolution projection images, whereas the atom-counts result from each single image. The number of atoms has been counted in the 40th atomic plane from the tip of the Au nanorod. Good agreement between the counts derived from the 3D reconstruction and from the statistics-based atom-counting method is obtained. Along the 0° projection, the width of the nanorod appears to be underestimated, which is possibly caused by artefacts introduced by the missing wedge. The missing wedge causes the intensities to be smeared out. As such, these intensities will be lower than the applied threshold to visualise the atoms in the orthogonal slice.

5.3.3 Toward 3D atomistic models using atom-counting

Reliable atom-counting results can be used as an input for creating 3D atomistic models [Jones 2014]. This approach provides an alternative to electron tomography for a 3D reconstruction at the atomic scale. Electron tomography requires multiple exposures which is not always feasible in practice. For example, in situ experiments or the characterisation of beam sensitive materials are nearly impossible using electron tomography. In this subsection, 3D atomistic models are created for the Au nanorod of subsection 5.3.2. Therefore, atom counts along with the prior knowledge of a face-centered cubic geometry are used to create an atomistic model. An energy minimisation using a Monte Carlo approach has then been used to relax the nanoparticle's 3D structure [Jones 2014]. The atomistic model built from the atom-counting results in Fig. 5.4(o) is shown in Fig. 5.6. The beam direction is arrowed in this figure. As expected, the surface roughness is higher along this direction. Nevertheless, different surface facets of the Au nanorod can be observed from this 3D reconstruction. These surface facets are of special interest for materials scientists since they determine the physical properties of nanostructures [Pecharromán 2008, Chang 2010, Katz-Boon 2011, Goris 2012a, Katz-Boon 2015].

5.4 Dose limited reliability for atom-counting in Pt/Ir nanoparticles

In the previous section, atom-counting has been demonstrated on Au nanorods which are relatively stable under the incoming electron beam. Here, ADF STEM experiments for an atom-counting analysis are conducted on a industrial bimetallic catalyst providing a severe characterisation challenge because of its beam sensitivity and limited size[6]. As discussed in chapter 4, the reliability of the statistics-based atom-counting method depends on different parameters which can be linked with the quality of the recorded images, such as total number of atomic columns in the experimental STEM image, the number of columns having a different number of atoms, and the amount of noise. In the previous section, it is shown that through a combination of the simulation- and statistics-based method, being completely independent of each other, one is able to count atoms with trustworthy single atom sensitivity. In this section, it will be shown that this combined method allows us to diagnose limits of atom-counting and to investigate the effect of dose, sampling, background behind the particle of interest, tilt, and sample geometry.

[6]These results are published in *A. De Backer*, G.T. Martinez, K.E. MacArthur, L.B. Jones, A. Béché, P.D. Nellist, and S. Van Aert, Dose limited reliability of quantitative annular dark field scanning transmission electron microscopy for nano-particle atom-counting, Ultramicroscopy 151 (2015) 56-61.

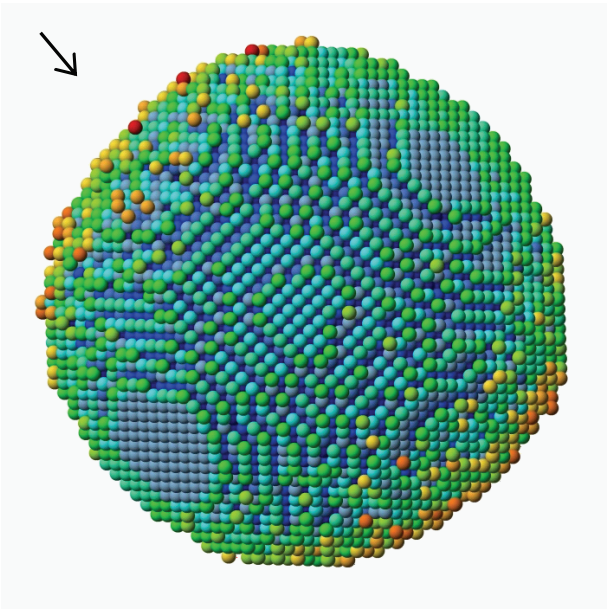

Figure 5.6: *Energetically relaxed 3D atomistic model of a Au nanorod viewed along the tip. The beam direction is indicated by the arrow. The colouring of the atoms indicates the determined nearest-neighbour coordination, from 1 in red to 12 in dark blue. (Model created by L. Jones)*

The latter parameters become important when studying industrially catalyst particles such as the Pt/Ir mixed alloy nanoparticles supported on carbon black discussed in this section.
In subsection 5.4.1, the material under study as well as the experimental and simulation details are presented. The methodology for counting the number of atoms for these catalyst particles is illustrated in subsection 5.4.2. The findings for atom-counting conducted on catalytic particles are discussed in subsection 5.4.3.

5.4.1 Experiment and simulations

Bimetallic nanoparticles have shown promise for hydrogen fuel-cell applications; not only do they provide a reduction in the amount of platinum used but they have also demonstrated a significantly higher catalytic activity. Pt/Ir particles in particular show improved resistance to CO poisoning, a by-product in the reforming of hydrocarbons to H_2 gas [Ralph 2002]. The Pt/Ir particles were supported on a three-dimensional carbon black support and received in powder form dusted onto a carbon coated copper grid. Images were taken at the Qu-Ant-EM, a double corrected FEI Titan^3 working at 300 kV with a 20.2 mrad semi-convergence angle under different dose conditions as shown in Fig. 5.7. The ADF detector ranges from 35 to 190 mrad corresponding to a camera length of 145 mm. For unique atom-counting results, we require a monotonic increase for the scattering cross-sections with thickness. As will be shown in chapter 6, for small enough particles such as in this study, a lower ADF detector inner angle is preferred for atom-counting because of the higher detected signal for a given incident electron dose. Although coherent contributions are present in the detected signal, a monotonic increase in scattering cross-section is observed for this ADF detector collection range. Furthermore, the scattering cross-sections are robust to tilt when using a lower ADF detector inner angle.

The experimental images were normalised with respect to the incident beam [LeBeau 2008b, Rosenauer 2009] in order to be comparable to image simulations. Image simulations were performed using the STEMsim software [Rosenauer 2008] under the frozen lattice approach. The simulation settings are listed in Table 5.2. The value for the Debye-Waller factor is taken from [Gao 1999]. Since the difference in atomic number only equals 1 for the two elements in the bimetallic nanoparticle, the simulated scattering cross-sections of Ir ($Z = 77$) and Pt ($Z = 78$) differ less than 3% up to 15 atoms in a projected atomic column and therefore for purposes of the analysis presented here they can be treated as being monometallic.

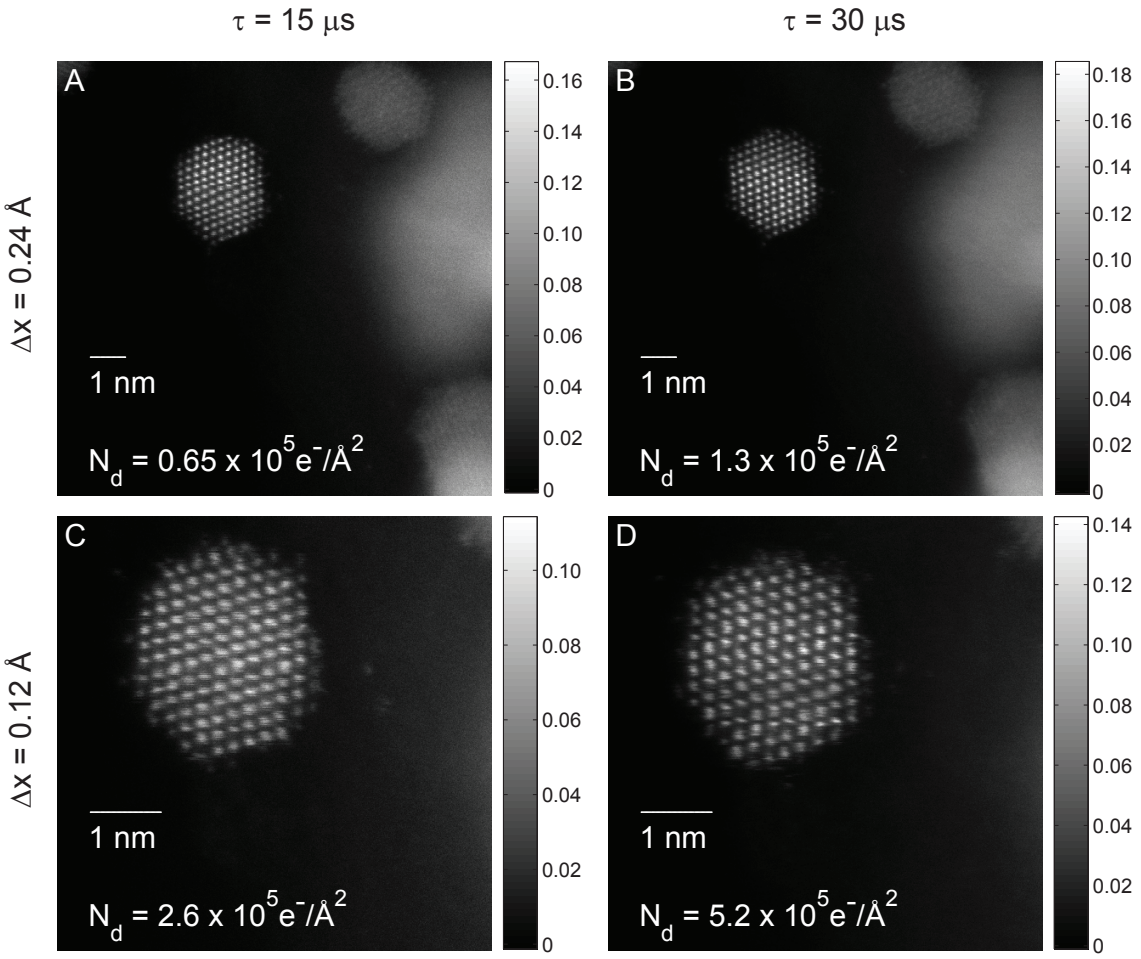

Figure 5.7: *Normalised ADF STEM images of an Pt/Ir particle together with the experimental conditions (dwell time τ, pixel size dx, and incoming electron dose N_d).*

5.4.2 Methodology

If a spatially varying background originating from e.g. the carbon support is present in the image, this background has to be subtracted since ignoring it may lead to errors in the quantitative atom-counting results. To account for the image intensity contribution of such a carbon support under the sample, a mask can be generated which contains the region of interest for quantification, i.e. the nanoparticle. The intensity outside this mask represents the contribution from the

Parameter	Symbol	Value
Acceleration voltage	V_0 (kV)	300
Defocus	ϵ (nm)	0
Spherical aberration	C_s (nm)	406
Objective aperture angle	α (mrad)	20.2
Spatial incoherence of source	FWHM (Å)	0.7
Inner detector angle	β_1 (mrad)	35
Outer detector angle	β_2 (mrad)	190
Debye-Waller factor	B (Å^2)	0.384
Pixel size	Δx (Å)	0.1154
Number of phonon configurations		20

Table 5.2: *Parameters for the frozen lattice simulation of Pt in* [110] *zone axis.*

support only and will be used to estimate the values within the mask using a technique known as in-painting. For small areas, and where the support does not contain abrupt changes the simplest form of in-painting, known as iterative Gaussian-blurring or isotropic diffusion can be used [Oliveira 2001].
Next, the scattering cross-sections can be quantified atomic column-by-atomic column by fitting the empirical imaging model to the background subtracted experimental images. The fitted model for the background subtracted version of image D is shown in Fig. 5.8(a). The scattering cross-sections are presented in Fig. 5.8(b) in the form of a histogram. By evaluating the Integrated Classification Likelihood criterion, as shown and arrowed in Fig. 5.8(c), the presence of 10 significant components has been found whose locations are indicated by means of coloured crosses in Fig. 5.8(b). From the estimated component locations, the number of atoms in each projected atomic column can be quantified leading to the result in Fig. 5.8(d).

5.4.3 Results and discussions: single atom sensitivity for challenging nanoparticles?

The ultimate goal is to obtain atom-counting results for nanoparticles of arbitrary shape, size, and atom type with high precision and high accuracy which are both necessary conditions to conclude single atom sensitivity. High precision can be observed from the Gaussian mixture model when there is nearly no overlap between neighbouring components, such as in Fig. 5.8(b) for image D. High accuracy can be confirmed when comparing the results of the statistics-based atom-counting method with simulated values from detailed image simulations as discussed in section 5.3. So far, this method has successfully been demonstrated on Au nanorods, which are relatively stable under the incoming electron beam, and this procedure promises single atom sensitivity. In this subsection, the accuracy of the atom-counting results is investigated for the catalyst of Fig. 5.7 for which the characterisation is more challenging because of the beam sensitivity and the limited size of the particles. Different parameters which affect the reliability of the atom-counting results are studied.

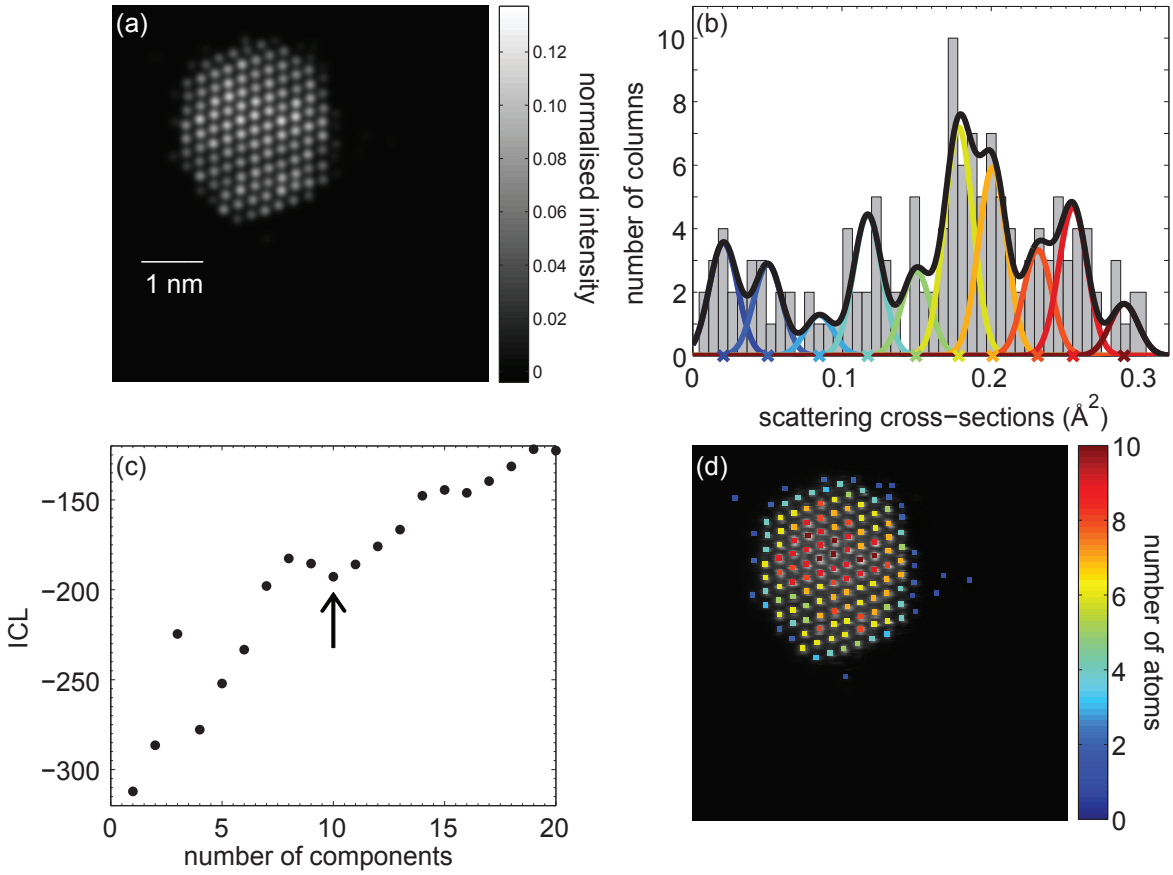

Figure 5.8: *(a) Fitted model of image D (Fig. 5.7). (b) Histogram of the scattering cross-sections of the atomic columns, The black curve shows the estimated mixture model; the individual components are shown as coloured curves which correspond to the colours for the number of atoms in (d). (c) ICL evaluated as a function of the number of Gaussian components in a mixture model. (d) Number of atoms per column.*

5.4.3.1 Effect of background subtraction

From Fig. 5.7 it can be seen that a spatially varying background is present in the images. This background has been subtracted following the method described in subsection 5.4.2. In Fig. 5.9, the effect of the background subtraction on the atom counts is illustrated. Fig. 5.9(a) shows the difference map of the atom counts per atomic column with and without background subtraction and Fig. 5.9(b) shows the vertically average mean error in atom counts. Ignoring the spatially varying background clearly leads to a counting error of ±1 atom. This type of error thus results from bias of the estimated scattering cross-sections caused by model misspecification [den Dekker 2005]. The subtracted background represents the carbon support and is shown in Fig. 5.9(c). As expected, the reconstructed carbon-ramp corresponds to the mean error in atom counts of Fig. 5.9(b).

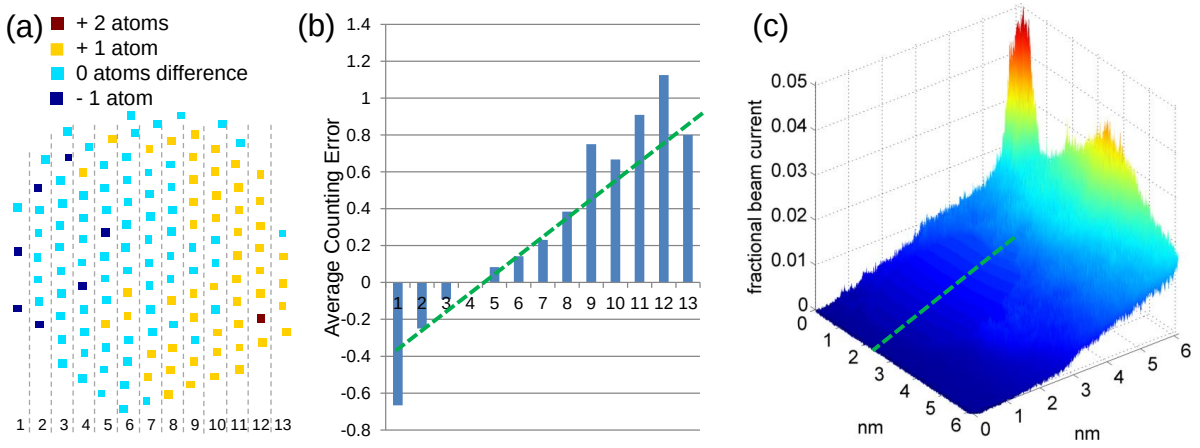

Figure 5.9: *(a) The error observed when the carbon intensity is not considered. (b) Vertically averaged error. (c) The observed carbon contribution in the background-only image.*

5.4.3.2 Comparison with simulations

In order to check the accuracy, the estimated mean scattering cross-sections of the components are compared with the library values from the detailed image simulations for this experiment. The library values are shown for Pt, the values for Ir are not plotted on this graph since they cannot be distinguished from the scattering cross-sections of Pt up to 15 atoms. From Fig. 5.10, where the simulated values are shown for Pt, it can be seen that for image D an excellent match has been found between the estimated mean scattering cross-sections from the experiment and the simulated values. The observed agreement is within the expected 5 – 10% error range proving that the number of components when using the ICL criterion as well as the locations of these components in Fig. 5.8(b) are accurately determined. Slight deviations cannot be avoided because of remaining uncertainties as discussed in subsection 5.3.1.
Similar analyses were performed for images A, B, and C and their results are also shown in Fig. 5.10. A mismatch between the estimated and simulated scattering cross-sections can be observed for image C, but is apparent and most pronounced for images A and B. For these images, the number of components in the Gaussian mixture model is considerably underestimated. Based on a comparison with the simulated values, 13 and 15 components are expected for images A and B, respectively. In the following subsections, the origin of the mismatch of images A, B, and C with the simulated values is discussed.

5.4.3.3 Effect of sample mis-tilt

The slight mismatch of image C from the simulated curve in Fig. 5.10 stems from a small sample mis-tilt [E 2013]. This can be understood from electron channelling. This phenomenon, where an aligned column of atoms parallel to the incident beam direction exhibits a small lensing effect on the beam, causes a column of atoms to have a larger scattering cross-section than the sum of the individual scattering cross-sections of its constituent atoms [E 2013]. This results in a percentage loss in scattering cross-section for small sample mis-tilts away from a low order zone axis. The mis-tilt measured based on a geometry calculation and the ellipticity of the column equals 31.6 mrad for image C. Based on image simulations, this corresponds to 7% loss of

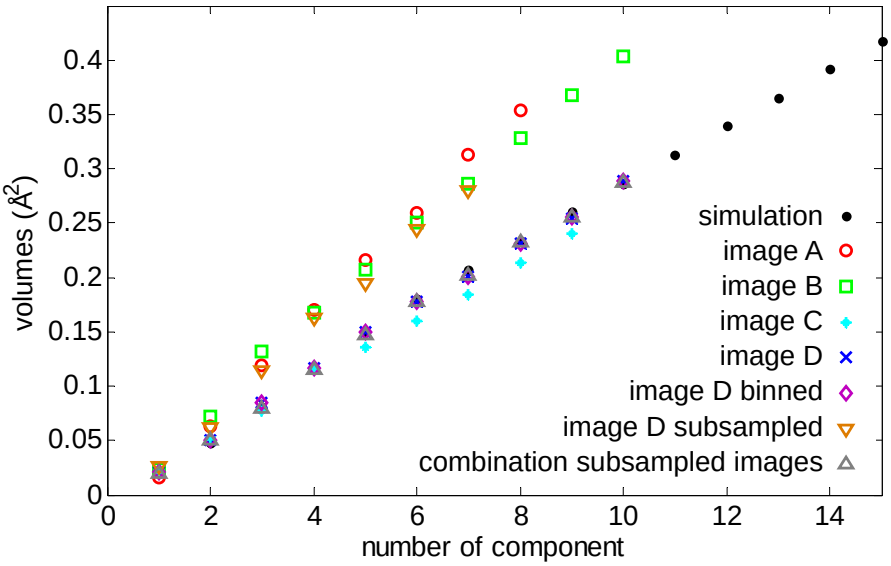

Figure 5.10: *Overview of the analysed data in comparison with the simulations.*

scattering cross-section which is in agreement with the results shown in Fig. 5.10. One should be particularly aware of this effect for beam sensitive samples which are liable to reconstruct and rotate under the beam.

5.4.3.4 Effect of sampling

The effect of sampling on the atom-counting results is considered since the pixel size of images A and B is double the pixel size (half the magnification) of image D, as can be seen from Fig. 5.7. Consequently, the number of sampling points in images A and B is a quarter of the number of sampling points in image D. In [E 2013], it is shown that pixel size has no effect on the scattering cross-sections in the absence of noise. Here, the effect of sampling on the atom-counting analysis is studied by analysing a new image generated by binning 2×2 pixels of image D. In that case, the estimated mean scattering cross-sections are perfectly in accordance with the simulated values as can be concluded from Fig. 5.10. This means that sampling itself has no effect on the accuracy of the atom counts so long as atomic resolution is preserved in the ADF STEM image. The underestimation of the model order for images A and B can thus not be explained as a sampling effect.

5.4.3.5 Effect of dose

In the previous subsection, the effect of sampling was studied as a possible reason for the underestimation of the number of components in images A and B. It should be noticed that while binning 2×2 pixels, the total recorded electron dose is preserved such that only the effect of sampling is studied. However, the electron dose is 4 times lower in image B as compared with image D, and even 8 times lower for image A. This suggests that a reduction of incoming electron dose causes an underestimation of the model order when evaluating the ICL criterion. The lower magnification and electron dose of image B with respect to image D can be mimicked by

subsampling image D, i.e. by taking every second pixel in x and y direction (one quarter overall). The result of the analysis of the subsampled image D is also shown in Fig. 5.10. This result resembles the analysis of images A and B thus explaining the mismatch with the simulation for these images. The reduced dose leads to less precise measurements of the scattering cross-sections resulting in insufficient statistics for the determination of the number of components by the evaluation of the ICL criterion. The effect of dose on the accuracy of the atom-counting results will be discussed in more detail in the following subsection.

5.4.3.6 Discussion of the accuracy of the atom-counting results

The most pronounced mismatch with the simulations in Fig. 5.10 can be explained as an effect of reduced dose, resulting in less accurate measurements for the number of atoms in an atomic column. This effect of the reduced dose can be studied in more detail from the Gaussian mixture model. If the dose is reduced the neighbouring components of the Gaussian mixture model start overlapping more, because of the less precise measurements of the scattering cross-sections. This significant overlap between neighbouring components in the Gaussian mixture model can be measured in terms of the relative width of the components. This relative width expresses the ratio of the width of the components of the Gaussian mixture model and the average increment in scattering cross-section for 1 extra atom, i.e. the σ/δ-ratio discussed in subsection 4.4.2 of chapter 4. In the mentioned subsection, it has been shown that this σ/δ-ratio in combination with the N/G-ratio is important when it comes to accurately determining the minimum of the ICL, where N is the number of analysed atomic columns in the ADF STEM image and G the true model order. This was summarised in Fig. 4.7. Here, the probability of choosing the correct number of components based on the minimum of the ICL is resumed in Fig. 5.11 as a function of the σ/δ-ratio and N/G-ratio. The corresponding values for image D and subsampled image D are indicated in Fig. 5.11 to illustrate the effect of the reduced dose. It is clear that the reduced dose widens the components hence limiting the precision. As a consequence the probability for choosing the correct minimum of ICL significantly decreases. Nevertheless, Fig. 5.11 suggests that this loss in accuracy can be compensated by increasing the N/G-ratio. In practice, this can be realised by analysing collectively the scattering cross-sections originating from images recorded under the same conditions. From Fig. 5.11, it can be seen that a combination of 4 images should be sufficient. The results of such a combined analysis of the collective scattering cross-sections originating from 4 different subsampled versions of image D are shown in Fig. 5.10. The estimated mean scattering cross-sections again coincidence with the simulated values. It is important to mention that this collective analysis only pays off in terms of accuracy but leaves the precision unaffected. Indeed, the precision of the atom-counting results is determined by the overlap in the Gaussian mixture model and is set by the precision with which the scattering cross-sections are known. This precision is characterised by the electron dose and the value of the scattering cross-sections, but is independent of the number of analysed scattering cross-sections. For low dose acquisitions, the precision could in principle be compensated when averaging 'identical' images prior to determination of scattering cross-sections. In practice, however, the assumption of multiple images of exactly the same structure is very unrealistic, especially for beam sensitive samples.

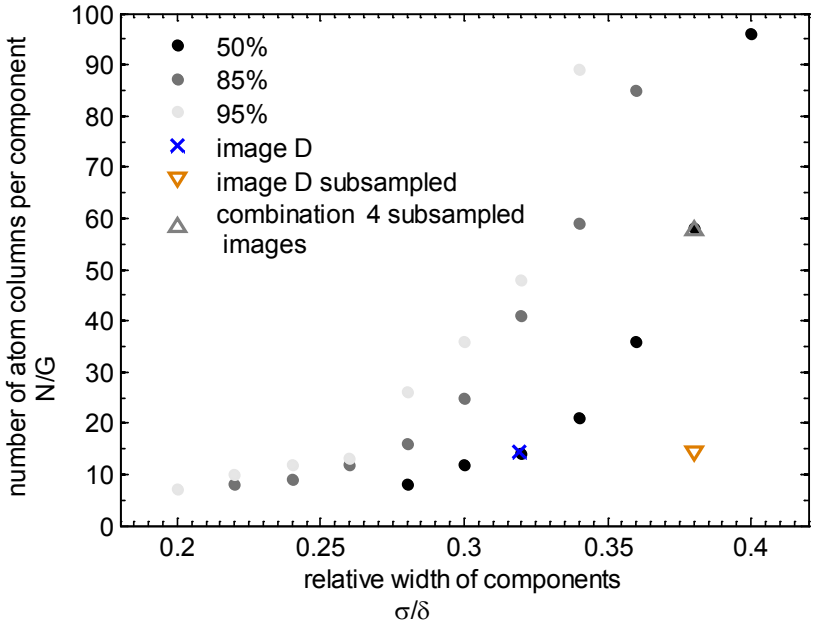

Figure 5.11: *Probabiltiy of choosing the correct number of components based on ICL as a function of* σ/δ *and* N/G*. The corresponding values for image D, subsampled image D, and a combination of* 4 *subsampled images are also shown.*

5.5 Conclusions

In this chapter, it has been shown how precise and accurate atom-counting results can be obtained for different types of nanoparticles from ADF STEM images. First, it has been illustrated that the statistics-based atom-counting method should be combined with another independent, complementary method. Here, a combination with a simulations-based approach or electron tomography is presented. The independence of both methods allows us initially to test the reliability of the atom counts obtained with the statistics-based approach.

The scattering cross-sections have been shown to be a very successful performance measure to count the number of atoms in an atomic column from a single STEM image, since they monotonically increase with the number of atoms in an atomic column (in contrast to the peak intensities which saturate beyond a certain thickness). Using the scattering cross-sections, it has been shown that for a Au nanorod, 80% of the analysed atomic columns has been measured without error and 20% with an error of 1 atom. Furthermore, it has been shown that the atom-counting results are consistent with the number of atoms counted from a slice through a 3D reconstruction obtained using atomic resolution electron tomography. In addition, it has been illustrated how atom-counting results can be used for the creation of 3D atomistic models.

In the atom-counting analysis of a industrial bimetallic catalyst, it has been shown that the interplay of several effects can greatly impact the reliability of atom-counting in quantitative ADF STEM. This includes not only parameters such as electron dose and lateral sampling, but also aspects often beyond the control of the experimentalist, including particle tilt and contrast contributions from the carbon support. Here, for the first time, a study of the minimum dose and sampling requirements to count atoms with single atom sensitivity could be reported using a

hybrid statistical and library method to quantify experimental images. It is discovered that a compensation should be made for the varying sample support in order to avoid atom-counting errors and that care must be taken in the interpretation of column intensities for slightly tilted nanoparticles. For samples that undergo transformation under the beam, poor image quality cannot be countered by simple image averaging, rather the frames must be analysed collectively. Finally, this study suggests that while dose is often lowered to reduce sample damage, some minimum level is required to retain single atom precision. This trade-off between damage and reliability then guides experiment design suggesting that optimum dose and sampling conditions exist for each instrument/sample such that the highest possible precision can be obtained from the hardware available.

In general, based on the analysis of the different experimental images, it can be concluded that single atom sensitivity can obtained for sufficiently high incident electron dose, whereas less precise but still accurate counting results can be obtained when imaging with a lower incident electron dose. The availability of accurate atom-counting results opens up new possibilities for the characterisation of materials where electron tomography cannot be applied. This includes beam sensitive materials or in-situ experiments, where the 3D atomic structure of the object under study changes. Furthermore, from an alternative point of view, the atom-counting results can be used as a reference to further improve the accuracy of imaging models and electron tomography reconstruction algorithms. On the one hand, the atom-counting results can help taking important physical effects into account in the development of new imaging models. On the other hand, a synergistic combination of atom-counting and compressive sensing reconstruction algorithms for electron tomography, will enable to include quantitative prior information on the number of atoms during the reconstruction. Since the atomic positions are not fixed during this reconstruction, this enables one to detect deviations from the perfect crystal structure, which is not possible when using only the atom-counting results. Moreover, this additional information in the reconstruction algorithm might reduce the number of 2D projection images that is needed and will allow for a reliable 3D reconstruction of larger nanoparticles at the atomic scale.

6

Optimal experiment design for nanoparticle atom-counting from ADF STEM images

6.1 Introduction

In the previous chapter, different practical applications are worked out using the statistics-based atom-counting method. From the last application, it is clear that for more challenging nanoparticles it is a very tedious task to determine the number of atoms from an ADF STEM image. Therefore, it is important to optimise the experiment design for atom-counting in order to increase the detected dose for atom-counting and to determine the minimally required electron dose in order to obtain a pre-specified precision.

In this chapter, the theoretical limits to the precision with which the number of atoms in a projected atomic column can be estimated from HR STEM images will be explored[7]. Therefore, STEM images are interpreted quantitatively and the optimal experiment design to count the number of atoms in a projected atomic column is investigated. So far, the Cramér-Rao lower bound has been proven to be an optimal tool to determine a theoretical lower bound on the precision with which continuous parameters such as atomic column positions and intensities can be estimated [Bettens 1999, den Dekker 1999b, Van Aert 2001, den Dekker 2001, Van Aert 2002b, Van Aert 2002a, Van Aert 2004b, Van Aert 2004a, den Dekker 2005, Van Aert 2005, Bals 2006, Van den Broek 2011, De Backer 2011, Wang 2012b, Van Aert 2012, den Dekker 2013]. However, this lower bound can only be derived for continuous parameters. Therefore, an alternative measure using the principles of detection theory will be introduced

[7]The results of this chapter are published in *A. De Backer*, A. De wael, J. Gonnissen, and S. Van Aert, Optimal experimental design for nano-particle atom-counting from high-resolution STEM images, Ultramicroscopy 151 (2015) 46-55.

[Kay 2009, den Dekker 2013, Gonnissen 2014] for problems concerning the estimation of the atomic number, which is a discrete parameter. This measure will here be extended to the atom-counting problem, where the number of atoms in a projected atomic column can also be considered as a discrete parameter.
Statistical detection theory allows us to derive a criterion to describe the performance of atom-counting provided that the expectations as well as statistical fluctuations of the experimental images can be accurately modelled. In this framework, the atom-counting problem is formulated as a statistical hypothesis test, where each hypothesis corresponds to a specific number of atoms in a projected atomic column. The optimality criterion can then be defined as the probability to choose the wrong hypothesis, i.e. the so-called probability of error. In order to compute this probability of error, use can be made of realistic simulations to describe the experimental images [LeBeau 2008a, Rosenauer 2008, Rosenauer 2009, Grieb 2012, Van Aert 2013], and knowledge about the statistics of the image pixel values. Ultimately, the image pixel values will be Poisson distributed because of the unavoidable presence of counting noise. This inherent presence of statistical fluctuations will therefore set fundamental limits to the precision with which the number of atoms can be determined.
Statistical detection theory enables us to decide between different image performance measures that can be used for atom-counting in an objective manner. Here this comparison will be performed for peak intensities, scattering cross-sections and image intensities on a pixel by pixel basis. In addition, by minimising the expression for the probability of error, the optimal experiment design can be derived. In this chapter, the optimal inner and outer angle of an annular STEM detector will be computed. So far, STEM imaging using a HAADF detector is often used for atom-counting [Pennycook 1988, Hartel 1996, Singhal 1997, Voyles 2002, Erni 2003, LeBeau 2010, Van Aert 2011, Bals 2011, Bals 2012, Van Aert 2013]. Here, it will be investigated if this imaging mode remains optimal in terms of atom-counting precision. This procedure to derive the optimal STEM detector can then be applied in practical future research problems so as to further improve the precision to count atoms in a projected atomic column.
The organisation of this chapter is as follows. In sections 6.2 and 6.3, detection theory is discussed and the probability of error is derived for both a binary and a multiple hypothesis test and the so-called sum of Kullback-Leibler divergences is introduced. In section 6.4, the proposed method will first be applied to a simple linear imaging model in order to study the dependence on the incident electron dose and number of atoms analytically. Secondly, the probability of error will be computed for a realistic simulation of a $SrTiO_3$-crystal in order to derive optimal inner and outer angles of the annular STEM detector. This will be done for a binary as well as for a multiple hypothesis test. In section 6.5, the results found for the binary hypothesis test will be discussed and compared to those for the multiple hypothesis test. In section 6.6, conclusions are drawn.

6.2 Detection theory: Binary hypothesis testing

When one is considering the problem of counting the number of atoms in a projected atomic column of a mono-type crystalline structure from HR STEM images, the goal is to obtain the number of atoms in a column as precise as possible. In this section, an expression for the probability to miscount the number of atoms, the so-called probability of error, will be derived. Also,

a tightly connected performance measure, the so-called sum of Kullback-Leibler divergences, will be introduced. To start simple a binary hypothesis test is used in which only two possible successive numbers of atoms are considered as possible outcomes. In the next section, this theory will be extended toward a multiple hypothesis test. In that case, all possible hypotheses up to a certain thickness for the atomic column have to be included.

In the case where one wants to know if there are n or $n+1$ atoms in a projected atomic column, the hypotheses are given by

$$\begin{aligned} \mathcal{H}_0 &: n_{\mathcal{H}_0} = n \\ \mathcal{H}_1 &: n_{\mathcal{H}_1} = n+1 \end{aligned} \tag{6.1}$$

where $\mathcal{H}_0$ is referred to as the null hypothesis, $\mathcal{H}_1$ as the alternative hypothesis and $n_{\mathcal{H}_i}$ denotes the number of atoms under hypothesis $\mathcal{H}_i$. In order to express a prior belief in the likelihood of the hypotheses, it is assumed that the prior probabilities $P(\mathcal{H}_0)$ and $P(\mathcal{H}_1)$ associated with these hypotheses are known. It is reasonable to assign equal prior probabilities of $1/2$ if both hypotheses are equally likely. Throughout this chapter, it will always be assumed that both hypotheses are equally likely. By following the quantitative method proposed in [den Dekker 2013], the goal is now to quantify the probability of assigning the wrong hypothesis. In a so-called Bayesian approach, this probability of error P_e is defined as:

$$\begin{aligned} P_\mathrm{e} =& \Pr\{\text{decide } \mathcal{H}_0, \mathcal{H}_1 \text{ true}\} + \Pr\{\text{decide } \mathcal{H}_1, \mathcal{H}_0 \text{ true}\} \\ =& P(\mathcal{H}_0|\mathcal{H}_1)\, P(\mathcal{H}_1) + P(\mathcal{H}_1|\mathcal{H}_0)\, P(\mathcal{H}_0) \end{aligned} \tag{6.2}$$

where $P\left(\mathcal{H}_i|\mathcal{H}_j\right)$ is the conditional probability of deciding $\mathcal{H}_i$ when $\mathcal{H}_j$ is true. Using the criterion of Eq. (6.2), the two possible errors are weighted appropriately to yield an overall error measure. Decision rules are now defined such that the probability of error is minimised. For this purpose, it is shown in [Kay 2009] that one should then decide $\mathcal{H}_1$ if:

$$\frac{p(w;\mathcal{H}_1)}{p(w;\mathcal{H}_0)} > \frac{P(\mathcal{H}_0)}{P(\mathcal{H}_1)} = \gamma = 1, \tag{6.3}$$

otherwise $\mathcal{H}_0$ is decided. In this expression $p(w;\mathcal{H}_i)$ is the conditional probability function assuming $\mathcal{H}_i$ to be true evaluated for a specific observation w. The exact expression for this probability function will be discussed for three different measures that can be used as a criterion to count the number of atoms in a projected atomic column: peak intensities (PI), scattering cross-sections (CS), and HR STEM image pixel values of a projected atomic column. The observations can be modelled as stochastic variables ω. The stochastic variable ω will take a different form for these three measures:

$$\omega^{\mathrm{PI}} \qquad \text{for peak intensities} \tag{6.4}$$

$$\omega^{\mathrm{CS}} = \sum_{k=1}^{K}\sum_{l=1}^{L} \omega_{kl} \cdot \Delta x^2 \qquad \text{for cross-sections} \tag{6.5}$$

$$\boldsymbol{\omega}^{\mathrm{Im}} = [\omega_{11}, \omega_{12}, \omega_{21}, \ldots, \omega_{kl}]^T \quad \text{for images} \tag{6.6}$$

where the variable ω_{kl} corresponds to the random variables describing the pixel intensities of the STEM image of the atomic column and ω^{PI} corresponds to the random variable describing the pixel intensity at the position of the atomic column. The index kl denotes the probe position $(x_k, y_l)^T$ for a set of KL pixel observations, and Δx denotes the pixel size of the STEM image.

6.2.1 Peak intensities

When assuming that the pixels in a STEM image are statistically independent electron counting results, which are modelled as a Poisson distribution, the conditional probability function for the pixel intensity at the position of a projected atomic column is given by:

$$p\left(\omega^{\mathrm{PI}};\mathcal{H}_i\right) = \frac{\left(\lambda^{\mathrm{PI}}_{\mathcal{H}_i}\right)^{\omega^{\mathrm{PI}}}}{\omega^{\mathrm{PI}}!} \tag{6.7}$$

where the parameter $\lambda^{\mathrm{PI}}_{\mathcal{H}_i} = \mathbb{E}_{\mathcal{H}_i}\left[\omega^{\mathrm{PI}}\right]$ corresponds to the expectation value for the pixel intensity of the STEM image at the position of the projected atomic column under $\mathcal{H}_i$. Since this expectation value will depend on which hypothesis $\mathcal{H}_i$ is assumed to be true, also the probability function depends on $\mathcal{H}_i$. In general, this expectation value can be computed under each hypothesis using software that allows one to simulate a STEM image for a given input material's structure and a given set of microscope parameters [Rosenauer 2008]. Following the decision rule of Eq. (6.3), for equal prior probabilities $P(\mathcal{H}_0) = P(\mathcal{H}_1) = 1/2$, one should decide $\mathcal{H}_1$ for a specific observation w^{PI} if

$$p\left(w^{\mathrm{PI}};\mathcal{H}_1\right) > p\left(w^{\mathrm{PI}};\mathcal{H}_0\right) \tag{6.8}$$

otherwise $\mathcal{H}_0$ is decided. An illustration of the conditional probability functions $p\left(\omega^{\mathrm{PI}};\mathcal{H}_i\right)$ of Eq. (6.7) of both hypotheses is given in Fig. 6.1(a) for the peak intensities of a Sr column consisting of either 15 or 16 atoms. The dark grey region denotes the error which is made if $\mathcal{H}_0$ is chosen while $\mathcal{H}_1$ is correct, and vice versa for the light grey region. It is clear from this figure that the probability of error corresponds to the overlapping area of the two conditional probability functions $p\left(\omega^{\mathrm{PI}};\mathcal{H}_0\right)$ and $p\left(\omega^{\mathrm{PI}};\mathcal{H}_1\right)$. This probability can analytically be computed using the cumulative distribution function of the Poisson distribution:

$$\begin{aligned} P_{\mathrm{e}} =& \frac{1}{2}P(\mathcal{H}_0|\mathcal{H}_1) + \frac{1}{2}P(\mathcal{H}_1|\mathcal{H}_0) \\ =& \frac{1}{2}F\left(x^{\mathrm{PI}};\lambda^{\mathrm{PI}}_{\mathcal{H}_1}\right) + \frac{1}{2}\left[1 - F\left(x^{\mathrm{PI}};\lambda^{\mathrm{PI}}_{\mathcal{H}_0}\right)\right] \end{aligned} \tag{6.9}$$

where $F\left(x^{\mathrm{PI}};\lambda^{\mathrm{PI}}_{\mathcal{H}_i}\right)$ equals the Poisson cumulative distribution function with parameter $\lambda^{\mathrm{PI}}_{\mathcal{H}_i}$ evaluated at the value x^{PI}, with x^{PI} the intersection between the two conditional distribution functions $p\left(\omega^{\mathrm{PI}};\mathcal{H}_0\right)$ and $p\left(\omega^{\mathrm{PI}};\mathcal{H}_1\right)$ given by:

$$x^{\mathrm{PI}} = \frac{\lambda^{\mathrm{PI}}_{\mathcal{H}_0} - \lambda^{\mathrm{PI}}_{\mathcal{H}_1}}{\ln\frac{\lambda^{\mathrm{PI}}_{\mathcal{H}_0}}{\lambda^{\mathrm{PI}}_{\mathcal{H}_1}}}. \tag{6.10}$$

6.2.2 Scattering cross-sections

As a second measure, next to the peak intensities, one can also use scattering cross-sections under both hypotheses. The scattering cross-section values are here computed in the following

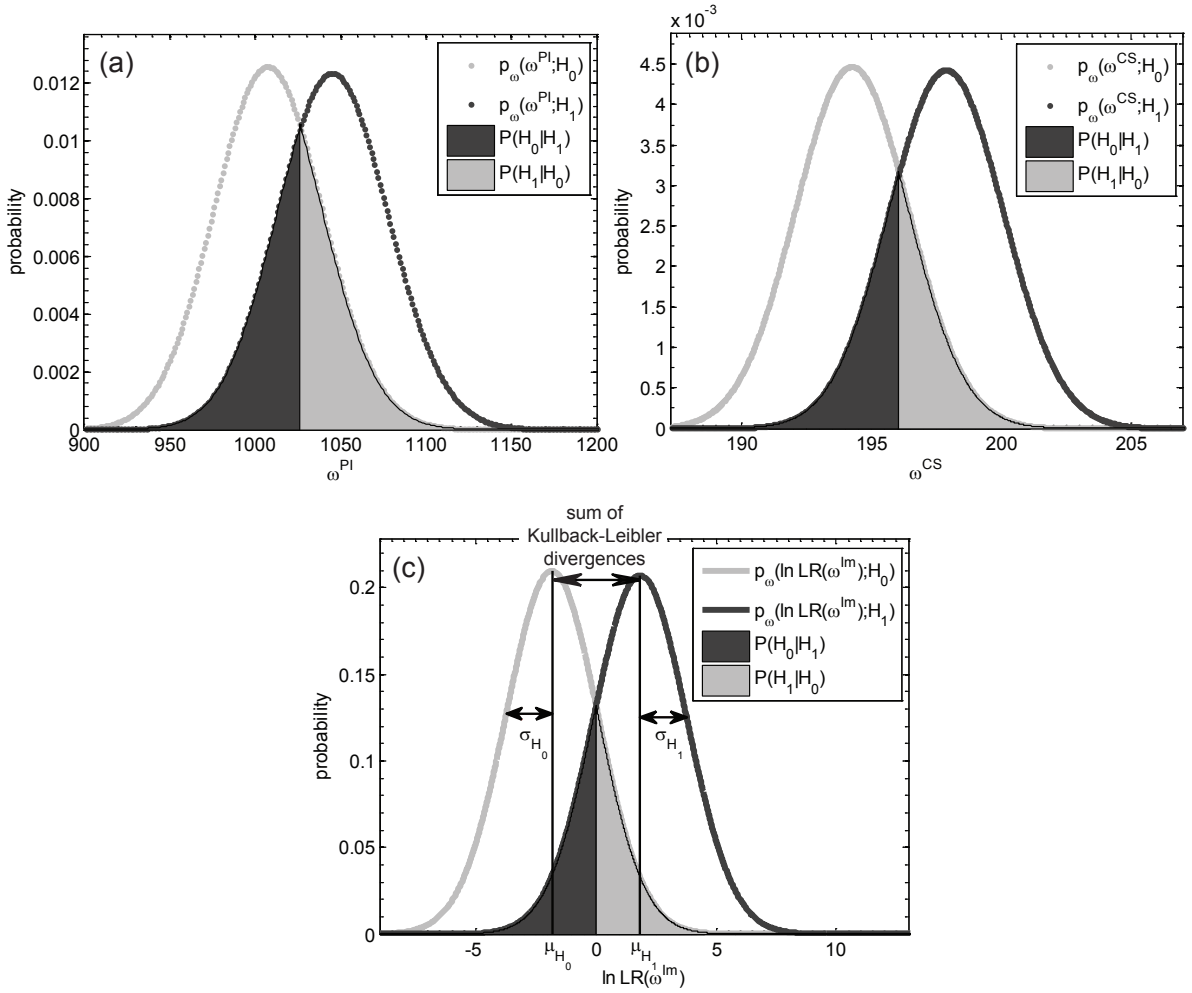

Figure 6.1: *Calculation of the probability of error for a binary hypothesis test for (a) peak intensities* ω^{PI} *(*$D = 10^6$ $e^-/Å^2$ *and* $n_{\mathcal{H}_0} = 15$*), (b) scattering cross-sections* ω^{CS} *(*$D = 10^5$ $e^-/Å^2$ *and* $n_{\mathcal{H}_0} = 30$*), and (c) images* ω^{Im} *(*$D = 10^5$ $e^-/Å^2$ *and* $n_{\mathcal{H}_0} = 30$*) of a Sr column with a detector collection range of* 60 − 100 mrad *and settings of Table 6.1 which are explained in subsection 6.4.3.*

way (Eq. (6.5)) [E 2013]:

$$\omega^{\mathrm{CS}} = \sum_{k=1}^{K} \sum_{l=1}^{L} \omega_{kl} \cdot \Delta x^2. \tag{6.11}$$

Voronoi cells are used to define the integration area for the computation of the scattering cross-sections. A Voronoi cell of an atomic column is the cell formed by the perpendicular bisectors of the direct connections to the neighbouring columns. This definition of the scattering cross-sections is used here for simplicity as the scattering cross-section values can directly be calculated from the simulated STEM images in this way, since the positions of the atomic columns are known from the simulation. The computed values from the integration of the Voronoi cells are equivalent to volumes under the estimated Gaussian peaks at atomic column positions as used in the previous chapters. The use of the volumes provides some extra advantages, since the parametric model takes into account overlap between neighbouring atomic columns. The

use of scattering cross-sections from the integration of Voronoi cells is afforded here, since there are no thickness variations in the simulations.
The expected scattering cross-section value equals:

$$\mathbb{E}_{\mathcal{H}_0}\left[\omega^{\mathrm{CS}}\right] = \sum_{k=1}^{K}\sum_{l=1}^{L} \lambda_{\mathcal{H}_0;kl} \cdot \Delta x^2 = \mathrm{CS}_n \tag{6.12}$$

$$\mathbb{E}_{\mathcal{H}_1}\left[\omega^{\mathrm{CS}}\right] = \sum_{k=1}^{K}\sum_{l=1}^{L} \lambda_{\mathcal{H}_1;kl} \cdot \Delta x^2 = \mathrm{CS}_{n+1} \tag{6.13}$$

where $\lambda_{\mathcal{H}_i,kl} = \mathbb{E}_{\mathcal{H}_i}[\omega_{kl}]$ corresponds to the expectation values for the pixel intensities of the STEM image of the atomic column and CS_n is the expected scattering cross-section for n atoms. Since a sum of independent Poisson distributed variables is known to be Poisson distributed [Mood 1974], the variable

$$\sum_{k=1}^{K}\sum_{l=1}^{L} \omega_{kl} \tag{6.14}$$

is therefore also Poisson distributed. The expected value $\lambda_{\mathcal{H}_i}$ then equals:

$$\lambda_{\mathcal{H}_i} = \sum_{k=1}^{K}\sum_{l=1}^{L} \lambda_{\mathcal{H}_i,kl}. \tag{6.15}$$

The conditional probability function for a scattering cross-section taking into account the constant factor Δx^2, is then given by:

$$p\left(\omega^{\mathrm{CS}};\mathcal{H}_i\right) = \frac{\left(\lambda_{\mathcal{H}_i}\right)^{\omega^{\mathrm{CS}}/\Delta x^2}}{\left(\frac{\omega^{\mathrm{CS}}}{\Delta x^2}\right)!} \exp\left(-\lambda_{\mathcal{H}_i}\right). \tag{6.16}$$

Analogous to the decision rule for the peak intensities of Eq. (6.8), one should decide $\mathcal{H}_1$ for a specific observed scattering cross-section w^{CS} when assuming equal prior probabilities $P(\mathcal{H}_0) = P(\mathcal{H}_1) = 1/2$ if

$$p\left(w^{\mathrm{CS}};\mathcal{H}_1\right) > p\left(w^{\mathrm{CS}};\mathcal{H}_0\right) \tag{6.17}$$

otherwise $\mathcal{H}_0$ is decided. This decision rule and the calculation of the probability function given by Eq. (6.16) is illustrated in Fig. 6.1(b). The probability of error is then reformulated as follows for the scattering cross-sections:

$$\begin{aligned} P_{\mathrm{e}} =& \frac{1}{2}P\left(\mathcal{H}_0|\mathcal{H}_1\right) + \frac{1}{2}P\left(\mathcal{H}_1|\mathcal{H}_0\right) \\ =& \frac{1}{2}F\left(\frac{x^{\mathrm{CS}}}{\Delta x^2};\lambda_{\mathcal{H}_1}\right) + \frac{1}{2}\left[1 - F\left(\frac{x^{\mathrm{CS}}}{\Delta x^2};\lambda_{\mathcal{H}_0}\right)\right] \end{aligned} \tag{6.18}$$

where $F\left(x^{\mathrm{CS}}/\Delta x^2;\lambda_{\mathcal{H}_i}\right)$ equals the Poisson cumulative distribution function with parameter $\lambda_{\mathcal{H}_i}$ evaluated at $x^{\mathrm{CS}}/\Delta x^2$ and x^{CS} is the intersection of the two probability functions $p\left(\omega^{\mathrm{CS}};\mathcal{H}_0\right)$ and $p\left(\omega^{\mathrm{CS}};\mathcal{H}_1\right)$ given by:

$$x^{\mathrm{CS}} = \frac{\left(\lambda_{\mathcal{H}_0} - \lambda_{\mathcal{H}_1}\right)\Delta x^2}{\ln\frac{\lambda_{\mathcal{H}_0}}{\lambda_{\mathcal{H}_1}}}. \tag{6.19}$$

6.2.3 STEM images

As a third measure to count the number of atoms, the STEM images of the atomic columns are considered. When assuming that the pixels in a STEM image are statistically independent electron counting results, the conditional probability function for a STEM image of an atomic column is given by:

$$p\left(\boldsymbol{\omega}^{\mathrm{Im}};\mathcal{H}_i\right)=\prod_{k=1}^{K}\prod_{l=1}^{L}\frac{\left(\lambda_{\mathcal{H}_i,kl}\right)^{\omega_{kl}}}{\omega_{kl}!}\exp\left(-\lambda_{\mathcal{H}_i,kl}\right). \tag{6.20}$$

Since the stochastic variable $\boldsymbol{\omega}^{\mathrm{Im}}$ of the STEM image of an atomic column is characterised by a *joint* probability function, it is not possible to compute the probability of error directly from the overlapping areas of $p\left(\boldsymbol{\omega}^{\mathrm{Im}};\mathcal{H}_0\right)$ and $p\left(\boldsymbol{\omega}^{\mathrm{Im}};\mathcal{H}_1\right)$. However, as shown in [Gonnissen 2014], it is possible to calculate this probability of error analytically by reformulating the decision rule using the so-called log-likelihood ratio $\ln \mathrm{LR}\left(\boldsymbol{\omega}^{\mathrm{Im}}\right)$. After reformulation of Eq. (6.3), one should then decide $\mathcal{H}_1$ for an observation $\mathbf{w}^{\mathrm{Im}}$, if:

$$\ln \mathrm{LR}\left(\boldsymbol{w}^{\mathrm{Im}}\right)\equiv \ln\left(\frac{p\left(\boldsymbol{w}^{\mathrm{Im}};\mathcal{H}_1\right)}{p\left(\boldsymbol{w}^{\mathrm{Im}};\mathcal{H}_0\right)}\right)>\ln(1)=0, \tag{6.21}$$

otherwise $\mathcal{H}_0$ is decided, for equal prior probabilities. This corresponds to choosing the hypothesis for which the log-likelihood function is maximal. The function $\mathrm{LR}\left(\boldsymbol{\omega}^{\mathrm{Im}}\right)$ is called the likelihood function since it indicates for each set of observations of $\boldsymbol{\omega}^{\mathrm{Im}}$ the likelihood of $\mathcal{H}_1$ versus the likelihood of $\mathcal{H}_0$. Given the decision rule of Eq. (6.21), the expression for the probability of error P_{e} given by Eq. (6.2), can be rewritten as follows:

$$\begin{aligned}P_{\mathrm{e}}=&\frac{1}{2}P\left(\mathcal{H}_0|\mathcal{H}_1\right)+\frac{1}{2}P\left(\mathcal{H}_1|\mathcal{H}_0\right)\\ =&\frac{1}{2}P\left(\ln \mathrm{LR}\left(\boldsymbol{\omega}^{\mathrm{Im}}\right)<0|\mathcal{H}_1\right)+\frac{1}{2}P\left(\ln \mathrm{LR}\left(\boldsymbol{\omega}^{\mathrm{Im}}\right)>0|\mathcal{H}_0\right).\end{aligned} \tag{6.22}$$

When using the conditional joint probability function for STEM images given by Eq. (6.20), the log-likelihood ratio defined by Eq. (6.21) can be rewritten as:

$$\begin{aligned}\ln \mathrm{LR}\left(\boldsymbol{\omega}^{\mathrm{Im}}\right)&=\sum_{k=1}^{K}\sum_{l=1}^{L}\ln\left(\frac{\lambda_{\mathcal{H}_1,kl}^{\omega_{kl}}\exp\left(-\lambda_{\mathcal{H}_1,kl}\right)}{\lambda_{\mathcal{H}_0,kl}^{\omega_{kl}}\exp\left(-\lambda_{\mathcal{H}_0,kl}\right)}\right)\\ &=\sum_{k=1}^{K}\sum_{l=1}^{L}\ln\left(\lambda_{\mathcal{H}_1,kl}^{\omega_{kl}}\right)-\lambda_{\mathcal{H}_1,kl}-\ln\left(\lambda_{\mathcal{H}_0,kl}^{\omega_{kl}}\right)+\lambda_{\mathcal{H}_0,kl}\\ &=\sum_{k=1}^{K}\sum_{l=1}^{L}\left(\omega_{kl}\ln\left(\frac{\lambda_{\mathcal{H}_1,kl}}{\lambda_{\mathcal{H}_0,kl}}\right)-\lambda_{\mathcal{H}_1,kl}+\lambda_{\mathcal{H}_0,kl}\right).\end{aligned} \tag{6.23}$$

Following the central limit theorem, the log-likelihood ratio tends to be normally distributed:

$$p\left(\ln \mathrm{LR}\left(\boldsymbol{\omega}^{\mathrm{Im}}\right);\mathcal{H}_i\right)=\frac{1}{\sigma_{\mathcal{H}_i}\sqrt{2\pi}}\exp\left(-\frac{\left(\ln \mathrm{LR}\left(\boldsymbol{\omega}^{\mathrm{Im}}\right)-\mu_{\mathcal{H}_i}\right)^2}{2\sigma_{\mathcal{H}_i}^2}\right). \tag{6.24}$$

For STEM images the expected value and variance characterising this normal distribution of $\ln \mathrm{LR}\left(\boldsymbol{\omega}^{\mathrm{Im}}\right)$ can be computed from Eq. (6.24) when assuming $\mathcal{H}_i$ to be true giving the following results:

$$\begin{aligned}\mu_{\mathcal{H}_i} =& \mathbb{E}_{\mathcal{H}_i}\left[\ln \mathrm{LR}\left(\boldsymbol{\omega}^{\mathrm{Im}}\right)\right] \\ =& \sum_{k=1}^{K}\sum_{l=1}^{L}\left(\lambda_{\mathcal{H}_i,kl}\ln\frac{\lambda_{\mathcal{H}_1,kl}}{\lambda_{\mathcal{H}_0,kl}} - \lambda_{\mathcal{H}_1,kl} + \lambda_{\mathcal{H}_0,kl}\right), \end{aligned} \tag{6.25}$$

$$\sigma^2_{\mathcal{H}_i} = \mathrm{var}_{\mathcal{H}_i}\left[\ln \mathrm{LR}\left(\boldsymbol{\omega}^{\mathrm{Im}}\right)\right] = \sum_{k=1}^{K}\sum_{l=1}^{L}\lambda_{\mathcal{H}_i,kl}\left(\ln\frac{\lambda_{\mathcal{H}_1,kl}}{\lambda_{\mathcal{H}_0,kl}}\right)^2. \tag{6.26}$$

In this derivation, use is made of the property that the variance of a Poisson distributed variable equals its expectation value, $\mathbb{E}_{\mathcal{H}_i}[\omega_{kl}] = \mathrm{var}_{\mathcal{H}_i}[\omega_{kl}] = \lambda_{\mathcal{H}_i,kl}$. The explicit description of the distribution of the log-likelihood ratio now enables us to unambiguously compute the probability of error given by Eq. (6.22), resulting in the following general expression:

$$P_{\mathrm{e}} = \frac{1}{2}\left[\Phi\left(\frac{-\mu_{\mathcal{H}_1}}{\sigma_{\mathcal{H}_1}}\right) + \Phi\left(\frac{\mu_{\mathcal{H}_0}}{\sigma_{\mathcal{H}_0}}\right)\right] \tag{6.27}$$

with $\Phi(\pm\mu/\sigma)$ the cumulative distribution function of the standard normal distribution evaluated at $\pm\mu/\sigma$. The meaning of the expected value $\mu_{\mathcal{H}_i}$ and variance $\sigma^2_{\mathcal{H}_i}$ characterising the normal distributions of $\ln \mathrm{LR}\left(\boldsymbol{\omega}^{\mathrm{Im}}\right)$ given by Eq. (6.24) under both hypotheses is illustrated in Fig. 6.1(c) based on STEM images for a Sr column consisting of either 30 or 31 atoms. The decision rule is also clarified: $\mathcal{H}_0$ is decided for $\ln \mathrm{LR}\left(\boldsymbol{\omega}^{\mathrm{Im}}\right) < 0$, otherwise $\mathcal{H}_1$ is decided to be correct. The dark grey region denotes the error which is made if $\mathcal{H}_0$ is chosen while $\mathcal{H}_1$ is correct, and vice versa for the light grey region. It is clear from this figure that the probability of error also here corresponds to the overlap between both distributions.

6.2.4 Sum of Kullback-Leibler divergences

A tightly connected performance measure that can be investigated as an alternative for the probability of error is based on the so-called Kullback-Leibler divergence [Kullback 1951, Kullback 1959]. This measure quantifies the difference between two probability distributions and can be defined for peak intensities, scattering cross-sections and STEM images. Here, the Kullback-Leibler divergence will be discussed for a general stochastic variable ω, which can be replaced by the one of the corresponding stochastic variables for peak intensities, scattering cross-sections or STEM images, respectively. The Kullback-Leibler divergence from $p_{\mathcal{H}_1} = p(\omega;\mathcal{H}_1)$ to $p_{\mathcal{H}_0} = p(\omega;\mathcal{H}_0)$ is defined as:

$$D\left(p_{\mathcal{H}_1}, p_{\mathcal{H}_0}\right) \equiv \mathbb{E}_{p_{\mathcal{H}_1}}\left[\ln\frac{p(\omega;\mathcal{H}_1)}{p(\omega;\mathcal{H}_0)}\right] = \mathbb{E}_{p_{\mathcal{H}_1}}\left[\ln \mathrm{LR}(\omega)\right] \tag{6.28}$$

where $\ln \mathrm{LR}(\omega)$ corresponds to the log-likelihood ratio as defined in Eq. (6.21) for the STEM images. This log-likelihood ratio can in the same way be defined for the peak intensities and scattering cross-sections using their respective probability functions. The Kullback-Leibler divergence from $p_{\mathcal{H}_1}$ to $p_{\mathcal{H}_0}$ of Eq. (6.28) corresponds to the expected or mean log-likelihood ratio

assuming $\mathcal{H}_1$ to be true. Similarly the Kullback-Leibler divergence from $p_{\mathcal{H}_0}$ to $p_{\mathcal{H}_1}$ equals:

$$\begin{aligned} D\left(p_{\mathcal{H}_0}, p_{\mathcal{H}_1}\right) =& \mathbb{E}_{p_{\mathcal{H}_0}}\left[\ln \frac{p\left(\omega; \mathcal{H}_0\right)}{p\left(\omega; \mathcal{H}_1\right)}\right] \\ =& -\mathbb{E}_{p_{\mathcal{H}_0}}\left[\ln \frac{p\left(\omega; \mathcal{H}_1\right)}{p\left(\omega; \mathcal{H}_0\right)}\right] = -\mathbb{E}_{p_{\mathcal{H}_0}}\left[\ln \mathrm{LR}(\omega)\right]. \end{aligned} \tag{6.29}$$

From Eqs. (6.28) and (6.29), it follows that:

$$D\left(p_{\mathcal{H}_1}, p_{\mathcal{H}_0}\right) + D\left(p_{\mathcal{H}_0}, p_{\mathcal{H}_1}\right) = \mathbb{E}_{p_{\mathcal{H}_1}}\left[\ln \mathrm{LR}(\omega)\right] - \mathbb{E}_{p_{\mathcal{H}_0}}\left[\ln \mathrm{LR}(\omega)\right]. \tag{6.30}$$

The sum of Kullback-Leibler divergences thus corresponds to the difference in mean log-likelihood ratio under $\mathcal{H}_1$ and the corresponding value when assuming $\mathcal{H}_0$ to be true. An illustration for the sum of Kullback-Leibler divergences is also given by Fig. 6.1(c), where the distance between $\mu_{\mathcal{H}_0}$ and $\mu_{\mathcal{H}_1}$ corresponds to the sum of Kullback-Leibler divergences for STEM images. The sum of Kullback-Leibler divergences only takes into account the separations between the distributions of the log-likelihood ratio whereas the probability of error also takes into account the width of the distributions. Since the width and the separation between the distributions are related as will be shown for the scattering cross-sections in subsection 6.4.2, it is likely to assume that the probability to assign the wrong hypothesis will decrease when the sum of Kullback-Leibler divergences increases.
Using a linear imaging model, the sum of Kullback-Leibler divergences enables us to derive analytical expressions as a function of experimental parameters such as incident electron dose N_d and number of atoms $n_{\mathcal{H}_0}$ considered in the imaging model. These expressions, discussed in subsection 6.4.1 can be used to have more physical insight on how the probability of error depends on these parameters. A more explicit expression for Eq. (6.30) can be derived using Eq. (6.23):

$$D\left(p_{\mathcal{H}_1}, p_{\mathcal{H}_0}\right) + D\left(p_{\mathcal{H}_0}, p_{\mathcal{H}_1}\right) = \left(\mathbb{E}_{\mathcal{H}_1}[\omega] - \mathbb{E}_{\mathcal{H}_0}[\omega]\right)\left(\ln \mathbb{E}_{\mathcal{H}_1}[\omega] - \ln \mathbb{E}_{\mathcal{H}_0}[\omega]\right). \tag{6.31}$$

6.3 Detection theory: Multiple hypothesis testing

A binary hypothesis test is no longer adequate if different choices of the two hypotheses lead to different designs. Therefore, the approach of binary hypothesis testing for atom-counting is extended toward multiple hypothesis testing. The multiple hypothesis test will be described for the scattering cross-sections, which are most optimal for atom-counting applications. The number of hypotheses in the multiple hypothesis test equals the maximum number of atoms in a projected atomic column which depends on the sample under study. In this case, a differentiation between $1, 2, \ldots, M$ atoms in a projected atomic column should be made and therefore one should decide among M possible hypotheses:

$$\{\mathcal{H}_0, \mathcal{H}_1, \ldots, \mathcal{H}_{M-1}\}. \tag{6.32}$$

In practice, the number of hypotheses that is included for the decision rule is chosen sufficiently large such that the observed scattering cross-sections for sure correspond to one of the considered hypotheses; M will typically be larger than the unknown thickness of the sample.

Equivalent to Eq. (6.3), the decision rule is now defined such that the probability of error is minimised. The minimum probability of error decision rule is then to decide $\mathcal{H}_k$ if:

$$p\left(w^{\mathrm{CS}};\mathcal{H}_k\right)P\left(\mathcal{H}_k\right) > p\left(w^{\mathrm{CS}};\mathcal{H}_i\right)P\left(\mathcal{H}_i\right) \qquad \forall i \neq k. \tag{6.33}$$

For equal prior probabilities $P\left(\mathcal{H}_i\right) = 1/M$, which is assumed here, one should decide $\mathcal{H}_k$ if:

$$p\left(w^{\mathrm{CS}};\mathcal{H}_k\right) > p\left(w^{\mathrm{CS}};\mathcal{H}_i\right) \qquad \forall i \neq k. \tag{6.34}$$

An illustration of the conditional probability functions of a multiple hypothesis test consisting of $M = 30$ hypotheses is given in Fig. 6.2. Analogously to the binary test of subsection 6.2.2, the probability of error for the scattering cross-sections of a multiple hypothesis test can be calculated from the overlapping areas of the conditional probability functions (weighted by their prior probability):

$$P_{\mathrm{e}} = \sum_{i=0}^{M-1}\sum_{j=0}^{M-1} C_{ij} P\left(\mathcal{H}_i|\mathcal{H}_j\right)P\left(\mathcal{H}_j\right), \tag{6.35}$$

where

$$C_{ij} = \begin{cases} 1 & i \neq j \\ 0 & i = j \end{cases}. \tag{6.36}$$

The number of terms for the calculation of the probability of error of a multiple hypothesis test used in Eq. (6.35) equals $M(M-1)$. Therefore, it is more efficient to calculate $P_{\mathrm{c}} = 1 - P_{\mathrm{e}}$, where P_{c} is the probability of a correct decision. In this case, the number of terms in the summation reduces to M:

$$P_{\mathrm{c}} = \sum_{i=0}^{M-1} P\left(\mathcal{H}_i|\mathcal{H}_i\right)P\left(\mathcal{H}_i\right). \tag{6.37}$$

This expression can be calculated analytically for the scattering cross-sections, since their conditional probability functions are well-known from Eq. (6.16). The probability of a correct decision for equal prior probabilities $P\left(\mathcal{H}_i\right) = 1/M$ then corresponds to:

$$\begin{aligned} P_{\mathrm{c}} = \frac{1}{M}\Bigg[& F\left(\frac{x^{CS_{0,1}}}{\Delta x^2}, \lambda_{\mathcal{H}_0^s}\right) \\ & + F\left(\frac{x^{CS_{1,2}}}{\Delta x^2}, \lambda_{\mathcal{H}_1^s}\right) - F\left(\frac{x^{CS_{1,0}}}{\Delta x^2}, \lambda_{\mathcal{H}_1^s}\right) \\ & + F\left(\frac{x^{CS_{2,3}}}{\Delta x^2}, \lambda_{\mathcal{H}_2^s}\right) - F\left(\frac{x^{CS_{2,1}}}{\Delta x^2}, \lambda_{\mathcal{H}_2^s}\right) \\ & + \ldots \\ & + \left(1 - F\left(\frac{x^{CS_{M-1,M-2}}}{\Delta x^2}, \lambda_{\mathcal{H}_{M-1}^s}\right)\right)\Bigg] \end{aligned} \tag{6.38}$$

where $\mathcal{H}_i^s$ denotes the sorted hypotheses according to the expected values of the scattering cross-sections, $x^{\mathrm{CS}_{ij}} = x^{\mathrm{CS}_{ji}}$ corresponds to the intersection between two neighbouring probability distribution functions which is given by Eq. (6.19), $\lambda_{\mathcal{H}_i}$ corresponds to Eq. (6.15), and

$F\left(x^{\mathrm{CS}_{ij}}/\Delta x^2, \lambda_{\mathcal{H}_i^s}\right)$ equals the Poisson cumulative distribution function with parameter $\lambda_{\mathcal{H}_i^s}$ evaluated at $x^{\mathrm{CS}_{ij}}/\Delta x^2$. This allows us to calculate analytically the probability of error P_e for atom-counting. For a multiple hypothesis test with M different hypotheses the maximum value for the probability of error equals $(M-1)/M$. This can be derived from the fact that when the decision for a certain hypothesis between M different hypotheses is completely random, the probability for a correct decision equals $1/M$ when assuming equal prior probabilities.
The probability of error and optimal experiment design can now be investigated for a a simplified model and a realistic simulation experiment, using the analytical expressions for the probability of error for both the binary and the multiple hypothesis test. The obtained results for the proposed measures (peak intensities, scattering cross-sections, or STEM images) will be compared.

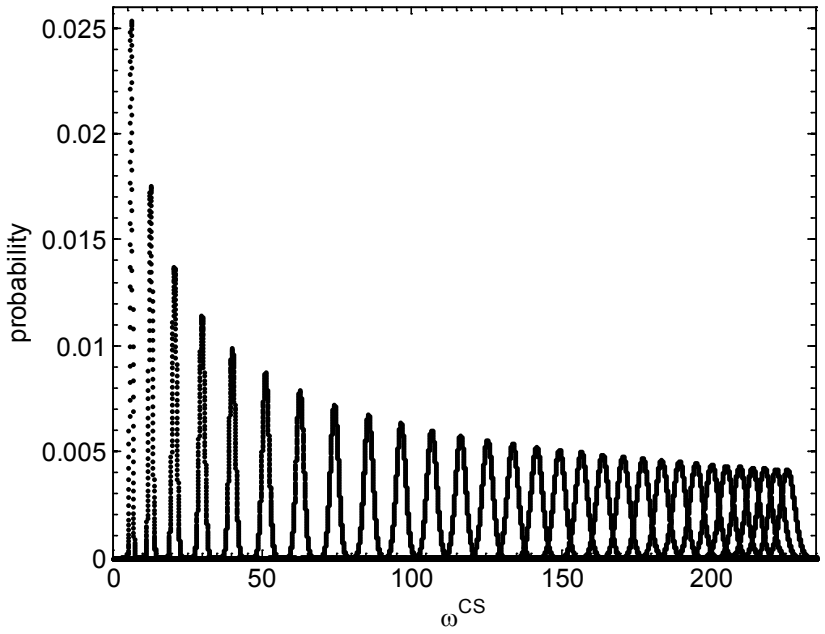

Figure 6.2: *Conditional probability functions for a multiple hypothesis test of* $M = 30$ *for a Sr column with* $D = 10^5\ e^-/\text{Å}^2$*, for a detector collection range of* $60 - 100$ mrad *and settings of Table 6.1 which are explained in subsection 6.4.3.*

6.4 Optimal experiment design

6.4.1 Analytical derivation for linear imaging model

In this subsection, the sum of Kullback-Leibler divergences and the probability of error for a binary hypothesis test will be studied for a linear imaging model, i.e. a simple Gaussian model that linearly increases with the number of atoms in the projected atomic column. The analysis here will be done for the three different measures: STEM images, scattering cross-sections, and peak intensities. Distinguishing between n and $n+1$ atoms can be formulated as a binary

hypothesis test as in Eq. (6.1). An isolated atomic column is considered for the linear imaging model. The parameters of the Gaussian model corresponding to a single atom equal $\rho = 0.5$ Å and $\eta = 1$. This Gaussian shape has been simulated in the centre of a two-dimensional grid consisting of $K \times L = 21 \times 21$ pixels having a pixel size $\Delta x = \Delta y = 0.2$ Å. This simulation then corresponds to the fraction of intensity with respect to the incoming electron beam of a single atom in a projected atomic column. This building block ΔI_{kl} for the linear imaging model is illustrated in Fig. 6.3. The sum of Kullback-Leibler divergences and probability of error can be calculated analytically for this model for the three different measures.

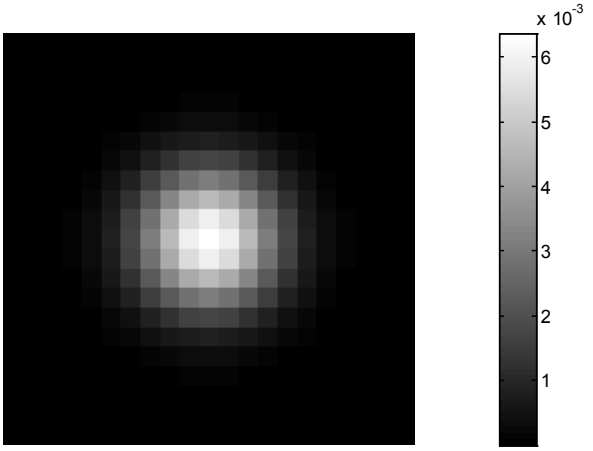

Figure 6.3: *Building block of the linear imaging model. Normalised intensity for 1 atom in a projected atomic column ΔI_{kl}.*

Peak intensities

For the linear imaging model, the expected value for the peak intensities $\lambda^{\mathrm{PI}}_{\mathcal{H}_i}$ can be reformulated as follows:

$$\mathbb{E}_{\mathcal{H}_i}\left[\omega^{\mathrm{PI}}\right] = \lambda^{\mathrm{PI}}_{\mathcal{H}_i} = N_p n_{\mathcal{H}_i} \Delta I^{\mathrm{PI}} \tag{6.39}$$

where N_p denotes the incident electron dose per pixel and ΔI^{PI} the pixel value at the position of the atomic column of the simulated Gauss corresponding to a single atom, i.e. the increase in peak intensity for a single atom. The sum of Kullback-Leibler divergences given by Eq. (6.31) then equals:

$$\begin{aligned} D\left(p_{\mathcal{H}_1}, p_{\mathcal{H}_0}\right) + D\left(p_{\mathcal{H}_0}, p_{\mathcal{H}_1}\right) =& \left(N_p n_{\mathcal{H}_1} \Delta I^{\mathrm{PI}} - N_p n_{\mathcal{H}_0} \Delta I^{\mathrm{PI}}\right)\left(\ln\left(N_p n_{\mathcal{H}_1} \Delta I^{\mathrm{PI}}\right) - \ln\left(N_p n_{\mathcal{H}_0} \Delta I^{\mathrm{PI}}\right)\right) \\ =& N_p \Delta I^{\mathrm{PI}}\left(n_{\mathcal{H}_1} - n_{\mathcal{H}_0}\right) \ln\left(\frac{n_{\mathcal{H}_1}}{n_{\mathcal{H}_0}}\right). \end{aligned} \tag{6.40}$$

For the detection of the difference of a single atom, the expression for the sum of Kullback-Leibler divergences reduces to:

$$D\left(p_{\mathcal{H}_1}, p_{\mathcal{H}_0}\right) + D\left(p_{\mathcal{H}_0}, p_{\mathcal{H}_1}\right) = N_p \Delta I^{\mathrm{PI}} \ln\left(\frac{n+1}{n}\right). \tag{6.41}$$

This expression linearly depends on the incident electron dose per pixel N_p and the intensity increase for a single atom ΔI^{PI} at the atomic column position. The intensity increase for a single atom ΔI^{PI} at the atomic column position for the linear imaging model as described in Eq. (6.39), depends on the atomic type Z and the STEM imaging conditions including the probe settings and detector angles. The dependence of the number of atoms is determined by $\ln(n + 1/n)$. This function decreases for an increasing number of atoms n.
The probability of error for the peak intensities is defined by Eq. (6.9) and takes also into account the width of the probability distribution. The expected value (and variance) of the peak intensities for the linear model having a conditional probability function given by Eq. (6.7) equals Eq. (6.39). The intersection x^{PI} between both probability distributions given by Eq. (6.10) for the linear model equals:

$$x^{\mathrm{PI}} = N_p \Delta I^{\mathrm{PI}} \frac{n_{\mathcal{H}_0} - n_{\mathcal{H}_1}}{\ln \frac{n_{\mathcal{H}_0}}{n_{\mathcal{H}_1}}} = \frac{N_p \Delta I^{\mathrm{PI}}}{\ln \frac{n+1}{n}}. \tag{6.42}$$

Scattering cross-sections

Similar to the derivation of the sum of Kullback-Leibler divergences and the probability of error for the peak intensities, these measures can be defined for the scattering cross-sections. The expected scattering cross-section for the linear imaging model following Eqs. (6.12) and (6.13) is given by:

$$\mathbb{E}_{\mathcal{H}_0}\left[\omega^{\mathrm{CS}}\right] = \mathrm{CS}_n = \sum_{k=1}^{L}\sum_{l=1}^{L} N_p n_{\mathcal{H}_0} \Delta I_{kl} \Delta x^2 = N_p n_{\mathcal{H}_0} \Delta \mathrm{CS} \tag{6.43}$$

$$\mathbb{E}_{\mathcal{H}_1}\left[\omega^{\mathrm{CS}}\right] = \mathrm{CS}_{n+1} = \sum_{k=1}^{L}\sum_{l=1}^{L} N_p n_{\mathcal{H}_1} \Delta I_{kl} \Delta x^2 = N_p n_{\mathcal{H}_1} \Delta \mathrm{CS} \tag{6.44}$$

where ΔI_{kl} is the increase in intensity relative to the incident electron beam of the STEM image at pixel (k, l) for a single atom and ΔCS corresponds to the normalised scattering cross-section for a single atom, i.e. the increase in scattering cross-section for a single atom. The sum of Kullback-Leibler divergences for the scattering cross-sections using the linear imaging model is given by:

$$\begin{aligned} D(p_{\mathcal{H}_1}, p_{\mathcal{H}_0}) + D(p_{\mathcal{H}_0}, p_{\mathcal{H}_1}) =& \left(N_p n_{\mathcal{H}_1} \Delta \mathrm{CS} - N_p n_{\mathcal{H}_0} \Delta \mathrm{CS}\right)\left(\ln\left(N_p n_{\mathcal{H}_1} \Delta \mathrm{CS}\right) - \ln\left(N_p n_{\mathcal{H}_0} \Delta \mathrm{CS}\right)\right) \\ =& N_p \Delta \mathrm{CS}\,(n_{\mathcal{H}_1} - n_{\mathcal{H}_0}) \ln\left(\frac{n_{\mathcal{H}_1}}{n_{\mathcal{H}_1}}\right). \end{aligned} \tag{6.45}$$

Also here, this expression can be rewritten for the detection of the difference of a single atom:

$$D(p_{\mathcal{H}_1}, p_{\mathcal{H}_0}) + D(p_{\mathcal{H}_0}, p_{\mathcal{H}_1}) = N_p \Delta \mathrm{CS} \ln\left(\frac{n+1}{n}\right). \tag{6.46}$$

This expression is similar to Eq. (6.41), but now linearly dependent of the increase in scattering cross-section for a single atom ΔCS instead of the image intensity increase for a single atom at the atomic column positions. The increase in scattering cross-section for a single atom ΔCS for

the linear imaging model as described in Eq. (6.44) also depends on the atomic type Z and the STEM imaging conditions such as the probe settings and detector angles.
The probability of error can be derived for the linear imaging model using Eq. (6.18). The expected value for the scattering cross-sections equals Eq. (6.44), where the scattering cross-sections have a probability function given by Eq. (6.16). The intersection between the two probability functions under $\mathcal{H}_0$ and $\mathcal{H}_1$ given by Eq. (6.19) is then given by:

$$x^{CS} = N_p \Delta \mathrm{CS} \frac{n_{\mathcal{H}_0} - n_{\mathcal{H}_1}}{\ln \frac{n_{\mathcal{H}_0}}{n_{\mathcal{H}_1}}} = \frac{N_p \Delta \mathrm{CS}}{\ln \frac{n+1}{n}}. \tag{6.47}$$

STEM image

Finally, the sum of Kullback-Leibler divergences and probability of error for the linear imaging model can be defined for STEM images. Here, the expected values at the pixel intensities (k, l) of the STEM image for the linear imaging model correspond to:

$$\mathbb{E}_{\mathcal{H}_i}[\omega_{kl}] = \lambda_{\mathcal{H}_i,kl} = N_p n_{\mathcal{H}_i} \Delta I_{kl}. \tag{6.48}$$

The sum of Kullback-Leibler divergences for the linear imaging model for the STEM images equals:

$$\begin{aligned} D(p_{\mathcal{H}_1}, p_{\mathcal{H}_0}) + D(p_{\mathcal{H}_0}, p_{\mathcal{H}_1}) &= \sum_{k=1}^{K} \sum_{l=1}^{L} \left(N_p n_{\mathcal{H}_1} \Delta I_{kl} - N_p n_{\mathcal{H}_0} \Delta I_{kl}\right) \left(\ln\left(N_p n_{\mathcal{H}_1} \Delta I_{kl}\right) - \ln\left(N_p n_{\mathcal{H}_0} \Delta I_{kl}\right)\right) \\ &= \sum_{k=1}^{K} \sum_{l=1}^{L} N_p \Delta I_{kl} \left(n_{\mathcal{H}_1} - n_{\mathcal{H}_0}\right) \ln\left(\frac{n_{\mathcal{H}_1}}{n_{\mathcal{H}_0}}\right) \\ &= N_p \frac{\Delta \mathrm{CS}}{\Delta x^2} \left(n_{\mathcal{H}_1} - n_{\mathcal{H}_0}\right) \ln\left(\frac{n_{\mathcal{H}_1}}{n_{\mathcal{H}_0}}\right). \end{aligned} \tag{6.49}$$

In the last line, the increase in scattering cross-section for a single atom as defined in Eq. (6.44) is introduced. Like for the peak intensities and the scattering cross-sections, also here the expression for the sum of Kullback-Leibler divergences is rewritten for detecting the difference of a single atom:

$$D(p_{\mathcal{H}_1}, p_{\mathcal{H}_0}) + D(p_{\mathcal{H}_0}, p_{\mathcal{H}_1}) = N_p \frac{\Delta \mathrm{CS}}{\Delta x^2} \ln\left(\frac{n+1}{n}\right). \tag{6.50}$$

The sum of Kullback-Leibler divergences for the STEM images depends on the scattering cross-sections and the magnification via the pixel size Δx.
The probability of error for the STEM images is given by Eq. (6.27). Whereas the sum of Kullback-Leibler divergences quantifies the distance between the two expected log-likelihood ratios, the probability of error quantifies the overlapping area between the distributions of the two log-likelihood ratios. The mean and variance of the normally distributed log-likelihood ratio are given by Eqs. (6.25) and (6.26):

$$\mu_{\mathcal{H}_i} = \sum_{k=1}^{K} \sum_{l=1}^{L} \left(\lambda_{\mathcal{H}_i,kl} \ln \frac{\lambda_{\mathcal{H}_1,kl}}{\lambda_{\mathcal{H}_0,kl}} - \lambda_{\mathcal{H}_1,kl} + \lambda_{\mathcal{H}_0,kl}\right)$$

$$= N_p n_{\mathcal{H}_i} \frac{\Delta \mathrm{CS}}{\Delta x^2} \ln \frac{n+1}{n} - \frac{N_p \Delta \mathrm{CS}}{\Delta x^2} \tag{6.51}$$

$$\sigma^2_{\mathcal{H}_i} = \sum_{k=1}^{K} \sum_{l=1}^{L} \lambda_{\mathcal{H}_i,kl} \left(\ln \frac{\lambda_{\mathcal{H}_1,kl}}{\lambda_{\mathcal{H}_0,kl}} \right)^2$$

$$= N_p n_{\mathcal{H}_i} \frac{\Delta \mathrm{CS}}{\Delta x^2} \left(\ln \frac{n+1}{n} \right)^2 . \tag{6.52}$$

The difference of the expected values of the log-likelihood ratio of Eq. (6.51) again corresponds to the sum of Kullback-Leibler divergences as derived in Eq. (6.50).

Discussion of the results

The analytical expressions of the sum of Kullback-Leibler divergences given by Eqs. (6.41), (6.46), and (6.50) and the probability of error for equal prior probabilities given by Eqs. (6.9), (6.18), and (6.27) for the linear imaging model will be used to calculate these measures as a function of the number of atoms and the incident electron dose. The results of this analysis are shown in Figs. 6.4 and 6.5. Fig. 6.4 shows the sum of Kullback-Leibler divergences and the probability of error as a function of the number of atoms $n_{\mathcal{H}_0}$ for an incident electron dose of 10^4 $e^-/\text{Å}^2$. In Fig. 6.5 the sum of Kullback-Leibler divergences and the probability of error is shown as a function of the incident electron dose for $n_{\mathcal{H}_0} = 10$ atoms. From these figures, it is clear that when the sum of Kullback-Leibler divergences increases, the probability of error decreases. Although, the analytical expressions of the Kullback-Leibler divergences are more easily to interpret as compared to the expressions for the probability of error, it can be seen from Figs. 6.4 and 6.5 that it is necessary to include the overlap of the distributions to compare different measures (peak intensities, scattering cross-sections, and STEM images) mutually. From Figs. 6.4(b) and 6.5(b) it can be concluded that the scattering cross-sections perform equally well as the STEM images and prove more robust than peak intensities, whereas this conclusion could not be drawn from the sum of Kullback-Leibler divergences shown in Figs. 6.4(a) and 6.5(a). This can also be seen from Eqs. (6.46) and (6.50) for the sum of Kullback-Leibler divergences where an extra factor $1/\Delta x^2$ is present in the expression for the STEM images. This explains the higher value of the sum of Kullback-Leibler divergences for the STEM images. For the calculation of probability of error, the width of the probability distributions is also taken into account. The increased width of the probability distributions for the STEM images compensates the increased distance between the distributions. As such, the probability of error for the scattering cross-sections equals the probability of error for the STEM images.
The probability of error increases with the number of atoms as can be seen from Fig. 6.4(b), meaning that it is easier to differentiate e.g. between 1 and 2 atoms as compared to 20 and 21 atoms. As expected, the probability of error decreases for an increasing incident electron dose as shown in Fig. 6.5(b). Figs. 6.4(b) and 6.5(b) can be combined into one summarising graph, where the probability of error is shown for different levels as a function of the number of atoms and the incident electron dose. This graph is shown in Fig. 6.6 for the scattering cross-sections or STEM images. From this figure, the minimally required incident electron dose for a certain probability of error can be deduced for a certain number of atoms.
In this subsection, a preliminary example for the probability error for atom-counting for a linear imaging model has been discussed. In the following subsections, the probability of error

will be calculated for realistic detailed STEM simulations. The sum of Kullback-Leibler divergences will no longer be considered since it has been shown for this preliminary example that the probability of error provides us a better insight into the precision that can be obtained for atom-counting.

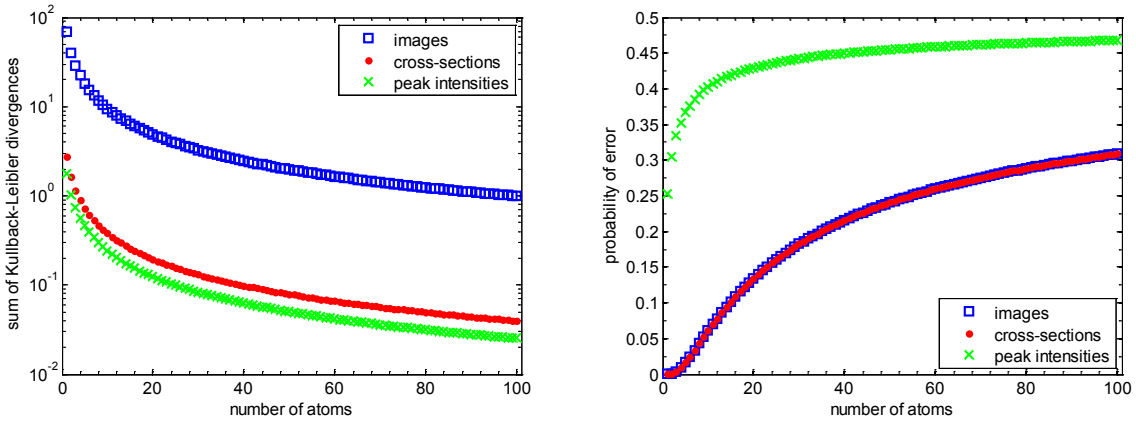

(a) sum of Kullback-Leibler divergences (b) probability of error

Figure 6.4: *Sum of Kullback-Leibler divergences and probability of error as a function of the number of atoms $n_{\mathcal{H}_0}$ in a projected atomic column for STEM images (blue squares), scattering cross-sections (red dots), and peak intensities (green crosses) for an incident electron dose of 10^4 $e^-/\mathring{A}^2$ using a linear imaging model.*

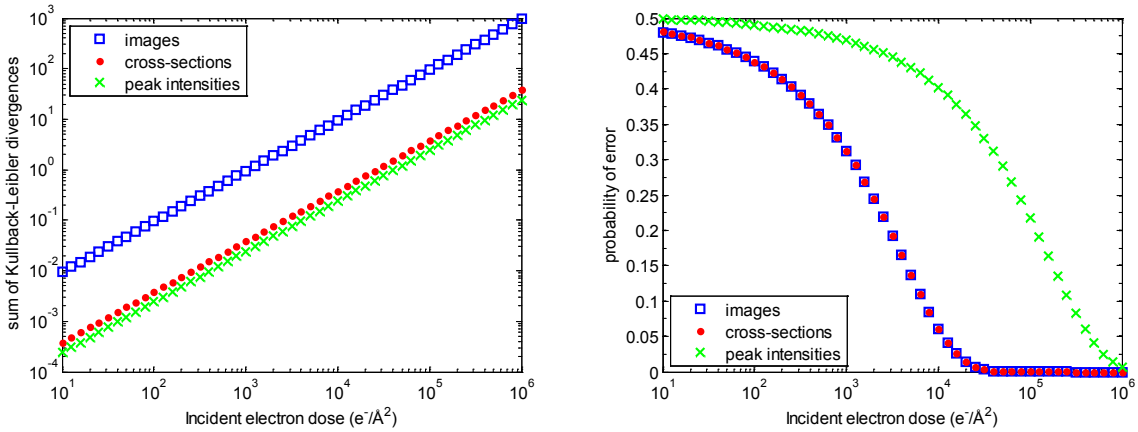

(a) sum of Kullback-Leibler divergences (b) probability of error

Figure 6.5: *Sum of Kullback-Leibler divergences and probability of error as a function of the incident electron dose for STEM images (blue squares), scattering cross-sections (red dots), and peak intensities (green crosses) for $n_{\mathcal{H}_0} = 10$ atoms using a linear imaging model.*

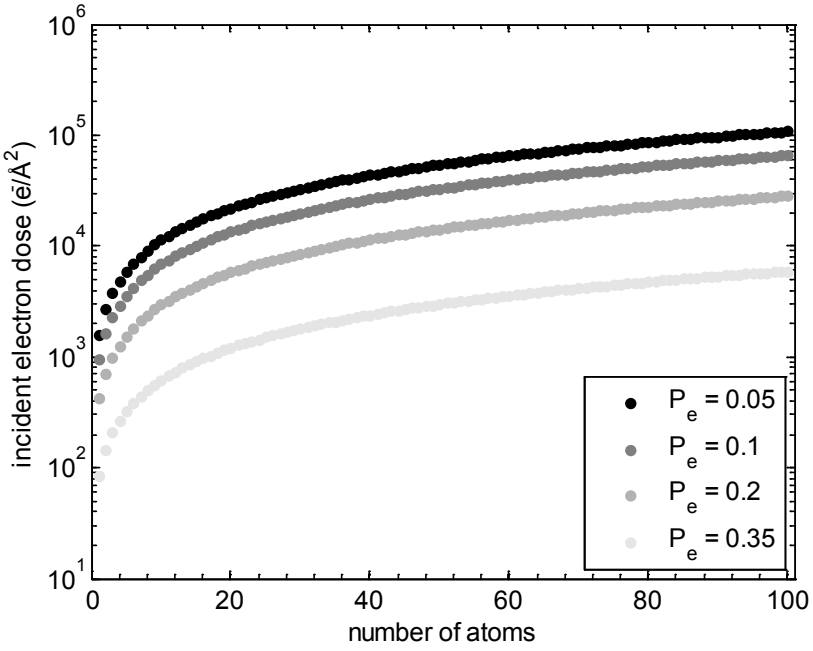

Figure 6.6: *Probability of error as a function of the number of atoms $n_{\mathcal{H}_0}$ and the incident electron dose for the scattering cross-sections or STEM images using a linear imaging model.*

6.4.2 General analytical expression for scattering cross-sections

Similar to the analytical derivation for the linear imaging model, the probability of error can be evaluated analytically for a general model. This will be done in this subsection for the scattering cross-sections, since they seem to prove more robust than peak intensities and perform similar as STEM images based on the results of the linear imaging model. From Fig. 6.1(b), it can be seen that the probability of error decreases if the two distributions are more separated. A high difference between the expected values is therefore desired, as well as small values for the width of the distributions. The difference between the expected values of ω^{CS} for each hypothesis can be expressed as:

$$\mathbb{E}_{\mathcal{H}_1}\left[\omega^{\mathrm{CS}}\right] - \mathbb{E}_{\mathcal{H}_0}\left[\omega^{\mathrm{CS}}\right] = (\mathrm{CS}_n + \Delta\mathrm{CS}_{n,n+1}) - \mathrm{CS}_n = \Delta\mathrm{CS}_{n,n+1} \tag{6.53}$$

with $\Delta\mathrm{CS}_{n,n+1}$ the expected difference in scattering cross-section between two columns having n and $n+1$ atoms. The difference in expected values of ω^{CS} for each hypothesis equals $\Delta\mathrm{CS}_{n,n+1}$. However, when $\Delta\mathrm{CS}_{n,n+1}$ increases, the variances also increase. The variances are calculated from the probability distribution given by Eq. (6.16) and can be expressed as:

$$\mathrm{var}_{\mathcal{H}_0}\left[\omega^{\mathrm{CS}}\right] = \mathrm{CS}_n \cdot \Delta x^2 \tag{6.54}$$

$$\mathrm{var}_{\mathcal{H}_1}\left[\omega^{\mathrm{CS}}\right] = (\mathrm{CS}_n + \Delta\mathrm{CS}_{n,n+1}) \cdot \Delta x^2. \tag{6.55}$$

Since the width of the distribution is proportional to $\sqrt{\mathrm{CS}_n}$ and $\sqrt{\mathrm{CS}_n + \Delta\mathrm{CS}_{n,n+1}}$ for $\mathcal{H}_0$ and $\mathcal{H}_1$ respectively, the probability of error will become smaller for increasing $\Delta\mathrm{CS}_{n,n+1}$, that is when the difference in scattering cross-section between two atomic columns increases.

6.4.3 Simulation experiments

In this and the next subsections, the results of a realistic simulation study will be presented. This study has been performed in order to investigate the probability of error defined in section 6.2 to evaluate and optimise the inner and outer detector radii of an annular STEM detector in terms of quantitative atom-counting. Simulations of STEM images are performed for a 30 nm thick $SrTiO_3$ crystal, i.e. a thickness of 75 atoms, using the STEMsim software [Rosenauer 2008], for an aberration-corrected microscope at Scherzer defocus. The multislice approach is used in which thermal diffuse scattering is included as an absorptive potential. The simulation parameters which are used are listed in Table 6.1. The values for the Debye-Waller factors are taken from [Abramov 1995, Peng 1997].

Parameter	Symbol	Value
Acceleration voltage	V (kV)	300
Defocus	ε (Å)	-14.03
Spherical aberration	C_s (mm)	0.001
Spherical aberration of fifth order	C_5 (mm)	0
Objective aperture angle	α (mrad)	20
Spatial incoherence of source	FWHM (Å)	0.7
Size of the supercell	$N_a \times N_b$ (nm^2)	4.3×4.3
Slice thickness	z_{slice} (Å)	1.95
Debye-Waller factor Sr	B (Å^2)	0.6214
Debye-Waller factor Ti	B (Å^2)	0.4398
Debye-Waller factor O	B (Å^2)	0.7323
Pixel size	Δx (Å)	0.1562
Total number of scanned pixels	$K \times L$	25×25

Table 6.1: *Parameter values used in the simulation software STEMsim [Rosenauer 2008].*

6.4.4 Results from binary hypothesis test

In Fig. 6.7, the results for the probability of error from a binary hypothesis test with equal prior probabilities, defined by Eq. (6.2) are shown as a function of the number of atoms $n_{\mathcal{H}_0}$ in a Sr column for the three proposed measures and for two different incident electron doses. The dose only changes the value of the probability of error; for higher electron dose, the probability of error becomes lower. It can be seen that the probability of error increases for an increasing number of atoms in a similar way as for the linear imaging model of which the results are shown in Fig. 6.4(b). This means that it is easier to differentiate between 1 and 2 atoms than to differentiate between 75 and 76 atoms in a column. Another important conclusion that can be drawn from this figure for the realistic simulations concerns the different results for the three measures which are considered. For the linear imaging model discussed in subsection 6.4.1, the scattering cross-sections have the same probability of error as the STEM images. Also for the detailed image simulation analysed here, the probability of error for the scattering cross-sections (red dots) using Eq. (6.18) almost equals the probability of error for the STEM

image (blue squares) for which Eq. (6.27) is used, whereas the probability of error for the peak intensities (green crosses), computed using Eq. (6.9) is significantly larger. This means that the scattering cross-sections contain almost the same amount of information as the images themselves in terms of atom-counting, provided that the scattering cross-sections monotonically increase with number of atoms. Thus, the detailed profiles of the atomic columns do not add extra information for atom-counting. These differences can only be detected when using the images, since the scattering cross-sections sum all the pixel values in a Voronoi cell in the image into one number defined by Eq. (6.11). This result is very beneficial since the scattering cross-sections are now often used as a measure to analyse the number of atoms in an atomic column and in addition the scattering cross-sections are far more robust to compare with simulations. Scattering cross-sections are independent of the FWHM of the source size uses, the defocus and other parameters [E 2013, Martinez 2014a].
In Fig. 6.8, the probability of error is shown as a function of the inner detector radius with a fixed outer detector radius of 100 mrad. The incident dose is chosen such that the values for the probability of error cover the whole range of values between 0 and 0.5. The optimal inner detector angle is not affected by the selected electron dose. In Fig. 6.8(a), results for P_e are shown for $n_{\mathcal{H}_0} = 1$ for the three different measures for a Sr column. From this, it can be concluded that the optimal inner detector radius equals 21 mrad since the probability of error reaches a minimum here, suggesting that imaging in the LAADF STEM regime is optimal for atom-counting, since the objective aperture angle equals 20 mrad. However, when choosing $n_{\mathcal{H}_0} = 75$, the optimal inner detector radius increases to 28 mrad, as can be seen in Fig. 6.8(b). For this value of $n_{\mathcal{H}_0} = 75$, an inner detector radius of 21 mrad can definitely not be considered as an optimum, whereas for $n_{\mathcal{H}_0} = 1$ an inner detector angle of 28 mrad is near-optimal for atom-counting. Because the optimal detector design depends on the choice of the hypotheses, we should move on toward multiple hypothesis testing as already suggested in section 6.2

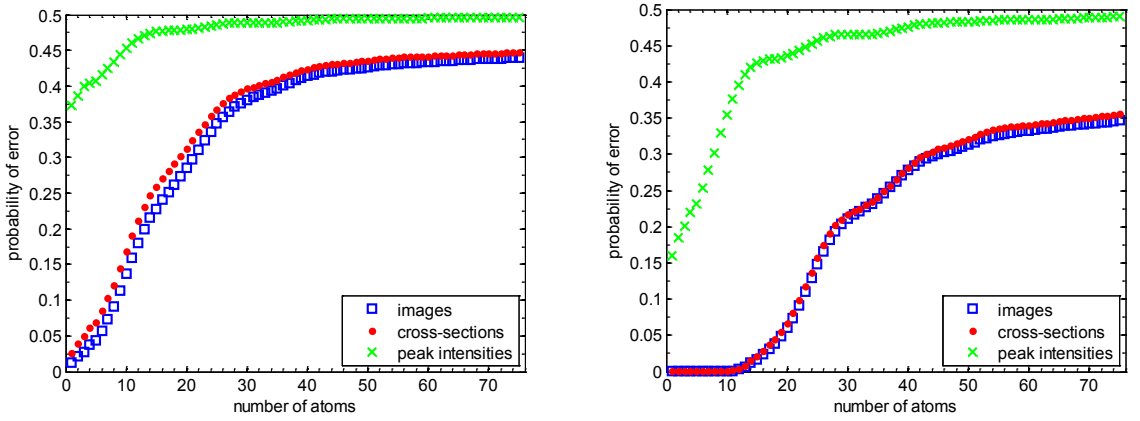

(a) $D = 10^4$ e$^-$/Å^2 (b) $D = 10^5$ e$^-$/Å^2

Figure 6.7: *Probability of error as a function of the number of atoms in a Sr column with* $D = 10^5$ $e^-/Å^2$, *for a detector collection range of* 60 − 100 mrad *using a binary hypothesis test.*

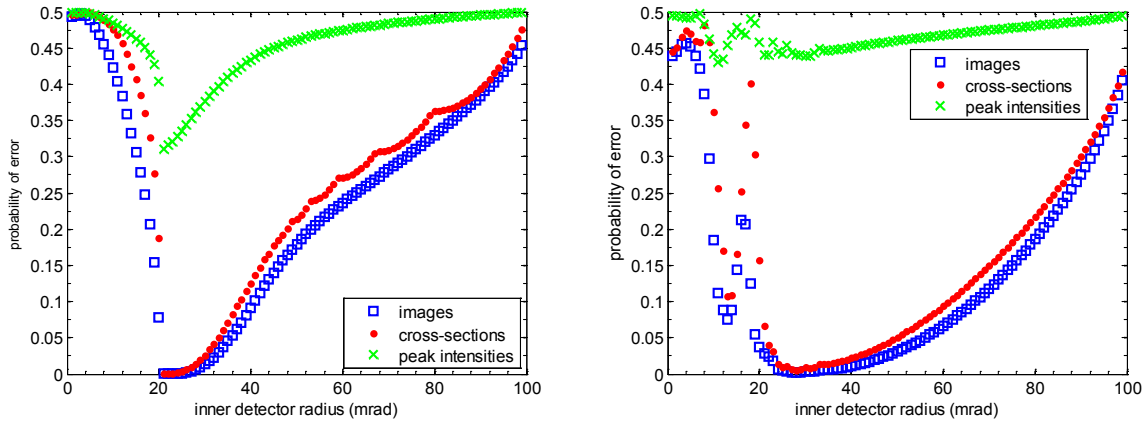

(a) $n_{\mathcal{H}_0} = 1$ and $D = 10^3$ e$^-$/Å^2 (b) $n_{\mathcal{H}_0} = 75$ and $D = 10^6$ e$^-$/Å^2

Figure 6.8: *Probability of error for a Sr column as a function of the inner detector angle with a fixed outer detector radius (*100 mrad*) using a binary hypothesis test.*

6.4.5 Results from multiple hypothesis test

When using a multiple hypothesis test, all possible numbers of atoms up to a certain thickness of the atomic column are considered. Since it is demonstrated in subsection 6.4.4 that for atom-counting the scattering cross-sections contain almost the same amount of information as the images, we proceed here with the scattering cross-sections, which are used in practice, as shown in the previous chapters. It can also be shown that in the case of a multiple hypothesis test the general optimal detector design does not drastically changes when using STEM images. Using Eq. (6.38), it is possible to determine the optimal detector design for the STEM detector in terms of inner and outer detector radius. Therefore, the probability of error is calculated for the different atomic columns in the $SrTiO_3$ crystal, i.e. the Sr, TiO, and O-columns, for a multiple hypothesis test with $M = 15$ hypotheses, i.e. for a thickness up to 15 atoms, and for a test with 75 hypotheses, i.e. for a thickness up to $M = 75$ atoms and assuming equal prior probabilities for the different hypotheses. Since the TiO column exists of an equal number of Ti and O atoms, only counting of one type of atoms is considered. The results are shown in Fig. 6.9 for the scattering cross-sections. The optimal detector angles do not critically depend on the atom type. For a thickness of 15 atoms, the optimal detector design is LAADF STEM with an inner detector radius of 21 mrad and the maximal outer detector radius of 100 mrad considered in the simulations. The optimal inner detector angle changes for a thickness of 75 atom. Here, a minimum for the probability of error of a Sr column is found for an inner detector angle of 28 mrad, for a TiO column for 33 mrad and for a O column for 30 mrad. Ideally, the design should be optimised for counting every atom type. This can be done by minimising e.g. an averaged probability of error for the three atomic column types.

The actual number of the probability of error not only depends on the choice of the detector but also on the incident electron dose. Once the optimal detector design has been derived, one can then be interested to investigate the lowest possible incident electron dose for which the probability of error reaches an acceptable low value. Therefore, the probability of error is computed as a function of the incident electron dose for scattering cross-sections, for the three

different atomic columns present in $SrTiO_3$. The results are shown in Fig. 6.10. It is clear from this figure, as one could expect, that the probability of error decreases for an increasing electron dose. The same trend was observed for the linear imaging model as shown in Fig. 6.5(b). If a maximum probability of error of 20% would be taken as acceptable, then an electron dose of 10^5 $e^-/Å^2$ would be necessary. This can be of great importance if one wants to reduce beam damage but at the same time still obtain an acceptable precision to count atoms.

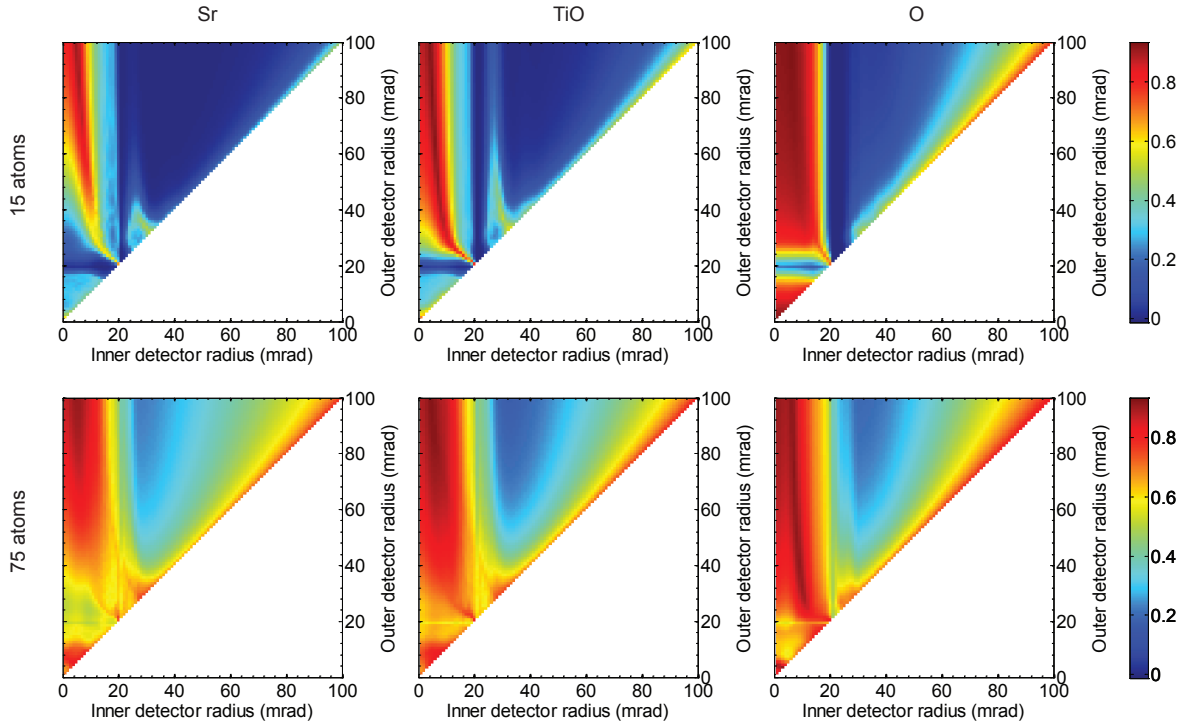

Figure 6.9: *Probability of error for scattering cross-sections as a function of inner and outer detector angle for the three different atom columns in* $SrTiO_3$ *for* $D = 10^5$ $e^-/Å^2$ *using a multiple hypothesis test. The upper and lower row show the results when the goal is to find the optimal settings when counting up to* $M = 15$ *and* $M = 75$ *atoms, respectively.*

6.5 Discussion

In order to understand the different obtained optimal designs for the different thicknesses shown in Figs. 6.8 and 6.9, the values of the integrated scattering cross-sections are investigated for three different detector designs for a Sr column. In Fig. 6.11(a) the normalised integrated scattering cross-sections are shown as a function of thickness, i.e. the number of atoms in a Sr column, for three different detector collection ranges. The red dots show the behaviour of the scattering cross-sections for a collection range of 21 – 100 mrad, the blue squares give the result for a detector collection range of 30 – 100 mrad, and the green crosses show the result for a detector ranging from 60 – 100 mrad. There is a clear difference in the results for the three detector settings, from which the optimal design shown in Fig. 6.9 can be understood. Up to a thickness of 20 atoms in a Sr column, there is a monotone increase in the values of the integrated

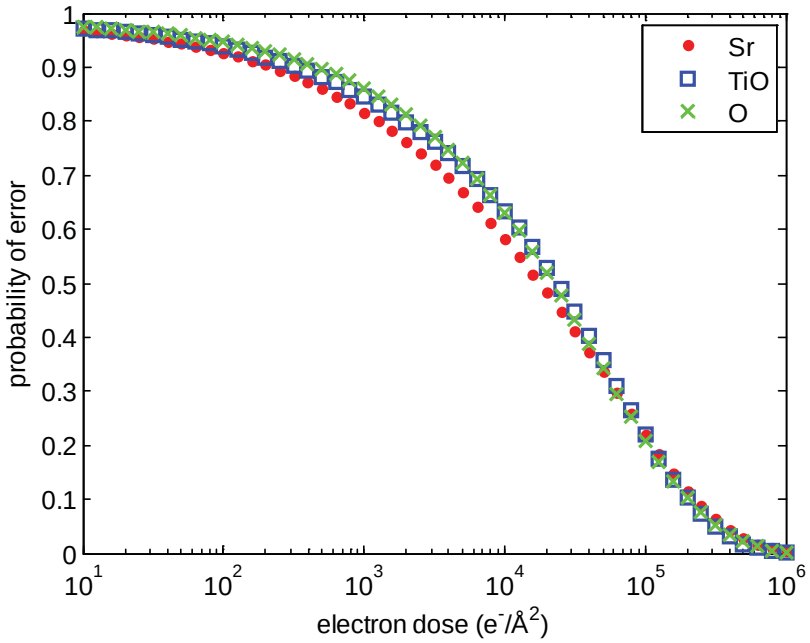

Figure 6.10: *Probability of error as a function of incident electron dose for detector angles* 30−100 mrad *and thickness of* $M = 75$ *atoms using a multiple hypothesis test.*

scattering cross-sections. However, it is clear from the image that for a low inner detector angle of 21 mrad, i.e. LAADF STEM, this increase is much steeper, which means that for this detector setting $\Delta CS_{n,n+1}$ from Eq. (6.53) is much larger than for the other detector setting shown. For this reason the lower inner collection angle of 21 mrad turns out to be the optimal detector design for a Sr column of 15 atoms thick as can be seen from the upper left figure of Fig. 6.9. For Sr columns thicker than 20 atoms, however, there appears to be a different behaviour in the scattering cross-sections for a detector collection range with a low inner detector angle of 21 mrad. The monotonic increase is interrupted by a sudden minimum, whereas for a higher inner detecotr angle of 30 mrad and 60 mrad the scattering cross-sections still increase as a function of thickness. This result shows us why for a thickness of 75 atoms in a Sr column, the detector collection range with a higher inner collection angle of 30 mrad becomes beneficial. Because the increase in scattering cross-sections for an inner detector angle of 30 mrad is steeper compared to an inner detector angle of 60 mrad, it is clear that this latter will lead to a higher probability of error and therefore does not result into the optimal design as can be seen from the bottom left image in Fig. 6.9. In a similar way, the obtained optimal detector designs for a TiO and pure O column given in Fig. 6.9 can be explained.

In order to understand why scattering cross-sections in the LAADF STEM regime no longer increase monotonically with the number of atoms as compared to the MAADF and HAADF regime, the coherent and incoherent contributions to the scattering cross-sections under different combinations of inner and outer detector angles are considered separately. The simulation software STEMsim allows one to save the coherent and incoherent contributions separately. Following [Ishizuka 2002], both parts are described by different potentials which are normally summed up in order to obtain the complete signal. In Fig. 6.11(b)-(d), the coherent and in-

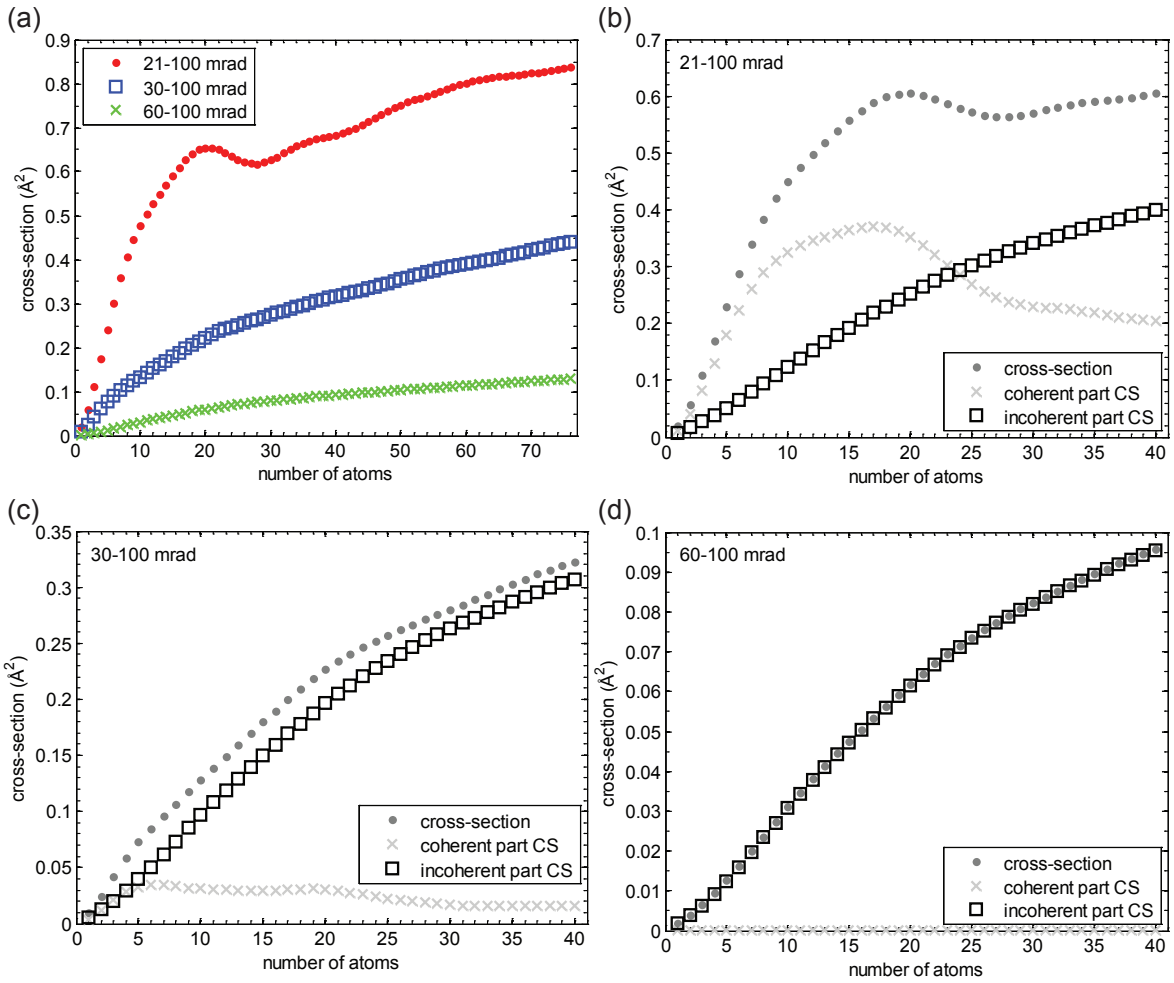

Figure 6.11: *(a) Integrated scattering cross-sections (fraction of incident electron dose) as a function of the number of atoms in a Sr column. The coherent and incoherent contribution to the scattering cross-sections are shown for (b)* 21 – 100 mrad*, (c)* 30 – 100 mrad*, and (d)* 60 – 100 mrad*.*

coherent contributions to the scattering cross-sections are separated for the different detector collection ranges of 21 – 100 mrad, 30 – 100 mrad, and 60 – 100 mrad respectively. As can be seen from Fig. 6.11(b), the coherent contribution to the scattering cross-section causes the non-monotonic increase. The relative contribution of the coherent part to the scattering cross-section decreases when increasing the inner detector angle as can be seen from Fig. 6.11(c) and (d). This analysis shows that the optimal detector design can be understood from the values of the scattering cross-sections, i.e. a combination of the coherent and incoherent contributions, as a function of the number of atoms in a projected atomic column.

6.6 Conclusions

In this chapter, the principles of detection theory have been used for quantifying the probability of error for atom-counting from HR STEM images. Therefore, binary hypothesis testing as well as multiple hypothesis testing has been worked out for atom-counting. In this way, the limits to

the precision with which the number of atoms in a projected atomic column can be estimated are studied. The here-described method is put forward as a powerful tool that can be used to optimise the design of an experiment by varying experimental parameters, such as the detector collection range, according to the experimental possibilities. Furthermore, the exact optimal experiment design will depend under the material under study. Nevertheless, the conclusions from the study conducted in this chapter give some general guidelines on optimal experiment design for atom-counting.

In this chapter, it is pointed out that the use of scattering cross-sections is afforded in the quantitative analysis of HR STEM images when the goal is to count the number of atoms as precise as possible. Scattering cross-sections perform almost equally well as compared to detailed STEM images of a projected atomic column and they outperform peak intensities. Furthermore, it has been shown that the probability of error increases for increasing number of atoms in the column. In other words, it becomes more difficult to count the number of atoms in a projected atomic column if the thickness increases. One could also use the proposed method of hypothesis testing to determine the minimally required electron dose in order to attain a pre-specified precision. In this way, beam damage can be kept to a minimum. Finally, it is shown that the optimal inner detector angle increases for increasing thickness when deriving the optimal STEM detector design for atom-counting.

7

General conclusions and future perspectives

In this thesis, atomic scale aberration corrected (scanning) transmission electron microscopy is pushed toward precise measurements of unknown structure parameters using advanced statistical techniques in a model-based framework. For this purpose, statistical parameter estimation theory has extensively been used. The aim of this theory is to measure unknown structure parameters, including atomic column positions and the number of atoms, as accurate and precise as possible from experimental images. The starting-point is the availability of a parametric model describing the expectations of the images. It has been assumed that the image intensities in high-resolution (S)TEM images can be described by a superposition of Gaussian functions peaked at the atomic column positions. The unknown parameters of this model, i.e. the position coordinates, the width, and the height of these Gaussian functions, are estimated by fitting this model to the experimental images using a criterion of goodness of fit, the least squares sum, which quantifies the similarity between the experimental images and the model.

The accuracy and precision with which structure parameters could be estimated using statistical parameter estimation theory have been evaluated for a focal series of HR TEM images recorded for exit wave reconstruction and for ADF STEM images. First, the attainable precision with which the atomic column positions can be estimated using a focal series of HR TEM images has been investigated. In theory, it was expected that the precision would considerably improve using the maximum likelihood estimator based on the full series of focal images. As such, the theoretical lower bound on the variances of the unknown atomic column positions can be attained. However, this approach is numerically demanding. Therefore, maximum likelihood estimation has been compared with the results obtained by fitting a model to the reconstructed exit wave rather than to the full series of focal images. By means of simulations, it has been shown that the reconstructed complex exit wave contains the same amount of information concerning the atomic column positions as the full series of focal images. Only for thin samples,

which act as weak phase objects, this information can be retrieved from the phase of the reconstructed complex exit wave, which is often used only in quantitative studies of exit waves reconstructed from a focal series of images.
Next, the accuracy and precision has been evaluated for the atomic column positions and the scattering cross-sections for ADF STEM images. These scattering cross-sections correspond to the volume under the estimated Gaussian function and have been shown to be an excellent measure for interpreting the ADF STEM intensities in terms of number of atoms in a projected atomic column. Using detailed ADF STEM multislice simulations, different noise realisations have been obtained for different incident electron doses. It turned out that accurate and precise measurements can be obtained for the estimated parameters of interest. Moreover, in this study it has been shown that the theoretical lower bound on the variance could be attained for the estimates of the scattering cross-sections and position coordinates using the least squares estimator. This result is of great importance, since this means that the position coordinates and scattering cross-sections are estimated with the highest possible precision from the ADF STEM images.
As summarised here, it has been shown that using statistical parameter estimation theory high precision measurements for structure parameters can be obtained using the least squares estimator. However, direct implementation of the least squares estimator in which all parameters are estimated at the same time, limits the field of view for which the parameters of the expectation model can be estimated. Therefore, an efficient algorithm has been proposed for the least squares estimation of the structure parameters. This algorithm allows one to analyse larger nanostructures in a quantitative way. Such analysis has been employed in order to reconstruct the 3D position and atom type of the atoms in a Au@Ag nanorod. In addition, displacement maps have been formed for the atomic column positions in a five-fold-twinned decahedral Au nanoparticle and for the Al columns within $LaAlO_3$. These examples have illustrated the increased possibilities for a quantitative analysis at the atomic scale with high precision by the availability of the new algorithm.

In the second part of the thesis the focus of the work has been shifted toward nanoparticle atom-counting from ADF STEM images using advanced statistical methods. First the possibilities for counting the number of atoms of single element crystalline nanostructure in the dimension perpendicular to the recorded image using a statistics-based method have been investigated. In order to count the number of atoms, it is assumed that the total intensity of scattered electrons scales with the number of atoms per atomic column. These so-called scattering cross-sections are quantitatively determined using model-based statistical parameter estimation theory. The distribution describing the probability that the scattering cross-sections are generated by atomic columns containing a specific number of atoms is inferred on the basis of the experimental scattering cross-sections. This probability distribution consists of normal components which are smeared out due to a combination of experimental instabilities and detection noise. Finally, the number of atoms can be quantified using this estimated probability distribution. This method has been discussed in detail together with a thorough study on the inherent limitations. It has been demonstrated that the number of atomic columns available in the observed STEM image, the number of components in the estimated probability distribution, the width of the components of the probability, and the typical shape of the criterion to assess the number of components in the probability distribution directly affect the accuracy and precision with which the number of atoms in a particular atomic column can be estimated. Nevertheless, it has been shown that

single atom sensitivity is feasible taking the latter aspects into consideration.

In this thesis, it has been illustrated that the statistics-based atom-counting method should be combined with another complementary method. Here, the method has been combined with a simulation-based method. In the literature, both methods are independently proposed. The simulation-based method uses libraries of simulated scattering cross-sections which can be compared to normalised experimental scattering cross-sections. Although this approach is straightforward, it critically depends on accurate knowledge of the experimental detector settings and a priori structure information. In practice, these parameters require careful measurement or calibration and are not always available, hence limiting the applicability of this method. The statistics-based method can be used without prior knowledge concerning the structure, is independent of simulations, and provides the percentage of atomic columns for which the number of atoms is identified with single atom sensitivity. However, the reliability also depends on different parameters which can be linked with the quality of the recorded images. Therefore, it has been concluded that only through a combination of the simulation- and statistics-based method, being completely independent of each other, one is able to count atoms with trustworthy single atom sensitivity.

One of the applications of the atom-counting method that has been investigated, is the determination of the number of atoms in a Au nanorod. In this analysis, the recorded image intensities have been normalised with respect to the incident beam by taking the detector sensitivity into account. This places STEM experiments on the same absolute intensity scale as used in theoretical image simulations. In order to validate the accuracy of the counting results, the experimental mean scattering cross-sections have been compared to the scattering cross-sections obtained from detailed HAADF STEM simulations. An excellent match of the experimental and simulated scattering cross-sections within the expected 5-10% error range has been found. The statistical model-based method enables to quantify the precision of the atom-counting results. For this Au nanorod, it has been found that in 80% of all atomic columns the number of atoms has been measured without error.
The atom-counting method has also been applied to a more challenging nanostructure, a Pt/Ir mixed alloy nanoparticle. Conducting the atom-counting method on such a industrial bimetallic catalyst provides a severe characterisation challenge because of the beam sensitivity and limited size of these catalysts. It has been shown that only through a combination of thorough statistical methods and detailed image simulations the limits of atom-counting can be diagnosed for this type of particles. This combined analysis has also brought forward the inherent limitations of the method which have been discussed earlier in a theoretical framework. From this study, it has been concluded that the interplay of several effects can greatly impact the reliability of atom-counting in quantitative ADF STEM. This includes parameters such as electron dose and lateral sampling, but also aspects often beyond the control of the experimentalist, including particle tilt and contrast contributions from the carbon support.

Finally, designing the optimal experiment for nanoparticle atom-counting can greatly enhance the reliability of the atom-counting results, which is of great importance when studying beam sensitive materials. Therefore, the principles of detection theory have been used to quantify the probability of error for atom-counting for optimal experiment design. Binary as well as multiple

hypotheses testing has been investigated in order to determine the limits to the precision with which the number of atoms in a projected atomic column can be estimated. The probability of error has been calculated for STEM images, scattering cross-sections, and peak intensities. Based on this analysis, it has been concluded that the scattering cross-sections perform equally well as images and prove more robust than peak intensities. The optimal STEM detector design for atom-counting has also been derived using the expression for the probability of error. It has been shown that for very thin objects a low angle annular dark field detector is optimal and that for thicker objects the optimal inner detector angle of the annular detector increases. This technique of hypothesis testing has also been used in order to determine the minimally required electron dose in order to attain a pre-specified precision.

As a general conclusion it can be stated that advanced statistical techniques are ideal tools for quantitative electron microscopy at the atomic scale. Obviously, the results presented in this thesis are only an intermediate endpoint in the development of quantitative methods. Significant improvements can be expected for the quantitative atom-counting method. So far, methods for counting the number of atoms perform well only for single element crystalline structures which are still relatively stable under the incident electron beam. As illustrated, the simulation- and statistics-based approach for atom-counting have their own advantages and disadvantages limiting the precision and accuracy that can be attained for the characterisation of challenging nanostructures. In this thesis, both approaches are independently used next to each other in order to validate counting results. However, it is envisaged that the development of a true hybrid method which combines the benefits of a statistical analysis and a comparison with simulations into the estimation of the probability distribution of the scattering cross-sections, will enhance the performance of atom-counting from ADF STEM images. Furthermore, a giant leap forward is expected if the number of atoms can be counted in mixed element nanostructures, since technologically important materials often consist of more than one chemical element. In this case, different types of elements together constitute an atomic column. For mixed columns, all types of elements will contribute differently to the scattering cross-section thus significantly complicating atom-counting as compared for single element nanostructures. In order to unscramble these mixed elements atomic columns novel quantitative methods should be explored. In addition, it is expected that significant advances can be made in the development of 3D reconstruction algorithms for electron tomography at the atomic scale using a synergistic combination of atom-counting and compressive sensing reconstruction algorithms. In this way, quantitative prior information on the number of atoms can be included during the reconstruction. Since the atomic positions are not fixed during such a reconstruction, this will enable one to measure atom positions in 3D.
As the work presented in this thesis opened up new possibilities for the characterisation of nanomaterials at the atomic scale, future developments of novel quantification methods will provide once more a wealth of possibilities to study nanomaterials on a new level. This continuous process helps step by step unravelling the unique link between structure and properties at the atomic scale.

Bibliography

[Abakumov 2013] A. M. Abakumov, A. A. Tsirlin, and E. V. Antipov. *2.01 - Transition-Metal Perovskites*. In Comprehensive Inorganic Chemistry II, K. Poeppelmeier, and J. Reedijk (eds.), 1 – 40. Elsevier, Amsterdam, Second edition, 2013.

[Abramov 1995] Y. A. Abramov, V. G. Tsirelsoon, V. E. Zavodnik, S. A. Ivanov, and I. D. Brown. *The Chemical Bond and Atomic Displacements in $SrTiO_3$ From X-ray Diffraction Analysis*. Acta Crystallographica, vol. B51, 942–951, 1995.

[Akaike 1974] H. Akaike. *A new look at the statistical model identification*. IEEE Transactions on Automatic Control, vol. 19, no. 6, 716–723, 1974.

[Akashi 2015] T. Akashi, Y. Takahashi, T. Tanigaki, T. Shimakura, T. Kawasaki, T. Furutsu, H. Shinada, H. Müller, M. Haider, N. Osakabe, and A. Tonomura. *Aberration corrected 1.2-MV cold field-emission transmission electron microscope with a sub-50-pm resolution*. Applied Physics Letters, vol. 106, 074101, 2015.

[Alem 2011] N. Alem, O. V. Yazyev, C. Kisielowski, P. Denes, U. Dahmen, P. Hartel, M. Haider, M. Bischoff, B. Jiang, S. G. Louie, and A. Zettl. *Probing the Out-of-Plane Distortion of Single Point Defects in Atomic Thin Hexagonal Boron Nitride at the Picometer Scale*. Physical Review Letters, vol. 106, 126102, 2011.

[Allen 2001] L. J. Allen, and M. P. Oxley. *Phase retrieval from series of images obtained by defocus variation*. Optics Communications, vol. 199, 65–75, November 2001.

[Allen 2003] L. J. Allen, S. D. Findlay, M. P. Oxley, and C. J. Rossouw. *Lattice-resolution contrast from a focus coherent electron probe. Part I*. Ultramicroscopy, vol. 96, 47–63, 2003.

[Allen 2004a] L. J. Allen, W. McBride, N. L. O'Leary, and M. P. Oxley. *Exit wave reconstruction at atomic resolution*. Ultramicroscopy, vol. 100, 91–104, 2004.

[Allen 2004b] L. J. Allen, W. McBride, N. L. O'Leary, and M. P. Oxley. *Investigation of the effects of partial coherence on exit wave reconstruction*. Journal of Microscopy, vol. 216, 70–75, 2004.

[Aveyard 2014] R. Aveyard, R. Ferrando, R. L. Johnston, and J. Yuan. *Modeling Nanoscale Inhomogeneities for Quantitative HAADF STEM Imaging*. Physical Review Letters, vol. 113, 075501, 2014.

[Bals 2006] S. Bals, S. Van Aert, G. Van Tendeloo, and D. Ávila-Brande. *Statistical Estimation of Atomic Positions from Exit Wave Reconstruction with a Precision in the Picometer Range*. Physical Review Letters, vol. 96, 096106, 2006.

[Bals 2007] S. Bals, K. J. Batenburg, J. Verbeeck, J. Sijbers, and G. Van Tendeloo. *Quantitative Three-Dimensional Reconstruction of Catalyst Particles for Bamboo-like Carbon Nanotubes*. Nano Letters, vol. 7, no. 12, 3669–3674, 2007.

[Bals 2011] Sara Bals, Marianna Casavola, Marijn A. van Huis, Sandra Van Aert, K. Joost Batenburg, Gustaaf Van Tendeloo, and Daniël Vanmaekelbergh. *Three-Dimensional Atomic Imaging of Colloidal Core-Shell Nanocrystals*. Nano Letters, vol. 11, no. 8, 3420–3424, 2011.

[Bals 2012] S. Bals, S. Van Aert, C. P. Romero, K. Lauwaet, M. J. Van Bael, B. Schoeters, B. Partoens, E. Yücelen, P. Lievens, and G. Van Tendeloo. *Atomic scale dynamics of ultrasmall germanium clusters.* Nature Communications, vol. 3, 897, 2012.

[Banfield 1993] J. D. Banfield, and A. E. Raftery. *Model-based Gaussian and non-Gaussian clustering*. Biometrics, vol. 49, 803, 1993.

[Batenburg 2007] K. J. Batenburg. *A Network Flow Algorithm for Reconstructing Binary Images from Discrete X-Rays*. Journal of Mathematical Imaging Vision, vol. 27, 175–191, 2007.

[Batson 2002] P. E. Batson, N. Dellby, and O. L. Krivanek. *Sub-ångstrom resolution using aberration corrected electron optics*. Nature, vol. 418, 617–620, 2002.

[Bettens 1999] E. Bettens, D. Van Dyck, A. J. den Dekker, J. Sijbers, and A. van den Bos. *Model-based two-object resolution from observations having counting statistics*. Ultramicroscopy, vol. 77, 37–48, 1999.

[Biermans 2010] E. Biermans, L. Molina, K. J. Batenburg, S. Bals, and G. Van Tendeloo. *Measuring porosity at the nanoscale by quantitative electron tomography*. Nano Letters, vol. 7, 5014–5019, 2010.

[Biernacki 1997] C. Biernacki, and G. Govaert. *Using the classification likelihood to choose the number of clusters*. Computing Science and Statistics, vol. 29, 451–457, 1997.

[Biernacki 1998] C. Biernacki, G. Celeux, and G. Govaert. *Assessing a mixture model for clustering with the integrated classification likelihood*. Rapport technique 3521, Rhônes-Alpes: INRIA, 1998.

[Biernacki 1999] C. Biernacki, G. Celeux, and G. Govaert. *An improvement of the NEC criterion for assessing the number of clusters in a mixture model*. Pattern Recognition Letters, vol. 20, no. 3, 267 – 272, 1999.

[Boothroyd 1998] C. B. Boothroyd. *Why don't high-resolution simulations and images match?* Journal of Microscopy, vol. 190, 99–108, 1998.

[Botti 2007] S. Botti, A. Schindlmayr, R. Del Sole, and L. Reining. *Time-dependent density-functional theory for extended systems*. Reports on Progress in Physics, vol. 70, 357–407, 2007.

[Broersen 1993] P. M. T. Broersen, and H. E. Wensink. *On Finite Sample Theory for Autoregressive Model Order Selection*. IEEE Transactions on Signal Processing, vol. 41, no. 1, 194–204, 1993.

[Broersen 1996] P. M. T. Broersen, and H. E. Wensink. *On the Penalty Factor for Autoregressive Order Selection in Finite Samples*. IEEE Transactions on signal processing, vol. 44, 748–752, 1996.

[Buban 2010] J. P. Buban, Q. Ramasse, B. Gipson, N. D. Browning, and H. Stahlberg. *High-resolution low-dose scanning transmission electron microscopy*. Journal of Electron Microscopy, vol. 59, 103–112, 2010.

[Buffat 1977] P.-A. Buffat. *Size effect modifications of the Debye-Waller factor in small gold particles*. Solid State Communications, vol. 23, 547–550, 1977.

[Cardinal 2010] M. F. Cardinal, B. Rodriguez-Gonzalez, R. A. Alvarez-Puebla, J. Perez-Juste, and L. M. Liz-Marzán. *Modulation of Localized Surface Plasmons and SERS Response in Gold Dumbbells through Silver Coating*. Journal of Physical Chemistry C, vol. 114, 10417–10423, 2010.

[Celeux 1996] G. Celeux, and G. Soromenho. *An entropy criterion for assessing the number of clusters in a mixture model*. Journal of Classification, vol. 13, no. 2, 195–212, 1996.

[Chang 2010] L. Y. Chang, A. S. Barnard, L. C. Gontard, and R. E. Dunin-Borkowski. *Resolving the Structure of Active Sites on Platinum Catalytic Nanoparticles*. Nano Letters, vol. 10, 3073–3076, 2010.

[Chen 2013] C.-C. Chen, Z. Chun, E. R. White, C.-Y. Chiu, M. C. Scott, B. C. Regan, L. D. Marks, Y. Huang, and J. Miao. *Three-dimensional imaging*

of dislocations in a nanoparticle at atomic resolution. Nature, vol. 496, 74–77, 2013.

[Clark 1965] B. C. Clark, R. Herman, and R. F. Wallis. *Theoretical Mean-Square Displacements for Surface Atoms in Face-Centered Cubic Lattices with Applications to Nickel*. Physical Review, vol. 139, no. 3A, A860–867, 1965.

[Coene 1992] W. Coene, and G. Janssen. *Phase Retrieval through Focus Variation for Ultra-Resolution in Field-Emission Transmission Electron Microscopy*. Physical Review Letters, vol. 69, no. 26, 3743–3746, 1992.

[Coene 1996] W. M. J. Coene, A. Thust, M. Op de Beeck, and D. Van Dyck. *Maximum-likelihood method for focus-variation image reconstruction in high resolution transmission electron microscopy*. Ultramicroscopy, vol. 64, 109–135, 1996.

[Cortie 2011] M. B. Cortie, and A. M. McDonagh. *Synthesis and Optical Properties of Hybrid and Alloy Plasmonic Nanoparticles*. Chemical Reviews, vol. 111, 3713–3735, 2011.

[Day 1969] N. E. Day. *Estimating the Components of a Mixture of Normal Distributions*. Biometrika, vol. 56, no. 3, 463–474, 1969.

[De Backer 2011] A. De Backer, S. Van Aert, and D. Van Dyck. *High precision measurements of atom column positions using model-based exit wave reconstruction*. Ultramicroscopy, vol. 111, 1475–1482, 2011.

[De Backer 2013] A. De Backer, G. T. Martinez, A. Rosenauer, and S. Van Aert. *Atom counting in HAADF STEM using a statistical model-based approach: methodology, possibilities, and inherent limitations*. Ultramicroscopy, vol. 134, 23–33, 2013.

[De Backer 2015a] A. De Backer, A. De wael, J. Gonnissen, and S. Van Aert. *Optimal experimental design for nano-particle atom-counting from high-resolution STEM images*. Ultramicroscopy, vol. 151, 46–55, 2015.

[De Backer 2015b] A. De Backer, G. T. Martinez, K. E. MacArthur, L. Jones, A. Béché, P. D. Nellist, and S. Van Aert. *Dose limited reliability of quantitative annular dark field scanning transmission electron microscopy for nano-particle atom-counting*. Ultramicroscopy, vol. 151, 56–61, 2015.

[De Graef 2003] M. De Graef. *Introduction to Conventional Transmission Electron Microscopy*. Cambridge University Press, 2003.

[de Jong 1993] A. F. de Jong, and D. Van Dyck. *Ultimate resolution and information in electron microscopy II. The information limit of transmission electron microscopes*. Ultramicroscopy, vol. 49, 66–80, 1993.

[Dempster 1977] A. P. Dempster, N. M. Laird, and D. B. Rubin. *Maximum Likelihood from Incomplete Data via the EM Algorithm (with discussion)*. Journal of the Royal Statistical Society B, vol. 39, 1–38, 1977.

[den Dekker 1999a] A. J. den Dekker, J. Sijbers, and D. Van Dyck. *How to optimize the design of a quantitative HREM experiment so as to attain the highest precision*. Journal of Microscopy, vol. 194, 95–104, 1999.

[den Dekker 1999b] A. J. den Dekker, J. Sijbers, and D. Van Dyck. *How to optimize the design of a quantitative HREM experiment so as to attain the highest precision*. Journal of Microscopy, vol. 194, 95–104, 1999.

[den Dekker 2001] A. J. den Dekker, S. Van Aert, D. Van Dyck, A. van den Bos, and P. Geuens. *Does a monochromator improve the precision in quantitative HRTEM?* Ultramicroscopy, vol. 89, 275–290, 2001.

[den Dekker 2005] A. J. den Dekker, S. Van Aert, A. van den Bos, and D. Van Dyck. *Maximum likelihood estimation of structure parameters from high resolution electron microscopy images. Part I: A theoretical framework*. Ultramicroscopy, vol. 104, 83–106, 2005.

[den Dekker 2013] A. J. den Dekker, J. Gonnissen, A. De Backer, J. Sijbers, and S. Van Aert. *Estimation of unknown structure parameters from high-resolution (S)TEM images: What are the limits?* Ultramicroscopy, vol. 134, 34–43, 2013.

[Donoho 2006] D. L. Donoho. *For most large undetermined systems of linear equations, the minimal l^1–norm solution is also the sparsest solution*. Communications on Pure and Applied Analysis, vol. 59, 797–829, 2006.

[E 2013] H. E, K. E. MacArthur, T. J. Pennycook, E. Okunishi, A. J. D'Alfonso, N. R. Lugg, L. J. Allen, and P. D. Nellist. *Probe integrated scattering cross sections in the analysis of atomic resolution HAADF STEM images*. Ultramicroscopy, vol. 133, 109–119, 2013.

[Erni 2003] R. Erni, H. Heinrich, and G. Kostorz. *Quantitative characterisation of chemical inhomogeneities in Al-Ag using high-resolution Z-contrast STEM*. Ultramicroscopy, vol. 94, 125–133, 2003.

[Erni 2009] R. Erni, M. D. Rossell, C. Kisielowski, and U. Dahmen. *Atomic-Resolution Imaging with a Sub-50-pm Electron Probe*. Physical Review Letters, vol. 102, 096101, 2009.

[Erni 2010] R. Erni, M. D. Rossell, and P. N. H. Nakashima. *Optimization of exit-plane waves restored from HRTEM through-focal series*. Ultramicroscopy, vol. 110, 151–161, 2010.

[Fertig 1981] J. Fertig, and H. Rose. *Resolution and contrast of crystalline objects in high-resolution scanning transmission electron microscopy*. Optik, vol. 59, no. 5, 407–429, 1981.

[Findlay 2013] S. D. Findlay, and J. M. LeBeau. *Detector non-uniformity in scanning transmission electron microscopy*. Ultramicroscopy, vol. 124, 52–60, 2013.

[Frank 1992] J. Frank (ed.). *Electron Tomography: Three-dimensional imaging with the transmission electron microscope*. Plenum Press, New York and London, 1992.

[Frieden 1998] B. R. Frieden (ed.). *Physics from Fisher Information - A Unification*. Cambridge University Press, Cambridge, 1998.

[Gao 1999] H. X. Gao, and L.-M. Peng. *Parameterization of the temperature dependence of the Debye-Waller factors*. Acta Crystallographica A, vol. 55, 926–932, 1999.

[Gao 2014] P. Gao, J. Britson, C. T. Nelson, J. R. Jokisaari, C. Duan, M. Trassin, S.-H. Baek, H. Guo, L. Li, Y. Wang, Y.-H. Chu, A. M. Minor, C.-B. Eom, R. Ramesh, L.-Q. Chen, and X. Pan. *Ferroelastic domain switching dynamics under electrical and mechanical excitations*. Nature Communications, vol. 5, no. 3801, 2014.

[Geuens 2002] P. Geuens, and D. Van Dyck. *The S-state model: a work horse for HRTEM*. Ultramicroscopy, vol. 93, 179–198, 2002.

[Geuens 2005] P. Geuens, and D. Van Dyck. *The S-State Model for Electron Channeling in High-Resolution Electron Microscopy*. Advances in Electronics and Electron Physics, vol. 136, 111–226, 2005.

[Gonnissen 2014] J. Gonnissen, A. De Backer, A. J. den Dekker, G. T. Martinez, A Rosenauer, J. Sijbers, and S. Van Aert. *Optimal experimental design for the detection of light atoms from high-resolution scanning transmission electron microscopy images*. Applied Physics Letters, vol. 105, no. 063116, 2014.

[Goris 2012a] B. Goris, S. Bals, W. Van den Broek, E. Carbo-Argibay, S. Gomez-Grana, L. M. Liz-Marzan, and G. Van Tendeloo. *Atomic-scale determination of surface facets in gold nanorods*. Nature Materials, vol. 11, 930–935, 2012.

[Goris 2012b] B. Goris, W. Van den Broek, K. J. Batenburg, H. Heidari, and S. Bals. *Electron tomography based on a total variation minimization reconstruction technique*. Ultramicroscopy, vol. 113, 120–130, 2012.

[Goris 2013] B. Goris, A. De Backer, S. Van Aert, S. Gómez-Graña, L. M. Liz-Marzán, G. Van Tendeloo, and S. Bals. *Three-Dimensional Elemental Mapping at the Atomic Scale in Bimetallic Nanocrystals*. Nano Letters, vol. 13, 4236–4241, 2013.

[Grieb 2012] T. Grieb, K. Müller, R. Fritz, M Schowalter, N. Neugebohrn, N. Knaub, K. Volz, and A Rosenauer. *Determination of the chemical composition of GaNAs using STEM HAADF imaging and STEM strain state analysis*. Ultramicroscopy, vol. 117, 15–23, 2012.

[Grzelczak 2008] M. Grzelczak, J. Pérez-Juste, P. Mulvaney, and L. M. Liz-Marzán. *Shape control in gold nanoparticle synthesis*. Chemical Society Reviews, vol. 37, 1783–1791, 2008.

[Haider 1998a] M. Haider, H. Rose, S. Uhlemann, B. Kabius, and K. Urban. *Towards 0.1 nm resolution with the first spherical corrected transmission electron microscope*. Journal of Electron Microscopy, vol. 47, no. 5, 395–405, 1998.

[Haider 1998b] M. Haider, S. Uhlemann, E. Schwan, H. Rose, B. Kabius, and K. Urban. *Electron microscopy image enhanced*. Nature, vol. 392, 768–769, 1998.

[Haider 2010] M. Haider, P. Hartel, H. Müller, S. Uhlemann, and J. Zach. *Information Transfer in a TEM Corrected for Spherical and Chromatic Aberration*. Microscopy and Microanalysis, vol. 16, 393–408, 2010.

[Haigh 2009] S. Haigh, H. Sawada, and A. I. Kirkland. *Optimal tilt magnitude determination for aberration-corrected super resolution exit wave reconstruction*. Philosophical Transactions of the Royal Society A, vol. 367, 3755–3771, 2009.

[Hao 2014] X. Hao, J. Zhai, L. B. Kong, and Z. Xu. *A comprehensive review on the progress of lead zirconate-based antiferroelectric materials*. Progress in Materials Science, vol. 63, 1–57, 2014.

[Hartel 1996] P. Hartel, D. Rose, and C. Dinges. *Conditions and reasons for incoherent imaging in STEM*. Ultramicroscopy, vol. 63, 63–114, 1996.

[Hashimoto 2009] A. Hashimoto, M. Shimojo, K. Mitsuishi, and M. Takeguchi. *Three-dimensional imaging of carbon nanostructures by scanning confocal electron microscopy*. Journal of Applied Physics, vol. 106, 086101, 2009.

[Hashimoto 2010] A. Hashimoto, M. Shimojo, K. Mitsuishi, and M. Takeguchi. *Three-Dimensional Optical Sectioning by Scanning Confocal Electron Microscopy with a Stage-Scanning System*. Microscopy and Microanalysis, vol. 16, 233–238, 2010.

[Hasselblad 1969] V. Hasselblad. *Estimation of Finite Mixture of Distributions from the Exponential Family*. Journal of the American Statistical Association, vol. 64, 1459–1471, 1969.

[Hawkes 1992] P. W. Hawkes. *Electron Tomography: Three-dimensional imaging with the transmission electron microscope*, The electron microscope as a structure projector. Plenum Press, 1992.

[Henderson 1995] R. Henderson. *The potential and limitations of neutrons, electrons and X-rays for atomic resolution microscopy of unstained biological molecules*. Quarterly Reviews of Biophysics, vol. 28, 171–193, 1995.

[Henglein 2000] A. Henglein. *Preparation and optical absorption spectra of Au core-Pt shell and Pt core-Au shell colloidal nanoparticles in aqueous solution*. Journal of Physical Chemistry B, vol. 104, 2201–2203, 2000.

[Heron 2014] J. T. Heron, D. G. Schlom, and R. Ramesh. *Electric field control of magnetism using $BiFeO_3$-based heterostructures*. Applied Physics Reviews, vol. 1, no. 021303, 2014.

[Herrmann 1997] K.-H. Herrmann. *Handbook of Microscopy - Applications in Materials Science, Solid-State Physics and Chemistry, Methods II*, Image recording in microscopy, 885–921. Weinheim VCH, 1997.

[Hodak 2000] J. H. Hodak, A. Henglein, and G. V. Hartland. *Coherent excitation of acoustic breathing modes in bimetallic core-shell nanoparticles*. Journal of Physical Chemistry B, vol. 104, 5053–5055, 2000.

[Houben 2006] L. Houben, A. Thust, and K. Urban. *Atomic-precision determination of the reconstruction of a 90° tilt boundary in $YBa_2Cu_3O_{7-\delta}$ by aberration corrected HRTEM*. Ultramicroscopy, vol. 106, 200–214, 2006.

[Hovden 2012] R. Hovden, and D. A. Muller. *Efficient elastic imaging of single atoms on ultrathin supports in a scanning transmission electron microscope*. Ultramicroscopy, vol. 109, 59–65, 2012.

[Hsieh 2004] W.-K. Hsieh, F.-R. Chen, J.-J. Kai, and A. I. Kirkland. *Resolution extension and exit wave reconstruction in complex HREM*. Ultramicroscopy, vol. 98, 99–114, 2004.

[Huang 2010] T. Huang, and X.-H. N. Xu. *Synthesis and characterization of tunable rainbow colored colloidal silver nanoparticles using single-nanoparticle plasmonic microscopy and spectroscopy*. Journal of Materials Chemistry, vol. 20, 9867–9876, 2010.

[Huijben 2006] M. Huijben, Rijnders G., D. H. A. Blank, S. Bals, S. Van Aert, J. Verbeeck, G. Van Tendeloo, A. Brinkman, and H. Hilgenskamp. *Electronically coupled complementary interfaces between perovskite band insulators*. Nature Materials, vol. 5, 556–560, 2006.

[Hÿtch 1994] M. J. Hÿtch, and W. M. Stobbs. *Quantitative comparison of high resolution TEM images with image simulations*. Ultramicroscopy, vol. 53, 191–203, 1994.

[Hÿtch 1998] M. J. Hÿtch, E. Snoeck, and R. Kilaas. *Quantitative measurement of displacement and strain fields from HREM micrographs*. Ultramicroscopy, vol. 74, 131–146, 1998.

[Hÿtch 2003] M. J. Hÿtch, J.-L. Putaux, and J.-M. Pénisson. *Measurement of the displacement field of dislocations to 0.03 Å by electron microscopy*. Nature, vol. 423, 270–273, 2003.

[Isaacson 1979] M. Isaacson, D. Kopf, M. Ohtsuki, and M. Utlaut. *Atomic imaging using the dark-field annular detector in the STEM*. Ultramicroscopy, vol. 4, 1979.

[Ishikawa 2015] R. Ishikawa, A. R. Lupini, Y. Hinuma, and S. J. Pennycook. *Large-angle illumination STEM: Toward three-dimensional atom-by-atom imaging*. Ultramicroscopy, vol. 151, 122–129, 2015.

[Ishizuka 2002] K. Ishizuka. *A practical approach for STEM image simulation based on the FFT multislice method*. Ultramicroscopy, vol. 90, 71–83, 2002.

[Jain 2007] P. K. Jain, I. H. El-Sayed, and M. A. El-Sayed. *Au nanoparticles target cancer*. Nano Today, vol. 2, 18–29, 2007.

[Jia 2004] C. L. Jia, M. Lentzen, and K. Urban. *High-Resolution Transmission Electron Microscopy Using Negative Spherical Aberration*. Microscopy and Microanalysis, vol. 10, 174–184, 2004.

[Jia 2008] C.-L. Jia, S.-B. Mi, K. Urban, I. Vrejoiu, M. Alexe, and D. Hesse. *Atomic-scale study of electric dipoles near charged and uncharged domain walls in ferroelectric films*. Nature Materials, vol. 7, 57–61, January 2008.

[Jia 2009a] C. L. Jia, S. B. Mi, J. Faley, U. Poppe, J. Schubert, and K. Urban. *Oxygen octahedron reconstruction in the $SrTiO_3/LaAlO_3$ heterointerfaces investigated using aberration-corrected ultrahigh-resolution transmission electron microscopy*. Physical Review B, vol. 79, 081405(R), 2009.

[Jia 2009b] C. L. Jia, S. B. Mi, K. Urban, I. Vrejoiu, M. Alexe, and D. Hesse. *Effect of a Single Dislocation in a Heterostructure Layer on the Local*

Polarization of a Ferroelectric Layer. Physical Review Letters, vol. 102, 117601, March 2009.

[Jia 2014] C. L. Jia, S. B. Mi, J. Barthel, D. W. Wang, R. E. Dunin-Borkowski, K. W. Urban, and A. Thust. *Determination of the 3D shape of a nanoscale crystal with atomic resolution from a single image*. Nature Materials, vol. 13, 1044–1049, 2014.

[Jinschek 2008] J. R. Jinschek, K. J. Batenburg, H. A. Calderon, R. Kilaas, V. Radmilovic, and C. Kisielowski. *3-D reconstruction of the atomic positions in a simulated gold nanocrystal based on discrete tomography:Prospects of atomic resolution electron tomography*. Ultramicroscopy, vol. 108, 589–604, 2008.

[Johnson 2008] C. L. Johnson, E. Snoeck, M. Ezcurdia, B. Rodriguez-Gonzalez, I. Pastoriza-Santos, L. M. Liz-Marzan, and M. J. Hytch. *Effects of elastic anisotropy on strain distributions in decahedral gold nanoparticles*. Nature Materials, vol. 7, 120–124, 2008.

[Jones 2014] L. Jones, K. E. MacArthur, V. T. Fauske, A. T. J. van Helvoort, and P. D. Nellist. *Rapid Estimation of Catalyst Nanoparticle Morphology and Atomic-Coordination by High-Resolution Z-Contrast Electron Microscopy*. Nano Letters, vol. 14, no. 11, 6336–6341, 2014.

[Katz-Boon 2011] H. Katz-Boon, C. J. Rossouw, M. Weyland, A. M. Funston, P. Mulvaney, and J. Etheridge. *Three-Dimensional Morphology and Crystallography of Gold Nanorods*. Nano Letters, vol. 11, 273–278, 2011.

[Katz-Boon 2015] H. Katz-Boon, M. Walsh, C. Dwyer, P. Mulvaney, A. M. Funston, and J. Etheridge. *Stability of Crystal Facets in Gold Nanorods*. Nano Letters, vol. 15, 1635–1641, 2015.

[Kay 2009] S. M. Kay. *Fundamentals of Statistical Signal Processing: Volume II Detection Theory*. Prentice-Hall, Inc., New Jersey, 2009.

[Ke 2010] X. Ke, S. Bals, D. Cott, T. Hantschel, H. Bender, and G. Van Tendeloo. *Three-dimensional analysis of carbon nanotube networks in interconnects by electron tomography without missing wedge artefacts*. Microscopy and Microanalysis, vol. 16, 210–217, 2010.

[Kim 2012] Y.-M. Kim, J. He, M. D. Biegalski, H. Ambaye, V. Lauter, H. M. Christen, S. T. Pantelides, S. J. Pennycook, S. V. Kalinin, and A. Y. Borisevich. *Probing oxygen vacancy concentration and homogeneity in solid-oxide fuell-cell cathode materials on the subunit-cell level*. Nature Materials, vol. 11, 888–894, 2012.

[Kim 2014] Y.-M. Kim, A. Morozovska, E. Eliseev, M. P. Oxley, R. Mishra, S. V. Selbach, T. Grande, S. T. Pantelides, S. V. Kalinin, and A. Y. Borisevich. *Direct observation of ferroelectric field effect and vacancy-controlled screening at the $BiFeO_3/La_xSr_{1?x}MnO_3$ interface*. Nature Materials, vol. 13, 1019–1025, 2014.

[Kimoto 2010] K. Kimoto, T. Asaka, X. Yu, T. Nagai, Y. Matsui, and K. Ishizuka. *Local crystal structure analysis with several picometer precision using scanning transmission electron microscopy*. Ultramicroscopy, vol. 110, 778–782, 2010.

[Kirkland 1995] A. I. Kirkland, W. O. Saxton, K.-L. Chau, K. Tsuno, and M. Kawasaki. *Super-resolution by aperture synthesis: tilt series reconstruction in CTEM*. Ultramicroscopy, vol. 57, 355–374, 1995.

[Kirkland 2004] A. I. Kirkland, and R. R. Meyer. *"Indirect" High-Resolution Transmission Electron Microscopy: Aberration Measurement and Wavefunction Reconstruction*. Microscopy and Microanalysis, vol. 10, 401–413, 2004.

[Kisielowski 2001a] C. Kisielowski, Principe E., B. Freitag, and D. Hubert. *Benefits of microscopy with super resolution*. Physica B, vol. 308-310, 1090–1096, 2001.

[Kisielowski 2001b] C. Kisielowski, C. J. D. Hetherington, Y. C. Wang, R. Kilaas, M. A. O'Keefe, and A. Thust. *Imaging columns of light elements carbon, nitrogen and oxygen with sub Ångstom resolution*. Ultramicroscopy, vol. 89, 243–263, 2001.

[Kisielowski 2008] C. Kisielowski, B. Freitag, M. Bischoff, H. van Lin, S. Lazar, G. Knippels, P. Tiemeijer, M. van der Stam, S. von Harrach, M. Stekelenburg, M. Haider, S. Uhlemann, H. Müller, P. Hartel, B. Kabius, D. Miller, I. Petrov, E. A. Olson, T. Donchev, E. A. Kenik, A. R. Lupini, J. Bentley, S. J. Pennycook, I. M. Anderson, A. M. Minor, A. K. Schmid, T. Duden, V. Radmilovic, Q. M. Ramasse, M. Watanabe, R. Erni, E. A. Stach, P. Denes, and U. Dahmen. *Detection of Single Atoms and Buried Defects in Three Dimension by Aberration-Corrected Electron Microscope with 0.5-Å Information Limit*. Microscopy and Microanalysis, vol. 14, 469–477, 2008.

[Klabunde 2002] K. J. Klabunde (ed.). *Nanoscale Materials in Chemistry*. John Wiley and Sons, Inc., 2002. doi: 10.1002/0471220620.

[Klingstedt 2012] M. Klingstedt, M. Sundberg, L. Eriksson, S. Haigh, A. Kirkland, Grüner D., A. De Backer, S. Van Aert, and O. Terasaki. *Exit wave reconstruction from focal series of HRTEM images, single crystal XRD and total energy studies on Sb_xWO_{3+y} (x 0.11)*. Zeitschrift für Kristallographie, vol. 227, 341–349, 2012.

[Koster 1987] A. J. Koster, A. van den Bos, and K. D. van der Mast. *An autofocus method for a TEM*. Ultramicroscopy, vol. 21, 209–222, 1987.

[Kullback 1951] S. Kullback, and R.A. Leibler. *On information and sufficiency*. Annals of Mathematical Statistics, vol. 22, 79–86, 1951.

[Kullback 1959] S. Kullback. *Information theory and statistics*. Springer Texts in Statistics. John Wiley and Sons, New York, 1959.

[Kundu 2014] P. Kundu, S. Turner, S. Van Aert, N. Ravishankar, and G. Van Tendeloo. *Atomic Structure of Quantum Gold Nanowires: Quantification of the Lattice Strain*. ACS Nano, vol. 8, 599–606, 2014.

[Lagarias 1998] J. C. Lagarias, J. A. Reeds, M. H. Wright, and P. E. Wright. *Convergence Properties of the Nelder-Mead Simplex Method in Low Dimension*. SIAM Journal of Optimization, vol. 9, no. 1, 112–147, 1998.

[Lawton 1971] W. H. Lawton, and E. A. Sylvestre. *Elimination of Linear Parameters in Nonlinear Regression*. Technometrics, vol. 13, no. 3, 461–467, 1971.

[LeBeau 2008a] J. M. LeBeau, S. D. Findlay, L. J. Allen, and S. Stemmer. *Quantitative Atomic Resolution Scanning Transmission Electron Microscopy*. Physical Review Letters, vol. 100, 206101, 2008.

[LeBeau 2008b] J. M. LeBeau, and S. Stemmer. *Experimental quantification of annular dark-field images in scanning transmission electron microscopy*. Ultramicroscopy, vol. 108, 1653–1658, 2008.

[LeBeau 2010] J. M. LeBeau, S. D. Findlay, L. J. Allen, and S. Stemmer. *Standardless Atom Counting in Scanning Transmission Electron Microscopy*. Nano Letters, vol. 10, 4405–4408, 2010.

[Li 2008] Z. Y. Li, N. P. Young, M. Di Vece, S. Palomba, R. E. Palmer, A. L. Bleloch, B. C. Curley, R. L. Johnston, J. Jiang, and J. Yuan. *Three-dimensional atomic-scale structure of size-selected gold nanoclusters*. Nature, vol. 451, 46–48, 2008.

[Li 2013] L. Li, P. Gao, C. T. Nelson, J. R. Jokisaari, Y. Zhang, S.-J. Kim, A. Melvill, C. Adamo, D. G. Schlom, and X. Pan. *Atomic Scale Structure Changes Induced by Charged Domain Walls in Ferroelectric Materials*. Nano Letters, vol. 13, no. 11, 5218–5223, 2013.

[Lichte 1986] H. Lichte. *Electron holography approaching atomic resolution*. Ultramicroscopy, vol. 20, 293–304, 1986.

[Liu 2004] M. Z. Liu, and P. Guyot-Sionnest. *Synthesis and optical characterization of Au/Ag core/shell nanorods*. Journal of Physical Chemistry B, vol. 108, 5882–5888, 2004.

[Liz-Marzàn 2003] L. M. Liz-Marzàn, and P. V. Kamat (eds.). *Nanoscale Materials*. Springer US, 2003. doi: 10.1007/b101855.

[Lubk 2013] A. Lubk, M. D. Rossell, J. Seidel, Y. H. Chu, R. Ramesh, M. J. Hytch, and E. Snoeck. *Electromechanical Coupling among Edge Dislocations, Domain Walls, and Nanodomains in $BiFeO_3$ Revealed by Unit-Cell-Wise Strain and Polarization Maps*. Nano Letters, vol. 13, 1410–1415, 2013.

[Ma 2010] Y. Y. Ma, W. Y. Li, E. C. Cho, Z. Y. Li, T. K. Yu, J. Zeng, Z. X. Xie, and Y. N. Xia. *Au/Ag Core-Shell Nanocubes with Finely Tuned and Well-Controlled Sizes, Shell Thicknesses, and Optical Properties*. ACS Nano, vol. 4, 6725–6734, 2010.

[MacArthur 2014] K. E. MacArthur, L. B. Jones, and P. D. Nellist. *How flat is your detector? Non-uniform annular detector sensitivity in STEM quantification*. Journal of Physics: Conference Series, vol. 522, no. 1, 012018, 2014.

[MacLaren 2014] I. MacLaren, and Q. M. Ramasse. *Aberration-corrected scanning transmission electron microscopy for atomic-resolution studies of functional oxides*. International Materials Reviews, vol. 59, no. 3, 115–131, 2014.

[Martinez 2014a] G. T. Martinez, A. De Backer, A. Rosenauer, J. Verbeeck, and S. Van Aert. *The effect of probe inaccuracies on the quantitative model-based analysis of high angle annular dark field scanning transmission electron microscopy images*. Micron, vol. 63, 57–63, 2014.

[Martinez 2014b] G. T. Martinez, A. Rosenauer, A. De Backer, J. Verbeeck, and S. Van Aert. *Quantitative composition determination at the atomic level using model-based high-angle annular dark field scanning transmission electron microscopy*. Ultramicroscopy, vol. 137, 12–19, 2014.

[Martinez 2015] G. T. Martinez, L. Jones, A. De Backer, A. Béché, J. Verbeeck, S. Van Aert, and P. D. Nellist. *Quantitative STEM normalisation: the importance of the electron flux*. Ultramicroscopy, 2015. submitted.

[McLachlan 2000] G. McLachlan, and D. Peel. *Finite Mixture Models*. Wiley series in probability and statistics. John Wiley and Sons, inc., 2000.

[Mehrtens 2013a] T. Mehrtens, K. Müller, M. Schowalter, D. Hu, D. M. Schaadt, and A. Rosenauer. *Measurement of indium concentration profiles and segregation efficiencies from high-angle annular dark field-scanning transmission electron microscopy images*. Ultramicroscopy, vol. 131, 1–9, 2013.

[Mehrtens 2013b] T. Mehrtens, M. Schowalter, D. Tytko, P. Choi, D. Raabe, L. Hoffmann, H. Jonen, U. Rossow, A. Hangleiter, and A. Rosenauer. *Measurement of the indium concentration in high indium content InGaN layers by scanning transmission electron microscopy and atom probe tomography*. Applied Physics Letters, vol. 102, 132112, 2013.

[Meyer 2002] R. R. Meyer, A. I. Kirkland, and W. O. Saxton. *A new method for the determination of the wave aberration function for high resolution TEM 1. Measurement of the symmetric aberrations*. Ultramicroscopy, vol. 92, 89–109, 2002.

[Midgley 2003] P. A. Midgley, and M. Weyland. *3D electron microscopy in the physical sciences: the development of Z-contrast and EFTEM tomography*. Ultramicroscopy, vol. 96, 413–431, 2003.

[Midgley 2009] P. A. Midgley, and R. E. Dunin-Borkowski. *Electron tomography and holography in materials science*. Nature Materials, vol. 8, 271–280, 2009.

[Miedema 1994] M. A. O. Miedema, A. van den Bos, and A. H. Buist. *Experimental design of exit wave reconstruction from a transmission electron microscope defocus series*. IEEE Transactions on Instrumentation and Measurement, vol. 43, 181–186, 1994.

[Mitchell 2003] R. H. Mitchell (ed.). *Perovskites - Mordern and Ancient*. Almaz, 2003.

[Mkhoyan 2008] K. A. Mkhoyan, S. E. Maccagnano-Zacher, E. J. Kirkland, and J. Silcox. *Effect of amorphous layers on ADF-STEM imaging*. Ultramicroscopy, vol. 108, 791–803, 2008.

[Mood 1974] A. M. Mood, F. A. Graybill, and D. C. Boes. *Introduction to the Theory of Statistics*. McGraw-Hill Book Company, Third edition, 1974.

[Muller 1999] D. A. Muller. *Why changes in bond lengths and cohesion lead to core-level shifts in metals, and consequences for the spatial difference method*. Ultramicroscopy, vol. 78, 163–174, 1999.

[Myung 2003] I. J. Myung. *Tutorial on maximum likelihood estimation*. Journal of Mathematical Psychology, vol. 47, 90–100, 2003.

[Nebel 2003] C. E. Nebel. *Semiconductor materials: From gemstone to semiconductor*. Nature Materials, vol. 2, 431–432, 2003.

[Nellist 1999] P. D. Nellist, and S. J. Pennycook. *Incoherent imaging using dynamically scattered coherent electrons*. Ultramicroscopy, vol. 78, 111–124, 1999.

[Nellist 2000] P. D. Nellist, and S. J. Pennycook. *The Principles and Interpretation of Annular Dark-Field Z-Contrast Imaging*. Advances in Imaging and Electron Physics, vol. 113, 147–203, 2000.

[Nellist 2004] P. D. Nellist, M. F. Chisholm, N. Dellby, O. L. Krivanek, M. F. Murfitt, Z. S. Szilagyi, A. R. Lupini, A. Y. Borisevich, W. H. Sides Jr., and S. J. Pennycook. *Direct sub-angstrom imaging of a crystal lattice*. Science, vol. 305, 1741, 2004.

[Nellist 2006] P. D. Nellist, G. Behan, A. I. Kirkland, and C. J. D. Hetherington. *Confocal operation of a transmission electron microscope with two spherical aberration correctors*. Applied Physics Letters, vol. 89, no. 124105, 2006.

[Oliveira 2001] M. M. Oliveira, B. Bowen, R. McKenna, and Y.-S. Chang. *Fast Digital Image Inpainting*. In Proceedings of the International Conference on Visualization, Imaging and Image Processing (VIIP 2001), Marbella, Spain, September 3-5, 2001 2001.

[Olson 1997] G. B. Olson. *Computational Design of Hierarchically Structure Materials*. Science, vol. 277, 1237–1242, 1997.

[Olson 2000] G. B. Olson. *Designing a new material world.* Science, vol. 288, 993–998, 2000.

[Op de Beeck 1996] M. Op de Beeck, D. Van Dyck, and W. Coene. *Wave function reconstruction in HRTEM: the parabola method*. Ultramicroscopy, vol. 64, 167–183, 1996.

[Papoulis 1965] A. Papoulis (ed.). *Probability, Random Variables, and Stochastic Processes*. McGraw-Hill, New York, 1965.

[Park 2011] K. Park, L. F. Drummy, and R. A. Vaia. *Ag shell morphology on Au nanorod core: role of Ag precursor complex*. Journal of Materials Chemistry, vol. 21, 15608–15618, 2011.

[Pastoriza-Santos 2007] I. Pastoriza-Santos, A. Sánchez-Iglesias, F. J. García de Abajo, and L. Liz-Marzán. *Environmental Optical Sensitivity of Gold Nanodecahedra*. Advanced Functional Materials, vol. 17, 1443–1450, 2007.

[Pecharromán 2008] C. Pecharromán, J. Pérez-Juste, G. Mata-Osoro, L. M. Liz-Marzán, and Mulvaney P. *Redshift of surface plasmon modes of small gold rods due to their atomic roughness and end-cap geometry*. Physical Review B, vol. 77, 035418, 2008.

[Peng 1997] L.-M. Peng. *Anisotropic Thermal Vibrations and Dynamical Electron Diffraction by Crystals*. Acta Crystallographica, vol. A53, 663–672, 1997.

[Pennycook 1988] S. J. Pennycook, and L. A. Boatner. *Chemically sensitive structure-imaging with a scanning transmission electron microscope*. Nature, vol. 336, 565–567, 1988.

[Pennycook 2011] S. J. Pennycook, and P. D. Nellist (eds.). *Scanning Transmission Electron Microscopy*. Springer, 2011.

[Ralph 2002] T. R. Ralph, and M. P. Hogarth. *Catalysis for Low Temperature Fuel Cells Part II: The Anode Challenges*. Platinum Metals Review, vol. 46, no. 3, 117–135, 2002.

[Rayleigh 1896] Lord Rayleigh. *On the Theory of Optical images, with Special Reference to the Microscope*. Philosophical Magazine, vol. 42, 167–195, 1896.

[Retsky 1974] M. Retsky. *Observed single atom elastic cross sections in a scanning electron microscope*. Optik, vol. 41, 127, 1974.

[Rosenauer 2008] A Rosenauer, and M Schowalter. *STEMSIM - a New Software Tool for Simulation of STEM HAADF Z-Contrast Imaging*. In Microscopy of Semiconducting Materials 2007, A.G. Cullis, and P.A. Midgley (eds.), vol. 120 of *Springer Proceedings in Physics*, 170–172. Springer Netherlands, 2008.

[Rosenauer 2009] A. Rosenauer, K. Gries, K. Müller, A. Pretorius, M. Schowalter, A. Avramescu, K. Engl, and S. Lutgen. *Measurement of specimen thickness and composition in $Al_xGa_{1-x}N$/GaN using high-angle annular dark field images*. Ultramicroscopy, vol. 109, 1171–1182, 2009.

[Rosenauer 2011] A Rosenauer, T. Mehrtens, K. Müller, K. Gries, M Schowalter, P. V. Satyam, S. Bley, C. Tessarek, D. Hommel, K. Sebald, M. Seyfried, J. Gutowski, A. Avramescu, K. Engl, and S. Lutgen. *Composition mapping in InGaN by scanning transmission electron microscopy*. Ultramicroscopy, vol. 111, 1316–1327, 2011.

[Sánchez-Iglesias 2006] A. Sánchez-Iglesias, I. Pastoriza-Santos, J. Pérez-Juste, B. Rodríguez-González, F. J. García de Abajo, and L. M. Liz-Marzán. *Synthesis and Optical Properties of Gold Nanodecahedra with Siz Control*. Advanced Materials, vol. 18, 2529–2534, 2006.

[Sanchez-Iglesias 2010] A. Sanchez-Iglesias, E. Carbo-Argibay, A. Glaria, B. Rodriguez-Gonzalez, J. Perez-Juste, I. Pastoriza-Santos, and L. M. Liz-Marzan. *Rapid Epitaxial Growth of Ag on Au Nanoparticles: From Au Nanorods to Core-Shell Au/Ag Octahedrons*. Chemistry- a European Journal, vol. 16, 5558–5563, 2010.

[Sawada 2009] H. Sawada, Y. Tanishori, N. Ohashi, T. Tomita, F. Hosokawa, T. Kaneyama, Y. Kondo, and K. Takayanagi. *STEM imaging of 47-pm-separated atomic columns by a spherical aberration-corrected electron microscope with a 300-kV cold field emission gun*. Journal of Electron Microscopy, vol. 58, 357–361, 2009.

[Schwarz 1978] G. Schwarz. *Estimating the dimension of a model*. Annals of Statistics, vol. 6, no. 2, 461–464, 1978.

[Scott 2012] M. C. Scott, C.-C. Chen, M. Mecklenburg, C. Zhu, R. Xu, P. Ercius, U. Dahmen, B. C. Regan, and J. Miao. *Electron tomography at 2.4-ångström resolution*. Nature, vol. 483, 444–448, 2012.

[Shibata 2010] N. Shibata, Y. Kohno, S. D. Findlay, H. Sawada, Y. Kondo, and Y. Ikuhara. *New area detector for atomic-resolution scanning transmission electron microscopy*. Journal of Electron Microscopy, vol. 59, no. 6, 473–479, 2010.

[Singhal 1997] A. Singhal, J. C. Yang, and J. M. Gibson. *STEM-based mass spectroscopy of supported Re clusters*. Ultramicroscopy, vol. 67, 191–206, 1997.

[Song 2010] F. Song, X. Wang, R. C. Powles, L. He, N. A. Marks, S. Zhao, J. Wan, Z. Liu, J. Zhou, S. P. Ringer, M. Han, and G. Wang. *Calibrating the atomic balance by carbon nanoclusters*. Applied Physics Letters, vol. 96, 033103, 2010.

[Springborg 2000] M. Springborg. *Methods of Electronic-Structure Calculations: From Molecules to Solids*. John Wiley and Sons, Chichester, UK, 2000.

[Talapatra 2005] S. Talapatra, P. G. Ganesan, T. Kim, R. Vajtai, M. Huang, M. Shima, G. Ramanath, D. Srivastava, S. C. Deevi, and P. M. Ajayan. *Irradiation-Induced Magnetism in Carbon Nanostructures*. Physical Review Letters, vol. 95, 097201, 2005.

[Tedsree 2011] K. Tedsree, T. Li, S. Jones, C. W. A. Chan, K. M. K. Yu, P. A. J. Bogot, E. A. Marquies, G. D. W. Smith, and S. C. E. Tsang. *Hydrogen production from formic acid decomposition at room temperature using a Ag-Pd core-shell nanocatalyst*. Nature Nanotechnology, vol. 6, 302–307, 2011.

[Thust 1996] A. Thust, W. M. J. Coene, M. Op de Beeck, and D. Van Dyck. *Focal-series reconstruction in HRTEM: simulation studies on non-periodic objects*. Ultramicroscopy, vol. 64, 211–230, 1996.

[Thust 2009] A. Thust. *High-Resolution Transmission Electron Microscopy on an Absolute Contrast Scale*. Physical Review Letters, vol. 102, 220801, June 2009.

[Urban 2008] K. W. Urban. *Studying Atomic Structures by Aberration-Corrected Transmission Electron Microscopy*. Science, vol. 321, 506–510, 2008.

[Van Aert 2001] S. Van Aert, and D. Van Dyck. *Do Smaller Probes in a STEM Result in More Precise Measurement of the Distances Between Atom Columns?* Philosophical Magazine B, vol. 81, 1833–1846, 2001.

[Van Aert 2002a] S. Van Aert, A. J. den Dekker, A. van den Bos, and D. Van Dyck. *High-Resolution Electron Microscopy: From Imaging Toward Measuring*. IEEE Transactions on Instrumentation and Measurement, vol. 51, no. 4, 611–615, 2002.

[Van Aert 2002b] S. Van Aert, A. J. den Dekker, D. Van Dyck, and A. van den Bos. *High-resolution electron microscopy and electron tomography: resolution versus precision*. Journal of Structural Biology, vol. 138, 21–33, 2002.

[Van Aert 2002c] S. Van Aert, A. J. den Dekker, D. Van Dyck, and A. van den Bos. *Optimal experimental design of STEM measurement of atom column positions*. Ultramicroscopy, vol. 90, 273–289, 2002.

[Van Aert 2004a] S. Van Aert, A. J. den Dekker, A. van den Bos, and D. Van Dyck. *Statistical Experimental Design for Quantitative Atomic Resolution Transmission Electron Microscopy*. Advances in Imaging and Electron Physics, vol. 130, 1 – 164, 2004.

[Van Aert 2004b] S. Van Aert, A.J. den Dekker, and D. Van Dyck. *How to optimize the experimental design of quantitative atomic resolution TEM experiments?* Micron, vol. 35, 425–429, 2004.

[Van Aert 2005] S. Van Aert, A. J. den Dekker, A. van den Bos, D. Van Dyck, and J. H. Chen. *Maximum likelihood estimation of structure parameters from high resolution electron microscopy images: Part II: A practical example*. Ultramicroscopy, vol. 104, 107–125, 2005.

[Van Aert 2006] S. Van Aert, D. Van Dyck, and A. J. den Dekker. *Resolution of coherent and incoherent imaging systems reconsidered - Classical criteria and a statistical alternative*. Optics Express, vol. 9, no. 14, 3830–3839, 2006.

[Van Aert 2007] S. Van Aert, P. Geuens, D. Van Dyck, C. Kisielowski, and J. R. Jinscheck. *Electron channelling based crystallography*. Ultramicroscopy, vol. 107, 551–558, 2007.

[Van Aert 2009a] S. Van Aert, L. Y. Chang, S. Bals, A. I. Kirkland, and G. Van Tendeloo. *Effect of amorphous layers on the interpretation of restored exit waves*. Ultramicroscopy, vol. 109, 237–246, 2009.

[Van Aert 2009b] S. Van Aert, J. Verbeeck, R. Erni, S. Bals, M. Luysberg, D. Van Dyck, and G. Van Tendeloo. *Quantitative atomic resolution mapping using high-angle annular dark field scanning transmission electron microscopy*. Ultramicroscopy, vol. 109, 1236–1244, 2009.

[Van Aert 2011] S. Van Aert, K. J. Batenburg, M. D. Rossell, R. Erni, and G. Van Tendeloo. *Three-dimensional atomic imaging of crystalline nanoparticles*. Nature, vol. 470, 374–377, 2011.

[Van Aert 2012] S. Van Aert, W. Van den Broek, P. Goos, and D. Van Dyck. *Model-based electron microscopy: From images toward precise numbers for unknown structure parameters*. Micron, vol. 43, no. 4, 509 – 515, 2012.

[Van Aert 2013] S. Van Aert, A. De Backer, G. T. Martinez, B. Goris, S. Bals, and G. Van Tendeloo. *Procedure to count atoms with trustworthy single-atom sensitivity*. Physical Review B, vol. 87, no. 064107, 2013.

[van Benthem 2005] K. van Benthem, A. R. Lupini, M. Kim, H. S. Baik, S. Doh, J.-H. Lee, M. P. Oxley, S. D. Findlay, L. J. Allen, J. T. Luck, and S. J. Pennycook. *Three-dimensional imaging of individual hafnium atoms inside a semiconductor device*. Applied Physics Letters, vol. 87, no. 034104, 2005.

[van Benthem 2006] K. van Benthem, A. R. Lupini, M. P. Oxley, S. D. Findlay, L. J. Allen, and S. J. Pennycook. *Three-dimensional ADF imaging of individual atoms by through-focal series scanning transmission electron microscopy*. Ultramicroscopy, vol. 106, 1062–1068, 2006.

[van den Bos 1982] A. van den Bos. *Handbook of Measurement Science*, vol. 1, Parameter estimation, 331–377. Chicester Wiley, 1982.

[van den Bos 2001] A. van den Bos, and A. J. den Dekker. *Resolution reconsidered - Conventional approaches and an alternative*. Advances in Imaging and Electron Physics, vol. 117, 241–360, 2001. San Diego: Academic Press.

[van den Bos 2007] A. van den Bos. *Parameter estimation for scientists and engineers*. Wiley, 2007.

[Van den Broek 2011] W. Van den Broek, S. Van Aert, P. Goos, and D. Van Dyck. *Throughput maximization of particle radius measurements through balancing size versus current of the electron probe*. Ultramicroscopy, vol. 111, 940–947, 2011.

[Van den Broek 2012] W. Van den Broek, and C. T. Koch. *Method for Retrieval of the Three-Dimensional Object Potential by Inversion of Dynamical Electron Scattering*. Physical Review Letters, vol. 109, 245502, 2012.

[Van den Broek 2013] W. Van den Broek, and C. T. Koch. *General framework for quantitative three-dimensional reconstruction from arbitrary detection geometries in TEM*. Physical Review B, vol. 87, 184108, 2013.

[Van Dyck 1990] D. Van Dyck, and M. Op de Beeck. *New direct methods for phase and structure retrieval in HREM*. In Proceedings of the XIIth International Congress for Electron Microscopy, 26–27, Seattle, 1990. San Fransisco Press.

[Van Dyck 1993] D. Van Dyck, M. Op de Beeck, and W. Coene. *A new approach to object wave function reconstruction in electron microscopy*. Optik, vol. 93, no. 3, 103–107, 1993.

[Van Dyck 1996] D. Van Dyck, and M. Op de Beeck. *A simple intuitive theory for electron diffraction*. Ultramicroscopy, vol. 64, 99–107, 1996.

[Van Dyck 1997] D. Van Dyck, E. Bettens, J. Sijbers, M. Op de Beeck, A. van den Bos, and A. J. den Dekker. *From high resolution image to atomic structure: how far are we?* Scanning Microscopy, vol. 11, 467–478, 1997.

[Van Dyck 1999] D. Van Dyck, and J. H. Chen. *Towards an exit wave in closed analytical form*. Acta Crystallographica, vol. A55, 212–115, 1999.

[Van Dyck 2002] D. Van Dyck. *High-Resolution Electron Microscopy*. Advances in Imaging and Electron Physics, vol. 123, 105–171, 2002.

[Van Dyck 2003] D. Van Dyck, S. Van Aert, A. J. den Dekker, and A. van den Bos. *Is atomic resolution transmission electron microscopy able to resolve and refine amorphous structures?* Ultramicroscopy, vol. 98, 27–42, 2003.

[Van Dyck 2012] D. Van Dyck, J. R. Jinscheck, and F.-R. Chen. *'Big Bang' tomography as a new route to atomic-resolution electron tomography*. Nature, vol. 486, 243–246, 2012.

[Voyles 2002] P. M. Voyles, D. A. Muller, J. L. Grazul, P. H. Citrin, and H.-J. L. Gossmann. *Atomic-scale imaging of individual dopant atoms and clusters in highly n-type bulk Si*. Nature, vol. 416, 826–829, 2002.

[Wang 2010a] A. Wang, F. R. Chen, S. Van Aert, and D. Van Dyck. *Direct structure inversion from exit waves Part I: Theory and simulations*. Ultramicroscopy, vol. 110, 527–534, 2010.

[Wang 2010b] P. Wang, G. Behan, M. Takeguchi, A. Hashimoto, K. Mitsuishi, M. Shimojo, A. I. Kirkland, and P. D. Nellist. *Nanoscale Energy-Filtered Scanning Confocal Electron Microscopy Using a Double-Aberration-Corrected Transmission Electron Microscope*. Physical Review Letters, vol. 104, 200801, 2010.

[Wang 2011] P. Wang, G. Behan, A. I. Kirkland, P. D. Nellist, E. C. Cosgriff, A. J. D'Alfonso, A. J. Morgan, L. J. Allen, A. Hashimoto, M. Takeguchi, K. Mitsuishi, and M. Shimojo. *Bright-field scanning confocal electron microscopy using a double aberration-corrected transmission electron microscope*. Ultramicroscopy, vol. 111, 877–886, 2011.

[Wang 2012a] A. Wang, F. R. Chen, S. Van Aert, and D. Van Dyck. *Direct structure inversion from exit waves. Part II: A practical example*. Ultramicroscopy, vol. 116, 77–85, 2012.

[Wang 2012b] A. Wang, S. Van Aert, P. Goos, and D. Van Dyck. *Precision of three-dimensional atomic scale measurements from {HRTEM} images: What are the limits?* Ultramicroscopy, vol. 114, 20 – 30, 2012.

[Wiesendanger 1994] R. Wiesendanger (ed.). *Scanning Probe Microscopy and Spectroscopy - Method and Applications*. Cambridge University Press, 1994.

[Wikipedia 2015] Wikipedia. *http://en.wikipedia.org/wiki/Materials_science*, February 2015.

[Willets 2007] K. A. Willets, and R. P. Van Duyne. *Localized surface plasmon resonance spectroscopy and sensing*. Annual Review of Physical Chemistry, vol. 58, 267–297, 2007.

[Williams 2009] D. B. Williams, and C. B. Carter. *Transmission Electron Microscopy: A Textbook for Materials Science*. Springer, Second edition, 2009.

[Wolfe 1970] J. H. Wolfe. *Pattern clustering by multivariate mixture analysis*. Multivariate Behavioral Research, vol. 5, 329–350, 1970.

[Xiang 2008] Y. U. Xiang, X. C. Wu, D. F. Liu, Z. Y. Li, W. G. Chu, L. L. Feng, K. Zhang, W. Y. Zhou, and S. S. Xie. *Gold nanorod-seeded growth of silver nanostructures: From homogeneous coating to anisotropic coating*. Langmuir, vol. 24, 3465–3470, 2008.

[Xu 2005] X. Xu, S. P. Beckman, P. Specht, E. R. Weber, D. C. Chrzan, R. P. Erni, I. Arslan, N. Browning, A. Bleloch, and C. Kisielowski. *Distortion and Segragation in a Dislocation Core Region at Atomic Resolution*. Phyical Review Letters, vol. 95, 145501, 2005.

[Yang 2006] Z. S. Yang, and H. T. Chang. *Anisotropic syntheses of boat-shaped core-shell Au-Ag nanocrystals and nanowires*. Nanotechnology, vol. 17, 2304–2310, 2006.

[Yang 2012] P. Yang, and J.-M. Tarascon. *Towards systems materials engineering*. Nature Materials, vol. 11, 560–563, 2012.

[Yang 2015] H. Yang, T. J. Pennycook, and P. D. Nellist. *Efficient phase contrast imaging in STEM using a pixelated detector. Part II: Optimisation of imaging conditions*. Ultramicroscopy, vol. 151, 232–239, 2015.

[Yankovich 2014] A. B. Yankovich, B. Berkels, W. Dahmen, P. Binev, S. I. Sanchez, S. A. Bradley, A. Li, I. Szlufarska, and P. Voyles. *Picometre-precision analysis of scanning transmission electron microscopy images of platinum nanocatalysts*. Nature Communications, vol. 5, 4155, 2014.

[Young 2008] N. P. Young, Z. Y. Li, Y. Chen, S. Palomba, M. Di Vece, and R. E. Palmer. *Weighing Supported Nanoparticles:Size-Selected Clusters as Mass Standards in Nanometrology*. Physical Review Letters, vol. 101, 246103, 2008.

[Zanchet 2001] D. Zanchet, B. D. Hall, and D. Ugarte. *Characterization of Nanophase Materials*, X-ray characterization of nanoparticles, 13–36. Wiley-VCH, 2001.

[Zeches 2009] R. J. Zeches, M. D. Rossell, J. X. Zhang, A. J. Hatt, Q. He, C.-H. Yang, A. Kumar, C. H. Wang, A. Melvill, C. Adamo, G. Sheng, Y.-H. Chu, J. F. Ihlefeld, R. Erni, C. Ederer, V. Gopalan, L. Q. Chen, D. G. Schlom, N. A. Spaldin, L. W. Martin, and R. Ramesh. *A Strain-Driven Morphotrophic Phase Boundary in $BiFeO_3$*. Science, vol. 326, 977–980, 2009.

[Zhao 2006] J. Zhao, J. X. Zhang, C. R. Yonzon, A. J. Haes, and R. P. Van Duyne. *Localized surface plasmon resonance biosensors*. Nanomedicine, vol. 1, 219–228, 2006.

List of symbols and abbreviations

Roman characters

Character	Page	Explanation
a_{m_i}	24	column dependent width of the function $\phi_{1\mathrm{s},m}(\mathbf{r}-\boldsymbol{\beta}_m)$
B	35	Debye-Waller factor
C_s	35	spherical aberration constant
C_5	35	spherical aberration of 5th order
CS_n	106	expected scattering cross-section for n atoms in a column
$D_{1\mathrm{s}}$	25	extinction distance
$D\left(p_{\mathcal{H}_1}, p_{\mathcal{H}_0}\right)$	108	Kullback-Leibler divergence from $p_{\mathcal{H}_1}$ to $p_{\mathcal{H}_0}$
d	28	interatomic distance
	63	number of parameters in the Gaussian mixture model
$\mathbb{E}$	17	expected value
E_0	24	incident electron energy
$E_{1\mathrm{s},m_i}$	24	energy of the $1s$-state
$EN(\hat{\tau})$	63	entropy associated with Gaussian mixture model
$F_{\boldsymbol{\theta}}$	19	Fisher information matrix
F_{rs}	19	(r, s)th element of the Fisher information matrix
$F_{\boldsymbol{\theta}}^{-1}$	19	inverse of the Fisher information matrix
$\hat{F}_{\boldsymbol{\theta}}$	34	estimated Fisher information matrix
$F\left(x;\lambda\right)$	104	cumulative distribution function of the Poisson distribution with parameter λ evaluated at x
$f_{kl}(\boldsymbol{\theta})$	17	expectation model as a function of the unknown parameters
$f_{kl}^{\mathrm{c}}(\boldsymbol{\theta})$	26	expectation model as a function of the unknown parameters for the complex exit wave
$f_{kl}^{\mathrm{i},m}$	27	expectation model as a function of the unknown parameters for the image intensity of the mth image of a focal series
$f_{kl}^{\mathrm{p}}(\boldsymbol{\theta})$	26	expectation model as a function of the unknown parameters for the phase of the exit wave
$f_{\mathrm{mix}}\left(\hat{\mathbf{V}};\boldsymbol{\Psi}_G\right)$	60	probability density function of a Gaussian mixture model having G components
G	20	length of vector function of vector parameters
	60	number of Gaussian components in Gaussian mixture model
g	20	index
$\mathcal{H}_0$	103	null hypothesis

$\mathcal{H}_1$	103	alternative hypothesis
$I(\mathbf{r}, z; C_s, \epsilon_m)$	27	intensity in the image plane
I_{det}	85	mean number of counts generated by the probe hitting the detector area
I_{exp}	85	experimental STEM image intensities
I_{norm}	27	normalisation factor
	85	normalised STEM image intensities
I_{vac}	85	mean number of counts in the vacuum due to the detector's amplifier offset
i	18	index
j	45	number of iteration in efficient fitting algorithm
K	17	number of pixels in x-direction of a HR(S)TEM image
k	17	index
L	17	number of pixels in y-direction of a HR(S)TEM image
$L(\mathbf{t})$	21	likelihood function
$L(\mathbf{\Psi}_G)$	61	likelihood function of parameter vector $\mathbf{\Psi}_G$
l	17	index
$\ln \text{LR}\left(\boldsymbol{\omega}^{\text{Im}}\right)$	107	log likelihood ratio of $\boldsymbol{\omega}^{\text{Im}}$
M	28	number of focal images
m	27	index for mth image of focal series
m_i	18	index: mth column of type i
N	44	total number of atomic columns in HR(S)TEM image
	37	sample size
N_d	27	incident electron dose per area
N_p	35	incident electron dose per pixel
N/G	69	number of observations per component in the Gaussian mixture model
n	44	index: nth column
	103	number of atoms in a projected atomic column
$n_{\mathcal{H}_0}$	103	number of atoms in a column under the null hypothesis
$n_{\mathcal{H}_1}$	103	number of atoms in a column under the alternative hypothesis
$P(I_g\|\phi_g)$	73	posterior probability with which a scattering cross-section belonging to component ϕ_g resides in I_g
$P(\phi_g\|I_g)$	73	posterior probability that a scattering cross-section belonging to I_g stems from component ϕ_g
P_{e}	103	probability of error
$P(\mathcal{H}_i)$	103	prior probability associated with $\mathcal{H}_i$
$P\left(\mathcal{H}_i\|\mathcal{H}_j\right)$	103	conditional probability of deciding $\mathcal{H}_i$ when $\mathcal{H}_j$ is true
$p(\boldsymbol{\omega})$	17	(joint) probability density function
$p_{C_s}(\mathbf{r}; C_s)$	25	point spread function for spherical aberration
$p_{\epsilon_s}(\mathbf{r}; \epsilon_m)$	25	point spread function for defocus
$p(\omega; \mathcal{H}_i)$	103	conditional probability function assuming $\mathcal{H}_i$ to be true
$p_{\mathcal{H}_i}$	108	$p(\omega; \mathcal{H}_i)$
R	17	number of parameters in the vector $\boldsymbol{\theta}$
r	17	index
	63	scaling parameter

$\mathbf{r}$	24	two-dimensional vector in the exit plane of the object, perpendicular to the incident beam direction
s	19	index
s_{β_x}	37	standard deviation of x-coordinate
s_V	37	standard deviation of scattering cross-section
$s^2_{\beta_x}$	37	sample variance of x-coordinate
s^2_V	37	sample variance of scattering cross-section
$\mathbf{t}$	21	vector of independent variables
$t_{1-\frac{\alpha}{2},N-1}$	37	$1-\frac{\alpha}{2}$-quantile of the Student's t distribution with $N-1$ degrees of freedom
V_n	60	stochastic variable for the scattering cross-section of nth atomic column
$\hat{V}_n$	105	estimated scattering cross-section of nth atomic column
$\bar{V}$	37	sample mean of the scattering cross-section
$\mathbf{V}$	77	vector of the stochastic variables for the scattering cross-sections
V_0	28	accelerating voltage
$\mathbf{w}$	17	vector of the available observations
w_{kl}	17	observation at the pixel value (k,l)
$w^{\mathcal{I}}_{kl}$	26	observation of the imaginary part of the complex exit wave at the pixel value (k,l)
$w^{\mathcal{R}}_{kl}$	26	observation of the real part of the complex exit wave at the pixel value (k,l)
x_k	18	x-coordinate at the pixel value (k,l)
y_l	18	y-coordinate at the pixel value (k,l)
Z	28	atomic number
z	35	object thickness

Greek characters

Character	Page	Explanation
α	35	objective aperture angle
	37	significance level
$\boldsymbol{\alpha}$	45	non-linear parameters of the expectation model
$\beta_{x_{m_i}}$	18	x-coordinate of the m_ith atomic column
β_{x_n}	44	x-coordinate of the nth atomic column
$\beta_{y_{m_i}}$	18	y-coordinate of the m_ith atomic column
β_{y_n}	44	y-coordinate of the nth atomic column
$\bar{\beta}_x$	37	sample mean of the x-coordinate
β_1	3	inner collection angle
β_2	4	outer collection angle
γ	28	focal step
$\boldsymbol{\gamma}(\boldsymbol{\theta})$	20	function of the parameters $\boldsymbol{\theta}$
$\hat{\boldsymbol{\gamma}}$	20	unbiased estimator of $\boldsymbol{\gamma}(\boldsymbol{\theta})$
ΔCS	113	increase in scattering cross-section relative to the incident electron beam for a single atom for a linear STEM imaging model

ΔI_{kl}	113	increase in intensity relative to the incident electron beam for a single atom
ΔI^{PI}	112	increase in peak intensity relative to the incident electron beam for a single atom for a linear STEM imaging model
Δx	35	pixel size in x-direction
Δy	35	pixel size in y-direction
δ	67	average increment between successive components of the Gaussian mixture model
ϵ	35	defocus
	28	mean focal value
ϵ_m	27	focal value of mth image of focal series
ζ	18	constant background
$\zeta_{\mathcal{I}}$	26	constant background of imaginary part of the complex exit wave
$\zeta_{\mathcal{R}}$	26	constant background of real part of the complex exit wave
η_{m_i}	18	column intensity of the m_ith Gaussian peak
$\eta^{\mathcal{I}}_{m_i}$	26	column intensity of the m_ith Gaussian peak of the imaginary part of the complex exit wave
$\eta^{\mathcal{R}}_{m_i}$	26	column intensity of the m_ith Gaussian peak of the real part of the complex exit wave
η_n	44	column intensity of the nth Gaussian peak
$\boldsymbol{\theta}$	17	vector of the true parameters
$\hat{\boldsymbol{\theta}}$	19	unbiased estimator of $\boldsymbol{\theta}$
$\hat{\boldsymbol{\theta}}_{ML}$	22	maximum likelihood estimator
$\hat{\boldsymbol{\theta}}_{LS}$	22	least squares estimator
λ_{kl}	18	expected value of the Poisson distribution at the pixel (k, l)
λ^m_{kl}	27	expected value of the Poisson distribution at the pixel (k, l) of the mth focal image
λ	24	electron wavelength
$\lambda^{\mathrm{PI}}_{\mathcal{H}_i}$	104	expectation value of the peak intensity under $\mathcal{H}_i$
$\lambda_{\mathcal{H}_i,kl}$	106	expectation values for the pixel intensities of a STEM image under $\mathcal{H}_i$
μ	17	expected value
μ_g	60	location of gth component in the Gaussian mixture model
$\mu_{\mathcal{H}_i}$	108	expected value of normal distribution of $\ln \mathrm{LR}\left(\boldsymbol{\omega}^{Im}\right)$ under $\mathcal{H}_i$
ν	46	scaling factor
$\boldsymbol{\xi}$	45	linear parameters of the expectation model
$\Phi(x)$	108	cumulative distribution function of the standard normal distribution evaluated at x
π_g	60	mixing proportion of the gth component in the Gaussian mixture model
ρ	33	width of the atomic column for mono-type crystalline structures
ρ_i	18	column type dependent width of a Gaussian
ρ_n	44	width of the nth atomic column
σ	60	width of the components of the Gaussian mixture model
σ^2	17	variance
$\hat{\sigma}^2$	34	estimated lower bound on the variance, estimated CRLB

σ_{eff}	73	effective width of the normal components of the Gaussian mixture model
σ/δ	67	relative width of the components of the Gaussian mixture model
$\sigma^2_{\mathcal{H}_i}$	108	variance of normal distribution of $\ln \text{LR}\left(\boldsymbol{\omega}^{Im}\right)$ under $\mathcal{H}_i$
$\tau_g\left(\hat{V}_n; \boldsymbol{\Psi}_G\right)$	61	posterior probability that the nth scattering cross-section $\hat{V}_n$ belongs to the gth components of the Gaussian mixture model
$\phi_g\left(\hat{\mathbf{V}}; \mu_g, \sigma\right)$	61	normal component of the gth component in the Gaussian mixture model
$\phi_{1\text{s},m_i}(\mathbf{r}-\boldsymbol{\beta}_n)$	24	eigenfunction of the $1s$-state
$\chi^2_{1-\frac{\alpha}{2},N-1}$	37	$1-\frac{\alpha}{2}$-quantile of the χ^2 distribution with $N-1$ degrees of freedom
$\chi^2_{\frac{\alpha}{2},N-1}$	37	$\frac{\alpha}{2}$-quantile of the χ^2 distribution with $N-1$ degrees of freedom
$\boldsymbol{\Psi}_G$	60	vector of the parameters of the Gaussian mixture model
$\psi_{\text{ex}}(\mathbf{r}, z)$	24	complex exit wave
$\psi_{\text{im}}(\mathbf{r}, z; C_s, \epsilon_m)$	25	image wave
$\psi_{\text{int}}(\mathbf{r}, z)$	24	interaction wave
$\boldsymbol{\omega}$	17	vector of the stochastic variables of the observations $\mathbf{w}$
ω_{kl}	17	stochastic variable for the pixel (k, l)
ω^{PI}	103	stochastic variable for the peak intensities
ω^{CS}	103	stochastic variable for the scattering cross-sections
$\boldsymbol{\omega}^{\text{Im}}$	103	stochastic variable for HR STEM image pixel values of a projected atomic column

Abbreviations

Abbreviation	Page	Explanation
2D	3	two-dimensional
3D	3	three-dimensional
ADF	4	annular dark field
AIC	63	Akaike's Information Criterion
BF	4	bright field
BIC	63	Bayesian Information Criterion
CLC	63	Classification Likelihood information Criterion
CCD	3	charge coupled device
CRLB	7	Cramér-Rao lower bound
EM	61	expectation maximisation
FWHM	35	full width half maximum
GIC	63	Generalised Information Criterion
HAADF	3	high angle annular dark field
HR(S)TEM	15	high-resolution (scanning) transmission electron microscopy
ICL	64	Integrated Classification Likelihood
LSE	22	least squares estimator
MLE	20	maximum likelihood estimator
PDF	6	probability density function
PF	6	probability function

STEM	3	scanning transmission electron microscopy
(S)TEM	2	(scanning) transmission electron microscopy
TEM	3	transmission electron microscopy
WPOA	28	weak phase object approximation

List of publications

Papers in journals included in the ISI Web of Science

- A. De Backer, S. Van Aert, and D. Van Dyck, High precision measurements of atom column positions using model-based exit wave reconstruction, Ultramicroscopy 111 (2011) 1475-1482.

- M. Klingstedt, M. Sundberg, L. Eriksson, S. Haigh, A. Kirkland, D. Grüner, A. De Backer, S. Van Aert, and O. Terasaki, Exit wave reconstruction from focal series of HRTEM images, single crystal XRD and total energy studies on Sb_xWO_{3+y} ($x \sim 0.11$), Zeitschrift für Kristallographie 227 (2012) 341-349.

- S. Van Aert, A. De Backer, G.T. Martinez, B. Goris, S. Bals, G. Van Tendeloo, and A. Rosenauer, Procedure to count atoms with trustworthy single-atom sensitivity, Physical Review B 87 (2013) 064107.

- A. De Backer, G.T. Martinez, A. Rosenauer, and S. Van Aert, Atom counting in HAADF STEM using a statistical model-based approach: methodology, possibilities, and inherent limitations, Ultramicroscopy 134 (2013) 23-33.

- A.J. den Dekker, J. Gonnissen, A. De Backer, J. Sijbers, and S. Van Aert, Estimation of unknown structure parameters from high-resolution (S)TEM images: what are the limits?, Ultramicroscopy 134 (2013) 34-43.

- B. Goris, A. De Backer, S. Van Aert, S. Gómez-Graña, L. Liz-Marzán, G. Van Tendeloo, and S. Bals, 3D elemental mapping at the atomic scale in bimetallic nanocrystals, Nano Letters 13(9) (2013) 4236-4241.

- G.T. Martinez, A. Rosenauer, A. De Backer, J. Verbeeck, S. Van Aert, Quantitative composition determination at the atomic level using model-based high-angle annular dark field scanning transmission electron microscopy, Ultramicroscopy 137 (2014) 12-19.

- G.T. Martinez, A. De Backer, A. Rosenauer, J. Verbeeck and S. Van Aert, Effect of probe inaccuracies on the quantitative model-based analysis of high angle annular dark field scanning transmission electron microscopy images, Micron 63 (2014) 57-63.

- J. Gonnissen, A. De Backer, A.J. den Dekker, G.T. Martinez, A. Rosenauer, J. Sijbers, and S. Van Aert, Optimal experimental design for the detection of light atoms from high-resolution scanning transmission electron microscopy images, Applied Physics Letters 105 (2014) 063116.

- A. De Backer, A. De wael, J. Gonnissen, and S. Van Aert, Optimal experimental design for nano-particle atom-counting from high-resolution STEM images, Ultramicroscopy 151 (2015) 46-55.
- A. De Backer, G.T. Martinez, K.E. MacArthur, L.B. Jones, A. Béché, P.D. Nellist, and S. Van Aert, Dose limited reliability of quantitative annular dark field scanning transmission electron microscopy for nano-particle atom-counting, Ultramicroscopy 151 (2015) 56-61.
- G.T. Martinez, L. Jones, A. De Backer, A. Béché, J. Verbeeck, S. Van Aert, and P.D. Nellist, Quantitative STEM normalisation: the importance of the electron flux, Ultramicroscopy (2015), submitted.

Conference abstracts

- A. De Backer, S. Van Aert, and D. Van Dyck, High Precision Measurements of Atom Column Positions using Model-Based Exit Wave Reconstruction, 17th International Microscopy Congress - IMC17, Rio de Janeiro, Brazil, September 19-24, 2010, I2.28.
- A. De Backer, S. Van Aert, and D. Van Dyck, High Precision Measurements of Atom Column Positions using Model-Based Exit Wave Reconstruction, Microscopy Conference - MC2011, Kiel, Germany, August 28 - September 02, 2011, IM2.P118.
- S. Van Aert, S. Bals, A. De Backer, K.J. Batenburg, and G.Van Tendeloo, Model-based electron microscopy: from 2D images toward precise 3D atomic structures, Microscopy Conference - MC2011, Kiel, Germany, August 28 - September 02, 2011, IM2.213.
- S. Van Aert, G.T. Martinez, A. De Backer, A. Rosenauer, and G. Van Tendeloo, Beyond the limits of imaging: advances and applications of model-based scanning transmission electron microscopy, Microscopy & Microanalysis 2012 Meeting, Phoenix, AZ, USA, July 29 - August 02, 2012.
- A. De Backer, G.T. Martinez, A. Rosenauer, and S. Van Aert, Atom counting in HAADF STEM using a statistical model-based method, European Microscopy Congress - EMC 2012, Manchester, UK, September 16-21, 2012, P624.
- G.T. Martinez, S. Van Aert, A. De Backer, A. Rosenauer, and J. Verbeeck, Atomic scale quantification of chemical composition using model-based HAADF STEM, European Microscopy Congress - EMC 2012, Manchester, UK, September 16-21, 2012, P647.
- S. Van Aert, A. De Backer, G.T. Martinez, and G. Van Tendeloo, Beyond the limits of imaging: recent advances and applications of model-based (scanning) transmission electron microscopy, European Microscopy Congress - EMC 2012, Manchester, UK, September 16-21, 2012, 900.
- S. Van Aert, A. De Backer, G.T. Martinez, E. Mudry, J. Gonnissen, K.J. Batenburg, and S. Bals, Model-based scanning transmission electron microscopy : from 2D images toward 3D atomic structures, 13ème colloque de la Société Française des Microscopies, July 2-5, 2013.

- J. Gonnissen, A. J. den Dekker, A. De Backer, J. Sijbers, and S. Van Aert, Estimation of atomic numbers from STEM images: what are the limits?, Microscopy Conference MC 2013, Regensburg, Germany, August 25-30, 2013, IM.1.P010.

- G. T. Martinez, A. De Backer, H. Shi, D. Schryvers, A. Rosenauer, J. Verbeeck, and S. Van Aert, Statistical parameter estimation theory as a tool for quantitative HAADF STEM, Microscopy Conference MC2013, Regensburg, Germany, August 25-30, 2013, IM.1.P027.

- A. De Backer, G.T. Martinez, K.E. MacArthur, L. Jones, A. Béché, P.D. Nellist, and S. Van Aert, Possibilities and limitations for atom counting using quantitative ADF STEM, 18th International Microscopy Congress IMC 2014, Prague, Czech Republic, September 7-12, 2014, IT-10-O-2253.

- A. De Backer, A. De wael, and S. Van Aert, Probability of error for counting the number of atoms from high resolution HAADF STEM images, 18th International Microscopy Congress IMC 2014, Prague, Czech Republic, September 7-12, 2014, IT-2-P-2255.

- S. Van Aert, J. Gonnissen, A. De Backer, J. Sijbers, and A.J. den Dekker, Measuring structure parameters from electron microscopy images: what are the limits?, International 18th Microscopy Congress IMC 2014, Prague, Czech Republic, September 7-12, 2014, IT-16-O-2356.

- B. Goris, A. De Backer, S. Van Aert, G. Van Tendeloo, L.M. Liz-Marzan, and S. Bals, 3D elemental mapping of the atoms in bimetallic nanocrystals, 18th International Microscopy Congress IMC 2014, Prague, Czech Republic, September 7-12, 2014, MS-1-O-1802.

- S. Bals, B. Goris, T. Altantzis, D. Zanaga, A. De Backer, S. Turner, S. Van Aert, B. Freitag, and G. Van Tendeloo, High Resolution Imaging of Nanomaterials in 3 Dimensions, MRS Spring Meeting, San Francisco, California, US, April 6-10, 2015.

- S. Van Aert, A. De Backer, A. De wael, J. Gonnissen, G. Martinez, A. Béché, K. MacArthur, L. Jones, and P. Nellist, Quantitative annular dark field scanning transmission electron microscopy for nano-particle atom-counting: What are the limits?, PICO 2015 - 3rd Conference on Frontiers of Aberration Corrected Electron Microscopy, Kasteel Vaalsbroek, The Netherlands, April 19-23, 2015.

- A. De Backer, A. De wael, J. Gonnissen, G.T. Martinez, A. Béché, K.E. MacArthur, L. Jones, P.D. Nellist, and S. Van Aert, Quantitative annular dark field scanning transmission electron microscopy for nanoparticle atom-counting: What are the limits?, MMC 2015 incorporating EMAG 2015, Manchester, UK, June 29 - July 2, 2015, submitted.

- J. Gonnissen, A. De Backer, G.T. Martinez, I. Lobato, A.J. den Dekker, J. Sijbers, and S. Van Aert, Optimal experiment design for atom-counting in atomic resolution TEM and STEM: possibilities and limitations to the precision for both imaging methods, MMC 2015 incorporating EMAG 2015, Manchester, UK, June 29 - July 2, 2015, submitted.

Samenvatting

De exacte structuur en chemische samenstelling bepalen de fysische eigenschappen van nanomaterialen. Het is dan ook belangrijk om structuurparameters, zoals de atoomposities, de atoomtypes en het aantal atomen te meten om het verband tussen de structuur en de eigenschappen van materialen volledig te begrijpen. Door middel van atomaire resolutie (raster)transmissie-elektronenmicroscopie ((S)TEM, (scanning) transmission electron microscopy) kan lokale informatie over de interne structuur van materialen worden verkregen. De huidige microscopen zijn uitgerust met correctoren voor lensaberraties waardoor de visuele interpretatie van de beelden is vereenvoudigd. Toch is het onmogelijk om structuurparameters te meten enkel door een visuele interpretatie. Daarom wordt in deze studie getracht om precieze metingen te verkrijgen uit atomaire resolutie aberratie gecorrigeerde (S)TEM beelden met behulp van geavanceerde modelgebaseerde statistische methoden. Het eerste deel van deze thesis concentreert zich voornamelijk op de methodologie voor deze kwantitatieve aanpak. In het tweede deel zal worden onderzocht hoe het aantal atomen in een geprojecteerde atoomkolom kan worden geteld.

Voor een kwantitatieve analyse wordt een fysisch model gebruikt dat afhankelijk is van onbekende structuurparameters en dat de verwachtingen van de beelden beschrijft. Op deze manier wordt kwantitatieve structuurbepaling herleid tot een statistisch parameterschattingsprobleem. De pixelwaarden in de opgenomen beelden zijn dan de waarnemingen waaruit de structuurparameters geschat kunnen worden. Dit gebeurt door het model te fitten aan de experimentele beelden gebruikmakende van een maat die de overeenkomst tussen het experimenteel beeld en het model uitdrukt. De precisie waarmee de parameters geschat kunnen worden, wordt in de limiet enkel bepaald door toevallige fluctuaties. Statistische parameterschattingstheorie levert een theoretische ondergrens voor variantie van de parameters, namelijk de haalbare precisie waarmee de intrinsieke limiet op de precisie wordt weergegeven. Dit concept kan gebruikt worden om te bepalen op welke manier structuurparameters geschat kunnen worden uit de beschikbare waarnemingen en om na te gaan of de hoogst haalbare precisie bereikt kan worden door gebruik te maken van een welbepaalde schattingsmethode.
Eerst werd onderzocht op welke manier de atoomkolomposities zo nauwkeurig en precies mogelijk geschat kunnen worden uit een serie beelden opgenomen bij verschillende focuswaarden. Een zogenaamde focusserie wordt vaak opgenomen om de golffunctie aan het uittreevlak van het object te reconstrueren. Deze uittreegolf is eenduidig gerelateerd aan de objectstructuur. Gebruikmakende van simulaties werd duidelijk dat de gereconstrueerde complexe uittreegolf dezelfde hoeveelheid informatie bevat als de beelden van de volledige focusserie. Bovendien kon aangetoond worden dat dezelfde hoeveeldheid informatie kan worden verkregen uit de fase van de gereconstrueerde uittreegolf voor dunne specimens waarvoor de benadering voor

zwakke faseobjecten geldt.
Verder werd de nauwkeurigheid en precisie van geschatte structuurparameters voor donkerbeeldvorming met een ringvormige detector (ADF, annular dark field) in STEM onderzocht. Hiervoor werden de atoomkolomposities en de verstrooiingdoorsneden bekeken. Deze laatste parameter beschrijft de totale intensiteit aan verstrooide elektronen door een atoomkolom en kan gebruikt worden voor een kwantitatieve interpretatie van de beeldintensiteiten van de ADF STEM beelden in termen van het atoomtype en het aantal atomen. Gebruikmakende van gedetailleerde simulaties kon worden aangetoond dat ook voor een lage invallende elektronendosis de theoretische ondergrens op de variantie van de schattingen bereikt kon worden door de structuurparameters te schatten met behulp van de kleinste kwadratenschatter.
De rechtstreekse implementatie van de kleinste kwadratenschatter waarbij alle parameters gelijktijdig geschat worden is enkel mogelijk wanneer een beperkt aantal atoomkolommen geanalyseerd moet worden. Daarom werd een efficiënt algoritme voorgesteld zodat structuurparameters over grotere gebieden gekwantificeerd kunnen worden. Het nieuwe algoritme om ongekende stuctuurparameters te schatten werd toegepast op verschillende experimentele data. Deze toepassingen illustreren de verscheidene mogelijkheden voor een kwantitatieve analyse op atomaire schaal met hoge precisie die nu mogelijk zijn door het verbeterde algoritme.

Het tweede deel van deze thesis bespreekt een statistische methode om uit ADF STEM beelden het aantal atomen van kristallijne nanostructuren met één atoomtype in detail te tellen samen met een grondige studie van de mogelijkheden en de inherente beperkingen. Om het aantal atomen te tellen wordt verondersteld dat de verstrooiingsdoorsnede schaalt met het aantal atomen in een geprojecteerde atoomkolom. De verdeling die de kans beschrijft dat een verstrooiingsdoorsnede afkomstig is van atoomkolommen met een bepaald aantal atomen kan worden afgeleid uit de experimenteel gemeten verstrooiingsdoorsneden. Het aantal atomen in een atoomkolom wordt dan bepaald aan de hand van de geschatte kansverdeling. Het aantal atoomkolommen in het waargenomen STEM beeld, het aantal componenten in de geschatte kansverdeling, de breedte van de componenten van de kansverdeling en de typische vorm van een criterium dat gebruikt wordt om het aantal componenten in de kansverdeling te bepalen, beïnvloeden rechtstreeks de nauwkeurigheid en precisie waarmee het aantal atomen in een specifieke atoomkolom kan worden geteld. Rekening houdend met deze resultaten kan theoretisch aangetoond worden dat het aantal atomen zonder fout geteld kan worden.
Deze methode werd ook gebruikt om uit experimentele ADF STEM beelden van verschillende nanostructuren het aantal atomen te tellen. Op deze manier kon ook experimenteel aangetoond worden dat het aantal atomen zonder fout geteld kan worden in de meeste geanalyseerde atoomkolommen. Uit deze experimentele analyses bleek ook dat de statistische methode moet worden gebruikt in combinatie met een complementaire methode om de telresultaten te valideren. Hiervoor werd voornamelijk een combinatie met een simulatiegebaseerde aanpak geïntroduceerd. De experimentele verstrooiingsdoorsneden worden dan vergeleken met de gesimuleerde verstrooiingsdoorsneden bekomen met behulp van gedetailleerde STEM simulaties.
Ondanks dat kwantitatieve ADF STEM een krachtige methode is om nanodeeltjes te karakteriseren op atomaire schaal, kan de bepaling van de atomaire structuur nog steeds een uitdaging vormen door de beperkte grootte en de stralingsgevoeligheid van deze deeltjes. Daarom is het belangrijk om de inkomende elektronendosis te beperken. Nochtans zal dit ook de betrouwbaarheid verminderen zoals experimenteel werd aangetoond voor het tellen van atomen in deze

thesis. De limieten voor het tellen van het aantal atomen werden dan ook vastgesteld met behulp van de combinatie van de volledig statistische methode en de gedetailleerde beeldsimulaties.
Als laatste werden de principes van detectietheorie gebruikt om de kans op een telfout te kwantificeren voor STEM beelden. Binaire en meervoudige hypothesetoetsen werden bestudeerd om de limieten voor de precisie te bepalen waarmee het aantal atomen geteld kan worden. De kans op een telfout werd berekend voor verschillende criteria: STEM beelden op pixelgewijze basis, verstrooiingsdoorsneden of piekintensiteiten. Op basis van deze analyse kon worden geconcludeerd dat de verstrooiingsdoorsneden even goed presteren als de beelden, en beter presteren dan de piekintensiteiten. Gebruikmakende van de kans op een telfout kunnen ook de optimale detector instelling met betrekking tot het tellen van het aantal atomen worden afgeleid. Hieruit blijkt dat voor dunne objecten donkerbeeldvorming met een ringvormige detector onder lage hoek optimaal is en dat voor dikkere objecten de optimale binnenhoek van de detector toeneemt.

Dankwoord

Tijdens mijn opleiding Fysica heb ik mijn bachelor- en masteronderzoek bij professor Sandra Van Aert bij EMAT gedaan. Ik raakte stilaan meer en meer gefascineerd om uit elektronenmicroscopiebeelden zoveel mogelijk informatie te halen door verschillende disciplines te combineren: ik leerde de theorie van de beeldvorming in een elektronenmicroscoop en ik leerde experimentele elektronenmicroscopiebeelden niet enkel te bekijken als mooie afbeeldingen, maar te analyseren aan de hand van (de door zovelen gevreesde) statistiek. Door de positieve ervaringen tijdens mijn studies, leek het me wel erg boeiend dat ik dit onderzoek kon verderzetten in een doctoraat. Het was dan ook heel leuk toen Sandra me tijdens een van de besprekingen over mijn masterthesis voorstelde om een doctoraat te starten.

Sandra verdient het dan ook zonder twijfel om hier op de allereerste plaats bedankt te worden. Sandra, je fijne begeleiding, enthousiasme en vertrouwen werken erg motiverend en dat waardeer ik enorm.
Uiteraard is een thesis niet enkel het werk van de doctoraatsstudent en haar promotor. Daarom wil ik hier toch een aantal mensen persoonlijk bedanken. Professor Staf Van Tendeloo wil ik bedanken voor alle steun en voor het verder uitbouwen van EMAT tot de mooie microscopiegroep die EMAT nu is. Next, I would like to thank the current members of 'the group of Sandra' within EMAT: Gerardo, Julie, Karel, and Marcos. Thank you for the many valuable discussions we had. Gerardo, thank you for all the simulations you did. Karel, jou wil ik ook nog bedanken voor Fig. 1.2. Ik weet dat de eerste versie van die figuur veel moeite heeft gekost. Verder wil ik ook professor Dirk Van Dyck bedanken die me tijdens mijn studies geïntroduceerd heeft in de theoretischere benadering van elektronenmicroscopie en voor zijn aanstekelijk enthousiasme. Professor Arjan den Dekker wil ik bedanken voor zijn waardevolle tips over statistiek. Professor Jan Sijbers wil ik bedanken voor de hulp bij het ontwikkelen van het efficiënte fitalgoritme. Professor Sara Bals en Bart wil ik bedanken om me verschillende mogelijkheden te hebben geven om experimentele beelden te analyseren. Het is altijd een leuke uitdaging om nieuwe methoden ook in de praktijk effectief toe te passen.
A part of the work in this thesis results from a collaboration with the group of professor Peter Nellist of the University of Oxford. I would like to thank him and Lewys Jones and Kate MacArthur of his research group for the valuable collaboration. I also enjoyed the ATOM workshops during which I was able to share and improve my research results.
I also would like to thank Shirley, Maria, and Dmitry for their help with contextualising the analysis of displacement mapping of the $LaAlO_3$ in my thesis text.
Daarnaast wil ik Kim ook bedanken voor het ontwerpen van de mooie cover van deze thesis. Koen wil ik ook graag bedanken om me te helpen met computergerelateerde problemen, zeker toen mijn laptop weigerde te werken tijdens de laatste momenten van het schrijven van mijn

thesis.
Uiteraard wil ik alle groepsleden en oud-groepsleden van EMAT bedanken die ik heb leren kennen gedurende de afgelopen jaren voor hun steun op verschillende vlakken. Thank you all EMAT-members.

Tot slot wil ik mijn familie bedanken. Een rijk leven is meer dan wetenschappelijk onderzoek alleen. Bedankt voor jullie onvoorwaardelijke steun en interesse in wat ik doe. Illya, de afgelopen jaren heb ik niet enkel een doctoraat afgewerkt, maar zijn er ook een aantal prachtige veranderingen geweest in ons leven samen, en jij weet hoe dankbaar ik je voor alles ben. Jinte, mijn kleine lieve meid, je beseft het nog niet, maar jij verzet mijn gedachten elke keer als ik thuiskom van zodra je enthousiast ‘mama’ roept! Hopelijk spartelen er binnenkort nog een paar voetjes vrolijk mee!

Annick De Backer